Single molecule interactions in biological systems

by Ingrid Tessmer, BSc(Hons), Dipl.Phys.

Thesis submitted to the University of Nottingham
for the degree of Doctor of Philosophy, December 2002

Da steh ich nun, ich armer Tor!

Und bin so klug als wie zuvor

Faust I (Johann Wolfgang von Goethe)

Contents

List of Figures

List of Tables

Abstract:

The interactions of biological molecules are traditionally investigated using ensemble techniques. These provide information on the molecular behaviour based on averaged data resulting from collective ensemble properties. While this has enabled the resolution of structure and function of many proteins and other biomolecules, an understanding of *how* and *why* the molecules go about structural changes and modulate inter- and intra-molecular interactions is difficult to gain using these approaches.

More recently, single molecule techniques have evolved. These allow us to follow the behaviour of the individual molecules over time and/or under changing conditions. From such data, subtle molecular changes can be resolved without the need to synchronise the system. Further, variations within a biological system can be detected which would be lost using the ensemble techniques, due to the concomitant averaging procedures. This is exploited to help understand the molecular procedures involved.

In this thesis, the application and comparison of two of the main single molecule techniques, optical tweezers and AFM, are described. With these, a range of systems was investigated; namely drug-DNA, protein-DNA, and cell adhesive interactions. The presented results provide new and complementary

information on the different biological systems, demonstrating the diversity of single molecule applications. The combination of different experimental approaches was further exploited to gain a more complete picture of the observed processes.

Chapter 1

Introduction: Single Molecule Studies

Information upon the interaction of biological molecules can be obtained using different experimental approaches. The established biochemical techniques provide data on collective, average properties of systems of millions of molecules. In contrast to this, measurements on single molecules offer the exciting prospect of approaching different molecules directly and separately, thus resolving in greater detail the effects on and the behaviour of the individuum. This has led to, for example, insight into the stepping of single myosin molecules along actin filaments in muscle movement [Veigel et al., 1998; Shepherd et al., 1990]. Further, mutant behaviour that would not show in the dominating large bulk systems can be detected with such techniques [Oberhauser et al., 1999], often giving important insight into the function of the whole system. From a practical point of view, such techniques also require very small amounts of sample material, and are therefore

valuable in the research on systems with low availability.

1.1 Measuring biomolecular interaction forces

Forces between biological molecules are composed of many different, non-covalent interactions, such as electrostatic attraction, ion-dipole or hydrophobic interactions, or hydrogen or van der Waals bonding. Under physiological conditions, all these interactions act over short distances of the order of 1 nm [Merkel, 2001] and involve binding enthalpies on the order of the thermal energy, k_BT (where k_B is the Boltzmann constant, and T is the absolute temperature), only [Creighton, 1993]. The weak local forces, however, act together to form the stable and specific bonds between receptor and ligand molecules [Merkel, 2001]. Further, the many interactions within different parts of one molecule determine its mechanical properties [Leckband, 2000].

Interaction forces are exploited to gain information on molecules at the single molecule level in non-optical imaging and force measuring techniques. In these experiments, a probe approaches a molecule, inducing a range of interactions between molecule and probe. Both attractive and repulsive interactions lead to fine displacements of the probe, which are detected using different technique specific methods. From the measured interaction forces, conclusions can be drawn on sample properties, such as surface topography, molecular elasticity, or specific interactions between the molecule and structures on the surface of the probe.

Recent developments have enabled the study of single biological molecules by a range of techniques. These can be divided into imaging and force mea-

suring applications. Figure 1.1 offers an overview of the versatile area of single molecule techniques. In the following sections, the different approaches will be discussed separately for clarity. Detailed overviews have also been published on single molecule imaging, for example by Colton et al. [1997], Hansma and Pietrasanta [1998], da Silva [2002], and Weiss [1999], and on single molecule force spectroscopy by Bustamante et al. [2000a], Clausen-Schaumann et al. [2000], and Merkel [2001].

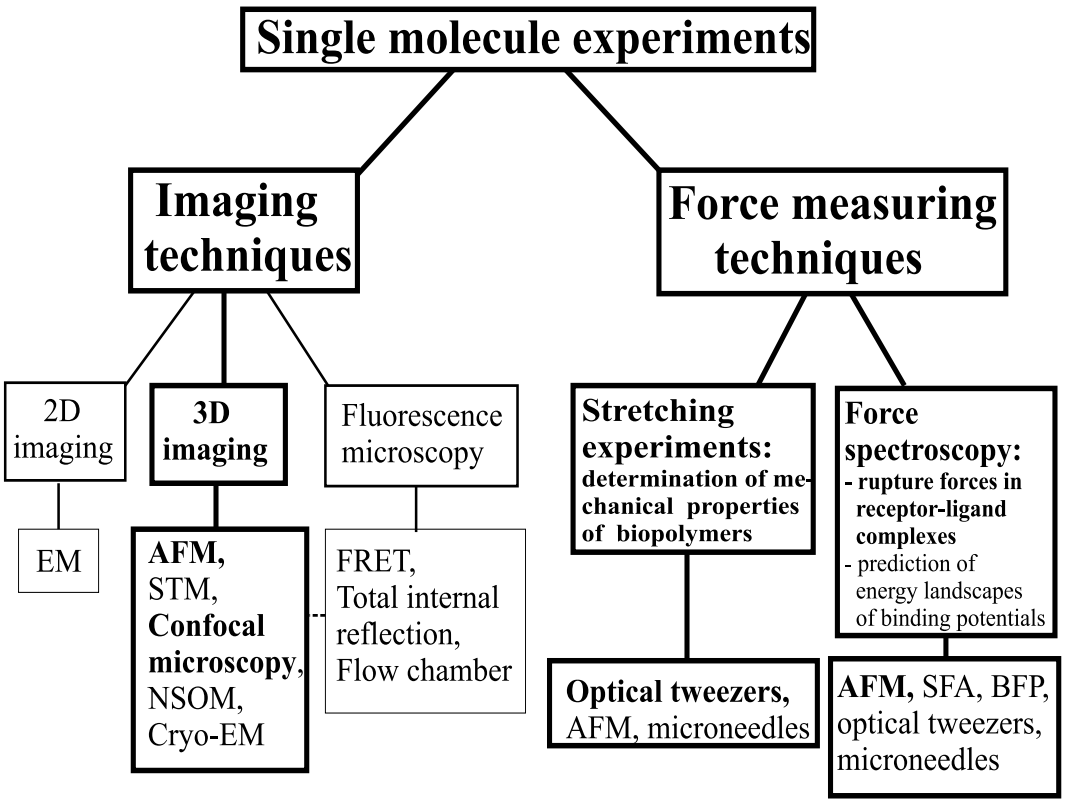

Figure 1.1: Single molecule techniques. Techniques employed within the work presented in this thesis have been highlighted.

1.2 Imaging of single molecules

The refinement of techniques has enabled imaging of individual biomolecules with molecular or submolecular resolution within the past few decades. For this, two different approaches are employed:

- "operation at a distance": optical detection of electromagnetic radiation (optical microscopy) or electrons (electron microscopy) after interaction with the biological sample (optical techniques)
- mechanical scanning of a surface: measuring forces between biological surfaces and a mechanical probe which is close to or directly in contact with the sample (non-optical techniques)

Therefore, imaging techniques can be again crudely divided into optical and non-optical techniques.

1.2.1 Optical techniques

Light microscopy resolution is limited by diffraction to approximately half the wavelength of the employed light. For visible light, this is $\gtrapprox$ 400 nm. Such resolutions are suitable only for complex biological objects such as whole cells which are of the order of magnitude of micrometers.

In the 1930s, the electron microscope (EM) was introduced, offering nanometer resolution of stained biological specimen [Sperrazza et al., 1984]. The sample preparation required for this technique, that operates in vacuum, however, does not allow imaging of functional biological particles.

The development of cryo-EM enabled access to three-dimensional information on frozen biological molecules at high resolution ($\gtrapprox$ 0.4 nm) [Murata et al., 2000; Unger, 2001].

An optical microscopy technique that enabled improved spatial resolution was developed with the confocal microscope. Confocal microscopy allows the acquisition of images of relatively thick samples, by restricting detection to single layers through the sample. From superposition of the data, three-dimensional information on the imaged samples can be obtained. This technique further provides the possibility of working in near physiological liquid environments. Its resolution is, however, still diffraction-limited to several hundreds of nanometers. However, the combination of confocal microscopy with fluorescent biomolecule markers has enabled improved spatial resolution of $\gtrapprox$ 200 nm, and was shown to be superior to conventional light microscopy for the study of biological structures [White et al., 1987].

Fluorescence single molecule detection has been brought forward rapidly since the early days of marking single antibody molecules with fluorophores in the 1970s [Hirschfeld, 1976]. Optical scanning microscopy with charge coupled device (CCD) cameras, in combination with total internal reflection has been employed to study dynamic systems such as fluorescently labelled single motor proteins [Funatsu et al., 1995; Vale et al., 1996; Tanaka et al., 2002] or components within cell membranes [Schmidt et al., 1996]. Computer aided precision detection of dye molecules, that present point light sources within a sample, have enabled resolutions of a few tens of nanometers [Weiss, 1999]. Interaction of two fluorophores by fluorescence resonance energy transfer (FRET), in which the fluorescence intensity of a

dye molecule is modulated dependent on its distance to the neighbouring dye molecule, can be exploited to resolve even smaller distances (2 to 8 nm) between two labelled sites in the sample [Weiss, 1999]. FRET has been used to study, for example, colocalisation within receptor-ligand systems [Schütz et al., 1998], or conformational changes in proteins and deoxyribonucleic acid (DNA) [Deniz et al., 1999; Deniz et al., 2000; Grunwell et al., 2001]. Improvement of the obtained signal to noise ratio in fluorescence microscopy can be achieved by limiting the illuminated sample volume, using techniques such as near-field scanning optical microscopy (see next section) or confocal microscopy [Moerner and Orrit, 1999]. Possibilities to access further information or greatly improve image resolution lie in different combinatory applications, for example interferometric or spatially modulated excitation combined with fluorescence microscopy [Schneider et al., 1998], or FRET combined with AFM [Vickery and Dunn, 2001].

1.2.2 Non-optical techniques

The early eighties brought the development of the scanning tunnelling microscope (STM) by Binnig et al. [1982]. Initially, the technique was applied to conductive surfaces under vacuum conditions only [Binnig et al., 1982]. However, STM can be used on non-coated biological samples in air under high humidity environmental conditions [Guckenberger et al., 1994; Patel et al., 1997]. Considerable sample preparation is, however, involved.

The STM has inspired a range of instruments which are termed, together with the STM, the family of scanning probe microscopes (SPMs). All of

these employ piezoelectric crystal devices to three-dimensionally control the position of a probe, while scanning the sample surface. Examples are the near-field scanning optical microscope (NSOM) [Pohl et al., 1984], the scanning thermal microscope [Williams and Wickramasinghe, 1986], the nuclear magnetic resonance force microscope [Rugar et al., 1990], and the atomic force microscope (AFM) [Binnig et al., 1986].

Since its invention by Binnig et al. in 1986, the AFM has become one of the most popular instrumental techniques in biophysical research. In contrast to EM, AFM provides the possibility to image biological objects under near native conditions, since it does not require staining of the sample and can further operate in liquid environments. This allows direct observation of dynamic processes in biological systems, such as condensation of DNA [Fang and Hoh, 1998; Martin et al., 2000], enzyme activity [Kasas et al., 1997; Guthold et al., 1999], or conformational changes in proteins [Müller et al., 1996; Müller et al., 1997; Müller et al., 1999a]. It further leads to the advantage of a relatively easy sample preparation. Another major advantage of this technique over EM is its possibility to provide three-dimensional images [daSilva, 2002]. Due to its ideal suitability for biological applications, the AFM is therefore today the most commonly employed amongst all SPMs in biophysical studies. Using this technique, nanometer [Walters et al., 1996; Allison et al., 1997; Wyman et al., 1997] and sub-nanometer resolutions [Scheuring et al., 1999; Engel and Müller, 2000] have been achieved on different biomolecules. An application of AFM high resolution imaging for the interpretation of protein-DNA binding interactions will be presented in chapter 5 of this thesis.

AFM imaging has further been applied to cells. Cell surfaces proved more difficult targets for imaging applications, allowing only resolutions $\gtrapprox$ 30 nm, likely due to deformations within the cell surface upon tip contact [Hansma and Hoh, 1994]. Nevertheless, important information on virus-cell interactions or dynamic processes within cells have been resolved with AFM [Butt et al., 1990; Fritz et al., 1993].

1.3 Single molecule force spectroscopy

The introduction of force probing techniques has made information on mechanical properties, subtle structural changes and interaction forces in biological systems available at the molecular level. The last two decades have seen major innovations in this field of instrumental development. Today, various force measuring techniques are available, spanning a wide range of accessible forces of between 10^{-14} and 10^{-6} N. Examples are listed in table 1.1, which also gives the accessible force range for each of the techniques, the most common applications, and specific advantages of each technique.

The principle of these techniques is the detection of the response of a single molecule or several molecules, to an applied force. While the surface force apparatus (SFA), the AFM, microneedles and micropipette aspiration use mechanical devices for the force probe, techniques have further been developed which employ external force fields to manipulate single molecules and detect the molecular forces exerted in response. Examples for such techniques are the flow chamber, and magnetic and optical tweezers, using flow, magnetic, and photon fields respectively [Bustamante et al., 2000a]. Within

Surface force apparatus (SFA)	10 nN - 1 μN	Bond strengths	Large contact areas (no single molecules)
AFM force probe	10 pN - 100 nN	Protein unfolding, Polysaccharides, Bond strengths	Imaging AND force measurements, Commercially available
Flow field	0.1 pN - 1 nN	DNA dynamics, RNA polymerase	Simplicity
Micropipette aspiration / Biomembrane force probe (BFP)	0.01 pN - 1 nN	Bond strengths	Tunable range of spring constants
Microneedles	1 pN - 100 pN	Motor proteins, Polymer strength	Good operator control
Optical tweezers	0.1 pN - 100 pN	Motor proteins, Protein unfolding, DNA elasticity	Precise manipulation, High force resolution
Magnetic tweezers	0.01 pN - 10 pN	Entropic elasticity, Topoisomerase activity	Torque introduction, Low spring constants

Table 1.1: Force measuring techniques, their approximate accessible force ranges, common applications, and advantages/disadvantages as taken from [Leckband, 2000; Bustamante et al., 2000a; Evans et al., 1995].

these techniques, forces on molecules often act indirectly through "handles". These are beads from various materials to the surfaces of which the molecules are attached. The force fields are then used to control the position of the handles, stretching the attached molecules. A brief description of each of the techniques will be given in the following sections.

Surface force apparatus

The SFA consists of two crossed cylinders. Their radii of curvature are typically between 1 and 2 cm, and the contact area between them is between 1 and 5 μm^2 [Leckband, 2000]. Interacting molecules are immobilised on the two opposing surfaces. The measurement of forces between them is based on high resolution ($\gtrapprox$ 0.1 nm) interferometric detection of the separation of the two cylinders and simultaneous determination of the inter-surface interactions. Although such large contact areas do not allow for the measurement of single molecule interactions, this technique offers the advantage of providing information on the free energy between the molecules directly [Leckband, 2000]. This enables access to equilibrium protein behaviour. With the SFA, forces $\gtrapprox$ 10 nN can be measured. The technique is used mainly for the study of bond strengths [Leckband et al., 1994].

AFM

The force probing AFM uses a fine tip (end diameter between 10 and 50 nm [Leckband, 2000; Thundat et al., 1992]) on a cantilever. The cantilever arm serves as a soft spring to measure forces between the tip and a substrate surface. Cantilevers are available between approximately 100 μm and 250 μm

long, offering spring constants of between approximately 10^5 and 1 pN/nm, respectively [Bustamante et al., 2000a]. The force resolution of AFM is limited by thermal noise to approximately 10 pN [Bustamante et al., 2000a]. The possibility of both force measuring and imaging applications is one of the great advantages of AFM. Furthermore, AFMs as well as standardised AFM probes are now readily available commercially [Bustamante et al., 2000a]. Uses of force probing AFM are versatile; it has been employed for both the determination of intra- and intermolecular interaction forces - for example, in DNA stretching experiments [Rief et al., 1999] or receptor-ligand interaction studies [Florin et al., 1994; Hinterdorfer et al., 1995; Benoit et al., 2000]. A detailed discussion of force probing AFM can be found in chapter 2 (Instrumental Methods) of this thesis.

Microneedles

Glass microneedles are typically 50 to 500 μm in length and 0.1 to 1 μm in diameter [Bustamante et al., 2000a]. The experimental principle is similar to that of AFM. Their different dimensions lead to much lower spring constants of between 1 and 10^{-3} pN/nm [Bustamante et al., 2000a], allowing the resolution of lower forces (see table 1.1). Microneedles have been used in the study of interaction forces for example between two actin monomers [Ishijima et al., 1991] or a cell selectin receptor and carbohydrate molecules [Tees et al., 2001].

Micropipette aspiration

Micropipette aspiration uses a cell membrane as force transducer. The cell is held by suction at the tip of a micropipette, while the test particle on the tip of a second, opposing micropipette is brought into contact with the cell. This particle can be a second cell, or a bead with proteins attached to its surface. The biomembrane force probe (BFP) is a rather recent modification of this technique [Evans et al., 1995], in which a bead is attached to the force probing cell. Functionalising of the surface of the bead allows measurements of interactions of a large range of molecules. Interactions between molecules on the surface of the bead and molecules on the surface of the opposing particle can be measured from deformations of the membrane, using, for example, reflectance interference contrast microscopy [Evans et al., 1995]. Here, the applied suction force with which the cell is held at the tip of the micropipette determines the membrane elasticity and thus the spring constant of the force probing system. This allows the detection of a tunable, broad range of accessible forces (see table 1.1). The BFP has thus proven an ideal tool for the investigation of energy profiles of receptor-ligand complexes. In particular, it has been used to study the prototype receptor-ligand system streptavidin-biotin [Merkel et al., 1999].

Flow field

In this technique, laminar flow serves to apply a drag force to a bead, which is tethered to the bottom surface of the surrounding liquid microchamber by a strand of DNA. Flow force has mostly been used in connection with

a magnetic field acting in orthogonal direction [Bustamante et al., 2000a]. The magnetic force on the molecule can be calculated from the known bead dimensions and the flow speed using Stokes' law, and the angle between the magnetic field and the DNA strand. An advantage of this technique is the ease of exchanging the surrounding buffer through the in- and outlets of the microchamber [Bustamante et al., 2000a]. The flow chamber assay is also a commonly employed technique in the study of cell adhesion [Tha et al., 1986; Alon et al., 1995; Chen and Springer, 2001], receptor-ligand interactions [Pierres et al., 1995], and DNA dynamics [Doyle et al., 2000].

Optical tweezers

A dielectric bead of typically 1 to 3 μm diameter generally serves as the force probe in optical tweezers. Biological molecules can be attached to the surface of the bead, which is held in the potential well of a laser light focus by the forces of the photon field. A soft spring constant can be ascribed to the laser focus potential. Displacement of the bead within the potential, due to interactions with molecules on a substrate surface, is detected and translated into a force on the bead. The theory and instrumentation of this technique, which is also referred to as single-beam gradient traps, are discussed in detail in chapters 2 and 3 of this thesis. The study of elastic properties of biopolymers [Bustamante et al., 1994; Liphardt et al., 2001] and cell membranes [Svoboda et al., 1992; Bronkhorst et al., 1995; Hénon et al., 1999], as well as dynamic protein processes [Kuo and Sheetz, 1990; Edidin et al., 1991; Wang et al., 1998; Veigel et al., 1998; Wuite et al., 2000] have been the most common applications of optical tweezers.

A second configuration for optical trapping has further been introduced [Ashkin, 1970a], in which two opposing laser beams are employed to achieve stable trapping. This technique, known as a dual-beam trap, enables trapping much deeper within a liquid sample cell (100 μm away from the surface) than the single-beam gradient trap [Ashkin and Dziedzic, 1985; Smith et al., 1996]. Dual-beam traps have been predominantly used for experiments on DNA elastic properties [Smith et al., 1996; Baumann et al., 1997].

Magnetic tweezers

This technique employs a magnetic bead of typically < 3 μm diameter, held in a magnetic field. Torsional force can be applied to a molecule tethered between the bead and a surface. The magnetic force on the molecule can be determined in combination with a flow microchamber by calibration against Stokes drag, or by employing the equipartition theorem on the thermal noise spectrum of the bead positions [Bustamante et al., 2000a]. The strength of magnetic tweezers is the low spring constant of this technique, enabling the resolution of forces as low as 0.01 pN [Bustamante et al., 2000a]. Magnetic tweezers have, for instance, been used to measure the low force, entropic elasticity of DNA [Smith et al., 1992]. Furthermore, magnetic tweezers are unique in the possibility to introduce a torque in a biopolymer tethered between a surface and a magnetic bead. This has been exploited to investigate the effect of supercoiling on the elastic properties of DNA [Strick et al., 1996].

Different types of experiments can be realised with force measuring techniques. As indicated in the diagram of figure 1.1, these are, on the one hand, experiments in which a molecule is stretched in order to determine its me-

chanical properties from its resistance to the applied stretching force. On the other hand, in the second type of experiment, complexes between interaction partners are pulled apart until rupture occurs (measurement of bond strengths). From a large number of rupture events collected, information on the underlying intermolecular interactions can be deduced. Both types of experiment are discussed in more detail in the following sections.

1.3.1 Stretching experiments

In order to investigate the elastic properties of biopolymers such as DNA or various proteins [Tskhovrebova et al., 1997; Kellermayer et al., 1997; Svoboda et al., 1993] these molecules are tethered between a stationary surface and the force probe. The connections to the two surfaces are based either on covalent bonds [Lee et al., 1994a; Allen et al., 1997; Hegner, 2000], strong receptor-ligand interactions [Smith et al., 1992; Baumann et al., 2000; Hegner, 2000] or bare physisorption [Rief et al., 1997a; Rief et al., 1999]. The force probe can then be described by a mechanical spring, used to stretch the polymer carefully without breaking the tether. Upon stretching, the polymer's resistance induces a force on the force probe, which pulls the probe minutely towards the surface. The resulting probe displacement can be detected by a range of mechanisms, partly depending on the employed force technique. From this, the force response of the stretched molecule can be calculated, using the probe's spring constant. This will be explained in detail for AFM and optical tweezers in chapter 2 (Instrumental Methods) of this thesis.

Measuring mechanical molecular properties

The complex processes of protein folding/unfolding have been followed with stretching experiments using AFM and optical tweezers. Proteins studied include the giant muscle protein titin [Rief et al., 1997b; Kellermayer et al., 1997] and the polysaccharide dextran [Rief et al., 1997a]. Conformational transitions of the molecules can be detected from kinks or discontinuities in the obtained force-extension curves. Supported by theoretical modelling studies, the observed stretching behaviour can be analysed in terms of molecular properties of the polymers [Rief et al., 1998]. For example, the force-extension curves of dextran displayed a kink at the relative high force of approximately 700 pN at the applied pulling rate. This was interpreted as the simultaneous flipping of a bond angle into a new position within each of the monomers making up the polysaccharide. In contrast, the curves obtained for titin displayed a "saw tooth" pattern, in which the eight "teeth" (peaks) of between 100 and 200 pN (at the applied pulling rate) were attributed to the successive unfolding of individual protein domains. The strongly contrasting stretching behaviour of titin and dextran reflects their different structures.

Due to its fundamental importance for life and its interesting physical structure, DNA has been one of the most extensively studied systems in biophysical research. Stretching experiments on DNA have been conducted using flow fields [Perkins et al., 1995; Doyle et al., 2000], microneedles [Léger et al., 1999], optical tweezers [Bustamante et al., 1994], magnetic beads [Smith et al., 1992], and AFM [Rief et al., 1999]. Theoretical polymer models have been developed to describe the stretching behaviour of this biopolymer

[Bustamante et al., 1994; Marko and Siggia, 1995a; Bustamante et al., 2000b]. Fitting these models to the experimentally obtained data provides mechanical properties of the molecule. A detailed discussion of the theoretical model of DNA stretching behaviour can be found in chapter 4.

Optical tweezers stretching applications further include the folding and unfolding of RNA structures [Liphardt et al., 2001], as well as the study of transmembrane proteins [Edidin et al., 1991], and the elastic behaviour of the red blood cell membrane skeleton [Svoboda et al., 1992; Bronkhorst et al., 1995; Hénon et al., 1999].

Study of dynamic motor protein processes

Motor proteins translate chemical energy into movement by production of mechanical force. For the study of the dynamic processes of motor proteins, a fast responding technique with high temporal resolution is required. Flow field studies, microneedles, and optical tweezers combined with video microscopy are ideally suited for such applications.

Microneedles have been used for example to manipulate single actin filaments in the absence and presence of myosin, to investigate the interactions involved in the system [Kishino and Yanagida, 1988]. Further, the introduction of optical tweezers has enabled high force and temporal resolution of such processes. The optical trap can exert a force on a motor protein opposing its direction of motion, while the force response of the molecule as well as the change in its velocity are recorded. This has been employed for the investigation of the stepwise translocation of myosin along actin filaments [Veigel et al., 1998; Shepherd et al., 1990] and kinesin along microtubules

[Svoboda and Block, 1994a; Block et al., 1990; Kuo and Sheetz, 1990].

Enzyme machineries such as polymerases can displace along strands of DNA in order to perform their various functions. Flow fields and optical tweezers have been used in experiments on polymerase-DNA complexes [Davenport et al., 2000; Yin et al., 1995; Wang et al., 1998]. DNA polymerases possess a further, exonuclease activity, producing single stranded DNA from double stranded DNA. In an elegant experiment, Wuite et al. [2000] exploited this and the different elasticities found for single and double stranded DNA, to measure the mechanical force generated by a polymerase molecule.

1.3.2 Rupture forces of receptor-ligand complexes

A second type of application of force measuring techniques is the determination of rupture forces of receptor-ligand complexes. Generally, these experiments involve the immobilisation of receptor molecules on a surface. A second surface, usually that of the force probe, is then coated with the corresponding ligand molecule. When the two surfaces are brought into contact, non-covalent bonds are formed between receptor and ligand molecules. The force probe is then retracted from the surface. The mechanical force on the complexes is proportional to the distance between the probe and the stationary surface, and the probe is pulled towards the surface, as described for stretching experiments above. The receptor-ligand complexes break up when the force exerted on them overrules the strength of the interactions.

The force probe jumps back upon the sudden release from the pulling force. Therefore, detection of the force experienced by the force probe provides information on the "strength" of receptor-ligand rupture events. The measured forces relate to the bond strengths of the complexes. For the determination of the interaction force between a single receptor and its ligand, patient sample preparation and blocking of the majority of receptor molecules is necessary in order to reduce the effective surface density of molecules.

As can be seen from table 1.1, techniques for the measurement of bond strengths are mainly the surface force apparatus (SFA), the AFM, and the micropipette aspiration technique, although formerly flow chambers have also been employed to this end [Tha et al., 1986]. The SFA is suitable for detection of high forces, in the nN- to μN-range. Due to its large contact area, it does however not easily allow the detection of interactions between single molecules. The SFA has been used mainly for the study of receptor-ligand interactions [Leckband et al., 1994], and properties such as charge density distributions of single layer immobilised orientated receptor molecules [Sivasankar et al., 1998].

The soft spring constant of the AFM force transducer arm and small contact area of the AFM force probe enable resolution of much lower forces and single molecule interactions [Florin et al., 1994]. Due to its particularly high affinity and specificity, the first receptor-ligand complex investigated in AFM force distance experiments was the streptavidin-biotin system [Lee et al., 1994b]. This and the almost identical avidin-biotin complex served as a model system to study the potential of AFM for the determination of intermolecular interaction forces and they are now amongst the

most thoroughly studied receptor-ligand systems (research for example by Florin et al. [1994], Moy et al. [1994], Allen et al. [1996], Wong et al. [1998]). Other examples of systems studied by AFM force distance measurements are antigen-antibody complexes [Hinterdorfer et al., 1995; Hinterdorfer et al., 1996; Allen et al., 1997], and interaction forces between single strands of DNA [Lee et al., 1994a] and between pairs of cell adhesion molecules [Benoit et al., 2000]. In chapter 6 of this thesis, studies of interaction strength and frequency on a neutrophil adhesion receptor molecule using AFM and optical tweezers will be presented.

More recently, approaches to combine the measurement of rupture forces with AFM imaging have further allowed the localisation of receptors on both functionalised surfaces [Raab et al., 1999] and living cells [Grandbois et al., 2000].

Building on early work on force-induced dissociation of single bonds using micropipette aspiration [Tha and Goldsmith, 1988], through the development of an improved version of this technique, the BFP, Merkel et al. have been able to show a dependency of the rupture force and bond survival time on the rate of applied force (loading rate) [1999]. An effect of the applied field force on receptor-ligand rupture forces was also established using the flow chamber technique [Tees et al., 1993; Alon et al., 1995]. These results have led to the realisation that a single yield rupture force is insufficient for the description of biological binding and unbinding processes. A new type of theoretical and experimental approach evolved, which was concerned with the investigation of energy landscapes of receptor-ligand bonds, governing the measured forces.

Probing energy landscapes

Energy landscapes of receptor-ligand bonds are accessible via the loading rate dependency of rupture forces [Evans and Ritchie, 1997]. The loading rate r_F of an experiment is the rate at which the mechanical force F is applied to the system. It is defined as the temporal derivative of the force, and equals the product of probe stiffness κ and velocity v:

$$r_F = \frac{\partial}{\partial t} F = \frac{\partial}{\partial t}(\kappa x) = \kappa v \tag{1.1}$$

where $\frac{\partial}{\partial t}$ is the partial derivative with respect to time and x is the separation of force transducing probe and surface.

The rupture force within an experiment is determined by the dominant potential barrier E_b within the energy landscape $E(x)$ along the microscopic reaction coordinate x of the system. As shown in figure 1.2, this barrier is lowered by the application of an external force F by the mechanical potential $Fx\cos\theta$, where θ gives the orientation of F relative to x:

$$E(F, x) = E(x) - Fx\cos\theta \tag{1.2}$$

where $E(F, x)$ is the energy along the microscopic reaction coordinate x in the presence of an external force F, and $E(x)$ is the energy in the absence of force.

The maximum in the distribution of rupture forces from a large number of repeated measurements defines the bond strength [Evans, 1998]. The connection between loading rate and measured bond strength of a complex follows from the Kramers-Smoluchowski theory for the transition rate for

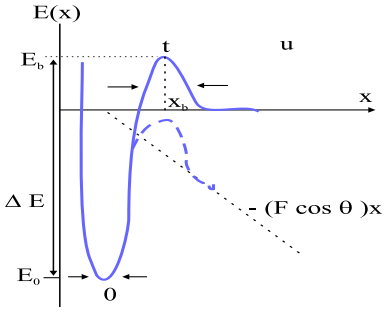

Figure 1.2: Schematic of an energy landscape of a molecular system in the presence of an external force F for a single energy barrier [Evans, 1998]. The energy of the barrier is $E_b = E_0 + \Delta E$, its distance from the potential minimum E_0 is x_b. The projection of F onto the microscopic reaction coordinate x, $F\cos\theta$, lowers the potential barrier of the transition state t between the bound state 0 and the unbound state u: $E_b(F) = E_b - Fx_b\cos\theta$. The action of F on E_b does not affect x_b for steep potential barriers. The transition rate from the bound into the unbound state is increased for lower E_b.

escape past a single sharp energy barrier from the bound into the unbound state [Bell, 1978; Evans, 1998]:

$$k_{off}(F) \approx (\frac{1}{t_0}) \exp \frac{F}{f_\beta} \tag{1.3}$$

where $k_{off}(F)$ is the force dependent transition rate from bound to unbound state, t_0 is the native life time of the bond, and $f_\beta = \frac{k_B T}{x_\beta}$ is termed the force scale of the system, with $x_\beta =< x_b \cos\theta >$ being the thermally averaged projection of the transition state on x. The applied force F rises linearly with probe-surface separation [Evans, 1998]. From equation 1.3 follows, that when the applied force $F = r_F t$ becomes larger than the thermal force scale f_β, the

escape rate out of the bound state is enhanced exponentially, and transition into the unbound state, i.e. bond rupture, occurs. Varying r_F and plotting the measured bond strengths versus the natural logarithm (ln) of r_F gives a linear relationship. The gradient of the line through the data is proportional to k_BT/x_β, its intercept with the $\ln r_F$ axis reflects the magnitude of the barrier energy [Evans, 1998]. This thus yields information on the energy landscape of a system. Scanning the bond strengths for a range of applied loading rates is termed dynamic force spectroscopy. Loading rate dependent rupture forces have been measured for the (strept)avidin-biotin and other receptor-ligand systems using AFM and BFP, and have served to explore the unbinding energy landscape of the receptor-ligand complexes [Evans, 1998; Strigl et al., 1999; Merkel et al., 1999; Heymann and Grubmüller, 2000; Yuan et al., 2000; Evans, 2001].

Linear fits to the obtained rupture forces plotted versus the natural logarithm of the applied loading rate supply characteristic forces of the binding potentials [Evans and Williams, 2002]. More than one linear regime is hereby indicative of an additional inner potential barrier [Merkel, 2001; Evans and Williams, 2002]. Results obtained from dynamic force spectroscopy on avidin-biotin were found to be in good agreement with theoretical results for the thermodynamic potentials from molecular dynamics computer simulation studies [Izrailev et al., 1997]. However, the determination of energy landscapes from measured rupture forces poses highly challenging requirements of accuracy and experimental control [Evans and Williams, 2002].

1.4 Specific aims of the research project

The study of single biological molecules is still a relatively new field. The ability of such studies to provide exciting detail on events involved in physiological or pathological *in vivo* processes, has encouraged the rapid development of high resolution imaging as well as force investigating techniques. Some of the fascinating experiments on single molecules may seem to possess mere entertainment value, such as tying knots into strands of DNA [Arai et al., 1999]. However, they demonstrate the great potential of these techniques in very diverse areas of application. These range from the resolution of rare mutant behaviour of individual biomolecules [Oberhauser et al., 1999], microsurgery [Steubing et al., 1991], the isolation and manipulation of single viruses and cells [Ashkin et al., 1987], or highly sensitive competitive immunoassays for the detection of femtomolar antigen concentration in solution [Helmerson et al., 1997] to the fabrication of fast nanomechanical or electronic biology based devices [Mao et al., 1999].

In the presented research project, different biophysical techniques, namely AFM and optical tweezers, were employed to study biological systems at the single molecule level. AFM and optical tweezers both allow the measurement of biologically relevant forces. The two techniques can complement each other predominantly due to their access to different force regimes. In the research set out in chapter 4, an advanced optical tweezers based force transducer was employed to study drug-binding effects on the elastic response of single DNA molecules to a stretching force. Forces in the very low force regime, in which entropic elasticity dominates DNA stretching behaviour, were resolved

with this technique. In contrast to earlier data from AFM force-extension experiments [Krautbauer et al., 2002a; Krautbauer et al., 2002b], the results from optical tweezers allowed the extraction of DNA molecular properties for different drug concentrations, using theoretical fits to the data.

Because of this technique's attractive possibilities for the study of biological polymers or interactions within receptor-ligand complexes, an optical tweezers system was also developed within this work (chapter 3). Early applications of the system include the study of drug effects on cell adhesion receptor interactions *in vitro* on living cells, presented in chapter 6. Here, the combination of experimental approaches was further exploited to provide a more complete picture of the observed processes. Complementary information on the studied interactions was provided by AFM force-distance experiments. Fluorescence confocal microscopy imaging was employed to support optical tweezers data on adhesive receptor interactions to ligand coated beads.

As outlined earlier in this chapter, one of the great advantages of AFM is its application in both force measurements and high resolution imaging. Chapter 5 describes experiments on interactions with DNA of a novel protein, using AFM as an imaging tool. The obtained data were able to complement results from genetic and biochemical techniques.

The range of biomolecular processes investigated within this research demonstrates the diverse applicability of single molecule studies. Chapter 2 discusses the theory and instrumental details of the two major biophysical techniques used within the work presented.

Chapter 2

Instrumental methods

The research presented in this thesis involved different approaches to the study of biomolecular interactions. High resolution AFM imaging of individual molecules of DNA was employed, in order to analyse protein-DNA interactions at the single molecule level. AFM was also used as a force probing device for the determination of drug effects on cell adhesion receptor interactions. Complementary data on these interactions were obtained, using an optical tweezers system, the development of which is also presented within this thesis. Optical tweezers were further employed to investigate drug effects on the mechanical properties of DNA. This chapter introduces the theory and instrumental set-up of the two techniques, AFM and optical tweezers. The specific experimental set-up particular to each experiment, however, varied between the different systems investigated and will be presented within the context of each of the experimental chapters 4 to 6 separately.

2.1 AFM

Owing to its force measuring as well as high resolution imaging ability [Müller et al., 1999b; Oesterhelt et al., 2000], AFM is one of the most popular biophysical applications for the study of single molecules. AFM is predestined for work on biological samples, because of its applicability to non-stained surfaces and suitability for measurement in liquid environments. In the following text, the principles and data analysis of imaging and force probing AFM will be presented.

2.1.1 AFM imaging

The principle of AFM is schematically shown in figure 2.1. A fine tip at the bottom end of a silicon (Si) or silicon nitride (Si_3N_4) cantilever serves to scan the sample surface. Cantilever arms are either beam shaped or made from two beams forming a triangle as in figure 2.1. The lateral position of the tip is precisely controlled using piezoelectric positioning elements, giving a lateral resolution which is predominantly limited by the diameter of the tip. For commercially available cantilevers, the tip apex is typically between 10 and 50 nm [Thundat et al., 1992]. Therefore, the lateral resolution of AFM imaging is much superior to light microscopy techniques, where resolution is limited by diffraction to half the light's wavelength (a few hundred nanometers). In vacuum, individually manufactured AFM tips have even enabled atomic resolution (approximately 0.1 nm) of a range of substrates [Ohnesorge and Binnig, 1993; Giessibl, 1995; Sokolov et al., 1997].

As the tip is scanned over the sample, it experiences attractive as well as

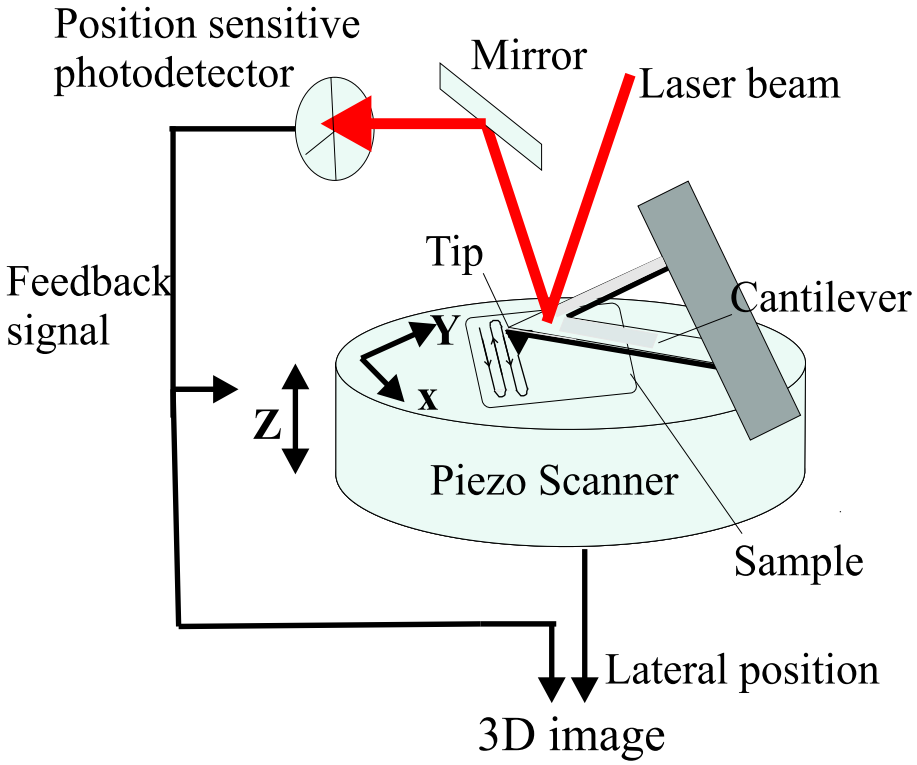

Figure 2.1: AFM instrumental set-up. The sample is attached to a stage, the x- and y-positions of which are precisely controlled by piezoelectric elements. The distance between tip and sample surface determines the deflection of the AFM cantilever through repulsive or attractive forces. This deflection is measured from the displacement of a laser beam that is reflected from the back of the cantilever, on a 2D photodiode array. In the most commonly employed feedback mode, mechanical forces on the sample through the tip are kept constant by using the laser displacement signal to re-regulate the separation between tip and sample surface. Both the feedback signal and the lateral position of the AFM tip are recorded at each sample position. A map of these data gives a topography image of the scanned sample.

repulsive forces [Israelachvili, 1992]. Initial surface contact of the tip involves small, attractive van der Waals forces between tip and surface. However, for some substrates, both attractive and repulsive electrostatic interactions dominate the van der Waals attraction. Upon further approach of the surface, the tip is pressed onto the surface, leading to its strong repulsion (Pauli exclusion principle). These forces cause deflections of the AFM cantilever; for attractive forces towards the surface, for repulsive forces away from the surface. Since the repulsive force on the tip increases with decreasing tip-surface separation, cantilever deflection is a useful indicator of sample height at a given position. Scanning the sample surface while recording the cantilever deflection at every surface point thus provides a topography image of the sample.

The AFM's detection mechanism is therefore based on measuring the cantilever deflection at each sample surface position. The most commonly applied method uses optical position sensitive detectors [Meyer and Amer, 1988], as schematically shown in figure 2.1, in which a laser beam gets reflected from the cantilever back surface onto a position-sensitive quadrant photodiode. The back of the cantilever is often coated with a gold-layer, to improve its reflectivity. Deflection of the cantilever leads to a displacement of the reflected laser beam position on the photodiode, proportional to the degree of deflection. Mapping the recorded cantilever deflection for the entire scanned surface thus produces a topography image of the sample. For biological applications, the feedback mode is often employed, in which the deflection signal serves to regulate the vertical (z) position of either sample or cantilever via piezoelectric positioning devices. The separation between

sample surface and AFM tip is thus kept constant, which serves to keep the force between them constant and prevent force-induced damage to the imaged material. In feedback mode, the surface topography image is produced from the z-position of the piezo-driven component (sample stage or cantilever).

Imaging of surface structures can occur in one of three different modes: contact mode, non-contact mode and tapping mode. The different functions and advantages of each mode will briefly be discussed in the following.

Contact mode

In contact mode, repulsive forces that arise on mechanical contact between sample and tip are responsible for the deflections of the cantilever. Generally, the force is kept constant by the use of a piezoelectric feedback system which permanently regulates the vertical (z) position of either the tip or the sample. This prevents the force between tip and sample from increasing too much, leading to damage of the sample. However, the reaction time of the height regulating mechanism is too long for fast, i.e. steep and large height changes. The height differences within the sample surface accessible to this mode are therefore very limited and contact mode is only suitable for very flat surfaces. Furthermore, due to direct contact with the sample, the scanning motion induces lateral forces onto the material which are intolerable for soft surfaces. In liquid systems, this is however still the imaging mode of choice, because alternative modes rely on cantilever oscillations (as discussed in the following text) which are dampened by fluid.

Non-contact mode

In non-contact mode [Lüthi et al., 1994], the tip does not touch the sample. It oscillates instead above the surface, with a frequency close to its resonance frequency and with small amplitude. Attractive surface forces are responsible for cantilever deflection here. This mode guarantees damage free samples, due to the sustained distance between tip and surface. However, its disadvantage lies in a significant decrease in resolution as a consequence of the lower sensitivity of attractive probe-surface interactions to subtle changes in surface topography [Maganov and Whangbo, 1996].

Tapping mode

In tapping mode [Hansma et al., 1993], the cantilever also oscillates close to its resonance frequency. The oscillation amplitude, however, is bigger than in non-contact mode, so that the tip gently touches the sample each time it reaches the lowest point. This causes a slight dampening of the oscillation and affects both oscillation amplitude and phase. Mapping of the data recorded for each sample point, simultaneously produces an amplitude image and a phase image. The amplitude image contains the height and therefore topography information. The phase image reflects probe-sample interactions which are due to, for example, sample viscoelasticity or adhesion. The resolution is considerably improved compared to the non-contact mode, whereas due to the shortness of the contact the load on the sample is not significantly increased and lateral contact forces are eliminated [Shao et al., 1996]. Damage-free imaging of biological samples has been shown using this mode

both in air and liquid [Hansma et al., 1994]. This is therefore the preferred mode for imaging applications in air.

One of the major advantages of AFM in biological applications is its suitability for experiments in a liquid environment [Drake et al., 1989]. These enable the measurements on biological samples under near native conditions. Additionally, for measurements in liquid systems, the strong capillary forces which otherwise occur on tip-sample contact can be neglected. Therefore, in buffer solution the dominant forces between tip and sample surface are of electrostatic and van der Waals nature [Janshoff et al., 2000; Müller and Engel, 1997].

2.1.2 Force spectroscopy

Besides its imaging function, AFM can also be utilised to directly measure forces. Its high vertical resolution (0.1 nm [Engel and Müller, 2000]) and speed, combined with its suitability for applications in liquid environment, provide the AFM with excellent qualities for the measurement of single biomolecule interaction forces.

For this, the deflection of the cantilever is recorded while the AFM-tip is lowered towards the surface and retracted. Figure 2.2 shows a schematic of the obtained force-distance curves. To begin with, the cantilever is in its free level position. Upon surface approach, at small tip-sample separation the above-mentioned small attractive forces between surface and tip [Israelachvili, 1992] cause the tip to jump into contact with the surface. The

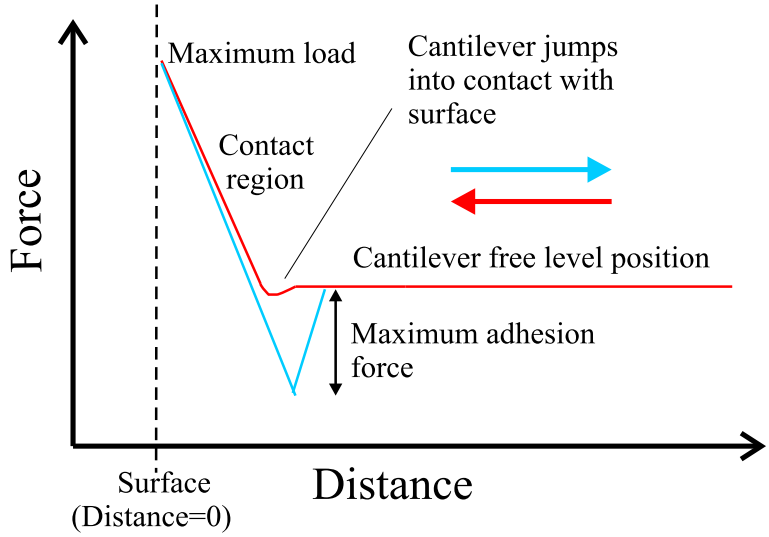

Figure 2.2: AFM force distance curve. The force on the AFM cantilever is obtained from its deflection towards or away from the surface and its spring constant, using Hooke's law, and plotted versus cantilever distance from the sample surface. Starting from its free level position, the cantilever approaches the sample surface (red path), until at small separation the tip jumps into contact with the surface. Further tip approach to the surface results in repulsive forces on the tip, which bend the cantilever away from the surface. An instrumentally pre-set maximum load restricts the pushing force of the tip onto the sample surface, limiting sample damage. At this point, the cantilever retracts from the surface (blue path). Bonds or tethers formed between the surface and the tip during contact are stretched upon tip retract, increasing the force onto the cantilever. The bonds break, as the pulling force becomes stronger than the connecting bonds with cantilever distance. This shows as discontinuities in the recorded force-distance curve (maximum adhesion force), where the tip jumps out of contact and back to its original free level position.

attractive forces bend the cantilever towards the surface, leading to negative cantilever deflection signals. Further tip approach to the surface results in repulsive forces on the tip, which bend the cantilever away from the surface, producing positive deflection signals (see figure 2.2). An instrumentally pre-set maximum load restricts the pushing force of the tip onto the sample surface, limiting sample damage. At this point, the cantilever retracts from the surface until it reaches its initial starting position. Retraction of the tip causes bonds or tethers formed between the surface and the tip during contact to break, as the pulling force on the connection becomes stronger than the connecting bonds with tip-surface separation. This shows as discontinuities in the retract trace of the recorded force-distance curve (maximum adhesion force), where the tip jumps out of contact and back to its original free level position.

The AFM cantilever behaves like a Hookian spring, i.e. the force acting on it is proportional to its deflection. The proportionality constant hereby is the spring constant κ (measured in N/m) of the force transducing cantilever. With knowledge of κ, cantilever deflection Δx (in m) can thus be translated into force F (in N) exerted by the resistance of the stretched bond, according to Hooke's law:

$$F = \kappa \cdot \Delta x \tag{2.1}$$

2.1.3 Spring constant determination

The cantilever spring constant κ is proportional to the elastic modulus E, and thus a measure of its elasticity:

$$\kappa = \frac{E \cdot w \cdot t^3}{4l^3} \tag{2.2}$$

for a beam-shaped cantilever [Cleveland et al., 1993], where w, t and l are width, thickness and length of the cantilever, respectively. V-shaped cantilevers can in good approximation be mathematically treated as two parallel beam-shaped cantilevers [Cleveland et al., 1993]. In imaging contact mode, cantilever elasticity determines the scanning speed, while for force spectroscopy applications it limits the force resolution.

Spring constants for commercially available AFM cantilevers vary from 1 to 10^5 pN/nm [Bustamante et al., 2000a]. For imaging applications the approximate knowledge of κ, as supplied as an average value by the manufacturer, is sufficient [Cleveland et al., 1993]. However, for force measurements a more precise knowledge of this value is required, since the obtained force depends subtly on κ. The cantilever spring constant has to be determined separately for each individual cantilever prior to an experiment. Different approaches to this have been developed, such as measuring the resonant frequency change caused by the addition of small end masses to the cantilever [Cleveland et al., 1993] or the thermal excitation method [Hutter and Bechhoefer, 1993].

In comparison to other methods, the thermal excitation method has been found to be superior in reproducibility of results for cantilevers with small κ

[Florin et al., 1995], which are employed predominantly in force measuring applications. This method has therefore been chosen for the determination of spring constants for the experiments presented within this thesis. In this method, the thermal noise spectrum of the free cantilever is recorded, digitalising its deflection signals. Fourier-transformation of this spectrum gives the power spectrum in frequency space. According to the equipartition theorem, each degree of freedom of a given system possesses the thermal energy $\frac{1}{2} \cdot k_B T$ at the absolute temperature T (where k_B is the Boltzmann constant). Therefore, fitting a harmonic oscillator potential $\frac{1}{2} \cdot \kappa \langle \Delta x^2 \rangle$ to the data over the lowest vibrational frequency (as the basic mode oscillation) gives the cantilever spring constant. The equipartition function thus gives:

$$k_B T = \kappa \cdot \langle \Delta x^2 \rangle \tag{2.3}$$

where $\langle \Delta x^2 \rangle$ is the average over time of the squared deflection.

For force spectroscopy, the smallest possible spring constants are desirable, as for such minimally stiff cantilevers the sensitivity of deflection Δx to forces is increased due to the higher magnification factor $1/\kappa$ (see equation 2.1). Further, the thermal force fluctuations, ΔF, of the cantilever are proportional to $\sqrt{\kappa}$:

$$\langle \Delta F^2 \rangle = \langle \kappa^2 \cdot \Delta x^2 \rangle = \langle \kappa \cdot k_B T \rangle \tag{2.4}$$

where $\langle \Delta F^2 \rangle$ is the average over time of the squared force fluctuations. This relationship leads to better force resolution for smaller spring constants κ, due to smaller noise signals.

Commercially available cantilevers allow force resolution by AFM down to approximately 10 pN [Bustamante et al., 2000a]. Since the signal-to-noise ratio is, however, independent of κ [Svoboda and Block, 1994a], higher spring constants can be useful for measurements on systems with high interaction forces ($\gtrapprox$ 100 pN) [Bustamante et al., 2000a].

For the imaging function of the AFM, on the other hand, the resonance frequency of the cantilever determines the resolution limit. Maximum possible resonance frequencies are desirable. For imaging, the cantilever spring constant is therefore chosen as small as possible for the required resonance frequency. Both imaging and force probing measurements in liquid additionally favour the smallest possible cantilevers, to minimise the induced hydrodynamic resistance that can alter the data [Walters et al., 1996].

2.2 Optical Tweezers

In atomic physics, laser light has been employed since the early 1970s to produce optical traps [Ashkin, 1970a; Ashkin, 1970b; Ashkin, 1974]. The principle of this technique, termed laser cooling, is the minimisation of the thermal energy of the atoms or atomic systems by inducing electronic transitions into their ground state with laser light. Since a temperature of almost absolute zero is aspired to in these experiments (relating to completely motionless atoms in their ground state), the instrumental system has to be placed within an extremely high vacuum. Further, the exact energy differences between initial and final electronic state have to be matched by the laser light.

In contrast to this, in biological macromolecules, the well-defined energy levels of the atomic systems are replaced by a continuous energy landscape. The electrons do not require the application of specific wavelengths or transition frequencies in order to undergo transitions to a lower energy level. Transitions occur on a much cruder, macromolecular scale, requiring several orders of energy less than in the laser cooling experiments on atoms. There is also no vacuum required in these experiments. Instead, aqueous solutions provide a good medium for trapping, offering the possibility of near native conditions for biological molecules.

Most biological samples consist of a high percentage of water, which shows increasing absorption of electromagnetic radiation for long wavelengths. In the near-infrared region of the electromagnetic spectrum, however, water absorbs conveniently little. Since most biological chromophores further absorb at wavelengths shorter than the near-infrared, the use of such wavelengths for laser trapping causes minimal interference with biological material [Ashkin et al., 1987]. The non-invasiveness of the technique, combined with its applicability in liquid environments, renders optical tweezers ideally suitable for biological experiments in near-physiological conditions.

The first such application of a laser trap for simple model structures of biological particles (in form of dielectric spheres) was introduced by Ashkin and colleagues in 1986. They called the technique optical tweezers [Ashkin et al., 1986], due to its ability to hold a trapped object steadily or to move it around in a controlled manner. Soon, Ashkin et al. [Ashkin and Dziedzic, 1987; Ashkin et al., 1987] also managed to show applications of optical tweezers to biological objects. Since then, trapping and manipulation

of objects as small as 25 nm [Block, 1992] and as large as 10 μm [Ashkin et al., 1986; Ashkin and Dziedzic, 1987] have been demonstrated. Further, small dielectric spheres (of the order of 1 μm diameter) have been trapped and employed as handles to manipulate biological particles. With these, precise displacement of as well as force application to the biological objects is possible.

Spring constants for optical tweezers typically display values several orders of magnitude lower than for AFM cantilevers. Therefore, the force resolution achievable with optical tweezers is high, $\gtrapprox$ 0.1 pN [Bustamante et al., 2000a]. An additional advantage of this technique is the possibility to introduce high speed detection for the resolution of dynamic processes. The principle of using an optical trap as force transducer with a high temporal resolution detection mechanism is discussed below, in section 2.2.2 of this chapter.

2.2.1 Theory of optical trapping

Optical tweezers utilise electromagnetic radiation forces to trap dielectric particles in three dimensions. For this, the refractive index of the particle has to be higher than that of the surrounding medium. Different regimes have to be considered, depending on the ratio of particle diameter and the wavelength of the trapping laser radiation.

For most optical tweezers experiments, the size of the trapped object (radius r) is of a similar order of magnitude as the laser wavelength λ. This defines the **Mie regime** ($\frac{\lambda}{20} < r$) [Zemánek et al., 1998]. Rayleigh scatter-

ing theory and the geometrical ray optics picture are special cases for very big and very small radius to wavelength ratios. Both regimes come out of the complete electromagnetic field calculations when the relevant boundary conditions for each case are considered. An exact description of the forces involved in optical trapping in the Mie regime, using electromagnetic theory, is beyond the scope of this thesis. Work on the derivation and discussion of the exact optical tweezers trapping forces has, however, been published recently, for example, by Neto and Nussenzveig [2000] and Nahmias and Odde [2002]. Here, for simplicity, optical trapping will be explained in the limits of very small and very large r/λ ratios.

In the **Rayleigh regime** ($r < \frac{\lambda}{20}$) [Zemánek et al., 1998], the complex electromagnetic theory simplifies to the description of an electric dipole. The Rayleigh scattering theory describes the forces on an electric dipole by the electromagnetic wave, inducing a counter-force in order to conserve total momentum in the system. This force is pushing the dielectric particle along the direction of laser light propagation. Opposing this force there is the Lorentz force acting on the induced dipole, which is also called the gradient force here, as it acts along the gradient of laser light intensity. The gradient force needs to dominate the scattering force to achieve trapping.

In the **geometrical optics limit** ($r \gg \lambda$) [Zemánek et al., 1998], as a simplifying model, the trapped objects are assumed to be perfectly spherical. Here too, laser light that strikes the surface of the dielectric sphere is scattered. This again (as in the dipole picture) leads to a force along the direction of the laser beam propagation, to compensate for the momentum change in the laser radiation. The laser light rays, depicted as vectors in

figure 2.3, are refracted according to their angle of incidence, upon entering the dielectric material as well as upon exiting. Due to the spherical shape of the object, this always results in a momentum change in the laser light for non-vertical incidence. Obeying the obligatory conservation of momentum in the entire system, this induces a compensating counter-force. For a focused laser beam this counter-force points towards the focus position, along the gradient of the laser light intensity (thus being called the gradient force, as for the dipole situation). This force pushes the particle towards the original laser focus position f for particle displacements away from the focus, leading to trapping of the particle. The momentum change (and therefore the gradient force on the particle) is proportional to the steepness of incidence of the entering laser light. Steep focussing of the laser beam is an essential criterion for optical trapping, since the gradient force towards the laser focus has to dominate the scattering force that pushes the particle along the direction of the laser beam, out of the trap. In the geometrical optics regime, the force on a large particle can be calculated by summation of the momentums of all light beams over the total sphere surface [Ashkin, 1992]. Balancing of scattering and gradient force leads to trapping of the dielectric sphere slightly below the original laser focus position. Geometrical optics results have been suggested to give good approximations for trapping forces on particles $\gtrapprox 6$ times the laser wavelength [Ashkin, 1992]. For smaller particles (and thus optical trapping in the Mie regime) reliable force calibration methods have been developed for the interpretation of experimental data, circumventing the necessity of an exact calculation of the involved optical forces. These methods are discussed in the next section (2.2.2).

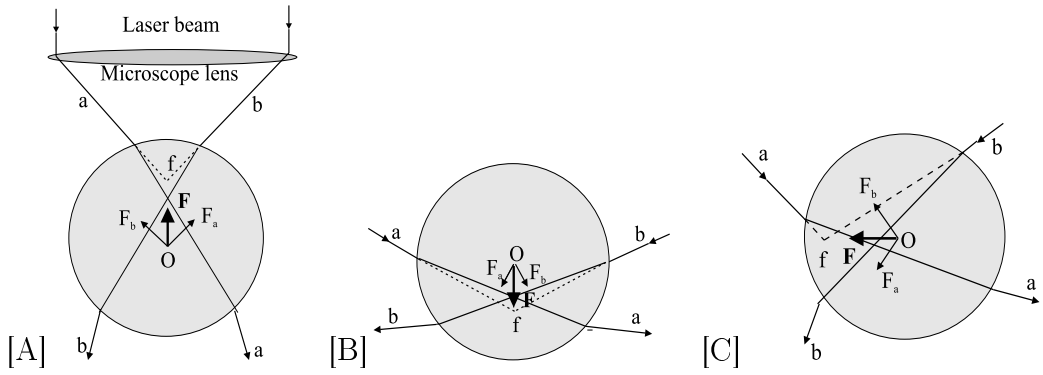

Figure 2.3: Laser light gradient forces of an optical trap in the geometrical optics regime, adapted from [Ashkin, 1992]. A laser beam is focused onto a point f. When a spherical particle with refractive index higher than that of the surrounding medium ($n > n_0$) is brought into the paths of the focussed light rays, the light is refracted through the particle. This causes a change in momentum between beams entering and exiting the particle. Conservation of momentum demands the introduction of a compensating counter-force, F (from compounds F_a and F_b), which points towards the original laser focus position along the gradient of the laser light intensity (the gradient force). As shown here, this force pushes the particle towards the original laser focus position f for displacements below (A), above (B) and beside (C) f, leading to trapping of the particle.

2.2.2 Force detection

For small displacements from the trap centre of $\lessapprox$ a particle radius, the optical trapping potential can be described by a harmonic potential [Ashkin, 1992; Wright et al., 1994; Simmons et al., 1996]. A harmonic potential displays Hookian spring-like behaviour: the restoring force is directly proportional to displacement. The proportionality factor is the spring constant

or stiffness of the trapping potential. Therefore, with the knowledge of the spring constant, the force on the trapped particle can be determined from its displacement from the trap centre, using Hooke's law (equation 2.1). This is illustrated schematically in figure 2.4.

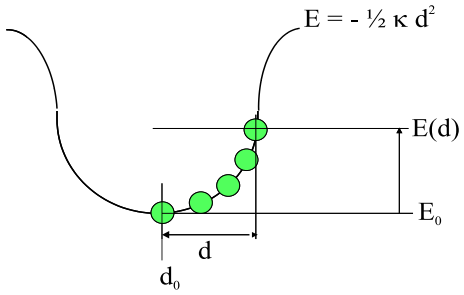

Figure 2.4: The optical tweezers potential can be approximated by a harmonic oscillator potential, E, for small displacements d from the trap centre d_0. A particle in the potential E possesses the energy $E(d)$ which depends on its distance d from d_0. The trapped particle behaves like a Hookian spring: the restoring force F (as the spatial derivative of E) on the particle increases linearly with d. The proportionality factor κ is thus referred to as the spring constant of the trapping potential.

Different techniques have been realised to measure the subtle displacement of a trapped particle within the laser trap with nanometer precision ($<$ 10 nm [Bustamante et al., 2000a]). In the most straight-forward approach, the trapped particle is magnified and imaged directly onto a CCD camera or a position sensitive photodetector [Finer et al., 1994; Molloy et al., 1995]. This detection mechanism was chosen for the optical tweezers system developed within the studies presented in this thesis, due to its relative ease of instrumentation, and will be discussed in more detail in chapter 3. A

further commonly used detection scheme employs interferometry [Svoboda et al., 1993; Pralle et al., 1999]. This method is based on the interference of the unscattered laser beam with the laser light scattered on a trapped bead [Gittes and Schmidt, 1998], and has been employed to measure one-, two-, and three-dimensional bead displacement [Ghislain et al., 1994; Denk and Webb, 1990; Pralle et al., 1999]. Resolutions of $\lessapprox 1$ nm and fast detection speed (maximum detectable frequencies of 100 kHz) have been achieved with interferometry-based detection [Merkel, 2001; Gittes and Schmidt, 1998].

The technique of optical tweezers offers very low spring constants, allowing the resolution of very low forces. Theoretically, spring constants as low as 10^{-7} pN/nm [Bustamante et al., 2000a] can be achieved. The exact value depends on the size and refractive index of the trapped particle, the refractive index of the surrounding medium, and on the power of the trapping laser light [Ashkin et al., 1986]. In most experimental set-ups, typical values of spring constants range from 0.001 to 0.1 pN/nm. Several methods have been developed for the determination of the trapping potential spring constant [Visscher et al., 1996; Florin et al., 1998]. One approach is the calibration against known forces, such as Stokes drag on a spherical particle in a laminar flow of known velocity [Felgner et al., 1995; Smith et al., 1996; Simmons et al., 1996; Singer et al., 2000]. A different approach relies on the observation of the thermal (Brownian) motion of a trapped bead in the optical tweezers potential [Ghislain et al., 1994; Svoboda and Block, 1994b; Pralle et al., 1998; Florin et al., 1998]. From the recorded spectrum, the mean square displacement, the energy profile of the potential (using Boltzmann statistics), and the cut-off frequency can be obtained and used to determine

the trap spring constant. In a comparison of different methods, Florin et al. [1998] have found the spring constant calibration methods based on Boltzmann statistics and on the determination of the mean square displacement to be the most accurate (both 7 % absolute error). Within the work presented in this thesis, both Stokes drag and the mean square displacement method were employed for the calibration of the trapping potential of an optical tweezers system. Details of this can be found in chapter 3.

Chapter 3

Optical Tweezers development

This chapter presents the construction of an optical tweezers based force transducer system for the manipulation of biomolecules under near physiological conditions, as well as the measurement of forces on stretched biopolymers or within receptor-ligand interactions. In the following text, the general set-up and function of an optical tweezers system will be introduced by the example of the specifically chosen set-up. Preliminary applications carried out on the developed system are then presented. Finally, the development of a position sensitive photodetector system is described. This enables the accurate measurement of minute forces on trapped particles.

3.1 General optical tweezers set-up

An optical tweezers based system used for force measuring experiments on biological objects consists of two subunits: a laser (or optical) trap and a detection system.

Figures 3.1 and 3.2 give an overview of the entire optical tweezers system. This includes the optical bench with the laser, an inverted optical microscope (Eclipse TE 300, Nikon Europe BV, Badhoeverdorp, The Netherlands), and the detection system, which consists of the CCD camera (Imager 3 QE, La Vision, Goettingen, Germany) and a home-built photodetector. The signals from both the CCD camera and the photodetector are sent to a personal computer (PC), where they can be displayed and further processed.

For stability, the complete set-up is mounted on an anti-vibration air table. To protect the eyes from exposure to laser light, wavelength-filtering goggles are provided. An interlock system secures that the laser power supply operates solely when the microscope eyepieces are covered, and the laboratory door is closed. This protects the operator from accidentally exposing the naked eye directly to the invisible infrared laser beam, and unprepared persons from entering the room.

In the following, the construction of trapping and detection parts of the optical tweezers based force transducer system will be presented separately. Applications to both (trapping of biological specimens for optical part, calibration results for detection part) will be presented as proof of principle.

3.2 The optical trap

The trapping, optical part of an optical tweezers based force transducer system basically consists of a laser and a strongly focussing objective. Generally, an optical bench is further included between the laser and the objective. This serves to optimise trapping intensity and provide means of steering the laser

trap.

Laser

In our set-up, a diode pumped Nd:YAG (Neodynium in yttrium aluminium garnet crystal) solid state laser (Forte 1060 Series, Laser Quantum Ltd., Laser Support Services, Pittenweem, Fife) with 1 W maximum power and 1064 nm wavelength was used. As explained in chapter 2, biological objects only absorb low amounts of laser light from this spectral origin, and damage to the sample by induced heat development is thus minimal [Ashkin et al., 1987; Neuman et al., 1999].

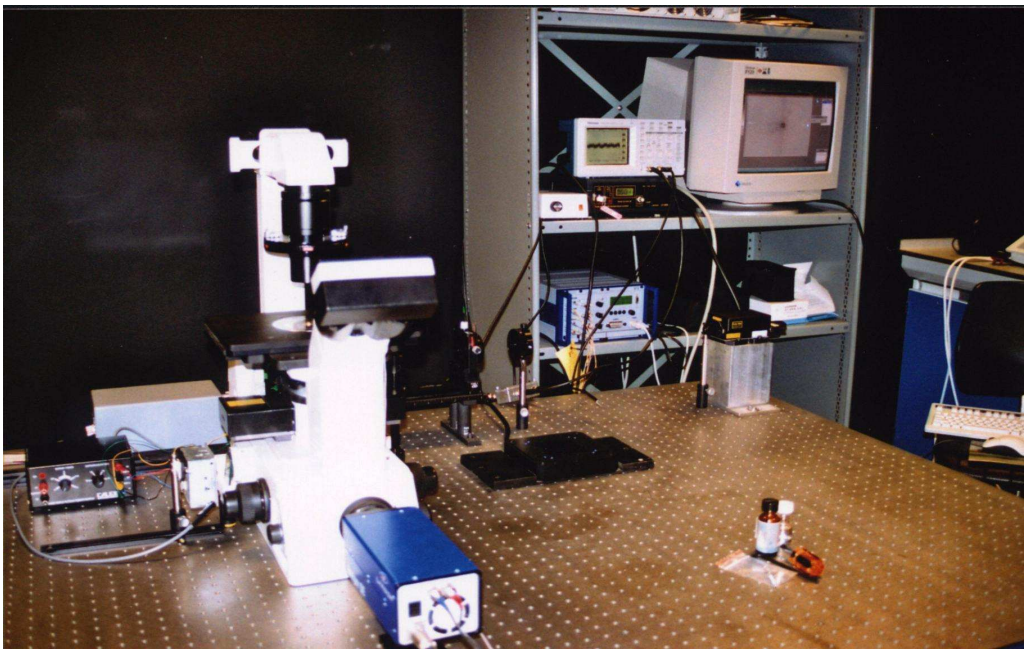

Figure 3.1: Complete optical tweezers set-up developed within this work. The individual components are labelled in the figure. Furthermore, the lenses of the optical bench can be seen between the laser and the microscope.

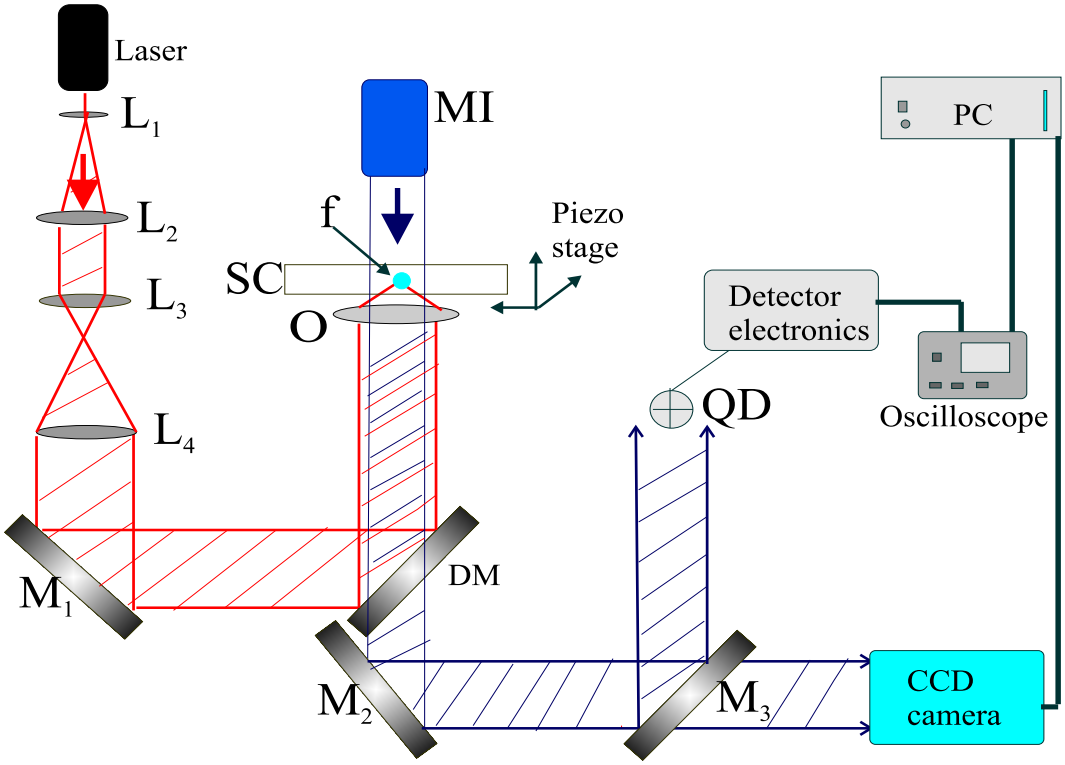

Figure 3.2: Schematic drawing of the developed optical tweezers system, which is integrated into an inverted optical microscope. A laser beam is expanded (lenses L_1 and L_2) and directed into a strongly focusing objective O through a telescope system (lenses L_3 and L_4), via mirror 1 (M_1) and a dichroic mirror (DM) within the microscope. The objective focuses the beam to a point f inside a liquid sample cell (SC). L_3 and L_4 can be translated, to axially move f. M_1 is mounted on a pivotal stage. Tilting of M_1 around its centre induces lateral displacement of f. A piezo-controlled positioning stage enables application of precise, computerised 3D displacements to the sample. Microscope illumination (MI) by a 30 W halogen lamp serves to image the sample onto a CCD camera (via mirror M_2), or a quadrant diode photodetector (QD) (via mirrors M_2 and M_3). Both the detector output and camera images are displayed and further processed on a PC.

Objective

The laser beam is focussed onto a diffraction-limited spot inside a liquid sample cell, by an infinity-corrected immersion oil objective (MrfO1400, Nikon) with a working distance of 220 μm, a magnification factor of x40, and a numerical aperture (NA) of 1.30. A high NA value of the objective is essential, as this results in steep focussing of the laser light. Light rays that are focussed more steeply lead to greater gradient forces onto a dielectric object near the laser focus. As shown in the theoretical introduction in chapter 2, the gradient forces need to overcome scattering forces in order to keep an object confined in the optical trap.

Supporting optical bench

An optical bench includes components to expand the laser beam and direct it into the back entrance aperture of the trapping objective. The elements of the optical bench are a beam expander, a telescope lens system, and two mirrors, as shown in figure 3.2.

Beam expander. The function of the beam expander is to ensure sufficient overfilling of the back entrance aperture of the trapping objective, by increasing the laser beam diameter. This improves trapping efficiency, as the outer beams get focussed more steeply and thus provide greater gradient forces.

Sufficiently overfilling the back entrance aperture of the objective with the laser beam further ensures constant trapping power, independent of the laser focus position. This is depicted in figure 3.3 using ray optics diagrams.

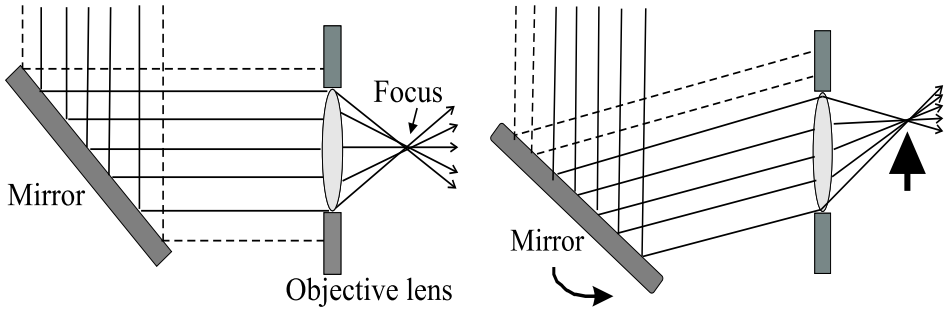

Figure 3.3: Schematic ray optics diagrams explaining lateral trap movement. The laser focus is displaced by inducing an angle in the incoming laser beam, using a tilted mirror. Sufficient overfilling of the back entrance aperture of the trap producing objective hereby ensures constant laser power at the focus, independent of the lateral trap position. To demonstrate this, dashed rays here indicate laser light that does not enter the microscope objective.

The beam expander in our system initially (set-up 1) consisted of an objective (magnification factor x40, NA 0.73; Newport Ltd., Newbury, Berkshire, UK) to enlarge the laser beam diameter, and a collecting lens L_0 to re-collimate the expanded beam. This increased the beam diameter approximately 20-fold, immediately after its exit from the laser source. With the slight additional expansion through the telescope lens system, the thus expanded beam sufficiently overfilled the 16 mm diameter back entrance aperture of the objective.

However, damage was induced in the beam expander objective due to its exposure to high intensity laser light. Objectives consist of systems of small expanding and focusing lenses. This led to extremely high laser light intensities per surface area within the final lens of the expander set-up. Within two years of using the optical tweezers system, the centre of the beam expander

objective lens showed a blurred appearance. This may be the result of a melting process within a coating film on the lens or within the surrounding frame parts of the final lens. Destruction of the glass material of the lens itself is considered unlikely even at these high laser light intensities.

Therefore, a lens system (set-up 2) consisting of a semiconcave lens (L_1) and a semiconvex lens (L_2) with back focal lengths ($f_b(i)$, $i = 1,2$) of -11.3 mm and 398.4 mm, respectively, replaced the previous beam expander system. To minimise spherical aberrations, the lenses were orientated with their concave and convex sides facing the collimated laser beam (entering and leaving the beam expander system). The lenses were mounted with the sum of their back focal lengths apart from each other. The lens system then produces a collimated, 35-fold expanded laser beam. The magnification γ of the beam expansion system can be calculated according to equation 3.1.

$$R = \frac{r \cdot f_b(2)}{f_b(1)} = r \cdot \gamma \tag{3.1}$$

where r is the radius of the laser beam entering, and R the radius of the beam leaving the lens system. The manufacturer (Laser Quantum Ltd.) guarantees beam radii < 0.4 mm after a laser warm up time of 10 minutes. R was measured to be approximately 10 mm ($\pm$ 1 mm), using an infrared detection card.

All presented experiments were carried out with set-up 1 (with the objective in the beam expander), except for the spring constant calibration of the optical trap (see section 3.5).

Telescope system. The telescope system consists of two planoconvex lenses L_3 and L_4 with focal lengths f_3 and f_4. It serves as the steering unit for the laser focus position in axial direction. The two lenses were mounted a distance of the sum of their focal lengths for the employed laser wavelength $(f_3 + f_4)$ apart from each other. These were measured to be $f_3 = 50$ mm $\pm 10\%$ and $f_4 = 30$ mm $\pm 10\%$. As described regarding the beam expansion system, the lenses were orientated with their convex sides facing the collimated beam, their planar sides facing the convergent part of the laser beam (inside the telescope system).

Both telescope lenses, as well as the collimating second lens of the beam expander, are mounted in micrometer positioning frames. These frames served to accurately adjust the lens positions horizontally and vertically, in order to centralise the path of the laser light rays.

Mirrors. Two mirrors (M_1 and DM, see figure 3.2) direct the expanded laser beam exiting the telescope into the back entrance aperture of the objective. DM is a dichroic mirror, transmitting optical wavelengths and reflecting the near infrared light from the laser. This mirror is part of the microscope set-up and is positioned inside the microscope, directly below the objective.

3.2.1 Trap movement

A central beam path along the middle axis through all optical components of the bench was first established. Then lateral and axial trap movement was induced.

Lateral trap displacement

M_1 was mounted on a pivotal stage, with which it can be manually tilted around its centre. This leads to lateral displacement of the laser focus within the liquid sample cell, as is indicated in figure 3.3.

Axial trap displacement

The lens holding frames of the telescope lenses L_3 and L_4 include a mechanical device with which the lenses can be moved along the laser beam axis (axial). Moving the lenses closer together or further apart induces an axial displacement of the laser focus, as shown in figure 3.4 using ray optics diagrams. Minimum distance between the two telescope lenses produces ma-

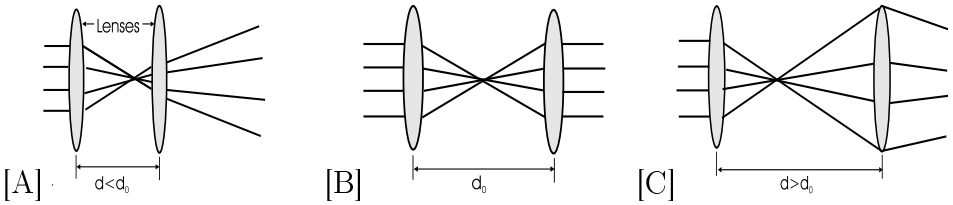

Figure 3.4: Schematic ray optics diagram showing axial steering of the trap. Minimum distance d between the two telescope lenses produces maximally divergent laser light leaving the telescope (A). Refraction of these light rays through the objective lens results in less steeply focussed rays than collimated light rays (B). The laser focus inside the sample cell, and thus the position of the optical trap, are therefore displaced away from the objective. Maximum distance between the two lenses produces maximally convergent light, exiting the telescope system (C). In this case the optical trap is moved downwards, towards the objective.

ximally divergent laser light leaving the telescope. In the ray optics picture, refraction of these divergent light rays through the objective lens results in less steeply focussed rays than collimated light rays. The laser focus inside the sample cell, and thus the position of the optical trap, are therefore displaced away from the objective. Maximum distance between the two lenses produces maximally convergent light, exiting the telescope system. In this case the optical trap is moved downwards, towards the objective.

3.2.2 Intensity losses through the optical system

The laser output power dropped by almost 50 % within 3 years. Figure 3.5 illustrates the reduction in power. Maximum laser power decreased from originally approximately 1100 mW in 1999 (manufacturer calibration information) to about 700 mW in 2002.

Laser light is lost through the components of the optical bench, as lenses and mirrors are not 100 % free of absorption. In order to determine losses through the individual systems, a 210 Power meter (Edmund Scientific, Barrington, NJ, USA) was employed to measure the laser power at different positions along the laser beam path. In our optical tweezers system, laser power is varied by controlling laser diode current supply. The laser power was therefore measured for increasing values of laser diode current. In figure 3.6, averages from at least three measurements obtained in 2000 on set-up 1 are plotted versus diode currents. From the figure, major losses can be seen to occur through the telescope and the objective. From the initial laser output, approximately 80 % were found after the beam expander, 60 % after

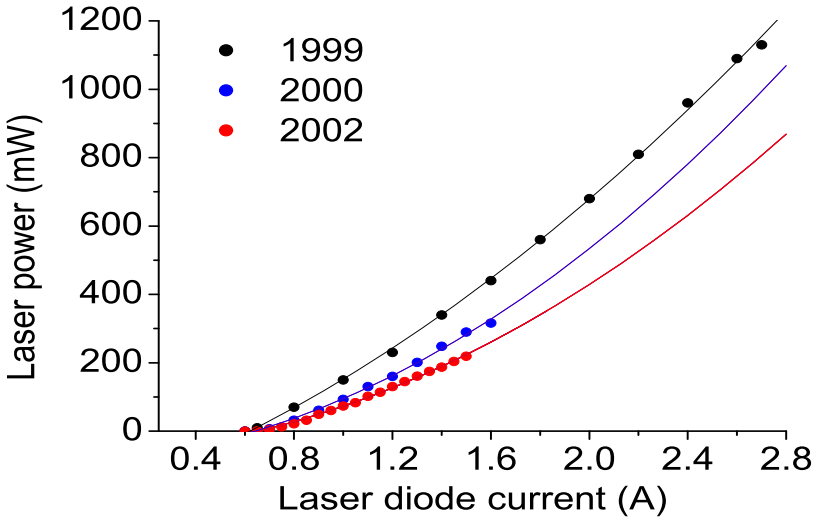

Figure 3.5: Reduction in laser output power over period of 3 years. Data points give the laser light power for increasing laser diode current as averages from at least three measurements. Error ranges are of the size of the data points. Black symbols indicate values from 1999, based on manufacturer information. Blue and red data points show power values as measured in 2000 and 2002, respectively. Measurements for laser output powers $>$ 300 mW were not possible with the employed power meter. Second order polynomial fits describe the power-current relationships well, and were used to extrapolate the curves given by the 2000 and 2002 data. 2000 data show reduction of output powers to approximately 70 %, 2002 data reduction to approximately 50 % of the original laser power.

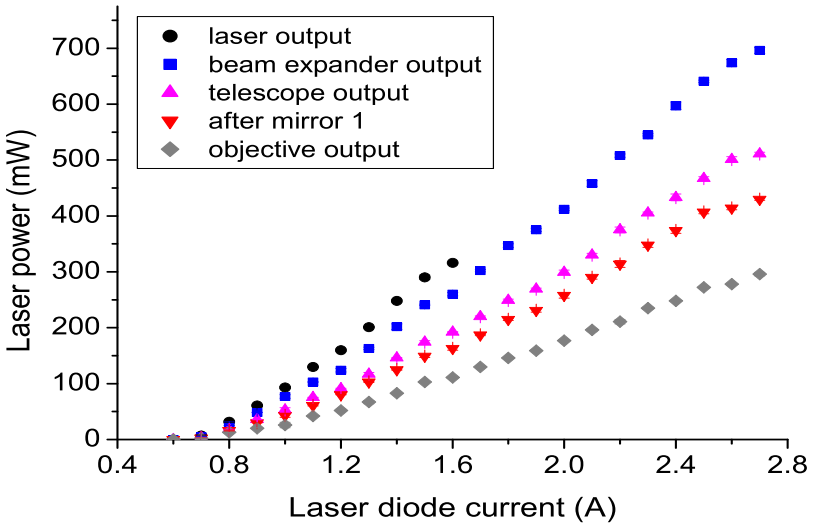

Figure 3.6: Laser light intensity losses over the optical components of set-up 1 for increasing laser diode current supply, obtained in 2000. Average values from at least three measurements of laser power at the direct laser output (black symbols), after the beam expander (blue), the telescope (pink), M_1 (red), and the microscope objective (grey) are shown. Error bars are of the size of the data points. The laser power measured behind the objective was used as trapping laser power in our experiments.

the telescope system, 50 % after the mirror M_1 before the microscope, and 35 % after the microscope objective. The linearity of the power-current relationship appeared to be disrupted for very low diode currents (< 0.7 A), for which only approximately 5 % of the original output power remained at the trap position. The value measured as the objective output power was taken as the laser power at the trap position. Measurements with a layer of immersion oil and a glass cover slip following the objective, as for trapping

within a liquid sample cell, showed no additional losses. From graph 3.6, the laser power at the optical trap position could therefore be deducted for each given laser diode current.

Further, laser light losses through the optical bench components were measured for set-up 2. Figure 3.7 shows a comparison of the laser light powers measured after the beam expanders of the two set-ups. When the re-

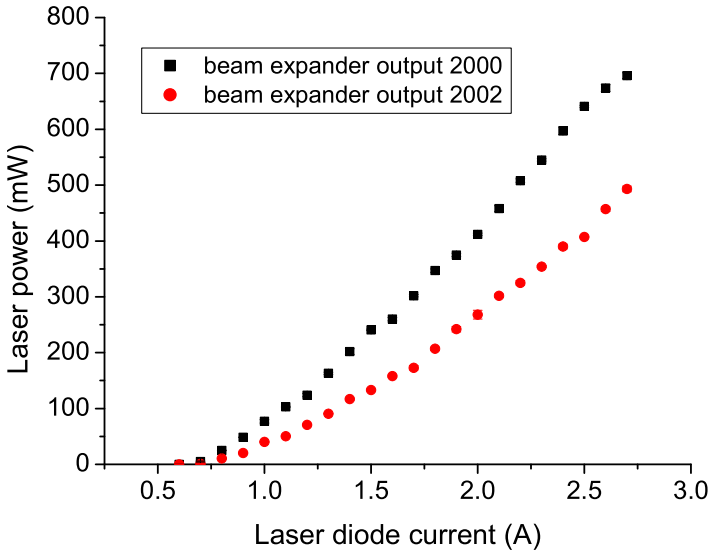

Figure 3.7: Comparison of laser light intensity losses over the beam expander for set-up 1 in 2000 and the later set-up 2 in 2002. Average values from at least three measurements of laser power are given for increasing laser diode currents. Errors are approximately 1 % (standard deviation) and of the size of the symbols. The reduction from 2000 to 2002 is compatible with the losses found in laser output power for the corresponding time interval (see figure 3.5), indicating equivalent quality of the beam expanding functions of the two set-ups.

duction in laser output power to approximately 70 % between the two measurements (2000 and 2002; see figure 3.5) is taken into account, the two beam expander set-ups show comparable losses. Set-up 2 is therefore superior to set-up 1, considering the low stability of set-up 1 in the laser beam.

3.3 Trapping applications on biological objects

In order to demonstrate the ability of our optical tweezers system to trap and manipulate dielectric particles, biological and non-biological objects were employed. Polystyrene-latex beads of various sizes, namely 1, 2, 3, and 5 μm diameter, were trapped and translated in liquid using the optical trap. Further, the suitability for the manipulation of biological samples was shown for red and white human blood cells, of approximately 7 and 12 μm diameter, respectively. Representative images will be shown in the following.

Erythrocytes

One drop of whole human blood was diluted approximately 10^6-fold in physiological sodium chloride solution (0.9 % w/v sodium chloride; Sigma-Aldrich Company Ltd., Poole, Dorset, UK; in deionised, filtered water). Red blood cells (erythrocytes) make up the major part of cellular components of whole blood, and were therefore the dominating component of the obtained solution.

A liquid sample cell was prepared by giving a drop of 50 μl of the solution onto a glass cover slip (22 x 22 mm^2, size 1.5; Chance Propper Ltd., West Midlands, UK). The edges of the cover slip were covered thinly with silicon

grease. A microscope glass slide (76 x 26 x 1.0-1.2 mm^3; BDH laboratory supplies, Dorset, UK) was covered with the cover slip, so that the grease provided both, a seal and a thin spacing for the liquid cell. The sample cell was placed on the microscope object table. The surface of the cover slip had been marked using a water resistant permanent pen, in order to determine the surface position inside the sample cell. The approximate distance of the trap from the bottom surface could thus be measured at each given position, using the objective fine positioning device of the microscope.

Stress was then applied to the cell membrane of erythrocytes. For this, a surface-attached cell was grasped with the optical trap and repeatedly pulled in the direction away from the surface. A maximum laser trapping force of approximately 160 pN was applied. The force was determined from the read out laser diode current, as will be explained in detail in section 3.5.1. Figure 3.8 shows the obtained elongation of a cell stretched up to a length of approximately 1.3 times its original diameter, in different directions. At this point, the strength of the cell's attachment to the surface dominated the maximum trapping force. The cell subsequently snapped back towards the surface, restoring its original shape.

The procedure was repeated for 8 erythrocytes, and the amounts by which they could be stretched were measured using the video recordings. An average elongation of 27 % $\pm$ 18 % was obtained. The diameter of the cell in the plane perpendicular to the applied force was determined to be diminished by 41 % $\pm$ 13 %. These results agree well with previously published findings by Hénon et al. [1999].

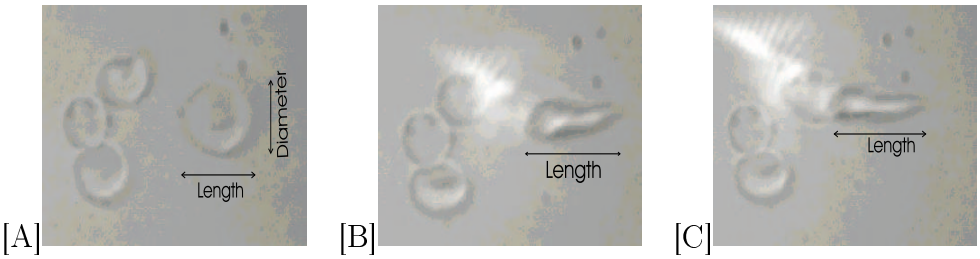

Figure 3.8: Erythrocyte cell membrane stretched with optical tweezers. The image sequence shows a cell attached to the sample cell surface (A), and stretched by holding on to the cell membrane and pulling away from the surface with the optical trap (B,C). The length in (B) and (C) is approximately 30 % longer than in (A), while the cell diameter is decreased by more than 50 % here. The shown cell elongations designate stretching maxima. For further stretching, the attachment to the surface dominated the trapping force and the cell jumped back towards the surface.

Granulocytes

The developed optical trap was used to manipulate a type of white blood cell, the neutrophilic granulocyte or short neutrophil. These cells have a diameter of approximately 12 μm. A series of images of a neutrophil, translated with the laser trap, is shown in figure 3.9. The upper and lower size limits of particles which can be trapped are defined by the efficiency of the trap and the particles' density, as will be detailed in section 3.5.1. For our set-up, particles between 1 and 15 μm have been manipulated using the optical trap.

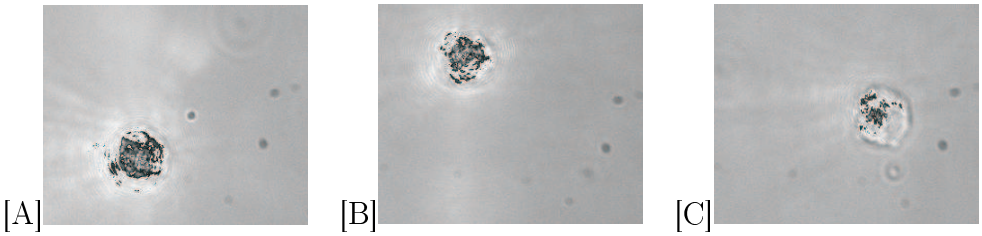

Figure 3.9: Neutrophil manipulated with optical tweezers. The image sequence shows trapping of the cell (A), and lateral translation (B,C) with the optical trap. The laser power was reduced from 210 mW (A), to 150 mW (B), and 35 mW (C), revealing a more clearly visible trapped cell within the reflected laser light. Translation of the cell was possible for $\gtrapprox$ 10 mW.

Further applications

Further, the presented optical tweezers system was used for qualitative adhesion studies, in which the optical trap was used to pull protein coated plastic beads off differently prepared surfaces. The percentage of detachable beads was determined for each surface, and served as identification of the most ideal sample preparation procedure for non-adhesive surfaces. The optical trap was further employed to qualitatively study antigen-antibody interactions. This work has been published in a recent thesis [Rigby-Singleton, 2002].

3.4 Force detection system

So far we have discussed the optical trap only. With this we can hold and manipulate dielectric objects in their native or near physiological environments. The technique of optical tweezers is, however, also particularly suited for force applications. As outlined in chapter 2, the trapping potential can

be approximated by a harmonic potential with very low spring constants κ (typically between 0.001 and 0.1 pN/nm), allowing access to the very low force regime.

In order to measure the forces on a trapped particle in the trapping potential, we need to determine both the spring constant of the potential, and the displacements of the particle from the trap centre. This can then with knowledge of the potential's spring constant be converted into force, using Hooke's law, as described in section 2.2.2. Measurement of the minute displacements involved can be achieved using a two-dimensional photodiode array. In our set-up, we project the trapped object onto a quadrant photodiode detector, using the microscope optics. The position of the shadow of the trapped particle in the microscope illumination can thus be detected on the photodiode array. The trapping objective serves hereby also to magnify the image.

The active surface area of a photodiode is proportional to the induced noise and therefore kept as compact as possible. The gap between the four single diodes in the array determines the resolution of the photo-detector, and is therefore also desired as small as possible. The quadrant diode model used in our set-up (S2856; Hamamatsu, Hamamatsu City, Japan) has a total active surface area of 4 times 0.295 mm x 0.595 mm (4 x 0.1755 mm^2). The width of the gap between the single diodes is 10 μm. Each photodiode detects light from wavelengths of 320 to 1060 nm with a peak sensitivity at 900 nm and a cut off frequency of 100 MHz.

Incoming photons produce a current signal in the photodiodes. The principle of position detection with the quadrant photodetector is based on the proportionality of this current to the incoming light intensity. The more

diode surface area is covered by the image, the less current is produced. When the image shadow of an object covers a sufficiently large part of the active detector surface area, then a position change from the detector centre alters the total current outputs of one or more diodes. The current signals are converted into voltages and amplified and further processed by the electronic detector circuit. Figure 3.10 shows a diagram of the electronic circuit employed, orientated on a previously published circuit diagram [Simmons et al., 1996].

A **headstage** case contains the quadrant photodiode and the first level of the signal processing circuit. Four operational amplifiers (op-amps, also: integrated circuit components, ICs) OPA121 (Burr-Brown, Tucson, AZ, USA), convert the current signals from each of the four single photodiodes into voltage signals, while simultaneously pre-amplifying them. For this, a high value resistor ($R = 100\ \mathrm{M\Omega} \pm 1\ \%$) was inserted in parallel to each of the op-amps.

The output of the headstage (stage 1) are the individual pre-amplified voltage signals of each of the photodiode segments. These are fed into the main photodetector circuit (stage 2 and 3) via a shielded cable. Both the headstage and main unit of the detector are enclosed by a metallic case. The separation of headstage and main circuit allows us to keep main circuit box and power supply on a shelf and off the vibration sensitive air buffered table of the optical set-up. Only the headstage is in the immediate proximity of the optical tweezers set-up, positioned at the microscope sideport.

The **second stage of the photodetector circuit** consists of two IC

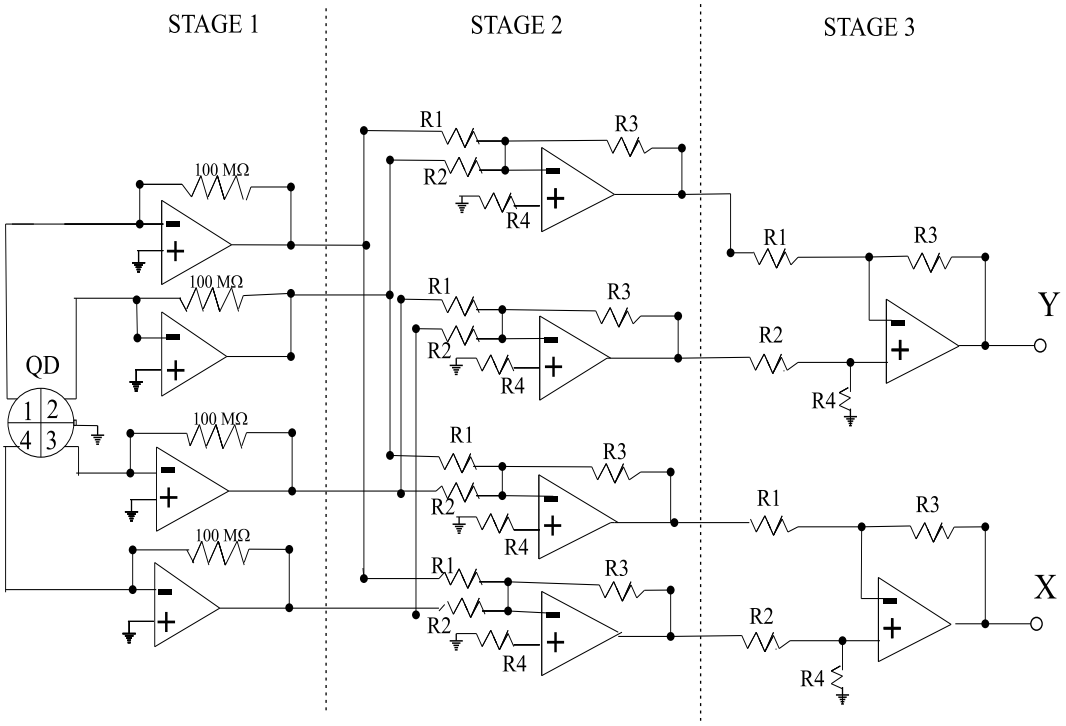

Figure 3.10: Circuit diagram of the position sensitive photodetector, adapted after [Simmons et al., 1996]. The circuit is made up from three stages. Stage 1 (head-stage) operational amplifiers (op-amps) serve to transform the current signals from the four single photodiodes of the quadrant detector (QD) into voltage signals and to pre-amplify these sufficiently. Stage 2 op-amps add the signals of different pairs of diodes, producing output sums of the two TOP, BOTTOM, LEFT and RIGHT diodes. In stage 3, two differential amplifiers subtract these sums suitably, to give TOP-BOTTOM and LEFT-RIGHT displacement signals y and x, respectively.

elements of the type OP270 (Analog Devices, Norwood, MA, USA). The OP270 is a dual precision amplifier with a very low noise level. Each of the ICs adds two separate pairs of signals from stage 1. The output voltages of stage 2 are therefore four sums, each from two different diodes of the photodetector array: the two top diodes (TOP), the bottom (BOTTOM), left (LEFT), and the two right diodes (RIGHT). Low ohmage resistors R_1 and R_2 (9.96 $\pm$ 0.01 kΩ) were inserted in the circuit between the stage 1 output pins and stage 2 inverse input pin (see circuit diagram in figure 3.10). In parallel to the IC elements of stage 2, resistors were introduced with values $R_3 = 99.8 \pm 0.1$ kΩ, leading to a further 10-fold amplification of the signal. The function of stage 2 is then described by the following formula:

$$V_{out} = -\left(\frac{R_3}{R_1} \cdot V_1 + \frac{R_3}{R_2} \cdot V_2\right) \tag{3.2}$$

Resistors R_4 were also provided between the input pins of the stage 2 op-amps and ground. To minimise offset voltages due to induction currents, the values of these were chosen to match the impedance at both IC entrance pins ($R_4 = 9.055 \pm 0.005$ kΩ), following equation 3.3:

$$R_4 = \frac{(R_3 \cdot R_{1/2})}{(R_3 + R_{1/2})} \tag{3.3}$$

where $R_{1/2}$ is the average value of the resistors between the output pins of stage 1 and the inverse input pin of stage 2, R_1 and R_2.

Stage 3 of the circuit is made up from two differential amplifiers of type AMP03 (Analog Devices). These each compare two of the sums from stage

2, and give out the difference between them: TOP-BOTTOM and LEFT-RIGHT. The difference signal was further amplified approximately 20-fold in this stage. For this, the resistance of the parallel resistor to the IC, R_3, was chosen to be 20 x the ohmage of the resistor in front of the inverse input pin, R_1. Correct function of the differential amplifiers was vouchsafed by insertion of resistors R_2 between stage 2 output pins and stage 3 input pin, and R_4 between the latter and ground, according to the following condition:

$$R_1 = R_2 \qquad R_3 = R_4 \tag{3.4}$$

Resistors R_1 to R_4 of value 25 kΩ were included in the IC by the manufacturer. 472 $\pm$ 1 kΩ resistors were added in series to both R_3 and R_4, to give amplifications of factor 19.85 $\pm$ 0.05. Stage 3 function is then described by the following equation:

$$V_{out} = \frac{R_3}{R_1} \cdot (V_1 - V_2) \tag{3.5}$$

where V_1 and V_2 are the output voltages from two of the adder op-amps of stage 2, either TOP and BOTTOM, or LEFT and RIGHT. The output voltages of stage 3 are the x (horizontal; LEFT-RIGHT) and y (vertical; TOP-BOTTOM) position signals.

The detector output voltages are filtered through a low pass filter, consisting of an RC-unit, with resistors R = 1 kΩ and four parallel capacitors C = 1 nF, giving a total of C= 4nF. The time constant of the filter τ determines the cut-off frequency ν of the unit, as given in equation 3.6:

$$\nu = \tau^{-1} = (R \cdot C)^{-1} \tag{3.6}$$

With the chosen values of R and C, signal frequencies of $\gtrapprox$ 250 kHz were therefore attenuated, leading to a noise reduction by a factor of 2. The RC-circuit is schematically shown in figure 3.11.

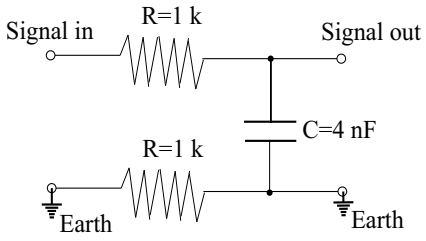

Figure 3.11: Low pass filter: the circuit consists of two 1 kΩ resistors R and a capacitor C, and is therefore also known as an RC-circuit. In our case, C is composed of four parallel 1 nF capacitors. The detector x and y output signals are both individually filtered through a low pass filter.

x and y displacement voltage signals are displayed on a two channel digital real time oscilloscope (Tektronix TDS 210, Tektronix Inc., Wilsonville, OR, USA). The oscilloscope contains an analog to digital converter card, enabling computer assisted data processing. Via its GPIB port, measured voltages are transferred to a PC. They can there be displayed and saved using Labview software (National Instruments Corporation, Austin, TX, USA).

All resistors, capacitors and IC's were purchased from RS electronic components Ltd (Corby, Northants, UK). Stage one and two ICs were chosen for their low noise features (6 nV/$\sqrt{Hz}$ at 10 kHz for the OPA121, 5 nV/$\sqrt{Hz}$ for the OP270). Since the electronic noise limits the resolution of the detector, it is essential to keep it as low as possible. Stage three op-amps possess

documented noise features of 20 μV/$\sqrt{Hz}$ at 10 kHz. The overall noise of our detector system was calculated from this, for our choices of signal amplification in the individual stages to be approximately 46 mV at 10 kHz. Equation 3.7 gives details of the calculation:

$$N_{total} = A_1 \cdot n_1/\sqrt{Hz} + A_2 \cdot n_2/\sqrt{Hz} + A_3 \cdot n_3/\sqrt{Hz} \tag{3.7}$$

where N_{total} is the total electronic noise in the circuit, n_i is the noise in stage i of the circuit per square root of Hz signal frequency, and A_i is the amplification within stage i. n_i are given by the manufacturers (see above). Equation 3.7 then gives at 10 kHz:

$$\begin{aligned} N_{total}(10kHz) &= 10^4 \cdot 6nV/\sqrt{Hz} + 10 \cdot 5nV/\sqrt{Hz} + 20 \cdot 20\mu V/\sqrt{Hz} \\ &= 6mV + 5\mu V + 40mV \approx 46mV \end{aligned}$$

Figure 3.12 shows the dark signal of our detector system, which is its output signal solely due to electronic noise. The detector output voltage is plotted versus time. A noise level of approximately 50 mV can be seen from the figure.

The principle of function of the developed detector is demonstrated in figure 3.13. Here, at 1.7 seconds, a metal 60 μm slot grid (Agar Scientific Ltd., Stansted, Essex, UK) was moved laterally, so that its image covered half the photodiode array. As can be seen from the figure, this induced an output voltage increase by almost 14 V. Only a third of the available microscope illumination power was used to obtain the presented signal. Higher light intensities quickly led to saturation of the electronic circuit, with 15 V maximum output voltage.

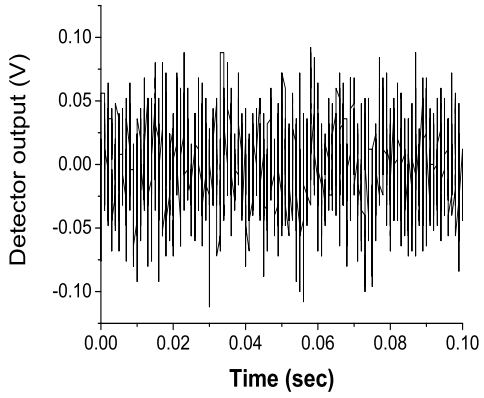

Figure 3.12: Position detector dark noise.

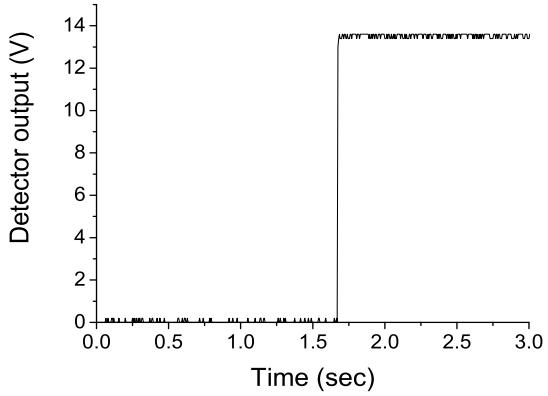

Figure 3.13: Position detector output signal. The voltage signal is plotted versus time. At 1.7 seconds, the border of a 60 μm metal slot grid was moved laterally using a piezo positioning stage. The metal part then covered exactly half the detector array. This induced a change in detector signal by almost 14 V.

The signals are calibrated against known displacements of beads, in order to interpret detector voltage signals in terms of position change. Results of detector calibration and a typical force measuring application of the developed system are presented in the following section.

3.5 Calibration

For models based upon spherical objects in a fluid, the friction, gravitational, and thermal forces are known and can be used to calibrate the unknown forces of our trapping potential. From optical tweezers studies on spherical dielectric beads, various properties of our set-up were thus derived, and compared to published data. Calibration with such particles therefore provides a further proof of principle for the developed optical tweezers system.

Without calibrating our optical tweezers system against known standards, we would only have a trap to hold and transport dielectric objects. We would not have any knowledge of the acting forces. Calibration of our system against known forces enables the determination of the maximum possible force of our trap (the drop out force). It further provides us with the spring constant (or stiffness) of the trapping potential, allowing us to translate displacement within the potential into a force on the trapped particle. In the following, the determination of the drop out forces and trap stiffness for the different laser powers of our optical trap will be presented.

3.5.1 Investigation of trap efficiency

The determination of the drop out force of the optical potential is of interest not only for the knowledge of the maximum force producible with our system. The drop out force also allows an estimation of the efficiency of the optical trap. This efficiency is typically expressed in terms of a quality factor, Q. Different lateral and axial values, Q_{lat} and Q_{ax}, exist due to the different potential landscapes along the two orthogonal directions.

Lateral drop out force

For the presented optical tweezers system, the lateral drop out forces for dielectric spherical beads in a laminar flow were calculated using Stokes drag. The advantage of this method is its relatively simple principle and realisation. The principle is based on the fact, that a spherical object in a laminar flow experiences a friction force F_{flow}, which can be calculated using Stokes' formula:

$$F_{flow} = 6\pi\mu r v \cdot \beta \tag{3.8}$$

where r is the radius of the sphere (in m), μ is the surrounding medium's viscosity or friction coefficient (μ=0.001025 Nsm^{-2} for water at 20°C [Gerthsen and Vogel, 1993]), v is the relative velocity between medium and sphere (in m/s) and β is a correction factor. β has to be introduced in real systems, to account for the finite distance to boundary surfaces. In our case the trapped sphere is several times its own diameter away from both surfaces. Since surface disturbances can be neglected in good approximation for distances of a

few sphere radii from the surfaces [Happel and Brenner, 1965; Svoboda and Block, 1994a], the correction factor was here set equal to 1.

To generate the viscous drag force after Stokes, a flow cell was designed, through which liquid could be pumped at a controlled velocity. The cell is shown in figure 3.14. A 2 mm thick solid brass frame contains a 1 mm thick mould for the liquid sample cell. In the thinner mould part, a central window of 20 mm diameter was spared for the objective. The preparation of a liquid sample cell, in which the surrounding solution can be exchanged easily, is simple and will be briefly described here.

A microscope slide (BDH Laboratory Supplies) had been provided with two 3 mm diameter holes at a distance of 28 mm (centre-to-centre). From parafilm (Parafilm "M", laboratory film, American National Can, Chicago, IL, USA), two rectangles are cut out to cover the entire of a 76x26 mm^2 glass cover slip (Chance Propper Ltd.). Before laying them onto the cover slip, a channel of approximately 8 mm width and 32 mm length is cut into the middle of each of these, using a razor blade. The parafilm pieces are then sandwiched between cover slip and microscope slide, so that the two holes in the slide are within the channel, formed by the cut parafilm. The ensemble is laid into the mould in the metal flow cell frame, with the cover slip facing down, the microscope slide on top. The two holes in the microscope slide are then surrounded by two small squares of parafilm each, with cut out windows of 3 mm diameter to spare the holes. This insulates the inlet and outlet of the cell, to which polytetrafluoroethylene (PTFE; Kinesis Ltd., Epping, CM16 4AS, UK) tubing of outer diameter 3 mm and inner diameter 1.7 mm is connected. The whole of this is fixed, by clamping the microscope

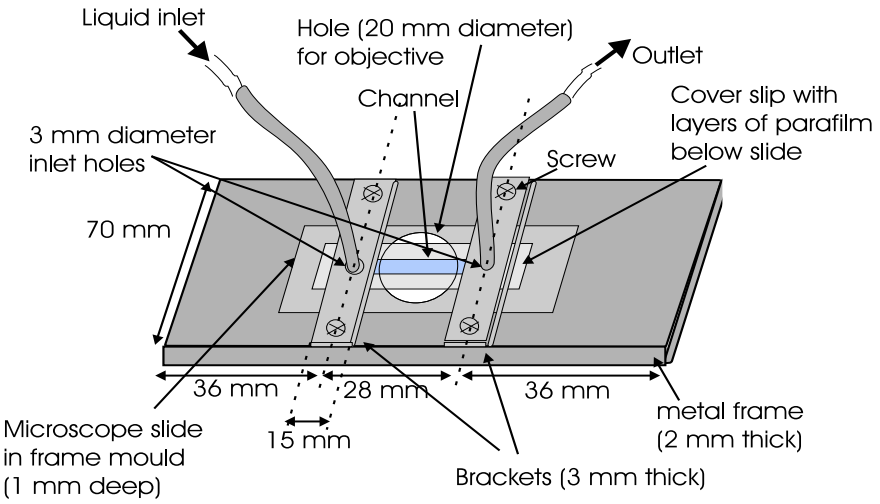

Figure 3.14: Schematic drawing of the flow cell, which has been employed in the drop out force calibration.

slide/cover slip ensemble to the metal plate base with two metal brackets. The brackets are screwed down carefully but tightly onto the frame. The cell is sealed by placing it on a heat plate at 200°C for approximately 1 minute, until the parafilm is observed to melt. The screws are refastened, and the ensemble is left to cool down for a minimum of 30 minutes before application of liquid.

The thickness of the flow cell channel between the two glass surfaces was estimated to be approximately 200 μm, from micrometer screw measurements on unmelted parafilm. This makes the volume of the cell approximately 50 μl.

The volume required for replacing the total contents of the flow cell was measured by sucking coloured liquid (gel loading buffer from gel electrophoresis kit, Sigma-Aldrich Company Ltd.) from a plastic Eppendorf tube (Eppendorf UK Ltd., Cambridge, UK) into the cell. The amount of liquid needed

until both the inlet tubing and the flow cell volume were filled was measured by recording the volume loss in the Eppendorf tube, when the blue colour reached the outlet of the cell. This volume was found to be 200 ($\pm$ 50) μl.

For calibration, spherical beads from latex with a polystyrene coating (polystyrene-latex (PSL); Sigma-Aldrich Company Ltd.) of 2 ($\pm$ 0.16) μm diameter were used. Deionised water (dH_2O; deionised and purified to 18.2 MΩcm resistivity using Elga Maxima system; Elga Ltd., High Wycombe, UK) served as the surrounding liquid. Water containing the beads in sufficiently low dilution was pumped into the flow cell through the inlet tube, using a peristaltic pump (12000 Varioperpex, LKB Bromma, address, UK). When the bead solution had filled the whole of the cell, a 5 ml plastic syringe was attached to the end of the tube, via a connection piece of silicon tubing (inner diameter 2 mm, outer diameter 4 mm; Fisher Scientific UK, Loughborough, UK). The syringe could be pushed with a range of speeds, using a motorised syringe driver (SP210iw syringe pump, WPI UK Ltd., World Precision Instruments, Aston, Stevenage, UK). The contents of the syringe would thus force the liquid from the tubing forward through the flow cell at the selected velocity.

Flow velocities were determined using a home built camera connected to a video recorder and TV screen. The time that beads of the applied diameters needed to travel a known distance was recorded. The distance was measured on the display screen. It was translated into real distance inside the liquid cell by dividing by the magnifications of the employed camera and the objective of 100 x and 40 x, respectively. Bead velocities were obtained from video recordings over 2 to 6 minutes, for each selected syringe driver push rate.

From the known flow velocity, the force F_{flow} on a spherical particle in laminar flow can then be calculated using Stokes law. The force F_{laser} on a bead in the trapping potential is proportional to the laser power P and the refractive index of the surrounding medium n_{medium} divided by the speed of light in vacuum c. The proportionality factor is the quality factor Q [Ashkin, 1992]:

$$F_{laser} = \frac{n_{medium} \cdot Q \cdot P}{c} \tag{3.9}$$

where $n_{medium} = 1.32$ for water at 20°C and for wavelength $\lambda = 1064$ nm [for the Properties of Water and Steam, 1997], and $c = 2.9979 \cdot 10^8$ m/s [Gerthsen and Vogel, 1993].

In the calibration experiments, a bead was trapped in the optical trap inside the flow cell. Liquid flow was then generated to apply a friction force to the trapped bead. The laser power was slowly reduced, until the trapping force would not suffice to hold the bead trapped against the viscous drag of the flow. The laser power, at which the particle dropped out of the trap, was noted. The measurement was repeated for 24 different beads of 2 μm diameter ($\pm$ 0.16, manufacturer information; Sigma-Aldrich Company Ltd.).

In our set-up, laser power is read out as the supplied laser diode current, which can be translated into laser power at the trap position via a calibration curve (see figure 3.6). The measured average laser diode current $I_{dropout}$, at which the beads were lost from the trap, was:

$$I_{dropout} = 0.70A(\pm 0.03A)$$

This translates into a laser trapping power of 2.4 mW. The read out error in the diode current was estimated to be 0.01 A for each single measurement. The found values showed a slightly bigger variation with a standard deviation (SD) of 0.03 A for the different beads. This translates into error margins from approximately 2 to 6 mW, according to the graph of figure 3.6. The spread of the data is likely to be due to slight variations in bead size and laser power fluctuations. A trapping power of 2.4 mW was assumed for a bead of exactly 2 μm diameter in the calculations of the drop out force.

The two forces F_{flow} and F_{laser} have to cancel each other, when the bead is freed from the trap. From the two equations, we thus obtain the proportionality factor Q, which defines the trapping efficiency of the optical trap. In this case, a force in lateral direction was applied, and therefore the resulting value is more specifically Q_{lat}.

The trap position was measured to be 15 μm above the bottom sample cell surface, using the microscope fine positioning dial of the objective. For the generated flow profile, a velocity of 71 ($\pm$ 15 SD) μm/s was measured at this position for 2 μm diameter PSL beads in water. For this velocity and the given geometry of the flow cell, we obtain a Reynold's number of the order of 10^{-3}, which defines laminar flow. The laser power at the trap position, for which the force due to Stokes drag overcomes the trapping force, was 2.4 mW, as discussed above. Inserting these values into equations 3.8 and 3.9 gives:

$$F_{flow} = 1.3(\pm 0.2)pN = F_{laser} = 10.6pN \cdot Q_{lat}$$

$$\boxed{Q_{lat} = 0.123(\pm 0.019)}$$

The obtained value for Q_{lat} on 2 μm diameter PSL beads at 15 μm depth was compared to values published for other set-ups. Q_{lat} values of 0.085 and 0.21 have been reported for 1 and 3 μm diameter latex beads at a distance of 13 μm from the sample cell surface [Felgner et al., 1995]. Another source gives Q_{lat}=0.19 for 2 μm beads [Singer et al., 2000], but with no mentioning of the depth of the trap within the sample cell. An exponential decrease of trapping force has been found at increasing depths [Felgner et al., 1995]. Our result therefore compares well with the previously published data of other set-ups, assuming a shorter distance of the trap from the sample cell surface for the latter results. The result is also in good agreement with theoretical predictions of trapping forces in the Ray optics regime with a Q value of 0.165 for polystyrene beads in water for an angle of 72° of the focussed laser beam [Ashkin, 1992]. In this regime, the trapping force does not depend on the particle size. Most trap calibration measurements for optical tweezers have been carried out with bead sizes in an intermediate regime, so that an effect of the bead diameter was observed.

Axial drop out force

In axial direction, gravitational (F_{grav}) and thermal force (F_{therm}) contributions are used to calculate the drop out force of a trapped particle [Felgner et al., 1995]:

$$\begin{aligned} F_{ax} &= F_{grav} + F_{therm} \\ &= \left(\frac{\pi}{6} \cdot (\rho_{sphere} - \rho_{medium}) \cdot d_{sphere}^3 \cdot g\right) + \left(\frac{2k_B T}{d_{sphere}}\right) \end{aligned} \tag{3.10}$$

where k_B is the Boltzmann constant, T the absolute temperature (in Kelvin), ρ_{index} is the density of either the sphere or the medium as indexed (ρ_{PSL} = 1.05 g/cm^3 (manufacturer information, Sigma-Aldrich Company Ltd.); ρ_{dH_2O} = 0.998 g/cm^3 at 20°C), d is the diameter of the spherical bead, and g the gravitational acceleration (g = 9.81 m/s^2).

In the axial drop out force calibrations on our set-up, 5 μm diameter PSL beads were employed. For these, a value of 0.035 pN is obtained for F_{ax} from equation 3.10. At a trap position 85 μm above the bottom sample cell surface, the beads were found to drop out of the trap for laser diode currents of $\leqq$ 0.65 A. Converting this into trapping laser power gives approximately 1.5 mW. Insertion into equation 3.9 and setting the calculated F_{ax} equal to the thus obtained F_{laser}, renders the axial quality factor of the optical trap, Q_{ax}.

$$F_{ax} = 0.035pN = F_{laser} = 6.610pN \cdot Q_{ax}$$

$$\boxed{Q_{ax} = 0.0053(\pm 0.0027)}$$

The estimation of an error is again difficult for the trapping laser power, and derives here mainly from the uncertainty in the laser power calibration graph (figure 3.6).

Comparison of our results to previously published values for Q_{ax} showed good agreement, considering that trap positions were at different depths in the sample cells, and different bead sizes were used. For a trap distance of 9 μm from the bottom surface and latex beads of 1 μm diameter, Q_{ax} was found to be 0.0058 for one set-up [Felgner et al., 1995], for a non-specified trap-surface distance and 2 μm diameter polystyrene beads 0.025 for a second [Singer et al., 2000]. For our much higher trap depth and 5 μm diameter PSL beads, the obtained value thus appears reasonable.

Trap quality

For our optical tweezers system, the quality factors are $Q_{lat} = 0.123$, $Q_{ax} = 0.0053$. Therefore $Q_{lat} \approx 23 \cdot Q_{ax}$. Although different trap positions were used for lateral and axial calibration, a crude comparison of the two values is possible. Our result is in reasonable agreement with previously published ratios for different optical tweezers set-ups [Felgner et al., 1995; Singer et al., 2000]. The axial trapping force is generally one order of magnitude lower than that in lateral direction. The ratio of $\frac{Q_{lat}}{Q_{ax}}$ at the same cell depths defines the eccentricity (ratio of major axes) of an ellipsoid, by which the trapping potential profile at this position can be described.

With the knowledge of Q_{lat} and Q_{ax} of our optical trap, we can therefore obtain the maximum possible trapping forces $F_{lat,max}$ and $F_{ax,max}$ (in horizontal and vertical direction) of our system. For 2 μm and 5 μm diameter PSL beads respectively, the maximum achievable lateral and axial forces were calculated to be:

$$\boxed{F_{lat,max} = \frac{n_{dH_2O} \cdot Q_{lat} \cdot P_{max}}{c} = \frac{1.32 \cdot 0.123 \cdot 300mW}{2.9979 \cdot 10^8 m/s} = 162pN}$$

$$\boxed{F_{ax,max} = \frac{n_{dH_2O} \cdot Q_{ax} \cdot P_{max}}{c} = \frac{1.32 \cdot 0.0053 \cdot 300mW}{2.9979 \cdot 10^8 m/s} = 7pN}$$

3.5.2 Trap stiffness calibration

The laser output can be determined with the help of a calibration curve via the diode current read out on the laser power supply display. By measuring the losses through the optical bench, we obtained the corresponding curve of the laser power at the trap position for each diode current (see figure 3.6). This power determines the trapping force.

The distances observed in the CCD images need to be put into the context of known distances, so that these in return can be used to control the sample stage movement, and eventually to interpret the output voltages of the position detector (see section 3.4) in terms of displacement amplitudes.

Finally calibration against known forces, as will be explained below, enables us to ascribe a force on the trapped particle to each measured displacement, as well as to determine the drop out force, at which the particle leaves the potential well.

There are therefore several systems within the optical tweezers based force transducer, that require calibration:

1. CCD camera length scale (to give distances measured on screen a real length)

2. Voltage output of detector (for precision displacement measurements on a trapped particle)

3. Spring constant of the trapping potential (to translate measured displacement into a force on the trapped particle)

These will be discussed separately in the following sections.

CCD camera calibration

The CCD camera (Imager 3 QE, La Vision) is connected to the front port of the microscope, for distance measurements and visualisation of sample and trapping dynamics. In order to be able to relate any position difference measured in our system to a real length, we have to calibrate it against a known length standard.

Stage micrometer standard. The CCD camera pixel-length ratio has been calibrated against a commercially available microscope stage micrometer (Graticules Ltd., Tonbridge, Kent, UK). The employed stage had a scale of 0.1 mm, 50 subdivisions of 0.002 mm length with a separating line width of 1 μm, and a guaranteed overall accuracy of $\pm$ 1 μm (relating to $\pm$ 1 %). The separation of the divisions was measured using the profile function of the CCD DaVis software (La Vision). In 100 measurements an average of 25.11 ($\pm$ 5.3 % SD) pixel was found for the 2 μm distances. This relates to a pixel to length ratio of 12.56 pixel/μm ($\pm$ 5 %).

Piezo-electric stage. A piezo stage (P517.3CL stage; Lambda Photometrics Ltd., Harpenden, Hertfordshire, UK) was used to translate the sample

cell on the microscope object table. The stage produces precise displacement, generated by the application of voltage signals through a piezo controller unit. The unit's display can indicate either the amplitude of the applied voltage, or the amplitude of the induced translation. The piezo displacement performance has been calibrated by the manufacturer to be of a precision of better than ± 0.07 % at 24°C, 982 mbar air pressure, and 46 % humidity. Piezo movement was compared against the CCD length standard, by imaging the displacement of a 3 μm diameter bead by a nominal 10 μm according to the piezo controller display. The bead was fixed within a polydimethylsiloxane gel (PDMS gel; Sylgard 184, silicone elastomere, DOW Corning GmbH, Wiesbaden, Germany) on a microscope slide, which was placed and secured on the piezo stage. 100 measurements gave a distance of 121.125 pixel (± 0.4 % SD). From this, a ratio of 12.1125 (± 0.5 %) pixel per 1 μm was found for the CCD scale. The diameter of the bead was further measured, and rendered a value of 2.93 (± 5 %) μm for 100 single measurements with the obtained pixel conversion factor. This result agrees well with the nominal bead diameter of 3 μm within the error margins of both the bead size and measurement accuracy.

The pixel conversion factor obtained using the piezo-positioning stage was considered more reliable than the CCD pixel calibration using the stage micrometer. The stage displacement distance offers better accuracy (0.07 %) than the separations of the micrometer standard (1 %). Further, due to the greater distance measured (10 μm) with this technique (as opposed to 2 μm for the micrometer measurement), a higher degree of precision can more easily be achieved. This is reflected in the standard deviations of the results

(0.5 % for greater distance, 5 % for short distance measurement). In the following, a CCD pixel/μm ratio of 12.1125 has therefore been assumed.

Calibration of detector output voltage

In order to use the detector system for position sensitive measurements, its voltage output signals were calibrated against known displacement of a particle image from the detector array centre. For this, spherical beads were translated by controlled distances, using the piezo stage. Different bead materials and sizes were investigated as well as the effect of illumination power.

PSL or polystyrene beads of diameters between 1 and 3 μm are generally employed in optical tweezers experiments. However, an image of these in the 30 W illumination of our set-up shows little contrast to the homogeneous background of the buffer solution in experiments (or the gel in the calibration studies). Figure 3.15 shows an example of a CCD image of a 3.3 μm diameter PSL bead in water, and the corresponding profile plot of CCD intensity counts along a chosen line through the image. Overlaid is the profile plot for the bead after x-displacement by 10 μm using the piezo stage. Weak intensity differences between bead image and background are demonstrated here. An approximate difference of 50 counts was found for the employed bead. The detector signal produced by the piezo controlled 100 μm amplitude oscillation in x-direction of a similar sized PSL bead fixed in PDMS gel is shown in figure 3.16. Small maximum/minimum detector output signals of approximately $\pm$ 0.15 V can be seen for coverage of the either left or right pairs of the diode array.

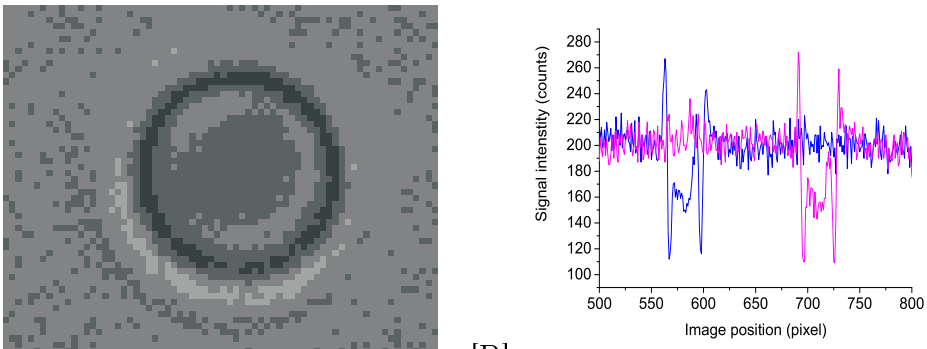

Figure 3.15: CCD image contrast for 3.3 μm diameter PSL bead in water: (A) CCD image, and (B) profile of intensity counts along image line through the bead. The two colours indicate profiles obtained from images before and after 10 μm displacement of the bead. The image intensity difference between bead and background is approximately 50 counts. From the profiles, the bead diameter was measured to be 3.3 μm ($\pm$ 0.1 μm measurement inaccuracy).

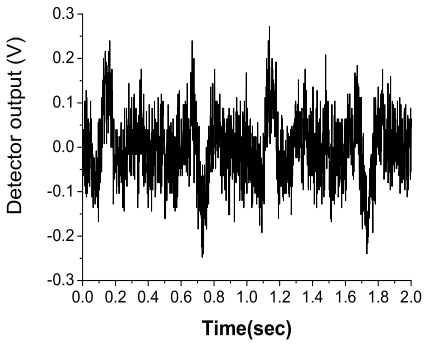

Figure 3.16: Detector output signal for a 3 μm diameter PSL bead. The bead was fixed in PDMS gel, and oscillated with 100 μm amplitude, using a piezo positioning stage. Positive peak signals can be seen at approximately 0.1 and 1.1 seconds, when the ratio of the left to the right pair of photodiodes is maximal, negative peaks at 0.7 and 1.7 seconds, when this ratio is minimal.

Effect of bead material

The effect of object-background contrast was investigated both theoretically and experimentally. Incoming light power P per diode area S was calculated for very transparent and very opaque beads. The resulting detector output signal D can be derived, assuming proportionality between current production in the photodiodes and incoming light power (proportionality factor α):

$$A = \pi(\frac{d}{2})^2$$
$$U = S - (1 - T) \cdot A$$
$$D = \alpha \cdot P(S - U) = \alpha \cdot P(S - (S - (1 - T) \cdot A)) = \alpha \cdot P(1 - T) \cdot A$$

where A is the diode surface covered by the shadow of the bead, d is the diameter of the bead image, U is the uncovered diode surface, and T is the bead's transparency in percent. A 10 times stronger signal D was found from this, for example, for a bead with 0 % transparency (tungsten) compared to a bead of an estimated 90 % transparency (silicon).

To compare the transparencies, CCD images and intensity profiles for both beads were obtained. These are displayed in figure 3.17. Intensity differences between bead and background are only 20 counts for the silicon, and 120 counts for the tungsten bead. This suggests only a 6-fold higher transparency for silicon than for tungsten, and a consequently 2.5 times stronger signal.

Detector signals produced with 8.8 μm ($\pm$ 0.2 μm) silicon and tungsten beads are shown in figure 3.18. The diameter of both beads was measured

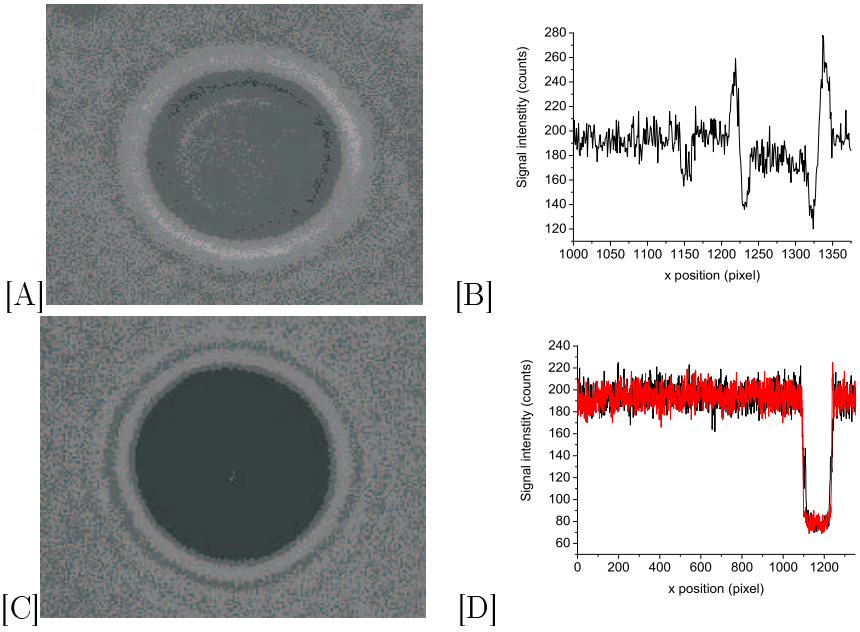

Figure 3.17: CCD image and intensity contrast profile for 8.7 μm silicon bead (A and B respectively) and 8.8 μm tungsten bead (C and D respectively).

from the intensity profile through the obtained CCD images, with a measurement inaccuracy of $\pm$ 0.1 μm.

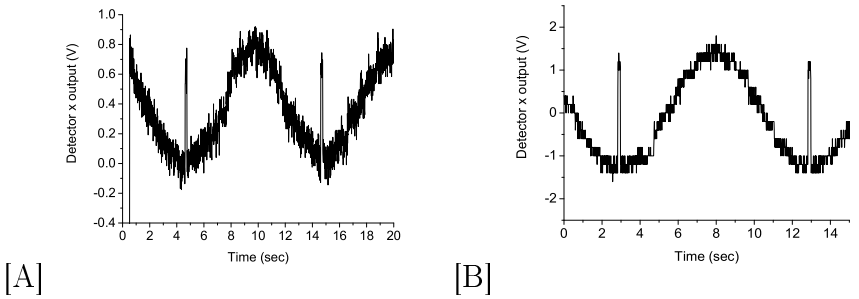

Figure 3.18: Detector x signals of a (A) 8.7 μm ($\pm$ 0.1 μm) diameter silicon and a (B) 8.8 μm ($\pm$ 0.1 μm) diameter tungsten bead, plotted versus time. Beads were attached to a glass cover slip, and oscillated in x direction with 1 μm amplitude, using a piezo positioning stage.

Comparison of the detector signals for 1 μm oscillations in x direction of silicon and tungsten beads showed a more than 4-fold higher detector output voltage for the tungsten bead. The higher signal increase than the predicted 2.5-fold effect is likely to be explained by slight position variations for the two different beads.

Effect of object size

To maximise signal output, the area of the image shadow A should cover a percentage X of the surface of the individual diodes S ($S = 0.1755$ mm^2) as close as possible to 100 % ($X = \frac{A}{S}$). However, the image area of a bead with diameter $d = 3$ μm for example occupies only 6 % of the surface area of a single diode after 40-fold magnification through the microscope objective. For a further magnification of the image of less than 4-fold, 100 % coverage of a single diode with subsequently 10 times stronger signals were calculated for a 3 μm diameter bead.

To experimentally test the effect of detector surface coverage by the bead image, the detector output signals for different sizes of tungsten beads were compared. The results are presented in figure 3.19. Theoretically, $X = 46$, 57, and 105 % for the investigated beads with approximately $d = 8$, 9, and 12 μm, respectively. The detector output signals obtained experimentally scaled similarly as the calculated values for X as can be seen from the figure. Table 3.1 summarises the results.

The results thus show a proportionality between surface coverage and the amplitude of the detector output signal. Therefore, additional magnification of the bead image on the photodiode array should result in considerably

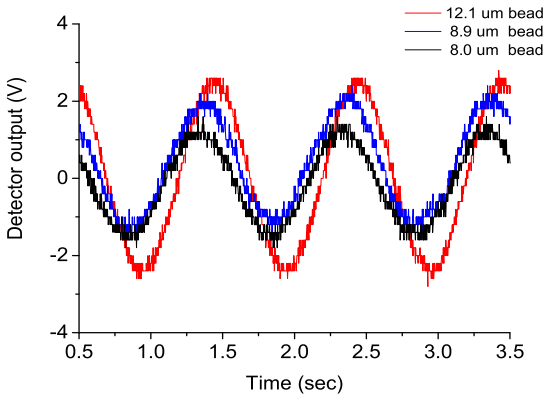

Figure 3.19: Effect of bead size on detector output. The detector signals for the 1 μm amplitude oscillation of an 8.0 (black), an 8.9 (blue) and a 12.1 (red) μm diameter tungsten bead are plotted over a time interval of 3 seconds.

higher signal to noise ratios for the typically employed PSL beads with diameters of 1 to 3 μm.

Additional magnification can be achieved by inserting an additional lens in the microscope side port. Alternatively, the use of an objective with a magnification factor of 100 increases the image diameter by a further factor of 2.5, resulting in a 6-fold increase of covered surface area of the detector to approximately $X = 40$ %. A further lens might still be optionally introduced at the side port for the detection of smaller (1 to 2 μm diameter) beads.

Effect of illumination

Contrast can be increased by changing illumination conditions. Replacement of the 30 W, by a 100 W illumination source increases the total light per diode surface area by a factor of approximately 3. The thus increased contrast be-

Bead diameter (μm)	**Surfaces coverage (%)**	**Output signal (V)**
8.0	46	2.8
8.9	58	3.3
12.1	105	5.0

Table 3.1: Effect of bead size on detector output. The peak-to-peak voltages are given as obtained form the detector signals shown in figure 3.19.

tween dark and light areas causes greater detector output voltages per bead displacement. The strong effect of illumination power was demonstrated by varying the amount of light on a 60 μm wide slot in a transmission EM copper grid. The slot was oscillated over a distance of 10 μm, so that the metal covered an area between all and none of the photodiode array. Maximum detector output is achieved for exactly half coverage. Detector signals are displayed in figure 3.20 for 20, 50, 80, and 100 % illumination from the 30 W halogen light source, the maximum output voltages detected are given in table 3.2. As can be seen from the values, the increase in output voltage increased by approximately the same factor as the illumination power. Therefore, replacing the 30 W by a 100 W illumination source and thus increasing the light power by 70 % can be expected to considerably increase the detector output voltages. Due to time limitations, this change could not be carried out within the presented work, since it involves major modifications of the microscope system.

Further, differential interference contrast (DIC) illumination is often employed in optical tweezers systems. DIC was found to enable better resolution by CCD imaging of subtle displacements within the trapping potential. De-

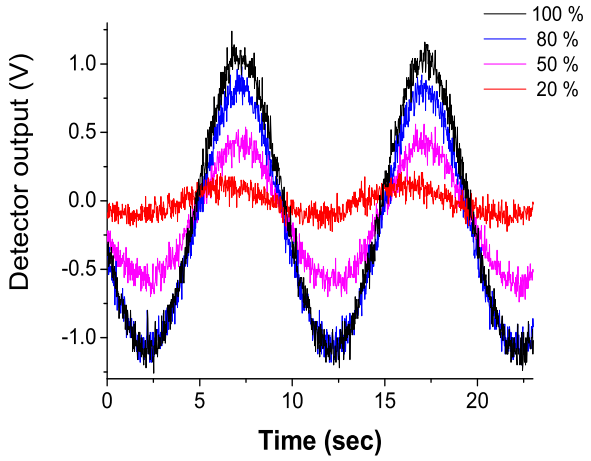

Figure 3.20: Detector signal of a slot within a copper surface, oscillating over a distance of 10 μm with 20, 50, 80, and 100 % of 30 W illumination.

pending on the intended applications of the optical tweezers system, replacing standard brightfield illumination by DIC may improve signal detection.

To summarise, we have shown proof of principle of the developed detector system. However, for the typically employed experimental systems ($\lessapprox$ 3 μm diameter beads as handles for biological samples in aqueous surrounding), the system is not yet optimised. Changes in the illumination source of the microscope and the magnification factor for the object images are required.

Calibration of the optical tweezers spring constant

The photodetector system described can be employed to measure the fine displacement (order of nm) of a trapped particle within the trapping potential with high temporal resolution (order of 100 ms). In order to translate

Illumination (%)	**Output signal (V)**	**Output signal (%)**
20	0.4	17
50	1.1	46
80	2.0	83
100	2.4	100

Table 3.2: Maximum detector output signal for 10 μm copper grid displacement with respect to degree of illumination.

the measured voltage signals into displacements of the bead, detector output voltages were obtained for a range of PSL beads (between 12 and 15 μm diameter). The detector signals were recorded for beads at the trap centre position, and after bead displacement by 1 μm. Figure 3.21 shows the obtained results. A linear fit through the data provided the factor for translation of voltage output into bead displacement for any bead size within this range.

In order to translate the measured displacement into a force experienced by the trapped particle, the knowledge of the spring constant of the trapping potential is required. There are different approaches to calibrating the stiffness or spring constant, κ, of the trapping potential. All are essentially based on comparison of the measured displacement of a trapped particle to an independent known force. Different calibration methods have been briefly discussed in the previous chapter (section 2.2.2). Here, thermal noise analysis [Ghislain et al., 1994; Svoboda and Block, 1994b; Pralle et al., 1998; Florin et al., 1998] and Stokes drag [Felgner et al., 1995; Smith et al., 1996; Simmons et al., 1996; Singer et al., 2000] were both applied and compared for

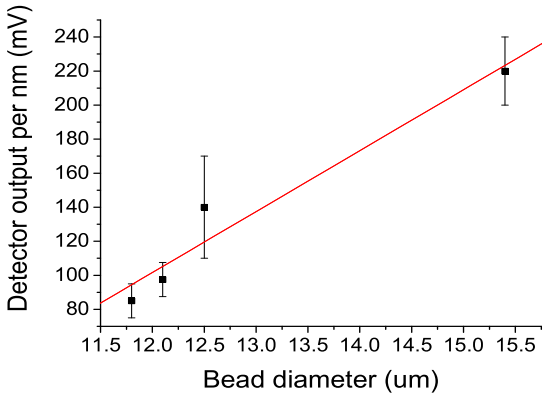

Figure 3.21: Detector voltage output calibration for large PSL beads. A linear fit through the voltage amplitudes obtained for four beads (11.8, 12.1, 12.5, and 15.4 μm) gives the voltage-displacement translation factor for any given bead size within this range.

the calibration of the trapping potential of the developed set-up.

Thermal noise spectra were recorded for a 12.1 μm diameter spherical silicon bead, held in the optical trap. The bead diameter was measured from an obtained CCD image of the bead. For laser trapping powers of approximately 125, 160, and 200 mW, the detector output signals were recorded over time intervals of 5 seconds. Laser powers were determined from the laser diode current read out using the graphs displayed in figures 3.5 to 3.7.

Histograms of bead displacements were thus plotted from the measured detector signals for each of the applied laser powers (see figure 3.22). The ensemble of obtained displacements r can then be described by a Boltzmann distribution $P(r)$ [Pralle et al., 1998], which defines the spring constant (κ) of the trapping potential:

$$P(r) = c \cdot \exp\left(\frac{-\frac{1}{2}\kappa r^2}{k_B T}\right) \tag{3.11}$$

with $T = 296$ K. For a 12.1 μm diameter PSL bead the signal translation factor was obtained from figure 3.21 as 1.0 mV/nm.

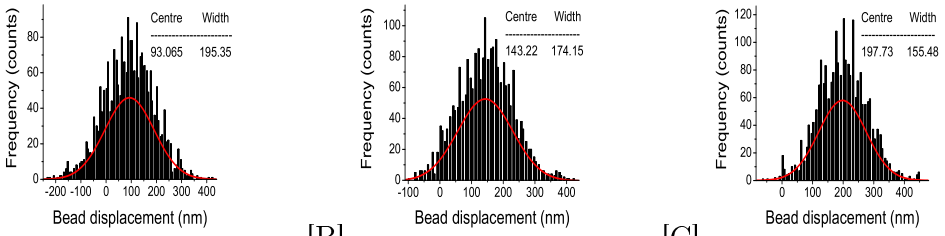

[A] [B] [C]

Figure 3.22: Thermal spectra (bin width 5 nm) of 12.1 μm diameter PSL bead in the optical trapping potential for 125 mW (A), 160 mW (B), and 200 mW (C). Also shown are the Gaussian fits to the distributions, with their centre and width parameters.

From a Gaussian fit to the data, the spring constant of the trapping potential is given as follows from setting the exponentials of the above given Boltzmann distribution and of the Gaussian curve equal:

$$y_{Gauss} \propto \exp\left(-2\frac{(x - x_C)^2}{w^2}\right)$$
$$>> w^2 = 4\frac{k_B T}{\kappa}$$

The spring constants were thus determined from the width of the Gaussian fits to be $\kappa = 4.3$, 5.4, and 6.8 x 10^{-4} pN/nm for 125, 160, and 200 mW laser power, respectively.

Stokes drag on a spherical particle in liquid flow was used to calculate κ from the displacement of a trapped bead in the optical tweezers potential.

The application of liquid flow force has already been introduced for the determination of the lateral trap efficiency (section 3.5.1). The same principle was exploited for the calibration of κ. Here, however, flow forces were kept low, in order to produce only small displacements of the trapped bead within, rather than escaping from the trap potential.

In the calibration experiments, a static liquid cell (as described in section 3.3), which contained water and spherical silicon beads, was employed. A bead of 14.7 μm diameter was held in the optical trap with a trapping power of 125 mW. Its diameter was measured from an obtained CCD image. The liquid cell was then translated along the x direction, using the piezo-controlled translation stage. The bead would experience a drag force exerted by the relative movement between the bead and the surrounding water. From equation 3.8, the resulting force on the bead can be calculated from this velocity and the bead diameter. A velocity of 2 μm/s was applied, resulting in a 0.28 pN force on the bead.

For bead displacements $\lessapprox$ the bead radius, a linear relationship between applied force and bead displacement can be assumed [Ashkin, 1992; Wright et al., 1994; Simmons et al., 1996]. The spring constant of the trapping potential can then be obtained from the displacement of the trapped bead, using Hooke's law (see chapter 2 equation 2.1). Figure 3.23 shows the detector signal following bead displacement in a 2 μm/s flow.

We obtained bead displacements between 2.7 and 3.5 μm for the applied 2 μm/s flow. For our set-up, a spring constant of between 0.95 and 1.0 x 10^{-4} pN/nm was thus found for the applied conditions.

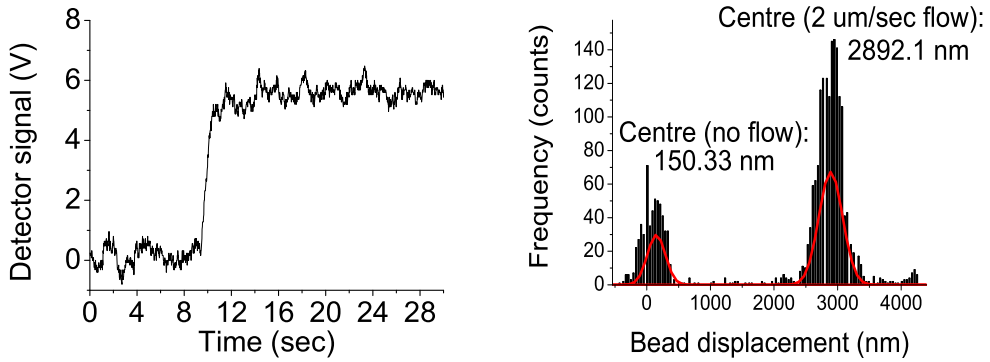

Figure 3.23: Stokes calibration of optical tweezers spring constant. (A) A 2 μm/s laminar flow was applied at approximately 10 seconds, using a piezo-controlled translation stage. (B) The average bead positions with and without flow are obtained from Gaussian fits to the distribution of measured bead displacements (bin width 20 nm). The difference in bead positions gives the overall displacement of the bead in the trapping potential.

Optical tweezers experiments are generally carried out using smaller PSL beads (1 to 3 μm diameter). We have, however, shown here the functionality of the developed detection system for larger beads of the same material. The above discussed modifications to the optical tweezers system will provide sufficient image magnification to enable the use of our detector on smaller beads.

Above bead diameters of approximately 2 μm, the spring constant decreases for trapping of larger PSL beads [Ghislain et al., 1994]. The spring constants of approximately 4 and 1 x 10^{-4} pN/nm obtained here at the same trapping power (125 mW) for diameters of 12.1 and a 14.7 μm respectively also demonstrate this tendency. Ghislain et al. [1994] reported a decrease

of κ by almost an order of magnitude between 2 μm and 6 μm polystyrene beads. For 2 μm diameter beads, we therefore predict our trap to display spring constants of the order of 10^{-2} pN/nm. The spring constants determined here for large beads thus suggest values comparable to other optical tweezers set-ups for smaller beads. Trapping applications and provisional force calibration have therefore been shown and provided proof of principle for the developed optical tweezers system.

Chapter 4

Small molecule binding to DNA; an optical tweezers study

Small molecules, such as drugs, which bind directly to DNA, can alter its mechanical properties, thus influencing transcription and DNA replication [Dervan and Bürli, 1999; Ansari et al., 2001; Dervan, 2001; Wegner and Grummt, 2001]. These properties render the drug molecules useful antiviral, antibiotic and anticancer agents. To improve and further develop this class of pharmaceuticals, an understanding of the molecular mechanisms of DNA-binding is essential.

Several biophysical and biochemical techniques have been applied to provide insight into binding modes, DNA affinity, and base pair selectivity of DNA-binding drugs. Examples are X-ray crystallography [Kopka et al., 1985; Laughton et al., 1996], nuclear magnetic resonance [Lane et al., 1991; Jenkins et al., 1993; Bostock-Smith et al., 1999], calorimetry [Taquet et al., 1998], footprinting analysis [Ward et al., 1988; Fish et al., 1988; Wegner and

Grummt, 2001], and electric linear and circular dichroism as well as other spectroscopic techniques [Colson et al., 1996; Laughton et al., 1996; Nordmeier, 1992]. However, all of these techniques allow access to averaged ensemble properties of large systems of molecules only. Fine detail of processes at the molecular level can thus not be resolved.

More recently, information on ligand binding processes to DNA at the single molecule level has become accessible using techniques such as AFM or optical tweezers [Krautbauer et al., 2002a; Krautbauer et al., 2002b; Bennink et al., 1999; Wuite et al., 2000]. These techniques provide complementary information to the traditional bulk property screening methods. They also require very little material and therefore have potential use in drug screening assays [Krautbauer et al., 2002a], where only small samples may be available. To this end, in a recent AFM study it was shown qualitatively that different binding modes of small DNA-binding molecules have distinctly different effects on the high force (> 15 pN) elasticity of DNA [Krautbauer et al., 2002a; Krautbauer et al., 2002b].

In a collaboration with Dr Justin Molloy, we have employed optical tweezers to investigate the influences of small DNA-binding molecules on the elastic response of single DNA molecules in the low force regime $\leqq 15$ pN. Such forces are below the current noise limit of AFM measurements. In particular, the effects of different modes of binding to DNA were compared. Force-extension curves were recorded in the presence of netropsin, a minor groove-binding drug; ethidium bromide, an intercalating fluorescent dye; and berenil, which has been proposed to exhibit both intercalative and minor groove-binding modes [Pilch et al., 1995; Colson et al., 1996]. From the experiments, me-

chanical properties of the DNA under the different applied conditions could be determined by fitting theoretical model curves to the obtained data.

4.1 DNA

This chapter is concerned with elastic properties of the biopolymer DNA. These are determined by the molecule's structure, which is introduced briefly in the following section.

4.1.1 DNA structure

Biological polymers, such as DNA, are molecules that consist of equal or similar subunits or segments. The building blocks of DNA are the nucleotides, each of which consists of a deoxyribose sugar molecule covalently linked to a base. Figure 4.1 shows the four possible bases, two purine (adenine (A) and guanine (G)) and two pyrimidine (cytosine (C) and thymine (T)) bases. The nucleotides are linked via the phosphorylated sugar molecules, that form a phosphate backbone (see figure 4.2A). The sequence of nucleotides is termed the primary structure of DNA, and serves to encode the genetic information. Under physiological conditions, two of the thus formed strands of DNA, termed single stranded DNA (ssDNA), connect to make up double stranded DNA (dsDNA). The interaction between the two strands is based on hydrogen bonds between the bases, whereby A pairs with T via two, and C with G via three bonds, as can be seen from figure 4.2B.

Biopolymers have the ability to fold into secondary and tertiary structures, held together by hydrogen bonds, van der Waals, electrostatic and

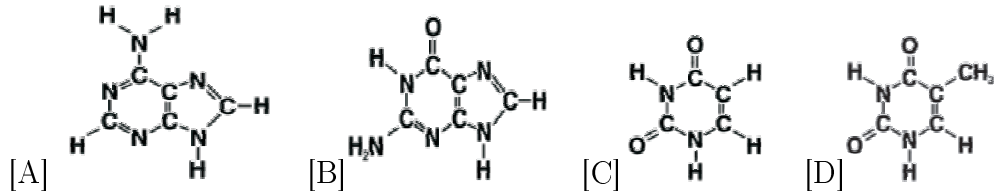

Figure 4.1: The DNA building blocks are the four nucleotides adenosine, guanine, cytosine, and thymidine. They consist of a phosphorylated deoxyribose sugar ring, covalently linked to one of the purine bases (A) adenine and (B) guanine, or the pyrimidine bases (C) cytosine and (D) thymine.

hydrophobic attractions. In the case of DNA, the secondary structure is a double-helix, which is energetically stabilised by hydrophobic interactions between the neighbouring stacks of base-pairs (see figure 4.2C). Under physiological conditions, the helix adopted by dsDNA is the B-form double helix conformation with a helix diameter of 2.37 nm, a rise per base pair of 0.338 nm, and 10 base pairs per helical turn [Saenger, 1984]. Other helix conformations can be found for DNA, for example, under low hydration conditions [Saenger, 1984], for particular base pair sequences [Alberts et al., 1990], or under mechanical strain [Smith et al., 1996; Cluzel et al., 1996]. The attachment of DNA-binding molecules can also alter DNA conformational properties by interfering with the structure of DNA intramolecular interactions [Krautbauer et al., 2000; Berge et al., 2002].

For each particular polymer, stretching behaviour is determined by its primary, secondary, and tertiary structure. Therefore, measuring molecular mechanical properties, such as elasticity or contour length, offers insight into the polymer's conformation. These properties are generally determined from

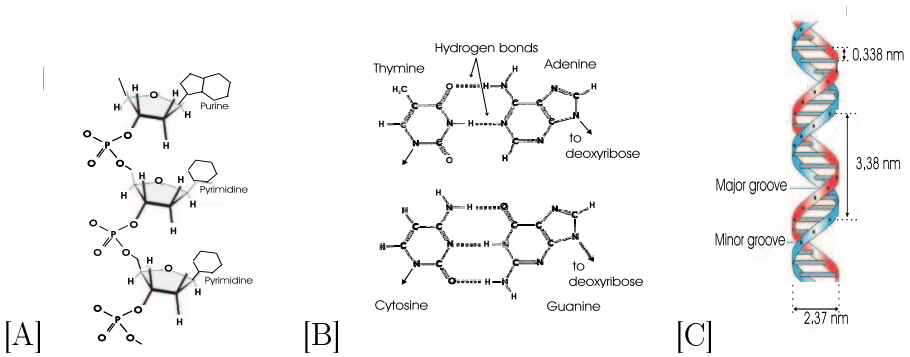

[A] [B] [C]

Figure 4.2: (A) DNA primary structure: The bases form strands of DNA via a sugar-phosphate-backbone. The strand ends are referred to as the 3'- (here bottom end) and the 5'-end (here top end). (B) Hydrogen bonds connect the two single strands of DNA to produce double stranded DNA. A pairs with T via 2, C with G via 3 bonds. (C) Secondary structure: The energetically favoured conformation of dsDNA under physiological conditions is the B-form helix shown here. The bases face the inside of the helix, forming a twisted ladder pattern. Figures after [BLC, 2002].

the experimental results by fitting a theoretical model curve to the obtained data.

4.1.2 Statistical description of polymers

Various theoretical models have been introduced to describe the conformations of chain polymers, such as DNA. These models treat the molecule as a chain consisting of N segments $\overrightarrow{r_n}$ $(n = 1 \rightarrow N)$ of length r_n. Here, $\overrightarrow{r_n}$ represent the vectors connecting the single atoms or groups that make up the chain. A basic chain model is shown schematically in figure 4.3.

The total end-to-end distance of the polymer strand can be described by

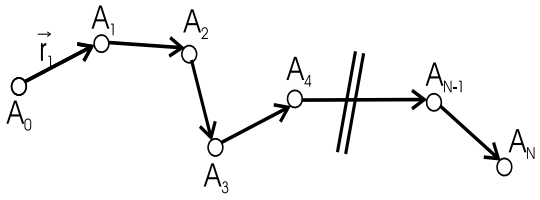

Figure 4.3: Schematic representation of a chain polymer, with chain elements A_m and connecting vectors r_n ($n = 1 \rightarrow N$, $m = n + 1$). For simplicity, we can assume here that all vectors possess the same length, r.

a vector $\overrightarrow{R}$. Its length is R, the square root of the scalar product of $\overrightarrow{R}$ with itself [Flory, 1969]:

$$\overrightarrow{R} = \sum_{n=1}^{N} \overrightarrow{r}_n \tag{4.1}$$

$$R^2 = \overrightarrow{R} \cdot \overrightarrow{R} = \sum_{n,m=1}^{N} \overrightarrow{r_n} \cdot \overrightarrow{r_m} = \sum_{n=1}^{N} r_n^2 + 2 \sum_{1 \leq n < m \leq N} \overrightarrow{r_n} \cdot \overrightarrow{r_m} \tag{4.2}$$

Statistical mechanics allows the derivation of all relevant observables of a system, such as for example its energy or temperature, from the system's partition function. The partition function gives the ensemble of all possible states for the system. The ensemble $\overrightarrow{r}$ of all bond vectors $\overrightarrow{r}_n$, which describe the molecule, has the canonical partition function Z:

$$Z = \int_0^{\infty} \exp\left(\frac{-E(\overrightarrow{r})}{k_B T}\right) d(\overrightarrow{r}) \tag{4.3}$$

where $E(\overrightarrow{r})$ is the energy of the combination of bonds $\overrightarrow{r}$, k_B is the Boltzmann constant ($1.38 \cdot 10^{-23}$ J/K) and T the temperature in Kelvin (K). The probability distribution of a given state of the system with energy $E(\overrightarrow{r})$ is given by $w(\overrightarrow{r})$:

$$w(\overrightarrow{r}) = \frac{\exp\left(\frac{-E(\overrightarrow{r})}{k_B T}\right)}{Z} \tag{4.4}$$

From this, the average value of any observable $X(\overrightarrow{r})$, $<X(\overrightarrow{r})>$, is derived from the probability distribution $w(\overrightarrow{r})$ as follows:

$$< X >= \int_0^\infty w(\overrightarrow{r}) \cdot X(\overrightarrow{r}) \cdot d(\overrightarrow{r}) \tag{4.5}$$

If a stretching force F is applied to the polymer, for example, its average length can be calculated from the partition function of the system. In the quasistatic case, only small variations in total molecular length R occur. For this case, the average length $< \overrightarrow{R} >$ is obtained from the partition function Z_F over the free energy of the system (E_{free}), for a given force F on the molecule [Krautbauer, 1999]:

$$Z_F = \int_0^\infty \exp\left(-\frac{E(\overrightarrow{r}) - \overrightarrow{F} \cdot \overrightarrow{R}}{k_B T}\right) d\overrightarrow{r} \tag{4.6}$$

$$E_{free} = -k_B T \cdot \ln Z \tag{4.7}$$

and therefore

$$< \overrightarrow{R} >= -\frac{\partial E_{free}}{\partial \overrightarrow{F}} = k_B T \cdot \frac{\partial \ln Z_F}{\partial \overrightarrow{F}} \tag{4.8}$$

Different assumptions can be made for the polymer, which each define a particular type of chain model. Each of the different models will describe polymer behaviour under various circumstances, such as upon stretching.

Comparing the theoretically obtained behaviour of a given model to that observed in experiments on the actual polymer can confirm the degree of agreement between this model and the polymer. Once the correct theoretical description of a polymer is determined, theoretical curves can be used to fit experimentally obtained data and extract various polymer properties from the fit parameters. In the following text, two different models will be introduced, which are most commonly used to describe DNA stretching behaviour.

Freely Jointed Chain (FJC)

In the FJC model there are no correlations between the individual vectors of the chain segments shown in figure 4.3. The average squared chain length of equation 4.2 is then proportional to N:

$$< \overrightarrow{r_n} \cdot \overrightarrow{r_m} >= 0 \text{ for } n \neq m \tag{4.9}$$

$$< \overrightarrow{R}^2 >= \sum_{n=1}^{N} \sum_{m=1}^{N} < \overrightarrow{r_n} \cdot \overrightarrow{r_m} >= \sum_{n=1}^{N} < (\overrightarrow{r_n})^2 >= Nr^2 \tag{4.10}$$

All possible orientations of the freely jointed chain are energetically equal and therefore equally likely. For large N, this results in a Gaussian distribution P for the end-to-end distances R. The freely jointed chain is therefore also sometimes referred to as a Gaussian chain [Flory, 1969]:

$$P(\overrightarrow{R}, N) = \left(\frac{3}{2\pi N r^2}\right)^{\frac{3}{2}} \cdot \exp\left(-\frac{3R^2}{2Nr^2}\right) \tag{4.11}$$

Integration over all possible conformational states gives $(4\pi)^N$. Since each

state possesses the same energy E, we obtain the following partition function Z in the absence of a force on the molecule:

$$Z = \int_0^\infty \exp\left(-\frac{E(\overrightarrow{r})}{k_B T}\right) d\overrightarrow{r} = (4\pi)^N \cdot \exp\left(-\frac{E}{k_B T}\right) \tag{4.12}$$

Without restriction of the general case, a force F can be assumed to be acting in direction z. Describing the bond vectors $\overrightarrow{r_n}$ in spherical coordinates using the two angles θ and ϕ ($\overrightarrow{r_n} = (r_n \sin\theta_n \cos\phi_n, r_n \sin\theta_n \sin\phi_n, r_n \cos\theta_n)$), then splits the partition function Z_F into N independent integrals $Z_F^{(i)}$ ($i = 1 \rightarrow N$):

$$\begin{aligned} Z_F &= \prod_{i=1}^{N} Z_F^{(i)} = \prod_{i=1}^{N} \left(\int_0^{2\pi} d\phi_i \int_0^{\pi} \exp\left(\frac{Fr\cos\theta_i}{k_B T}\right) \cdot \sin\theta_i \cdot d\theta_i \right) \\ &= \left(4\pi \cdot \frac{k_B T}{Fr} \cdot \sinh\frac{k_B T}{Fr}\right)^N \end{aligned} \tag{4.13}$$

From this equation, the average end-to-end distance $< R_F >$ of a molecule under an applied force F can be obtained, given small fluctuations around the average molecular length and large N. The average end-to-end distance of a molecule corresponding to a given force F is thus described by the Langevin function $\mathcal{L}(x)$, which is defined in the following equation[Smith et al., 1992]:

$$< R_F >= Nr \cdot \left(\coth\frac{Fr}{k_B T} - \frac{k_B T}{Fr}\right) = Nr \cdot \mathcal{L}\left(\frac{Fr}{k_B T}\right) \tag{4.14}$$

The FJC model postulates segments of a uniform length, from which the polymer chain is made up. These segments are called Kuhn segments. Their length, termed the Kuhn length r_k, indicates the stiffness of the chain. The longer the segments, the less flexible the chain. The polymer is treated as a

chain of N_K of these segments. Therefore, the contour length of the molecule, L_C, is given by:

$$L_C = N_K r_K \tag{4.15}$$

The length of the Kuhn segments can thus be mathematically obtained from the system partition function. This function, however, only describes entropic contributions to the molecule's elasticity. A molecule that can be stretched above its contour length also possesses an intrinsic elasticity of enthalpic origin. To additionally consider this enthalpic elasticity, the equation for the length of each segment is extended by a force induced length. For this, a spring constant k is ascribed to the segments. Inclusion of intrinsic molecular elasticity therefore leads to an extended FJC model, in which a term NF/k is added in the average end-to-end distance, as shown in the following equation:

$$< R_F >= Nr \cdot \mathcal{L}\left(\frac{Fb}{k_B T}\right) + \frac{NF}{k} \tag{4.16}$$

Single stranded DNA, for example, is generally believed to be well described by the extended FJC model [Smith et al., 1996]. This model also fits dsDNA force-extension data well in the very low force regime [Bustamante et al., 2000b]. For forces $\gtrapprox 0.1$ pN, the FJC curve, however, deteriorates from the experimentally found behaviour of dsDNA.

Worm-like Chain (WLC)

As opposed to the FJC model, the WLC (figure 4.4) does not consider the chain to be built up from segments of a defined length, but describes it by a semiflexible continuous rod.

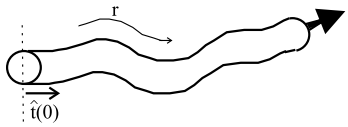

Figure 4.4: Schematic representation of the worm-like chain, which describes the polymer by a semiflexible continuous rod of length L_C. Its elasticity is expressed in terms of the persistence length L_P, after which the orientational correlation $G(r)$ of the chain is lost. This is defined as the projection of the unit tangent vector $\hat{t}(r)$ onto the first, $\hat{t}(0)$: $G(r) = <\hat{t}(0) \cdot \hat{t}(r)> = <\cos(\theta(r) - \theta(0))> \propto \exp(-|r|/L_P)$; after [Bruinsma, 2002].

Starting from the FJC, in the WLC model the fixed angles in a realistic molecule are also accounted for. If we consider the N bond vectors r_n ($n = 1 \rightarrow N$) to be at fixed predetermined angles to each other, but able to freely rotate otherwise, then the average projection of a segment onto a neighbour from equation 4.2 becomes:

$$< \overrightarrow{r_i} \cdot \overrightarrow{r_{i+1}} >= r^2 \cdot \cos\theta \tag{4.17}$$

where θ is the angle between the neighbouring segments. With this, the average squared end-to-end distance $< R^2 >$ becomes bigger than for the FJC model:

$$\begin{aligned} < \overrightarrow{R}^2 > &= \int \frac{1}{(4\pi)^N} \cdot \int \left(\sum_{i=1}^{N} \overrightarrow{r_i}^2 + 2 \cdot \sum_{i<j}^{N} r^2 \cdot \cos\theta^{i-j} \right) d(\overrightarrow{r}) \\ &= N\overrightarrow{r}^2 + 2r^2 \cdot \sum_{i<j} \cos\theta^{i-j} \end{aligned} \tag{4.18}$$

In the limit of long chains ($N \to \infty$) this becomes:

$$< \overrightarrow{R}^2 >= Nr^2 \cdot \frac{1+\cos\theta}{1-\cos\theta} =: Nr^2\alpha \tag{4.19}$$

So we can consider this model so far as a freely rotating FJC chain with $N_K = \frac{N}{\alpha}$ Kuhn segments of length $r_K = \alpha r$. α is the factor, by which $< \overrightarrow{R}^2 >$ has increased from the FJC model value [Flory, 1969; Krautbauer, 1999].

In the WLC model, the persistence length is a measure of the chain's elasticity, as was the Kuhn segment length for the FJC. Due to thermal fluctuations, a local orientation of the chain loses its correlation to that of the previous section after a length L_P, referred to as its persistence length. For an infinitely elastic chain, L_P=0. In this case, there is no correlation between the orientation of two neighbouring points, connected parts do not hinder each other. An infinitely stiff chain on the other hand would be made up from one single long segment. The size of the L_P value is proportional to the stiffness of the chain.

L_P is obtained as the limit for $N \to \infty$ of the average projection $< \Phi^2 >$ of all segments onto the first, $\overrightarrow{r_1}$ [Krautbauer, 1999]:

$$< \Phi^2 >= \frac{\overrightarrow{R} \cdot \overrightarrow{r_1}}{r_1} = r \sum_{i=0}^{N-1} \cos\theta^i \tag{4.20}$$

$$L_P := \lim_{N\to\infty} < \Phi^2 >= \frac{r}{1-\cos\theta} \tag{4.21}$$

From this preliminary model, the WLC model is obtained by increasing the number N of segments while keeping the contour and persistence length values L_C and L_P constant [Vologodskii, 1994]. For $N \to \infty$ and $\cos\theta \to 1$, equations 4.19 and 4.21 give:

$$< \overrightarrow{R}^2 >= 2L_P L_C \tag{4.22}$$

Therefore for direct comparison of the mean root squares of the end-to-end distances from the two models, the persistence length of the WLC proves to be half the Kuhn length of the FJC model:

$$r_K = 2L_P \tag{4.23}$$

An extended version introduces a force into the WLC equation. From this, the free energy of a stretched WLC polymer is obtained as the energy of the quantum mechanical ground state of a dipolar rotator in an electric field. The rotator's angular momentum translates into the WLC property L_P, the electric field into the force on the polymer F [Fixman and Kovac, 1973].

The experimentally observed stretching behaviour of dsDNA, for example, has been shown to be described well by this extended WLC theory [Bustamante et al., 1994; Vologodskii, 1994; Marko and Siggia, 1995a]. Bustamante et al. [Bustamante et al., 1994] have suggested an approximation,

termed the inextensible WLC, which fits the force-extension behaviour of dsDNA well in the limits of small and high forces:

$$\frac{FL_P}{k_BT} = \frac{1}{4 \cdot \left(1 - \frac{x}{L_C}\right)^2} - \frac{1}{4} + \frac{x}{L_C} \tag{4.24}$$

For DNA extensions that do not divert too much from the molecule's contour length, this equation can be simplified in good approximation to give the following:

$$F \approx \frac{k_BT}{4L_P} \cdot \frac{1}{\left(1 - \frac{x}{L_C}\right)^2} \tag{4.25}$$

For the analysis of the experimental work presented in this chapter, this approximation has been employed to fit the data. For the relatively small forces of our measurements ($\lessapprox 15$ pN), the entropic elasticity of the molecule strand dominates the stretching behaviour of DNA. For higher forces, the molecule is stretched above its contour length. Extensions of a molecule above its contour length cannot be explained by a purely entropic elasticity of the polymer strand. These arise from an intrinsic, enthalpic elasticity of the molecule, due to bends and curvature in the polymer strand.

Therefore, a stretching coefficient S has to be introduced into the WLC equation in the high force regime. The additional term describes the derivation from the WLC model due to the molecule's intrinsic elasticity, which enables molecule extensions above its contour length. The following interpolation suitably describes dsDNA stretching behaviour between 5 and 50 pN, including both entropic and enthalpic contributions to DNA elasticity [Bustamante et al., 2000b]:

$$x = L_C \left(1 - \frac{1}{2}\sqrt{\frac{k_B T}{F L_P}} + \frac{F}{S}\right) \tag{4.26}$$

Generally, intrinsic elasticity contributes measurably only for molecule extensions near or above its contour length [Marko and Siggia, 1995a]. In section 4.1.3 the different contributions to polymer elasticity will be discussed in more detail for dsDNA.

4.1.3 DNA elasticity

Entropic elasticity of a stiff polymer chain stems from thermal fluctuations, causing small deviations from the molecular axis. The persistence length due to purely entropic elasticity of dsDNA has also been referred to as dynamic persistence length ($L_{P_{dyn}}$). It was proposed to be approximately 70 nm [Trifonov et al., 1987; Smith et al., 1992].

The molecule's tertiary structure gives rise to a second type of elasticity, which is of enthalpic origin. Deviations from the molecular axis caused by this intrinsic molecular elasticity can be considerably bigger than those thermally induced ones, based on entropic elasticity. Persistence length due to enthalpic elasticity has also been named a static persistence length ($L_{P_{stat}}$), since it is based on permanent local curvature in the molecular axis. In some cases, the enthalpic persistence length can be found to be of the order of the lengths of the polymer subunits themselves. For DNA, enthalpic persistence length has been predicted to be between 40 and 175 nm, dependent on the applied buffer ionic strength and the employed analysis model [Baumann et al., 1997; Smith et al., 1992].

At high ionic concentrations ($\gtrapprox 100$ mM), the enthalpic L_P value is higher than the entropic value. When the ionic strength of the surrounding solution is lowered ($\lessapprox 20$ mM), however, the entropic DNA persistence length becomes considerably larger, predominantly due to an increase in electrostatic repulsion [Baumann et al., 1997]. For low ionic buffer strengths, the enthalpic persistence length is smaller than the entropic.

The persistence length of 50 nm measured for dsDNA in force-extension experiments contains contributions from both the entropic (dynamic) and enthalpic (static) elasticities. The two values add up as their inverse sum to give the total apparent persistence length of the polymer:

$$\frac{1}{L_{P_{app}}} = \frac{1}{L_{P_{dyn}}} + \frac{1}{L_{P_{stat}}} \tag{4.27}$$

For the low forces of the experiments presented in this chapter, the entropic (dynamic) contributions to L_P are considered to dominate dsDNA elasticity [Baumann et al., 2000]. In the following text, no distinction will be made between the measured and the entropic persistence length value.

As briefly mentioned above, L_P of dsDNA has been found to depend on the applied ionic strength of the measurements. This is to a great part a consequence of the high surface charge of this particular polymer. In monovalent salt solution, values of approximately 95 and 50 nm have been measured for approximately 1 and 100 mM Na^+ respectively [Baumann et al., 1997]. The nonlinear Poison-Boltzmann theory for homogeneously charged cylinders describes the behaviour of L_P with varying ionic strength I well [Baumann et al., 1997]:

$$L_P = L_{P_0} + L_{P_{el}} = L_{P_0} + \frac{1}{4\kappa^2 l_B} = L_{P_0} + \frac{0.0324}{I} nm \qquad (4.28)$$

where κ is the inverse Debye-Hückel screening length, and l_B is the Bjerrum length, which is 0.714 nm for dsDNA in water at 25^oC [Baumann et al., 1997]. L_{P_0} describes non-electrostatic and $L_{P_{el}}$ electrostatic contributions to L_P. In experiments using for example optical tweezers or light scattering [Baumann et al., 1997; Sobel and Harpst, 1991], non-electrostatic contributions were found to dominate for $I > 20$ mM, and a constant value for L_P was observed for these ionic concentrations. For higher valencies of the applied ions, L_P was further found to decrease to considerably lower values.

DNA elastic behaviour has been investigated in single molecule experiments using AFM [Rief et al., 1999; Anselmetti et al., 2000; Krautbauer et al., 2002b; Krautbauer et al., 2002a], magnetic beads [Smith et al., 1992; Strick et al., 1996], and optical tweezers [Baumann et al., 1997; Bustamante et al., 2000b; Baumann et al., 2000; Husale et al., 2002]. In these experiments, single DNA molecules have been repeatedly pulled and relaxed, to maximum extensions of approximately twice their contour lengths. Figure 4.5 shows a typical force-extension curve for dsDNA obtained with AFM. The force at which the DNA is pulled is plotted versus molecular extension.

It can be seen from the figure that upon stretching the DNA, a rapid increase in the molecule's force response is measured, when the molecular contour length is approached. The force-extension curve is well fitted by the extensible WLC model (equation 4.26) up to approximately 50 pN (see

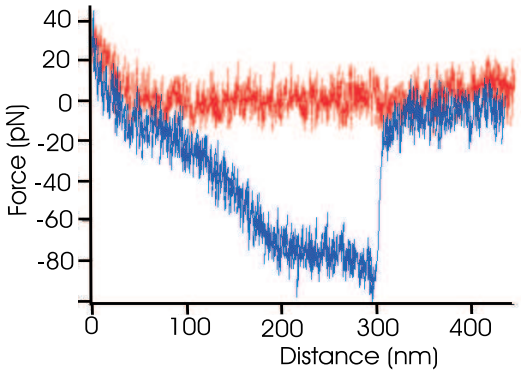

Figure 4.5: Typical force-extension curve for dsDNA, obtained with AFM. The force at which the DNA is pulled is plotted versus molecular extension (red curve: tip approach, blue curve: molecule stretching). The dsDNA undergoes a structural transformation at approximately 70 pN, visible from the plateau in the stretching curve. This is interpreted as a transition from physiological B-form DNA into a stretched S-form conformation. The constant force response of the molecule shows high cooperativity of the transition. At the end of the plateau, the entire molecule has been transformed into the S-form. Further stretching again leads to a -here only slight- increase in force response, until the DNA tether disconnects from the AFM tip, and the cantilever jumps back into its free level position.

section 4.1.2). At forces between 65 and 70 pN, however, the experimental curve deviates from WLC behaviour, and the force is found to flatten into a plateau. The little increase in force of the plateau demonstrates a high cooperativity transition. The plateau has been interpreted as a structural transition of the dsDNA from its physiologically dominant B-form into a so-called S-form helix [Smith et al., 1996; Cluzel et al., 1996; Rief et al., 1999]. The postulated S-form DNA has been found from experimental and theo-

retical studies to be approximately 1.7 times longer than B-form DNA, with a 0.58 nm helical rise per base pair [Cluzel et al., 1996; Lebrun and Lavery, 1996; Smith et al., 1996; Ahsan et al., 1998; Léger et al., 1999]. It should, however, be noted that in a recent study Rouzina and Bloomfield [2001a; 2001b] have suggested a different interpretation of the plateau as a one-dimensional melting transition of dsDNA into ssDNA, due to the collective breaking up of hydrogen bonds. The authors argue that the theoretical curves obtained using this model fit the high cooperativity of the transition better than curves based on the BS-transition model.

At higher stretching forces, the dsDNA force-extension curves show a second shorter plateau (not shown in figure 4.5). This is explained as the complete melting of dsDNA into two single strands [Rief et al., 1999].

Experimental conditions can influence DNA stretching behaviour. Using AFM, a dependence of the melting transition on the applied loading rate has been found [Rief et al., 1999]. This identifies dsDNA melting as a nonequilibrium process within the accessible time scale of AFM experiments. Typical pulling speeds range from between 0.15 to 3 μm/s. The loading rate r_F on the pulled particle equals the product of the spring constant of the employed force transducer and its velocity (see section 1.3.2). The BS-transition has, however, been found to be not affected by a difference in applied pulling rates [Rief et al., 1999]. It is therefore an equilibrium transition on the time scale of the AFM experiments. This means, that the BS-transition is a much faster process than dsDNA melting.

DNA stretching behaviour has been found to be dependent on the base-pair composition of the molecule. Unbinding forces of base pairs have been

measured by unzipping hairpins in dsDNA of controlled sequences, using AFM. For A-T an unbinding force of approximately 10 pN, for G-C 15 to 20 pN were found [Rief et al., 1999; Essevaz-Roulet et al., 1997]. G/C-rich sequences thus resist higher forces than A/T-rich sequences, so that the melting transition from dsDNA into ssDNA will occur at higher forces for these. Typical melting forces of around 300 pN have been found for pure G/C-sequences, compared to approximately 150 pN for mixed sequence DNA [Rief et al., 1999]. For pure A/T-sequences, observed DNA force-extension curves suggested a gradual continuous conversion into ssDNA below even the BS-transition due to the decreased mechanical stability of the DNA and thus weaker resistance to melting [Rief et al., 1999].

Recent experimental studies on DNA in the presence of small DNA-binding ligands have also revealed effects of molecule attachment to DNA on the polymer's stretching behaviour [Krautbauer et al., 2000; Krautbauer et al., 2002a; Krautbauer et al., 2002b; Husale et al., 2002].

4.2 DNA-binding molecules

Small molecules bind to DNA via three major distinguishable modes. These are crosslinking, groove-binding, and intercalation. In previous studies, the binding mode of a molecule has been found to greatly determine its effects on DNA mechanical properties [Krautbauer et al., 2002a; Krautbauer et al., 2002b; Husale et al., 2002]. The studies presented in this chapter are concerned with small DNA ligands with two different binding modes, namely groove-binding and intercalation. Schematics of these are shown in figure 4.6.

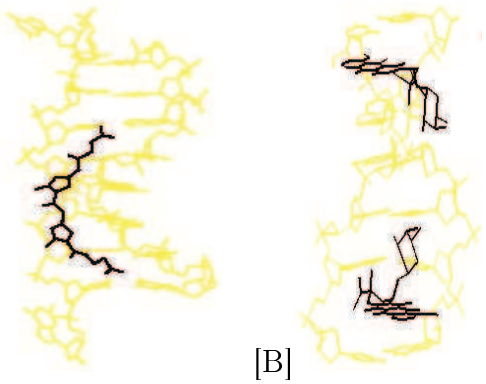

Figure 4.6: The DNA-binding modes (A) groove-binding, and (B) intercalation. Groove-binders attach within the major or the minor grooves of the DNA double-helix, with their well-adopted shapes providing a perfect fit into these sites. Intercalators push themselves between adjacent base-pairs of the double-helix, increasing the base-pair separation and elongating the total length of the DNA molecule. DNA is schematically shown in yellow, ligands in black. Note the different scales of the figures which were taken from the nucleic acid database [Database, 1995].

Groove-binders

Groove-binding is governed by reversible interactions of electrostatic, van der Waals, and hydrogen bonding nature. The interactions were found to have a stabilising effect on the B-form double helix of DNA [Krautbauer et al., 2002a]. Groove-binders bind into either the major or the minor groove of the DNA double-helix (see figure 4.6). DNA-binding proteins generally bind in the larger, major groove. Therefore, most DNA groove-binding small molecules as produced in nature by viruses and fungi, have developed to target the free, minor groove.

From NMR, X-ray and computer modelling studies, small molecules with

this mode of binding to DNA have been found to show a perfect geometrical fit into the minor groove of DNA [Laughton et al., 1990; Bostock-Smith et al., 1999]. In particular, AT-rich sequences are targeted by most of these ligands [Bostock-Smith et al., 1999]. In GC-rich minor grooves, the exocyclic amino group of guanine proved a steric obstacle [Neidle, 2002]. Minor grooves containing predominantly A- and T-bases also show a narrower shape, which is perfectly matched by these DNA-binders. The electrostatic potential of AT-rich minor grooves is reduced, causing increased attraction for the molecules.

Protein binding to DNA is known to often affect DNA tertiary structure, inducing bends in the DNA molecular axis or partially unwinding the double-helix [Anselmetti et al., 2000]. The X-ray crystal structures of DNA complexes with small groove-binding molecules have also revealed the introduction of slight bends in the DNA axis by binding of these molecules [Kopka et al., 1985]. Netropsin, for example, was found to force the minor groove of DNA open by 0.05 to 0.2 nm, back-bending the DNA axis by 8° [Kopka et al., 1985]. Groove-binding of small molecules is, however, not considered to have an effect on DNA contour length [Coury et al., 1996].

Intercalators

As for groove-binding, the process of intercalation involves physical reversible interactions. Intercalators bind nonspecifically to DNA by inserting themselves between adjacent base pairs, forcing them apart from each other, as illustrated in figure 4.6. In order to squeeze in between adjacent DNA base-

pairs, intercalators are very flat molecules, often consisting of multiple aromatic rings.

The intercalation process partially unwinds the DNA double-helix, and locally increases the distance between the affected base-pairs. Several studies have found the increase in base-pair separation by intercalative binding to be 0.34 nm [Coury et al., 1996; Wang, 1974]. This affects the total length of the DNA molecule as well as its superstructure (see chapter 5). The total increase in DNA contour length is determined for saturating concentrations, which vary for different intercalators.

Several experimental studies have shown a stiffening of the DNA by intercalation [Berge et al., 2002; Wang, 1974]. A stabilising effect of intercalative binding on DNA by improved base stacking energies and higher melting temperatures has been proposed by Berge et al. [2002]. Consistent with this, evidence for an inhibition of force-induced melting or accelerated reannealing of the two separated strands has been found in a recent AFM study [Krautbauer et al., 2002a]. For higher concentrations of intercalating molecules, experimental results, however, also revealed increasing polymer elasticity [Nordmeier, 1992; Husale et al., 2002].

For the low forces ($\lessapprox$ 15 pN) applied in the presented stretching experiments, the physiological canonical B-DNA helix is not perturbed. Effects on helix geometry and elasticity observed upon drug binding, as it is investigated in this chapter, should therefore provide useful insights into how drugs alter *in vivo* processes.

4.3 Materials and methods

All experiments were carried out in 150 mM NaCl containing TE buffer (TE150; 10 mM tris(hydroxymethyl)aminomethane (Tris), 1 mM ethylendiamintetraacetic acid (EDTA)), pH 8.0. Water was purified to 18.2 MΩcm resistivity and filtered using a 0.2 μm pore filter.

DNA

Restriction enzymes (ApaLI and BstEII, New England Biolabs, Inc. (NEB), Beverly, MA, USA) were used to excise a 14046 base pair (bp) fragment from T7 bacteriophage DNA. This fragment was differentially labelled at the 3'-ends with biotin-14-dCTP (Sigma-Aldrich Company Ltd.) and digoxigenin-14-dUTP (DIG, Roche) using terminal transferase (NEB). The end-labelled fragments were purified using gel electrophoresis and stored at 4°C in TE200 buffer (identical to TE150 except 200 mM NaCl instead of 150 mM).

The DNA fragments were chosen for their length (4776 nm) and base pair content. DNA tethers were required to be $\gtrapprox$ 4500 nm long in order for the force transducing probes to be sufficiently separated. This enabled imaging of the two probes onto two separate photodiode arrays. The DNA contained relatively equal ratios of the different bases (50.7 % A/T and 49.3 % C/G). This facilitates generalisation from our results to DNA of random sequences.

DNA-binders

Ethidium bromide (molecular weight (MW) 394.3), netropsin (MW 503.4), and berenil (1,3-bis(4'-amidinophenyl)triazene; MW 515.5) were obtained

from Sigma-Aldrich. Netropsin and ethidium bromide are well-characterised DNA-binding agents, exhibiting classical minor groove-binding and intercalative binding modes, respectively [Taquet et al., 1998]. For experiments, different concentrations of the ligands were prepared in TE150 buffer. The affinity constant, K_a, of a ligand is defined as the required quantity of substance to achieve a half maximum saturation of DNA binding sites, and is the reciprocal of its dissociation constant. For ethidium bromide, netropsin, and berenil, $K_a \approx 1$ μM at the applied conditions [Lane et al., 1991; Nordmeier, 1992; Smith et al., 1992; Ward et al., 1988]. However, for groove-binders (netropsin and berenil), the exact values depend on the base pair composition of the DNA, due to their pronounced affinity differences for A/T and C/G sequences [Bostock-Smith et al., 1999]. For intercalators (ethidium bromide), K_a has been shown to be sensitive to solution ionic strength [Nordmeier, 1992].

4.3.1 Sample preparation

A custom-built microscope flow cell (Biology Department, York, UK) with a sample volume of 20 μl was employed for the experiments. Top and bottom surfaces of the cell consisted of cover slips (22 x 22 mm^2, size 1.5; Chance Propper Ltd.). Silicon grease served as seal between the two surfaces and a channel frame. The bottom cover slip surface was sparsely decorated with glass beads (diameter = 2 μm), which were suspended in a 0.1 % nitrocellulose solution. These beads allowed the cover slip surface to be located with ease in the experiment. The walls of the flow cell were blocked with bovine

serum albumin (BSA; Sigma-Aldrich Company Ltd.) to reduce non-specific binding, by incubating a 1 mg/ml acetylated BSA solution in the flow cell for 5 minutes.

Optical tweezers handles

Prior to the experiments, streptavidin-coated polystyrene-latex spheres (1.0 μm diameter; Interfacial Dynamics Corporation, Portland, OR, USA) were washed repeatedly in TE buffer to remove the 2 mM NaN_3 phosphate buffered saline (PBS) storage buffer, pH 7.1. They were then redispersed in TE150 buffer to give a 0.168 % (w/v) beads solution. To attach the biotinylated end of the DNA fragment to a bead surface, 25 μl of the streptavidin-coated bead solution was mixed with 4 μl of 4.2 nM DNA solution (in TE200 buffer) and incubated for $>$ 1 hour at 4°C.

Immediately before the tethering experiment, 0.5 μl of a solution of fluorescent anti-digoxygenin F_{ab} coated (Roche, Sigma-Aldrich Company Ltd.) 1.1 μm beads (Interfacial Dynamics) were added to this mixture. The beads were labelled with the fluorescent dye tetramethylrhodamine-isothiocyanate (TRITC) coupled to BSA. This enabled identification of the two sorts of beads by fluorescence microscopy. Since a heterogeneous bead pair was required for attachment of both DNA molecule ends (see figure 4.7), differentiation between the two kinds of beads facilitated the DNA tethering process.

The mixture was diluted with TE150 buffer to give a final DNA strand concentration of 0.84 pM and a bead density of 8.4 x 10^{-5} % (w/v).

4.3.2 Experimental technique: optical tweezers

The employed experimental set-up is shown in figure 4.7. Single molecules of DNA were tethered between two optically trapped beads. To form a DNA tether, an antiDIG/TRITC-BSA-coated bead was captured in one of the laser traps and a DNA-tagged, streptavidin-coated bead was captured in the second trap. Bright-field and epifluorescence microscopy were utilised to visualise the non-fluorescent and fluorescent beads, respectively. The beads were then brought into close proximity and the stage/flow cell position oscillated (5000 nm amplitude at 3 Hz) using a computer controlled piezo-electric nanopositioning stage (Physika Instrumente). This served to flow the bulk solution past the beads, thus extending the DNA tether and facilitating binding of the free DNA end (labelled with DIG) to the anti-DIG coated bead. Once a DNA tether between the two beads was established, the beads were used as handles to manipulate (stretch) the biomolecule with the optical traps. Both streptavidin-biotin and antiDIG-DIG complexes are widely used for tethering in this sort of experiment, due to the strong interaction forces of these receptor-ligand complexes [Cluzel et al., 1996; Sakato-Sogawa et al., 1998; Koch et al., 2002]. At the laser power employed, the DNA tethers could be maintained for hours, thus laser-induced photodamage to the tether was assumed to be minimal. The molecule was then slowly stretched, by moving one of the traps away from the other in 100 nm steps. Precise control of laser trap position was maintained using two orthogonally mounted acousto-optic modulators (NEOS Technologies, Melbourne, FL). Displacement of the bead in the stationary optical trap and overall separation of the two beads

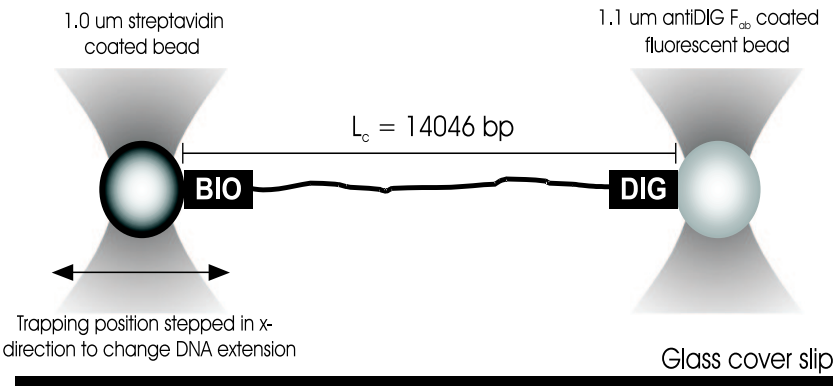

Figure 4.7: Schematic of the experimental set-up. Two independent optical tweezers are produced by chopping an infrared (1064 nm) laser beam, produced by a diode-pumped Nd:YAG laser, between two sets of x, y coordinates with acousto-optical devices. These serve to trap polystyrene latex beads of diameter 1.0 and 1.1 μm, which are coated with streptavidin and anti-digoxygenin (anti-DIG) F_{ab} fragments, respectively. DNA fragments (14046 bp in length) were end-labelled with biotin and digoxygenin (DIG) and bound to streptavidin-labelled beads prior to the experiment. Using the optical tweezers, two bead types were trapped and brought into close proximity, enabling DNA tether formation via binding of the free DIG labelled DNA end to the anti-DIG F_{ab} labelled bead. The optical tweezers-based force transducer was constructed around a Zeiss inverted microscope and is described in detail elsewhere [Veigel et al., 1998]. A charge-coupled device (CCD) camera and computer frame grabber card were used to capture images of the trapped beads to determine the DNA molecular extension during the stretching experiment.

was measured by capturing 10 video frames at each DNA extension. Images were analysed by a least squares fitting procedure to calculate the centroid position of each bead, as has been described by Veigel et al. [1998].

Transducer Calibration

The spring constants of the optical traps used in the current study were calibrated for every series of measurements. To do this the piezo-electric nanopositioning device was used to move the flow cell, and hence the bulk solution, past the trapped beads at known velocities. The viscous drag on the bead was used to calibrate the resulting bead displacements using Stokes law, yielding the optical trap stiffness (typically 0.08-0.09 for these experiments).

Data Analysis

The inextensible worm-like chain (WLC) model [Bustamante et al., 2000b; Baumann et al., 1997] is generally accepted to describe the stretching behaviour of dsDNA at low forces (see section 4.1.2). Its two free parameters, contour length (L_C) and persistence length (L_P), can be adjusted to give good fits to dsDNA stretching data [Bustamante et al., 2000b; Baumann et al., 1997]:

$$\frac{FL_P}{k_BT} \backsimeq \frac{1}{4 \cdot \left(1 - \frac{x}{L_C}\right)^2} + \frac{x}{L_C} - \frac{1}{4} \tag{4.29}$$

where F is the force on the DNA molecule, x is the molecule extension, k_B is the Boltzmann constant and T the absolute temperature ($T = 296\ K$ for these experiments). Near full extension, x approaches L_C as $\frac{1}{\sqrt{F}}$ (equation

4.30). In this force regime, plots of $\frac{1}{\sqrt{F}}$ versus x yield L_C upon extrapolation to infinite force from the intercept with the x-axis, while L_P is extracted from the y-axis intercept (equations 4.31 and 4.32):

$$\frac{1}{\sqrt{F}} \approx \sqrt{\frac{4L_P}{k_B T}} \left(1 - \frac{x}{L_C}\right) \tag{4.30}$$

$$\frac{1}{\sqrt{F}} = 0 \text{ for } L_C = x \tag{4.31}$$

$$x = 0 \Rightarrow L_P = \frac{k_B T}{4F_0} \tag{4.32}$$

where F_0 stands for the force at zero extension ($x = 0$). This approximation has been previously shown to suitably describe DNA elastic behaviour in the regime of high force entropic elasticity applied here, with extensions near the molecule's contour length but stretching forces below the enthalpic elasticity regime [Baumann et al., 2000].

4.4 Results and discussion

The stretching behaviour of native DNA has been investigated extensively in theoretical as well as experimental studies, and from these, L_P has been established to be approximately 50 nm for DNA under *in vivo* conditions (i.e. in the presence of circa 150 mM Na^+ ions) [Hagerman, 1988; Smith et al., 1996; Baumann et al., 1997]. The contour length of the employed DNA under native conditions can be calculated using a B-helix rise of 0.338 nm/bp [Saenger, 1984]. Therefore, in the presented study, the stretching behaviour of native DNA in TE150 was characterised and the obtained L_P

and L_C values were used to verify the experimental protocol and data analysis techniques. Examples of typical force-extension curves are shown in figure 4.8 for three different DNA molecules.

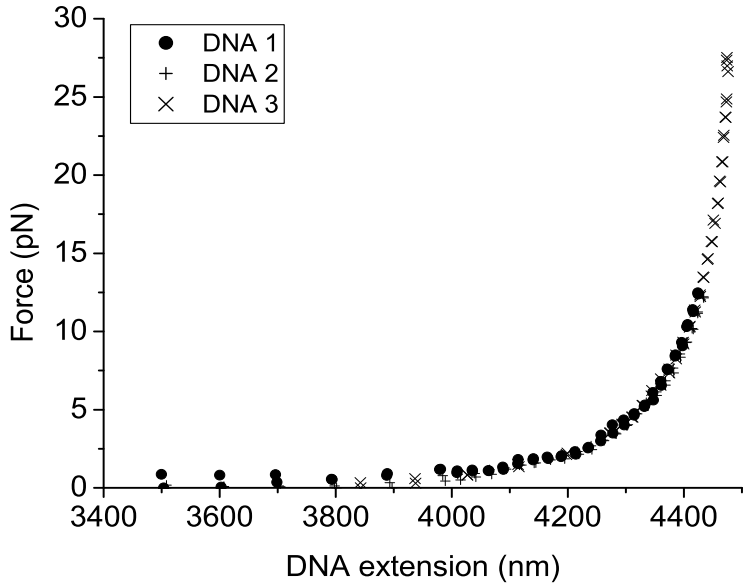

Figure 4.8: Typical force versus molecular extension plots for three different native DNA molecules (depicted by the symbols •, +, and ×). The stretching curves for the different molecules overlay closely, demonstrating good experimental reproducibility.

As can be seen from figure 4.8, the data for the different molecules overlay closely, demonstrating good experimental reproducibility. Values of L_C and L_P were obtained by linear regression of $1/\sqrt{F}$ versus x plots (see figure 4.9), using inextensible WLC theory. For the native DNA molecules in TE150 buffer from figure 4.8, this provided the parameters L_C = 4577 (± 20) nm and L_P = 50 (± 5) nm. The result is consistent with the calculated L_C value

for the 14046 bp fragment of 4748 nm to within 4 %, and with the known L_P value of DNA in high monovalent salt.

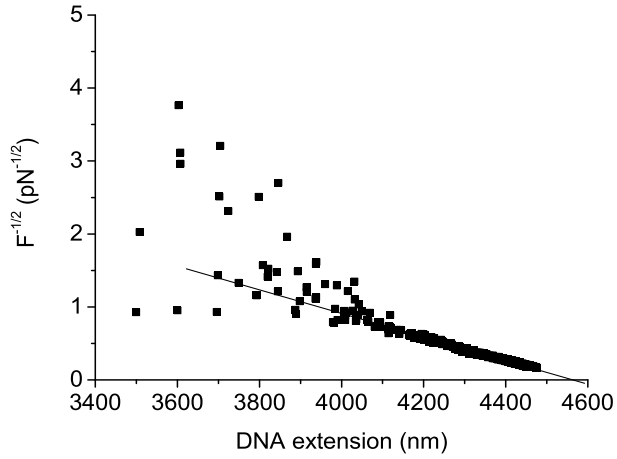

Figure 4.9: Inextensible WLC fit (equation 4.30) to the data presented in figure 4.8. The inverse square root of the applied force is plotted versus DNA molecular extension. Linear regression of the data yields the following equation: y = -0.0015298x + 7.0021. Values of L_P = 50 nm and L_C = 4577 nm are obtained from the slope and x-axis intercept, respectively.

4.4.1 Pure binding mode agents

Pure binding mode agents, namely the minor groove-binding drug netropsin and the intercalator ethidium bromide, served to identify the contributions of the different modes to changes in DNA mechanical properties. Figure 4.10 shows representative force-extension curves obtained on DNA in the presence of 10 μM netropsin and 1 μM ethidium bromide. For reference purposes, the WLC curve of native DNA is also included in the figure. Different effects of

groove-binding and intercalation can be observed. Netropsin induced only small changes in the force-extension curves, whereas ethidium bromide produced a considerable deviation from the native DNA curve.

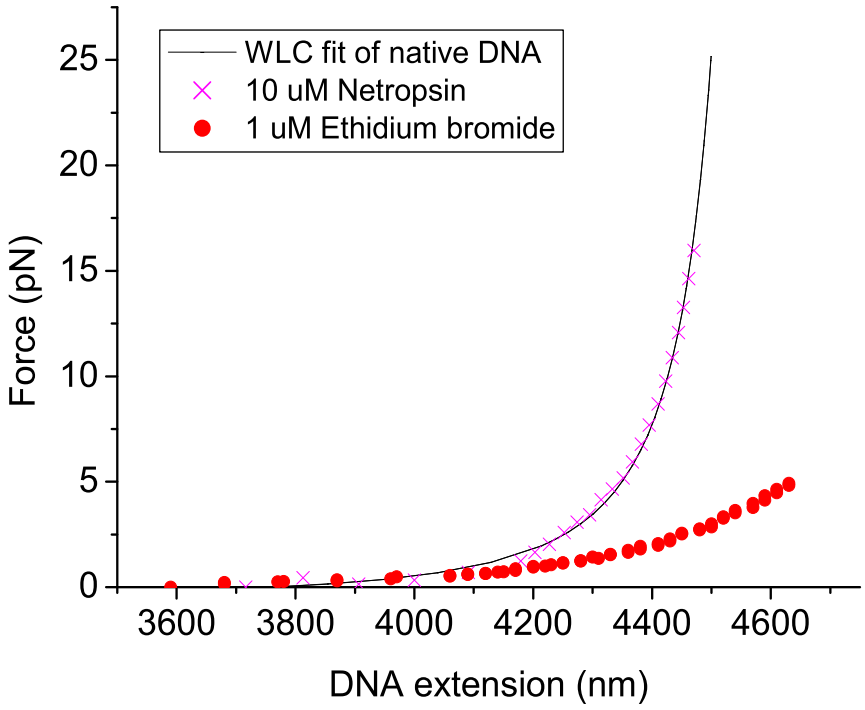

Figure 4.10: Representative DNA force-extension curves obtained in the presence of the minor groove-binding drug netropsin (×) and the intercalating dye ethidium bromide (•). For comparison, a calculated force-extension curve for native DNA (solid line) has been included. The behaviour of DNA stretched in the presence of netropsin was not vastly different from that of native DNA. In contrast, the intercalating dye ethidium bromide altered the stretching behaviour drastically compared to native DNA.

Effects on L_C, as previously found for intercalative binding [Bennink et al., 1999; Coury et al., 1996; Wang, 1974; Quake et al., 1997], appeared to dominantly affect the appearance of the DNA stretching curves (see figure 4.10). The effects on the mechanical properties of DNA have been quantified by fitting the inextensible WLC approximation (equation 4.30). Values of L_C and L_P were obtained as averages from 5 measurements on 3 to 4 different DNA molecules for each condition, and are summarised in table 4.1.

Compared to ethidium bromide, netropsin produced little change in the mechanical properties of DNA but did induce a significant increase in L_P (of 22 %). This is consistent with a stiffening of the DNA molecule upon groove-binding of netropsin. Binding of drugs into the grooves of the DNA double helix is believed to have no apparent effects on DNA contour length [Coury et al., 1996], in agreement with our results. Small DNA groove-binding molecules display a close isohelical fit into the pre-dictated DNA geometry. This process is conceived to not elongate the DNA, but stabilise B-form helix structure [Krautbauer et al., 2002a]. From X-ray studies, netropsin binding to DNA has been reported to induce a slight distortion in the DNA double-helix [Kopka et al., 1985], which could explain the decrease in bending flexibility found in this study.

Ethidium bromide gave a large and significant increase in L_C (of 10 %), in agreement with previously found DNA length increases upon ethidium bromide binding [Wang, 1974; Coury et al., 1996]. Further, a significant decrease in L_P (of 50 %) was found for the intercalator, suggesting increased elasticity of the DNA molecule. The effectively decreased bending rigidity of DNA in the presence of ethidium bromide can be explained by a partial neutralisation

of the DNA charge by the positively charged intercalator [Nordmeier, 1992].

Intercalative drug binding has previously been found to have a stabilising effect on DNA structure, which causes apparent stiffening of the DNA double helix [Wang, 1974; Berge et al., 2002]. Consistent with this, an increase in L_P was obtained in this study at lower concentrations of ethidium bromide. Figure 4.11 shows DNA force-extension data in the presence of $<$ 1 μM ethidium bromide. At this concentration, ethidium bromide induced an increase in L_P (to $\approx$ 75 nm) whereas L_C showed a similar increase (to $\approx$ 5240 nm) as for the higher intercalator concentration of figure 4.10.

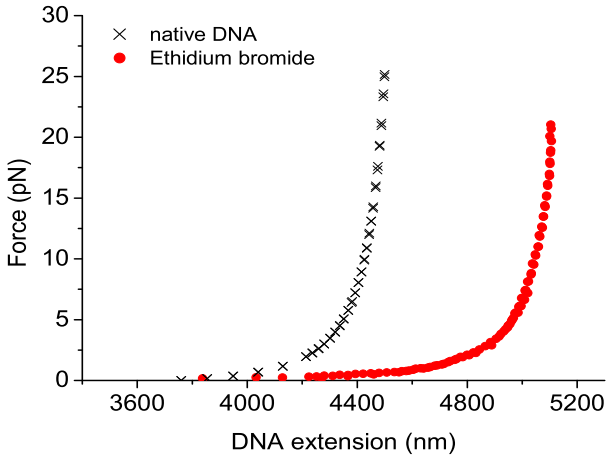

Figure 4.11: Representative force-extension curves obtained on DNA in the presence of a low ($<$ 1 μM) concentration of ethidium bromide (•). A WLC curve for native DNA is also shown for reference (×). A similar shift towards higher molecule extensions as in figure 4.10 for a 1 μM solution was found for the low ethidium bromide concentration. This is due to the dominating effect of the increase in L_C value by intercalation.

	L_C (nm) ± SD	L_P (nm) ± SD	n
Control (TE150 buffer)	4624 ± 25	46 ± 2	5
Netropsin (10 μM)	4629 ± 9	56 ± 4	5
Ethidium bromide (1 μM)	5134 ± 54	23 ± 5	5

Table 4.1: Effect of netropsin and ethidium bromide on elastic properties of DNA: SD = standard deviation, n = number of measurements.

4.4.2 Studies on berenil

To elucidate the mode(s) of berenil binding to DNA, DNA stretching behaviour over a range of added berenil concentrations was monitored. Experiments were performed using different single molecules under the same set of conditions to look for variability between molecules, and also performed on single molecules over a range of berenil concentrations to ensure reversibility and repeatability on a single DNA molecule. Obtaining data on one and the same single molecule of DNA in the presence of different drug concentrations does further reveal effects of the drug on DNA mechanical properties directly. Very little variability was found between individual molecules tested (see for example figure 4.8). Figure 4.12 shows the stretching behaviour of an individual DNA molecule measured over a range of berenil concentrations from 0.3 to 300 μM. While the force-extension curves at berenil concentrations $\leqq 3$ μM are very similar, there is a pronounced difference in the curves obtained at higher berenil concentrations. After drug application, native DNA stretching behaviour could be restored by washing with drug-free TE150 buffer, indicating complete reversibility of drug-induced effects.

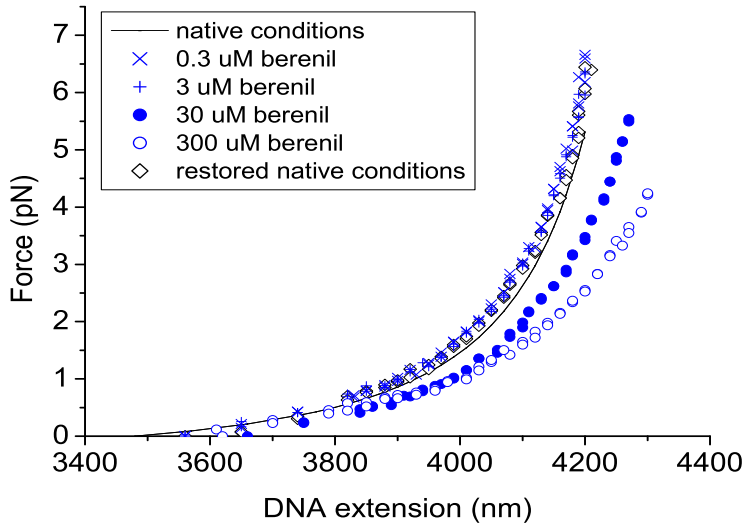

Figure 4.12: Force-extension curves obtained with a single molecule of DNA in the absence (solid line shows WLC fit to native DNA stretching curve), and presence of berenil concentrations of 0.3 (×), 3 (+), 30 (•) and 300 μM (∘). A pronounced effect on DNA stretching behaviour was detected for solutions containing $\geqq$ 30 mM, consistent with an intercalative mode of binding at high berenil concentrations. After drug application, native DNA stretching behaviour could be completely restored by washing with drug-free buffer solution (⋄).

The dependence of L_C and L_P on berenil concentration for a representative DNA molecule is given in table 4.2. The data shown are averages of 2 to 3 stretching cycles for each condition. No effect on L_C was observed at the low berenil concentrations ($\leqq$ 3 μM) tested here. At higher berenil concentrations (300 μM) there was an approximately 4 % increase in L_C. Groove-binding is not considered to increase DNA contour length, as outlined in the discussion on the results on netropsin [Coury et al., 1996]. Therefore,

	L_C (nm) ± SD	L_P (nm) ± SD	n
Control (TE150 buffer)	4467	47	1
0.3 μM berenil	4459 ± 8	84 ± 8	3
3 μM berenil	4467 ± 16	69 ± 8	3
30 μM berenil	4524 ± 13	54 ± 2	3
300 μM berenil	4649 ± 21	46 ± 1	2

Table 4.2: Effect of berenil on elastic properties of DNA: SD = standard deviation, n = number of measurements.

the observed contour length increase for high concentrations of berenil ($\geqq$ 30 μM) suggests an additional mode of DNA-binding, interpreted as intercalation. At low berenil concentrations, L_P was consistent with decreases in helix bending flexibility (L_P increased by almost 80 %), while at higher concentrations L_P returned to values found for native DNA. This apparent increase in bending flexibility at high berenil loadings may represent increased flexibility due to partial DNA charge neutralisation by saturating drug concentrations.

To investigate saturation of berenil-binding to DNA, force-extension curves were obtained on the same DNA molecule under near native conditions, and in buffer solutions containing 600 and 1200 μM berenil. The resulting curves are shown in figure 4.13. The DNA stretching path in 1200 μM berenil shows distinct features (see arrows in figure 4.13). A possible interpretation of these may be a sufficient charge neutralisation of the DNA strand due to the high number of berenil molecules in the solution, at a simultaneous lengthening of the molecule due to intercalative drug binding. This may lead to attractive intra-strand interactions along the DNA, causing a partial folding of the

molecule onto itself. For the high stretching forces applied, these interactions would then break up gradually, leading to the observed pattern. As can be seen from the figure, the relaxation path of these force-extension curves was found to overlay with curves obtained in the lower drug concentration. The 14064 bp DNA was therefore assumed to be saturated for berenil concentrations $\gtrapprox 600$ μM.

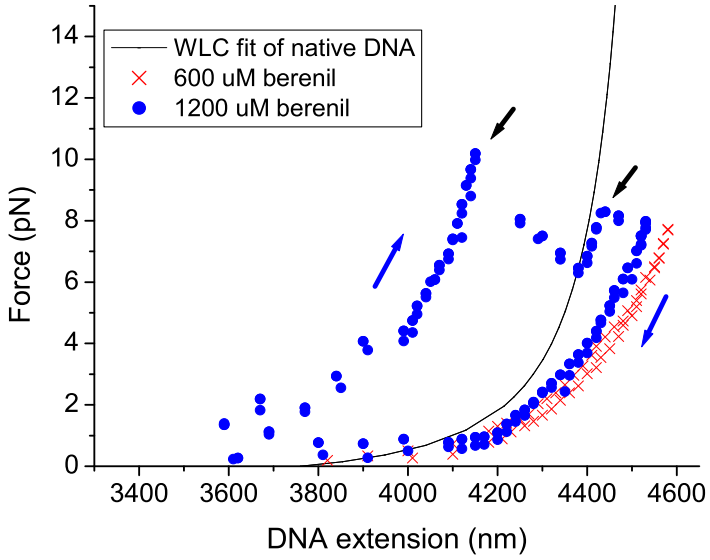

Figure 4.13: Saturating concentration of berenil. DNA stretching data in the presence of 600 μM ($\times$) and 1200 μM ($\bullet$) berenil. The solid black line represents a WLC fit for native DNA. For the 1200 μM concentration, the stretching path (see blue arrow) shows distinct features (black arrows), while the relaxation path overlays with that of DNA in half the drug concentration.

4.5 Conclusions

The presented results show how optical tweezers can be used to measure the force-extension behaviour of a single DNA molecule and, in this study, identify different drug binding modes to DNA. The low force noise level of optical tweezers allows the entropic, low force regime of DNA stretching behaviour to be studied, enabling a quantitative analysis of drug effects on helix geometry and bending flexibility. Using the minor groove-binding drug netropsin and the intercalating dye ethidium bromide as references, two different modes of binding for berenil could be identified. For clarity, the results are summarised separately for each drug type below:

Netropsin: Low molecular weight minor groove-binders, like netropsin, are expected to have little apparent effect on the mechanical properties of DNA, as binding should not perturb the DNA lattice structure [Coury et al., 1996]. However, X-ray crystallographic studies of netropsin binding to DNA indicate that there is a small distortion to the DNA helix [Kopka et al., 1985]. This observation might explain the small increase in L_P, consistent with bound netropsin causing a slight decrease in the apparent bending flexibility of the DNA.

Ethidium bromide: Intercalation of ethidium bromide between adjacent base pairs of dsDNA has been determined to increase the inter-base pair distance by 0.34 nm [Wang, 1974; Coury et al., 1996], leading to an increase in L_C. Such effects on L_C dominate the appearance of the obtained DNA force-extension curves (as can be seen for example in figure 4.10). However, there

is also a stabilising effect by intercalative drug binding on DNA structure, which causes apparent stiffening of the DNA double helix. Consistent with this we also found an increase in L_P at low concentrations of ethidium bromide. However at higher concentrations, the positively charged intercalator caused a reduction in bending rigidity, which might be explained by partial neutralisation of the DNA charge.

Berenil: Berenil produced a significant increase in L_P at low drug concentrations ($\leqq 3$ μM) (similar to the minor groove-binder netropsin). However, at higher concentrations (> 10 μM), berenil caused a significant increase in L_C while L_P re-approached that of native DNA. At low concentrations, the increase in L_P can be interpreted as a stiffening of the DNA molecule by minor groove-binding of berenil, consistent with the effects of netropsin. At high berenil concentrations, the increase in L_C is consistent with the effects of high concentrations of the intercalating dye ethidium bromide.

By comparing the effects of berenil, netropsin, and ethidium bromide on the mechanical properties of DNA, the obtained results show a combination of groove-binding and intercalation for berenil at high drug concentrations. Further experiments will enable the separation of the contributions from each binding mode and the determination of their individual binding affinities.

Chapter 5

Protein binding to DNA; a study with AFM

As explained in chapters 1 and 2, AFM has two possible major modes of application, the force measuring mode and the imaging mode. In contrast to the work presented in the previous chapter, this chapter deals with imaging experiments on DNA-binding. AFM was employed here as a complementary technique to molecular biological assays to obtain information on the DNA binding properties of a novel protein. While these assays present bulk methods, giving information on the average behaviour of large numbers of protein and DNA molecules, the strength of AFM measurements lies in the resolution of single molecules.

Proteins are typically one to two orders of magnitude larger than the small DNA-binding molecules discussed in chapter 4. This makes the protein visible in high-resolution AFM images as a peak on the DNA strand, whereas drug molecules would not be detectable by this method. Visualising

the position of the protein along the DNA strands gives access to complementary types of information. AFM images of protein/DNA complexes can for example be used to determine possible binding sites and oligomeric states for the protein on the DNA [Wyman et al., 1997; Allison et al., 1997], to visualise topological changes in the DNA strand through protein binding [Anselmetti et al., 2000; Rippe et al., 1997; Rees et al., 1993], or they can serve to quantify protein binding to DNA in stoichiometric measurements [Erie et al., 1994; Wyman et al., 1995]. It is even possible to observe protein activity over time by sequential imaging in a liquid environment [Radmacher et al., 1994; Kasas et al., 1997]. AFM imaging also offers a complementary approach to measuring properties, which can be studied with force measuring techniques, such as effects on DNA length.

Here, AFM high resolution imaging was employed to determine functional properties of the novel protein called RdgC. RdgC from *Escherichia coli* (*E. coli*) has only recently been purified, and was shown to bind DNA in gel retardation assays [Moore, 2002]. Using genetic methods, a role of RdgC in DNA replication has been established [Ryder et al., 1996; Moore, 2002]. However, its mechanism of action has not yet been elucidated.

5.1 DNA-binding proteins and superstructure of DNA

In-vivo, DNA readout (transcription) and maintenance (repair and recombination) are regulated by the binding of proteins to particular sites along the

DNA strand [Alberts et al., 1990; Ryder et al., 1996]. Proteins can either bind specifically or non-specifically to DNA. Specifically binding proteins attach to a particular binding site on the DNA, which is defined by its geometry and/or base pair sequence. Non-specific binding occurs anywhere along the DNA, often combined with migration of the proteins along the DNA strand to their site of action. Both kinds of protein-DNA interactions are generally based on hydrogen bonding, often in conjunction with electrostatic attractions. An example of specifically binding proteins are restriction enzymes or transcription factors, which have to recognise their specific binding sequence in order to start gene transcription. In DNA repair on the other hand, the proteins involved in detecting and correcting mismatch DNA bind independent of the DNA sequence, and instead recognise the features of damaged nucleotides (exposed chemical groups). Further, during DNA replication, specific "branched" structures in DNA are bound, from which strand synthesis may be initiated.

Protein binding to DNA can thus be subject to particular structural requirements such as either a double or single strand, or certain types of DNA superstructures (see below) [Léger et al., 1998]. The type of targeted DNA structure is dictated by the specific enzymatic function of the protein, or by the host conditions (such as bacterial proteins specialised for underwound DNA). For example, helicases bind to single stranded parts of DNA to open neighbouring double stranded DNA (dsDNA), by moving along the single strand and pushing the two strands apart. Other proteins assist this process by stabilising the single stranded DNA (ssDNA) form. These kinds of proteins therefore attach preferentially to ssDNA [Alberts et al., 1990]. For

the RecA protein, for example, which is responsible for the introduction of a DNA strand into another DNA double-helix during general genetic recombination in *E. coli*, the binding energy for protein-DNA complex formation was found to be reduced for particular DNA conformational states [Bennink et al., 1999]. The spatial DNA structure may thus be used as additional means (besides base pair sequence), to regulate protein binding to DNA.

The attachment or binding of proteins can also alter DNA tertiary structure [Strick et al., 1998; Bennink et al., 1999; Bustamante and Rivetti, 1996; Anselmetti et al., 2000]. Some DNA-binding molecules, including some proteins, are capable of locally unwinding DNA. This can induce bends in the DNA, at the same time increasing DNA contour length. The unwinding of DNA will however not only change the molecule's length. It will also affect, for example, the number of twists and the number of cross-overs (called writhe) within one DNA double-strand, thus changing the molecule's superstructure. This is exploited in cooperative binding, where the attachment of a protein alters the DNA shape locally so that additional binding of further proteins is supported.

As illustrated in chapter 4, DNA-binding molecules have different modes of binding, which modulate DNA superstructure in different ways. Thus, since the function of a protein is often dependent on a particular DNA binding substrate, knowledge of this can provide clues on the potential function of a DNA-binding protein.

Figure 5.1 illustrates the different geometrical forms that define DNA superstructure [Bauer and Vinograd, 1968; Marko and Siggia, 1995b]. A twisted rod, which is fixed at both its ends, can be transformed either into

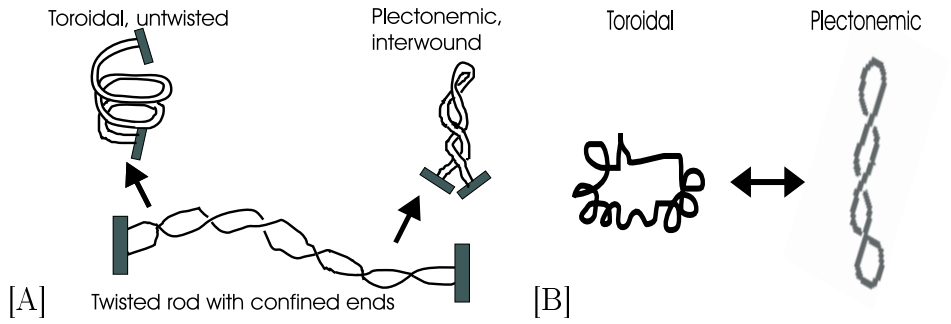

Figure 5.1: DNA superstructure. The tertiary conformation of the DNA double-helix is called its superstructure. Regarding the dsDNA helix as a geometrical rod, different structures can be assumed [Bauer and Vinograd, 1968]. (A) A twisted rod with two confined ends can be transformed into either a toroidal or a plectonemic form. (B) Circular plasmid DNA can be regarded as having two "confined ends".

a toroidal, untwisted spiral structure, or by releasing the tension, into a relaxed, interwound or plectonemic structure. Geometrically regarded, DNA can be described by an elastic rod. When both ends of such a rod are fixed, as is the case, for example, for circular plasmid DNA, twisting it will therefore either induce open ring-like (toroidal) structures, or on the other hand "messy telephone cord-like" (plectonemic) structures, in which the DNA double-helix is wound around itself. These structures are known as the supercoiling states of DNA. The different tertiary conformations can be converted into each other in changing surrounding conditions [Vologodskii and Cozzarelli, 1994a; Vologodskii and Cozzarelli, 1994b].

Further, treating DNA as an elastic rod allows us to describe its geometry in a mathematical language [White, 1969; Vologodskii and Cozzarelli, 1994a; Vologodskii and Cozzarelli, 1994b]. The twist number (T_W) of a DNA double-helix is a measure of the number of times that the double-strand spins about

its axis. The writhe number (W_R) is the number of crossings of the axis of a closed, circular DNA double-strand. These crossings have either a positive or a negative sign; positive sign for homo-directional and negative sign for hetero-directional crossing, as illustrated in figure 5.2.

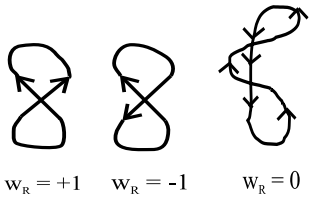

Figure 5.2: Positive and negative writhe of a polymer strand. The writhe number w_R is defined as +1 for each unidirectional crossing of strands, and as -1 for crossing of strands in opposite directions. The overall writhe number of a polymer strand is the sum of all writhe numbers from all crossing events within the strand.

The ratio of the number of base pairs in the DNA molecule and the mean number of base pairs per turn of the DNA double helix is a topological invariant. It is called the linking number (Lk) of a DNA double-strand. The three properties, Lk, W_R, and T_W, are linked by White's theorem. This theorem states that for a constant linking number of a polymer strand, the twist and writhe values will have to adjust themselves accordingly, turning twisted shapes into untwisted, interwound ones and vice versa:

$$Lk = T_W + W_R \tag{5.1}$$

5.2 RdgC

Professor R. Lloyd's group (Institute of Genetics, University of Nottingham) has been investigating a novel protein called RdgC. They found that RdgC has a molecular weight of approximately 34 kDa, and in solution exists in dimeric form. Gel retardation assays have shown that RdgC preferentially binds to dsDNA, forming fewer complexes with ssDNA [Moore, 2002]. Also, the complexes with dsDNA proved more stable than those with ssDNA, for incubations over the same length of time and for the same number of DNA nucleotides. This is illustrated in figure 5.3, showing results from gel retardation assays [Moore, 2002]. The protein does not show any sequence selectivity in dsDNA according to Systematic Evolution of Ligands by EXponential enrichment (SELEX) assays [Moore, 2002].

Studies on *E. coli* in which the *rdgC* gene had been deleted showed that lack of RdgC alone does not affect cell growth (see figure 5.4A and B). However, RdgC was required for cell viability in strains lacking certain other proteins. For example, figure 5.5 shows an agar plate with *E. coli* cells in which a gene involved in DNA replication (*priA*) had been deleted, as well as the same strain with additional deletion of *rdgC* (AG181 + *rdgC::Tm* [Moore, 2002]). The cells grew comparably to wild type cells on agar plates only if RdgC was present. This suggests that RdgC plays an essential role in the DNA replication of these mutants. In the employed *priA2::Km* (*priA* deleted) *E. coli* strain (AB1157 derivative AG181 [Gregg et al., 2002]), the defects associated with deletion of *priA* were suppressed by a mutation in *dnaC*. Light and fluorescence microscopy images of these cells as well as wild

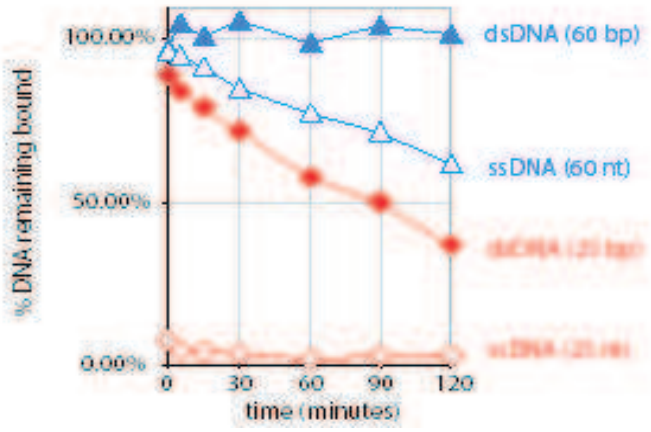

Figure 5.3: For both dsDNA and ssDNA, higher numbers of basepairs (bp) or nucleotides (nt) displayed DNA/RdgC complexes that were more stable over 120 minutes incubation time in the presence of a competitor. Further, the percentage of DNA bound by RdgC was found to reduce much more rapidly for ssDNA than for dsDNA for the same number of nucleotides. [Moore, 2002]

type *E. coli* cells are shown in figure 5.4. As can be seen from the images, while AG181 strain cells showed similar appearance to wild type cells, additional deletion of *rdgC* led to the cells growing into long filaments, with unorganised DNA structure [Moore, 2002].

The exact role of RdgC in DNA replication is however still unclear. No nuclease or other enzymatic activity could be detected for RdgC in different types of assays [Moore, 2002]. This rules out a range of possible working mechanisms for this protein. Thus, in order to gain further insight into the way this protein works, complexes of RdgC with both linear and circular plasmid DNA were imaged with AFM. Different protein to DNA ratios were applied, to investigate the effect of increasing RdgC concentration.

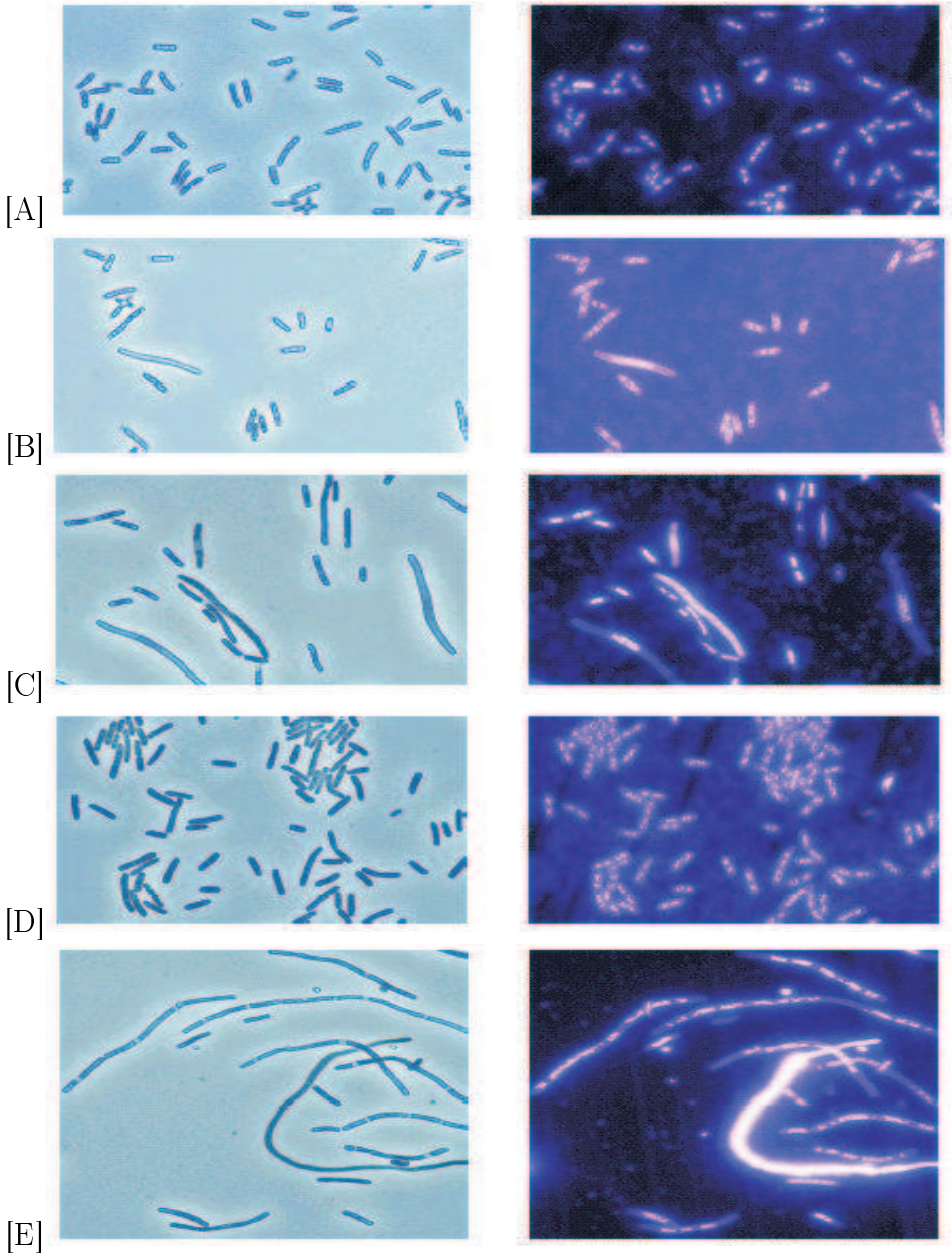

Figure 5.4: Deleting the RdgC gene I [Moore, 2002]. Light and fluorescence microscopy images of E. coli cells: (A) wild type cells from strain AB1157, (B) *rdgC* deleted AB1157 cells, (C) *priA* deleted AB1157 cells, (D) *priA* deleted AB1157 cells with mutation in *dnaC* (strain AG181), (E) *rdgC* deleted AG181 cells.

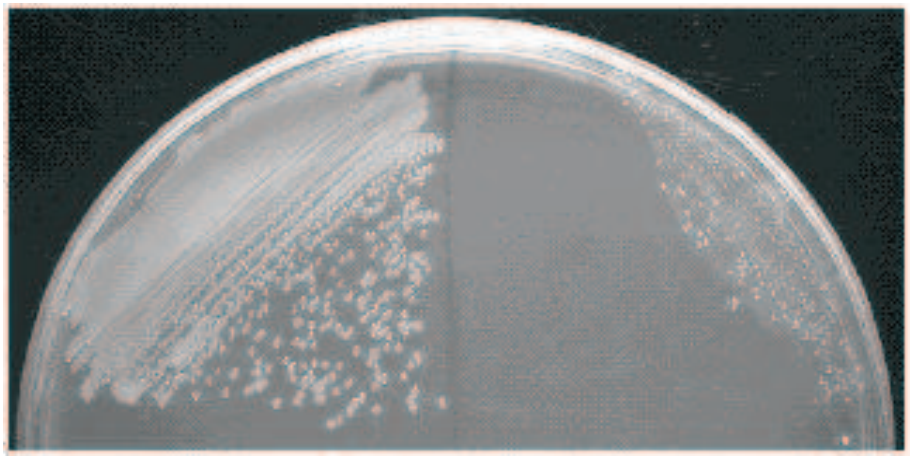

Figure 5.5: Deleting the RdgC gene II [Moore, 2002]. Bacterial colony growth of the same *E. coli* strain with deletion of the *priA* gene only (left pattern on the agar plate) and with deletion of both, the *priA* and the *rdgC* gene (right). Both mutation strains carried a DnaC suppressor (*priA2::Km dnaC212* [Gregg et al., 2002]), to suppress defects associated with *priA* deletion. RdgC function is necessary for healthy cell growth under these mutant conditions.

5.3 Materials and methods

DNA

The DNA used in these experiments was chosen according to the experimental requirements. Firstly, smaller scan areas in AFM imaging allow an increase in image resolution. Therefore, the linear DNA strands employed for the detection of protein binding positions were chosen to be of a short sequence. The DNA used in these experiments were fragments of bacterial DNA from *Vibrio anguillarum* (*V. anguillarum*), kindly supplied by Dr David Kirk from the Quorum Sensing group (Molecular Microbiology) within

the Department. The DNA sequence consists of 1101 base pairs (bps) and encodes for the protein VanP [Kirke, 2002], which is a homologue of LuxP [Bassler et al., 1994; Kirke, 2002]. *VanP* was cloned from *V. anguillarum* and amplified by the artificial replication technique, polymerase chain reaction (PCR). During the PCR DNA amplification process, a total of 32 bases are added to the strand ends due to primer attachment, to produce 1133 bps dsDNA. The employed polymerase enzyme Taq also causes addition of a few (of the order of 5 bases) adenosines at the DNA strand ends. These short sequences at the ends of the linear dsDNA are single stranded. For physiological B form DNA, 1133 bps relate to an approximate contour length of 385 nm.

A second criterion for the choice of DNA was a relatively equal percentage of different bases, to minimise potential effects due to base pair composition. The sequence used here was made up of circa 58 % A/T and 42 % G/C.

The DNA was obtained as a 0.86 nM solution (concentration of 0.6 μg/ml) in deionised water, and stored at -20 degrees Celsius (°C) as aliquots of 50 μl to avoid strand breaking due to repeated defrosting and refreezing.

The circular DNA used in studying the effect of RdgC on DNA superstructure was the gene encoding for PUC19, obtained from *E. coli*. PUC19 DNA is a 2686 bps long, circular plasmid DNA fragment. PUC19 was extracted from a *rec*$^-$ strain of *E. coli* to avoid dimer formation, and purified on an agarose tris borate EDTA (TBE) gel to minimise the amount of nicked plasmid. It was kindly supplied by Dr Moore (Institute of Genetics, University of Nottingham) as a 20 nM solution (33.1 μg/ml) in 10 mM Tris, 2mM EDTA. Again the DNA was frozen at -20°C for storage.

RdgC

RdgC from the bacterium Escherichia coli (at least 95 % purity) was stored as 0.53 mg/ml (8 μM solution) in a solution of 50 % glycerol, 50 mM DTT (Tris.HCl pH 7.5, 1mM EDTA, 1mM dithiothreitol), at -20°C. DTT addition to the storage buffer is neccessary to protect the protein against oxidisation damage. RdgC was also supplied by Dr Moore.

5.3.1 Sample preparation

Magnesium buffer (20 mM Tris, 10 mM $MgCl_2$) was used to dilute the protein and DNA to the required concentrations. Small multivalent cationic ions are necessary to stabilise the DNA and to support physisorption of the DNA molecules to the substrate surface [Vesenka et al., 1992; Hansma and Laney, 1996]. DNA itself is highly negatively charged. Mica, which serves as substrate surface in these experiments, is also negatively charged. Therefore the presence of positively charged ions along the DNA is required for attraction of the DNA to the surfaces. Divalent cations are more potent chelating agents than monovalent metal ions. Magnesium buffer showed a drastically reduced salt background in the high resolution images compared to buffer containing sodium chloride.

For the experiments to determine the protein position on the DNA strands and the effect of protein binding on DNA length, linear DNA and RdgC from *E. coli* were mixed in the ratios 1:0, 1:1, 1:10, and 1:100. The final DNA concentration in these experiments was 0.4 nanomolar (nM).

For the experiments on DNA superstructure, circular plasmid DNA from

E. coli was mixed with RdgC in ratios of 1:0, 1:2, 1:20, 1:30, 1:60, and 1:100. In these experiments, the final DNA concentration in the RdgC/DNA mix was 2.5 nM for the ratios 0:1, 10:1, and 100:1, 2 nM for 20:1 and 60:1, and 1.7 nM for 30:1.

The mica pieces used as substrate surface for the imaging were acquired from Agar (Agar Scientific Ltd., Stansted, Essex, UK). They were cut into pieces, 1x1 cm^2 in size, and attached to a flat metal platelet using thermoplastic glue (Tempfix adesive; Agar Scientific Ltd.). Those platelets could then be firmly fixed on the AFM stage for the imaging process using the magnetic attraction between the platelet and the AFM scanner head.

After mixing the DNA and the protein, the solution was left to incubate at room temperature for 10 minutes. After this time, 2 μl of the mix was pipetted onto a freshly cleaved mica surface, and washed off gently after 30 seconds using 10 ml deionised, filtered (0.2 μm pore filter; Sartorius AG, Goettingen, Germany) water from a water deionisation system (Elga Maxima; Elga Ltd., High Wycombe, UK). The samples were blow dried with nitrogen, and imaged immediately (or less than 4 hours later).

5.3.2 Experimental technique: AFM imaging

Images were taken with a Nanoscope IIIa DI MultiMode AFM (Veeco, Santa Barbara, California, USA). All experiments were carried out in air on dried samples and in tapping mode. Beam shaped AFM cantilevers (TESP, Veeco) with spring constants between 30 and 41 N/m and resonant frequencies between 280 and 300 kilo-Hertz (kHz) were used. Data were collected at a scan

rate of typically 2 Hz and pixel resolution of 512x512.

To acquire high-resolution images on the short, linear DNA fragments, an A-type piezo-scanner was used, with a maximum scan area 1x1 μm^2. The images on the larger numbers of circular DNA molecules were taken using an E-type scanner, which allows a maximum sample surface area of 14x14 μm^2.

Statistical analysis

Statistical analysis of the protein binding positions, DNA length changes, and the separation of the strand ends was carried out using Scion Image software (Scion Corporation, Maryland, USA; based on NIH Image by Wayne Rasband, National Institutes of Health, USA). The peak heights were determined in 3D plots of the images. For this, the underlying DNA strand was used as a baseline, and peak height measured from here, using DI imaging software. High resolution images of 19 to 43 linear DNA molecules for each of the four different protein concentrations were analysed.

To determine the effect of RdgC on DNA superstructure, between 150 and 300 molecules of circular DNA for each of the six different RdgC/DNA ratios were sampled and analysed using DI imaging software.

5.4 Results and discussion

AFM images were obtained on native linear and circular bacterial DNA fragments (see materials and methods section). Linear fragments were imaged at high resolution, scanning areas of 1x1 μm^2 and below. Large numbers of circular DNA strands were further imaged to give statistical information

on DNA superstructure. In these experiments, plasmid DNA from *E. coli* was employed, which is negatively supercoiled in its physiological state. Gel electrophoresis assays were run on a sample of the DNA to ensure a high percentage ($\geqq$ 90 %) of the DNA was nick free. Nicks in the DNA strands would supply free ends to relax induced twist in the double-helix. Since this would eliminate effects on DNA superstructure, which are studied here, the presence of nicked DNA molecules was undesirable. Figure 5.6 shows representative examples of obtained images on linear and circular native DNA.

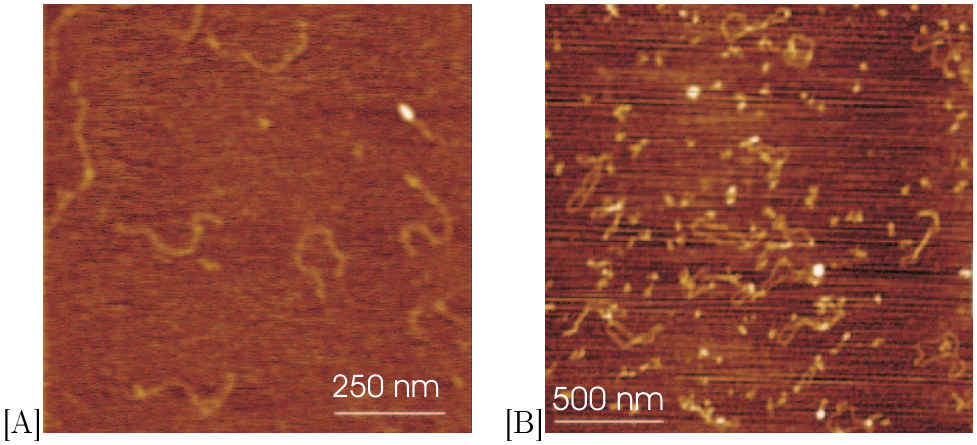

Figure 5.6: AFM images of native linear (A) and circular (B) DNA fragments. Scale bars indicate 250 and 500 nm for (A) and (B) respectively. Images are of a height range of 2 nm.

The DNA was incubated with different concentrations of the DNA-binding protein RdgC. Figure 5.7 shows representative images of the linear DNA for each of the applied RdgC/DNA ratios of 1:1, 10:1, and 100:1. All images are of a height range of 2 nm, scale bars indicate a length of 250 nm. From the images, binding positions of the protein, as well as length changes and effects on DNA geometry as a result of RdgC binding were determined.

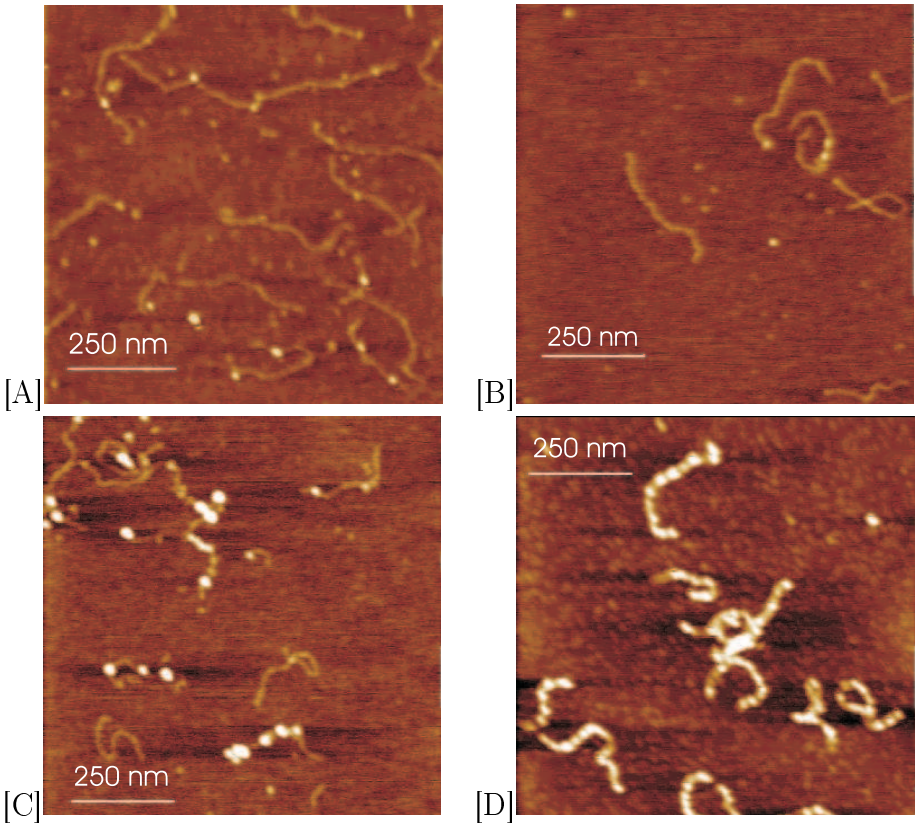

Figure 5.7: High-resolution AFM images of RdgC complexed with linear DNA at protein/DNA ratios of (A) 1:1, (B) 10:1, (C) 100:1, and (D) 1000:1. All images are of a height range of 2 nm. Scale bars indicate 250 nm.

The attachment of molecules to DNA can often alter the DNA's superstructure [Strick et al., 1998; Bennink et al., 1999; Bustamante and Rivetti, 1996; Anselmetti et al., 2000]. This was investigated for RdgC binding, using the circular DNA, in which the ends are restrained by ring-closure, so that an induced twist in the DNA axis cannot be "disposed of". Effects on the supercoiling state of circular DNA induced by protein binding can therefore be observed. In figure 5.8, representative AFM images of circular DNA in the presence of different concentrations of RdgC are shown.

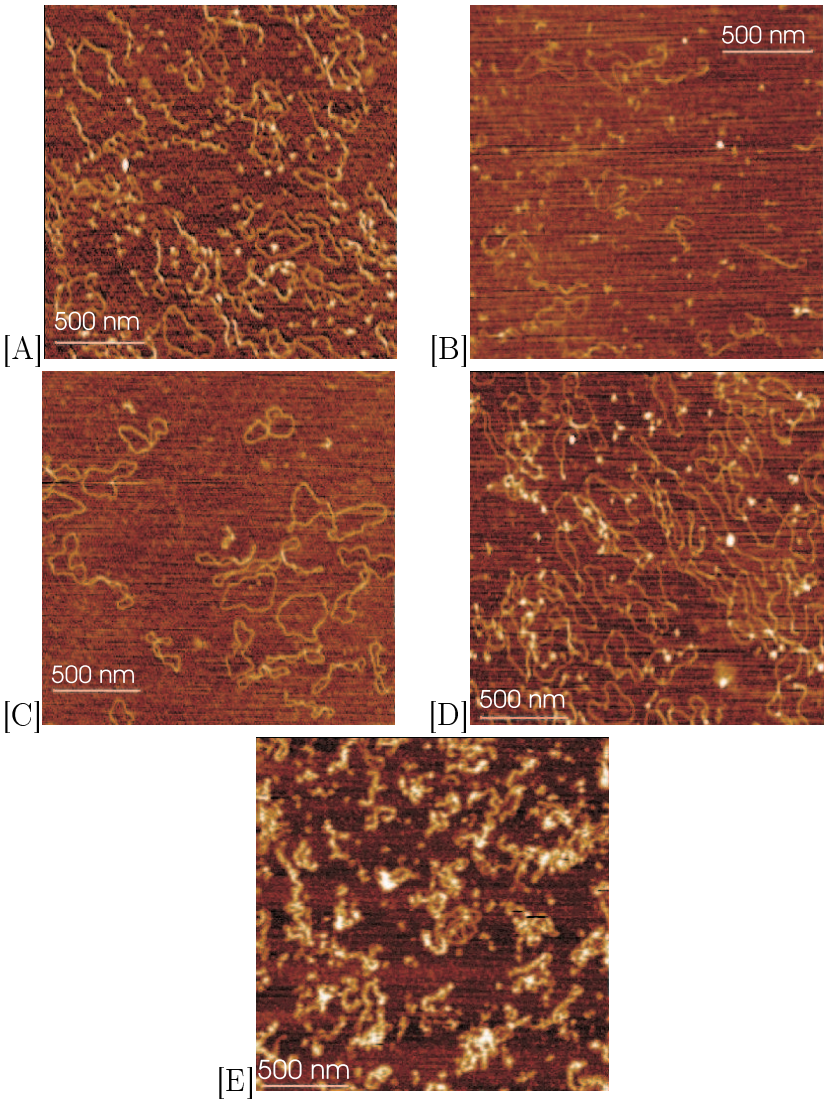

Figure 5.8: AFM images of RdgC complexed with circular plasmid DNA at protein/DNA ratios of (A) 2:1, (B) 20:1, (C) 30:1, (D) 60:1, and (E) 100:1. All images have a hight range of 2 nm, with exception of the 100:1 ratio image (3.5 nm). Scale bars are 500 nm.

5.4.1 Protein binding position

From the high-resolution AFM images of linear dsDNA in the presence of different protein concentrations (see figure 5.7), the protein binding positions along the DNA were determined. In these images, bound RdgC is observed as peaks on the DNA strands. In the normal top-view display of AFM imaging software, they appear as blobs on the DNA (see figure 5.9). Their diameter is circa 10 nm, so that they stand out over the diameter of the DNA strand. The position of these peaks along the DNA strand can thus be observed.

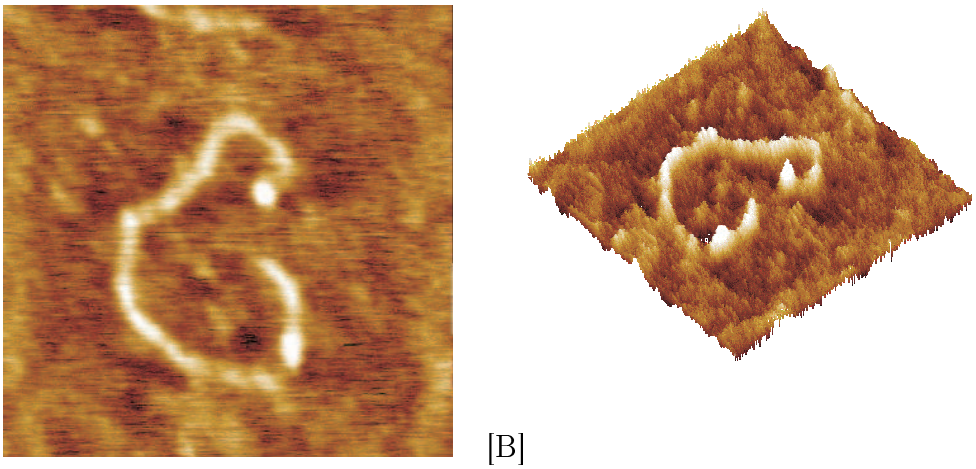

[A] [B]

Figure 5.9: RdgC/DNA complexes can be seen as peaks on the DNA (black arrows). Top (A) and 3D (B) view of single DNA molecule with two protein peaks.

Firstly, to investigate any potential preferences in binding locations of RdgC, all observed peaks were classed into middle and end positions, according to their positions along the DNA strands. For this, the height of each individual peak was measured from the baseline defined by the DNA strand height. Peak heights were found to vary from 0.4 to 2.3 nm. Since such variations are likely to represent different numbers of protein bound, each peak

was further weighted with its height. The peak distribution was investigated for 31 (± 12) DNA molecules for each of the different RdgC/DNA ratios.

Figure 5.10 shows the statistical distribution of RdgC molecules bound to the DNA strands, for the different protein/DNA ratios. It can be seen that the frequency of middle positions increases about seven times more than that of end positions from native DNA to a RdgC/DNA ratio of 1:1, and approximately equally between 1:1 and 10:1. Assuming a binding site size of approximately 20 base pairs [Moore, 2002], on a DNA strand of 1133 bps there are, however, two orders of magnitude more middle than end positions

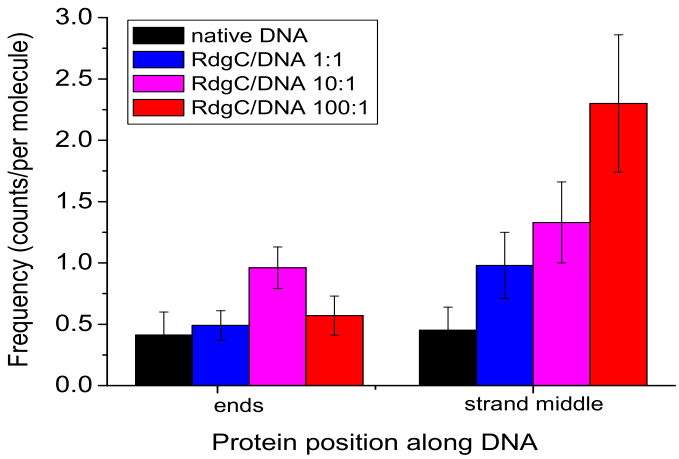

Figure 5.10: Distribution of RdgC positions between dsDNA ends and strand middle, for protein/DNA ratios 0:1, 1:1, 10:1, and 100:1. Bars give the frequency at which end positions and middle positions on the DNA strands are found per molecule. Between 19 and 43 molecules have been considered in this analysis. Error bars are due to an assumed height measurement error for the individual peaks of ± 0.2 nm.

available as protein binding positions. Considering the much lower number of strand end than middle positions, the obtained distribution therefore suggests that RdgC binds preferentially to the ends of the DNA strands initially, although not exclusively. This would indicate a dsDNA-end position related function of RdgC.

PCR amplified fragments of dsDNA, such as the ones used in these experiments, have short end sections with free (unpaired) ssDNA, arising from the production procedure. Therefore, a possible interpretation for the found distribution would be a preferential targeting of ssDNA by RdgC. However, gel retardation assays have shown that RdgC forms more complexes with dsDNA than ssDNA, which are also more stable (see section 5.1). This explanation is hence ruled out. In these assays, the binding site for RdgC was also found to require approximately 20 base pairs [Moore, 2002]. The single stranded DNA end fractions of the employed linear DNA fragments are approximately 5 bases only, and would therefore not suffice for RdgC binding. Since RdgC displayed no nuclease activity in a series of tests (see section 5.1), binding to the single stranded ends as part of a repair mechanism also offers no explanation for the observed behaviour. It is therefore not yet understood why end binding would be initially favoured by RdgC.

As can be seen from figure 5.10, the average amount of protein situated at the strand end positions was found to stagnate for protein/DNA ratios $\geqq$ 10:1. The slight decrease in the distribution for a ratio of 100:1 may be a false effect due to the enhanced average strand height for this high protein concentration, in which the non-increased end peaks are more prone to being unnoticed. In contrast to this, the middle position value continues to rise

monotonously with protein concentration, as free positions along the middle of the strands are filled up.

In order to determine potential specific DNA binding sites of RdgC, the precise distance of each protein peak from the strand ends was also determined, using image analysis software (see section 5.3.1). Plotting the distances of all the individual peaks on the linear DNA from both strand ends over half the DNA length, gives the frequency with which RdgC binds to each position along the DNA. This analysis method has to be employed here, as in the images the two ends of the DNA cannot be differentiated. Figure 5.11 shows the emerging patterns of binding frequency for distances along the DNA grouped in segments of 10 nm length. A more frequently targeted sequence within the DNA would appear as a maximum in the distribution. This technique thus allows the determination of specific binding sites for the protein. As can be seen from the graphs for the different protein/DNA ratios shown in this figure, the emerging pattern of the distribution indicates no favoured position along the strand. The result suggests that RdgC does not target any specific binding site on the DNA. This is in agreement with prior observations from gel retardation techniques [Moore, 2002].

5.4.2 DNA topology

In our images, for protein/DNA ratios of 10:1 and higher, sharp angled kinks and bends in the DNA strands were found relatively frequently at protein peak positions (see figure 5.12). The total amount of peaks that are positioned at bends in the DNA strands was investigated for the different pro-

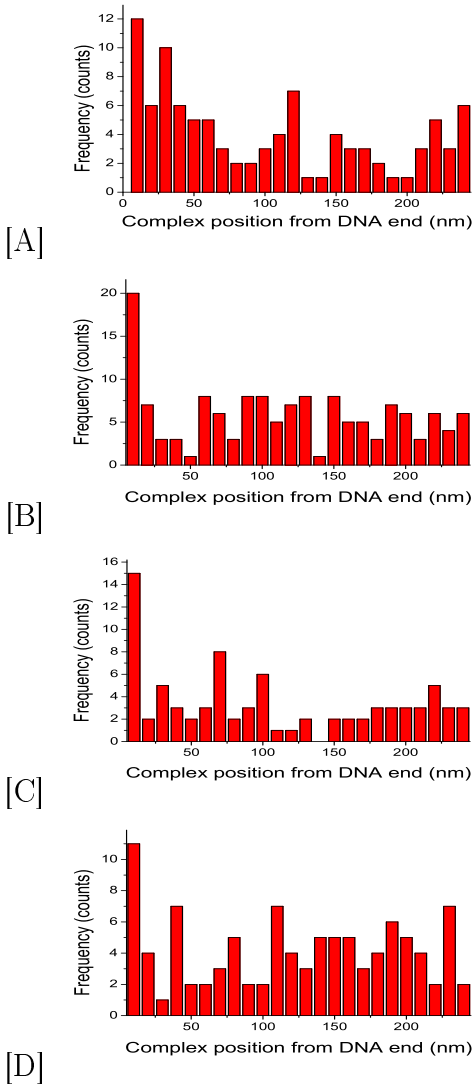

Figure 5.11: Peak positions along linear DNA strand for (A) native DNA, (B) 1:1, (C) 10:1, and (D) 100:1 ratio of RdgC to DNA. The frequency of appearance of each peak position along the strands, measured from both ends, is shown for half the strand length. Since distances were measured from both ends, only one half of the strand length is plotted here, so that every position is represented once. Sequences along the DNA that are predominantly targeted by RdgC would lead to enhanced features in the frequency plot.

tein/DNA ratios.

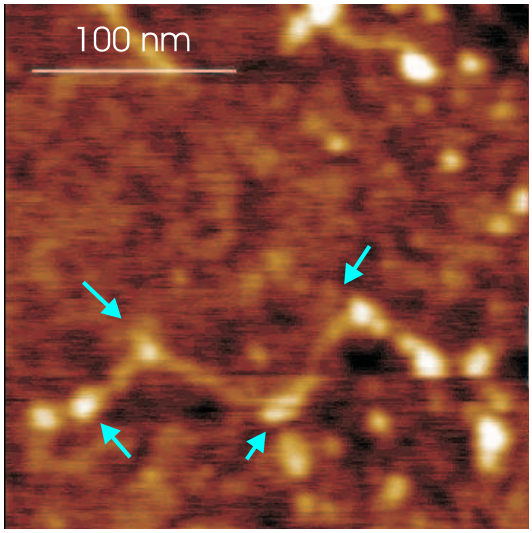

Figure 5.12: Bends and kinks in the DNA strand appear to be a favourable position for RdgC binding (blue arrows).

Statistical analysis of this is shown in figure 5.13. The figure shows the amount of both peaks at bend positions and peaks at unbent positions along the strands for increasing RdgC concentration. It should be noted that only binding positions along the middle of the DNA strand were considered, since binding at the strand ends will not induce bends in the DNA. The values are plotted as the sum of heights of all peaks at each of the two different kinds of positions separately. To facilitate comparison between the results for the different protein/DNA ratios, the values were averaged by dividing by the total number of molecules for each ratio. This gives the average sum of peak heights per molecule.

As can be seen from the figure, from native DNA to a protein/DNA ratio of 1:1, the total of peak heights averaged per molecule increased approxi-

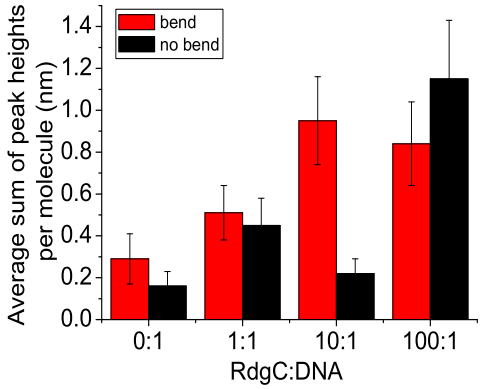

Figure 5.13: Coinciding protein binding position with DNA bend. For all binding events along DNA strand middle positions, the distribution into positions coinciding with either bends (red bars) or no bends (black bars) in the DNA strand, is plotted for the different RdgC/DNA ratios. Each peak is weighted with its height and divided by the number of molecules for the particular ratio. So the values represent the average height of all bend- or no bend-peaks per molecule. Error bars in the plot indicate the uncertainty due to measuring inaccuracy assumed to be ± 0.2 nm for each individual peak.

mately equally for both, bend (increase by 0.22) and no-bend (increase by 0.29) positions. For a ratio of 10:1, a much more pronounced growth of peaks at bend positions along the DNA was observed (+ 0.44). A slight reduction was found for the no-bend position peaks (- 0.23), which is however still within the error margins of the analysis method. The errors are indicated in the graph, and represent the standard deviations between the individual results for the different molecules. From the RdgC/DNA ratio of 10:1 to 100:1, the amount of peaks at bend positions remained constant within the

error margins (- 0.11). The sum of peak heights at unbent strand positions on the other hand "caught up" (+ 0.93), so that for this ratio approximately equal numbers of proteins appeared to be bound at both, bent and unbent DNA strand positions.

On average, along the middle of the DNA strands, 57 % (± 25 %) of all additional peaks after RdgC application were found to be positioned at bends or kinks in the DNA strands. For lower protein/DNA ratios only (≦ 10:1), 67 % (± 24 %) of peaks were situated at bend positions. The error in these values is the standard deviation for the contributions from the different ratios. This suggests a slight preference of bends in the DNA strands as binding positions for initial binding of RdgC at low protein concentration.

This analysis does however not distinguish between the protein preferentially binding to bends, and the protein binding itself causing a local bending of the DNA strands. In order to elucidate this question, the average number of bends per DNA molecule and end-to-end separation of the strands was further measured for the different protein concentrations. An increase in the number of bends with protein concentration would indicate the introduction of these by the binding of the protein. The end-to-end separation of the DNA strands reflects the overall curvature of their axis, which is again correlated to strand bending. The results are displayed in table 5.1 for 31 (± 12) molecules for each of the applied protein/DNA ratios.

No change in the average number of bends per molecule was found between the native DNA and a protein/DNA ratio of 1:1, whereas a slight increase from approximately 5 to 6 and 7 was obtained for ratios of 10:1 and 100:1, respectively. This suggests an introduction of bends into the DNA

RdgC/DNA ratio	Bends/molecule	End separation/DNA length
native DNA	5.3 (± 1.7)	0.64 (± 0.23)
1:1	5.2 (±1.6)	0.62 (± 0.22)
10:1	6.3 (± 2)	0.54 (± 0.26)
100:1	7 (± 1.3)	0.54 (± 0.22)

Table 5.1: The average number of bends per molecule and strand end separation in units of the individual molecular length. The indicated errors (in brackets) are the standard deviations of the values for the 31 ± 12 molecules investigated for each of the applied RdgC/DNA ratios.

strands by RdgC binding at these protein concentrations.

The results displayed in table 5.1 show no significant effect of RdgC binding on the average separation of strand ends and therefore on the overall curvature of the DNA strands. Individual local bends however would only be expected to add up to an increased curvature for cooperative protein binding to DNA. Random binding would lead to compensating bending through RdgC, potentially showing effects on the length (see section 5.4.3) but unlikely on the overall curvature of the DNA.

If RdgC binding was to introduce bends in the DNA strands, we would therefore expect an effect of RdgC on DNA superstructure. To follow this up, 307 (± 43 %) molecules of circular DNA were analysed for each of 5 different protein/DNA ratios. Under native conditions, at least 90 % of the DNA was negatively supercoiled, as detailed earlier.

The molecules were classed according to their structural appearance on the substrate surface into four categories: open circular, toroidal, plectone-

mic, and rod-like shapes, schematics of which are given in figure 5.14. Open circular shapes were interpreted as molecules, which were forced into a tense ring by DNA self-repulsion. Toroidally supercoiled shapes were considered to be intermediates between open circular and plectonemic supercoiled forms. They often resembled relaxed molecules, which had landed on the surface in random geometry. Therefore this group could have been more prone to error through inclusion of relaxed, non-supercoiled DNA molecules. However, since there are only maximally 10 % of non-supercoiled strands in the sample (nick-containing DNA which could relax tension), it was considered that this is not likely to be a significant problem in the interpretation of our results. Rod-like shapes were interpreted as highly supercoiled forms. These were believed to arise from plectonemic forms by further winding the DNA into more tightly coiled structures, which then curl up into dense, linear shapes.

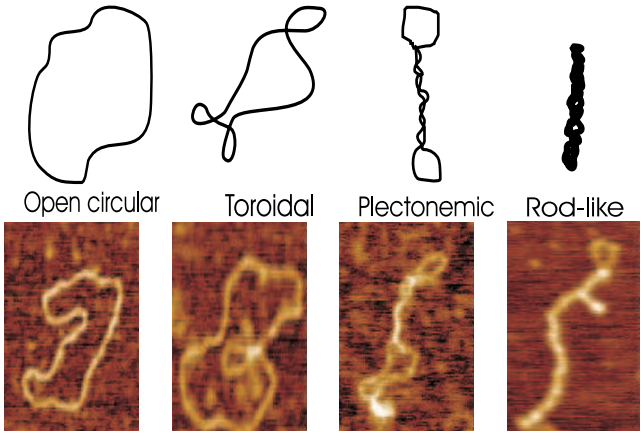

Figure 5.14: Schematic drawings (top) and AFM images (bottom) of the classification of observed DNA shapes.

In the absence of RdgC, the DNA was found predominantly in supercoiled forms. Plectonemic shapes presented the dominant form of supercoiled struc-

tures for the native DNA. This agrees with the general belief, that plasmid DNA adopts this superstructure under physiological conditions.

Figure 5.15 gives the distribution of the observed shapes of the plasmid DNA for the different protein/DNA ratios. This distribution shows no change in appearance for protein/DNA ratios of up to 20:1, compared to native DNA. In the images for an increased RdgC/DNA ratio of 30:1 and even more pronounced for a 60:1 ratio, a shift towards open circular forms was apparent. The number of plectonemic and rod-like supercoiled forms decreased. Upon increasing the concentration of RdgC further, this tendency was reversed again. At 100:1 Rdgc/DNA ratio, almost all DNA existed as highly supercoiled, plectonemic shapes.

However, these plectonemic shapes showed a different appearance to the original, negatively supercoiled plectonemic shapes, as can be seen in figure 5.16. Here, a comparison of a representative supercoiled shape for native DNA and one for a 100:1 RdgC/DNA ratio is presented. Apart from the increased height of the DNA at the 100:1 ratio, due to bound protein, the original negatively supercoiled shape appears more regularly wound than the one at high RdgC concentration.

An initially increasing number of open circular and reducing number of plectonemic shapes, followed by an almost exclusive presence of plectonemic shapes for increasing RdgC concentrations, has been consistently observed in repeated experiments. Only the exact RdgC concentration at which the change in shape distribution occured appeared to vary slightly between experiments. We, however, explain this through a slight variation in the supplied concentrations of DNA.

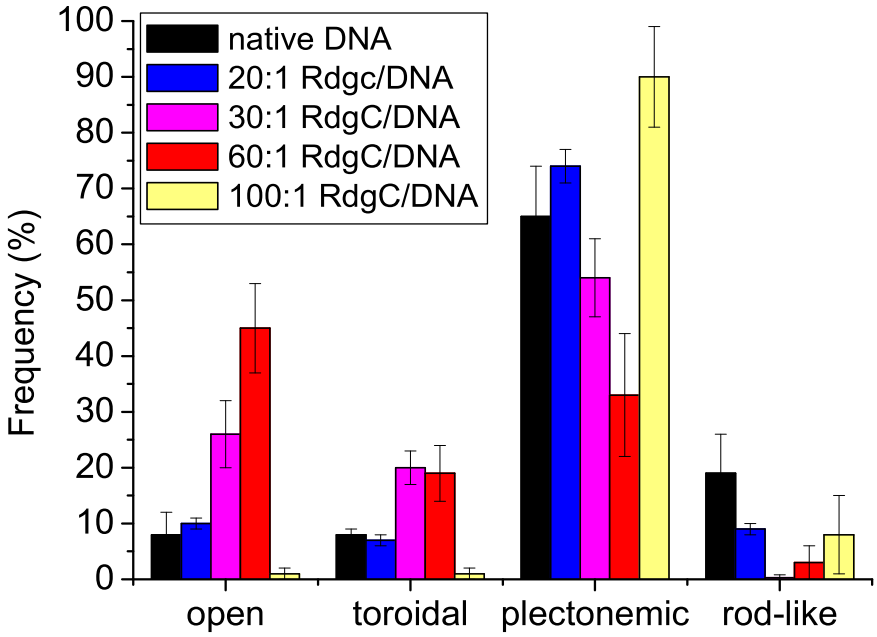

Figure 5.15: Effect of RdgC binding on DNA shapes. Observed DNA shapes have been grouped into 4 categories: open circular, toroidal, plectonemic, and rod-like shapes. The frequency of these is shown here for native 2686 bps *E. coli* plasmid DNA, and different RdgC/DNA ratios. In the absence of RdgC, the DNA is predominantly in the plectonemic supercoiled state. With increasing protein concentration, the number of open circular and toroidal supercoiled shapes grows while that of plectonemic and rod-like supercoiled forms decreases. At a protein/DNA ratio of 60:1 the open circular shape dominates above all other shapes. Upon increasing the concentration of RdgC further, this tendency is reversed again. At 100:1 Rdgc/DNA ratio, almost all DNA exists as plectonemic supercoiled shapes.

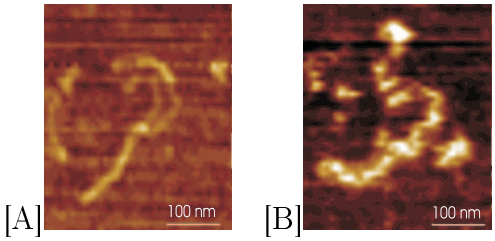

Figure 5.16: Comparison of plectonemic shapes found for (A) native DNA and (B) for an RdgC/DNA ratio of 100:1.

The results can be interpreted in terms of an unwinding of negatively supercoiled DNA in the presence of increasing concentrations of RdgC. Binding of RdgC to the DNA may induce the formation of open ring-like DNA structures, and upon further protein addition, wind the DNA further, producing positively supercoiled DNA, as schematically indicated in figure 5.17. This kind of transition from negative to positive supercoiling has previously been

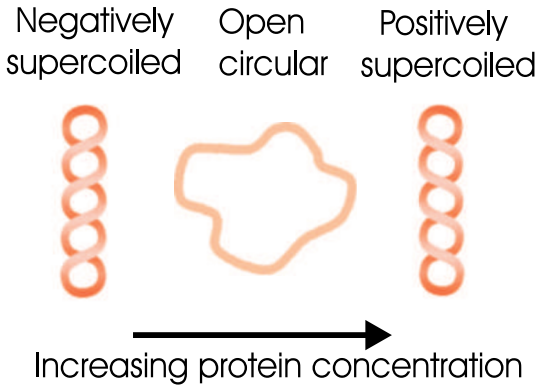

Figure 5.17: Proposed effect of RdgC on DNA supercoiling. The negatively supercoiled DNA may be unwound by the protein, to form open circular, tense structures. Upon increasing the protein concentration, the DNA then might get continuously wound until it adopts a positively supercoiled form.

observed for increasing ethidium bromide concentration, using sedimentation velocity, gel electrophoresis, and electron and atomic force microscopy [Crawford and Waring, 1967; Pulleyblank and Morgan, 1975; Bates and Maxwell, 1993; Pope et al., 2000]. The dissimilarity in appearance of the plectonemic shapes in native DNA and at the high RdgC concentration supports this interpretation, as it indicates different kinds of structures.

5.4.3 Effect on DNA length

Effects on DNA superstructure are often concomitant with changes in DNA contour length. As shown in chapter 4, effects of molecule binding on DNA contour length can provide information on the binding processes. The lengths of 29 (± 8 SD) molecules of linear DNA were measured at near native conditions, and at each of the protein/DNA ratios 1:1, 10:1, and 100:1. The resulting statistics are presented in figure 5.18.

In order to show the validity of the obtained results, we compared them with the theoretical contour length for physiological B-form DNA. Calculation of the contour length of B-form DNA of 1133 bps, as was employed in the experiments, renders a value of 383 nm, assuming a helical rise per base pair of 0.338 nm [Saenger, 1984]. In the experiments, the majority of DNA molecules can be expected to not be spread out entirely flat on the mica surface. Measured lengths will therefore vary. The maximum value of the length distribution was taken as the actual contour length of the molecule at the given condition. Using this approach, we obtain a value of 390 nm (± 10 % measurement inaccuracy) for the native DNA contour length from

the distribution displayed in figure 5.18. The experimental result therefore agrees reasonably well with the expected contour length of the DNA.

Gaussian fits to the obtained length distributions provided the average length values for each of the applied RdgC/DNA ratios. As can be seen from figure 5.18, changes in the average length correlated with those in the maximum length value for all applied conditions. The average length therefore served to quantify DNA length changes under increasing protein concentrations. From the distributions displayed in figure 5.18, an average length of 343 nm (± 25 nm) was found for native DNA. Errors were determined as the half width of the Gaussian curves. The measured average length of 353 nm (± 29 nm) for a protein/DNA ratio of 1:1 represents only a slightly higher value than that found in the absence of RdgC. For a protein/DNA ratio of 10:1, the DNA was, however, found to have an increased average length of 380 nm (± 13 nm). Upon application of a higher RdgC/DNA ratio (100:1), no further length increase in the DNA was found (379 nm ± 14 nm). These results suggest a contour length increase of DNA by approximately 10 % from native DNA to protein/DNA ratios of $\geqq$ 10:1. RdgC therefore appears to slightly stretch the DNA molecule upon binding.

The distributions in figure 5.18 clearly become narrower for higher protein/DNA ratios. The increased attraction between DNA complexed with RdgC and the mica surface, compared to native DNA, may cause more consistent and higher length values for the higher protein concentrations applied. This is consistent with the fact, that for higher protein/DNA ratios, we also found an increase in surface density of DNA molecules. This therefore may present an interfering effect for the measurement of length changes at increas-

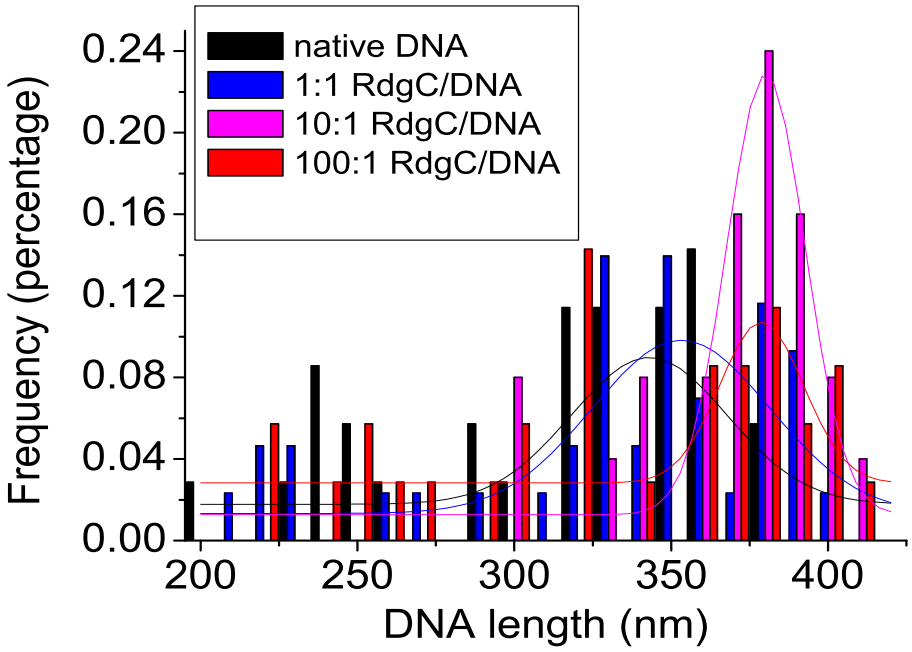

Figure 5.18: Distributions of DNA contour lengths, as measured from AFM images on 29 (± 8) molecules of linear DNA for different RdgC/DNA ratios (bin width of 10 nm). Also included are the Gaussian fits to each of the distributions.

ing protein concentration. It also has to be considered, that accurate length measurements become increasingly difficult for higher protein/DNA ratios, as the DNA strands are often densely populated with protein and also partly entangled. The found distribution of DNA lengths for a protein/DNA ratio of 100:1 showed however good consistency of the individual measurements, indicating comparable reliability to those at lower protein/DNA ratios.

Further, the effect of RdgC binding on DNA length was compared to that induced by ethidium bromide. Ethidium is an intercalating dye (see chapter 4). Its binding pushes adjacent DNA base pairs away from each

other, thus partially unwinding the helix. This increases the distance between base pairs by a factor of approximately 2, as has been previously determined by AFM measurements [Coury et al., 1996]. DNA contour length in the presence of ethidium bromide was measured for 21 molecule. A comparison of lengths for DNA complexed with RdgC and ethidium bromide is illustrated in figure 5.19. From the figure, similar length increases for an RdgC/DNA ratio of 10:1 and an ethidium bromide/DNA ratio of 1:1, can clearly be recognised. An average length of 375 nm ($\pm$ 15 nm) was found in the presence of ethidium bromide, form a Gaussian fit. The intercalator was therefore found to elongate the DNA by approximately 9 % at this ratio.

To appreciate the relative effect of RdgC protein on DNA length, the amount of molecules bound at these concentrations were taken into account. The binding site of ethidium spans 2 to 4 base pairs [Taquet et al., 1998]; and in saturation, 20 % of nucleotides are bound by dye molecules [Nordmeier, 1992]. In agarose gel electrophoresis assays on short DNA, RdgC has been found to require between 15 and 20 base pairs for binding, with a maximum occupancy of the entire DNA strand by protein [Moore, 2002]. From our data, only circa 0.3, 2 and 4 molecules of RdgC were found on average to be bound per DNA molecule for the protein/DNA ratios 1:1, 10:1, and 100:1 respectively. Therefore, the comparable increase in DNA length for RdgC and ethidium translates into a considerable effect per bound protein molecule. Results for other DNA-binding proteins have previously been found to give similarly large extensions of the DNA. For example, contour length increases by as much as a factor of 1.5 have been found for DNA complexed with the protein RecA [Stasiak et al., 1981].

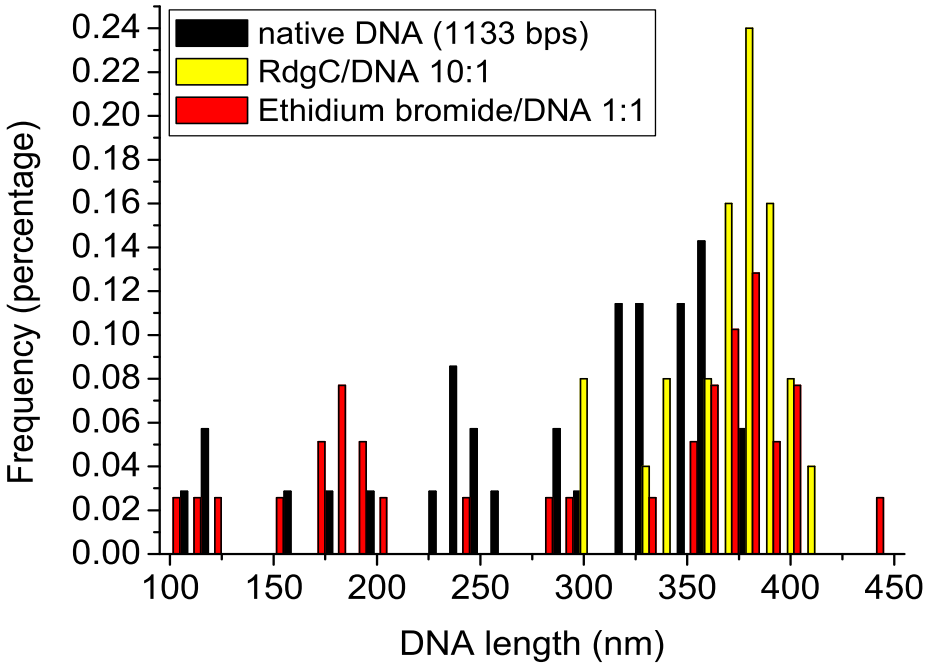

Figure 5.19: Comparison of RdgC induced length increase in DNA to that by the intercalator ethidium bromide (bin width of 10 nm).

RdgC binding was found here to increase the contour length of DNA. Although considerable measurement uncertainties have to be taken into account, a lengthening of the DNA by RdgC-binding agrees with the observed effect on DNA superstructure.

5.5 Conclusions

In this chapter, AFM imaging has been applied as a complimentary technique to molecular biology assays, to investigate the DNA binding behaviour

of RdgC protein, as well as any resultant changes in DNA structure. High resolution scans were obtained of linear DNA fragments with a series of different concentrations of RdgC deposited on mica. From these images, the protein positions along the DNA strands were identified for each RdgC/DNA ratio. This allowed an initial interpretation of the binding preferences of RdgC to DNA. DNA strand length and topology was investigated for the different protein concentrations using linear and circular plasmid DNA to detect possible changes in DNA geometry through RdgC binding. A statistical distribution of the observed shapes for the individual DNA molecules under the different conditions was obtained, to facilitate speculation on the working mechanism of RdgC.

From these experiments, we can conclude that RdgC appears to show an initial slight preference for binding at the ends of the linear dsDNA, compared to middle positions along the strands. RdgC binding of DNA was further found to not specifically target any DNA sequence.

More than 50 % of all RdgC binding positions were found to coincide with bends in the DNA molecules. It could however not unambiguously be distinguished from our data, whether bending was induced by the binding of the protein, or whether protein binding preferentially occurred at pre-existing bends in the DNA strands.

Bending of the DNA helix would suggest an effect of RdgC binding on DNA superstructure. We found, that binding of the protein to DNA appeared to unwind negatively supercoiled DNA, and to further wind the molecule strand upon increasing protein concentration, producing positively supercoiled DNA. Our data further suggested an increase in DNA contour length

compared to native DNA by approximately 10 % for protein/DNA ratios of 10:1. It may therefore be concluded, that RdgC binding unwinds negatively supercoiled DNA, while simultaneously increasing DNA contour length, as schematically shown in figure 5.20:

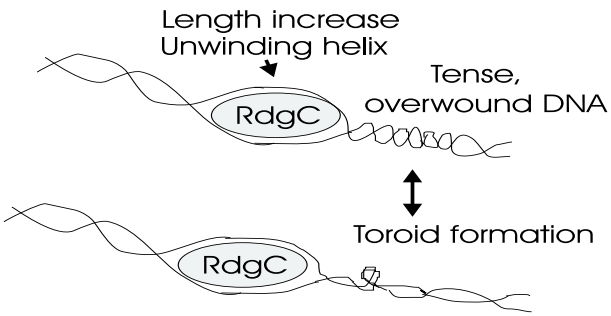

Figure 5.20: Schematic of proposed RdgC binding. The obtained data suggest, that the binding of the protein to DNA may locally unwind the DNA double-helix, as shown here. This would result in a compensatory overwound state of the DNA double-helix behind the protein binding position. In order to return to the energetically favoured B-form helix, the DNA double strand can adopt either plectonemic or toroidal superstructures. The formation of a toroid is shown here as an example.

The obtained results provide valuable information on the binding behaviour of RdgC. This information can serve to pinpoint biologists in the right direction, in order to determine the function of RdgC.

Chapter 6

Receptor-ligand interactions in the neutrophil system; a single cell study

Adhesion to proteins is an important property of human neutrophil polymorphonuclear granulocytes (neutrophils). It is essential for the diverse functions of these blood cells in immune defence. These range from penetration of blood vessel walls and migration to sites of tissue injury to the chemical attack and phagocytosis of invading particles [Isacke and Horton, 2000; Shappell and Smith, 1994]. In some cases, these processes can lead to unwanted inflammation due to accumulation of neutrophils at tissue sites, leading to pain and further tissue damage. Examples of this include rheumatoid arthritis and post-surgical reperfusion injury after strokes [Heinecke, 1999; Zweier, 1999]. Inhibition of neutrophil adhesion can therefore be of therapeutic interest.

Neutrophil Inhibitory Factor (NIF) was discovered and patented by the

pharmaceutical company Corvas International N.V. (San Diego, CA, USA) as a result of their search for anti-inflammatory agents. *In vitro*, NIF blocks neutrophil adhesion to various ligands. Pfizer Global Research and Development (Pfizer GR&D, Sandwich, UK) have recently obtained the rights to develop NIF as a potential drug, intended for the treatment of ischaemic stroke victims. Unfortunately, the clinical development of NIF for ischaemic stroke was discontinued after it failed to show efficacy in key Phase II studies. Although the compound is a potent inhibitor of neutrophil adhesion *in vitro*, this did not translate to clinical efficacy in this indication.

What causes a promising drug candidate such as NIF, that passed all *in vitro* tests successfully, to eventually be ineffective *in vivo*? To further our understanding of this, it is beneficial to probe the molecular basis of the underlying interactions. Established techniques for the measurement of cell adhesion are based on detecting the average behaviour of large cell systems. The individual underlying interactions are not resolved with these techniques. In the presented studies, we aimed at developing an assay for the study of cell receptor interactions at the single molecular level. Single molecule assays offer the advantage of being able to focus on individual receptor-ligand complexes, and follow changes in their behaviour upon drug addition [Benoit et al., 2000; Rigby-Singleton et al., 2002]. Varying the surrounding conditions may then help gain an insight into the interplay of interactions in the complex *in vivo* system. Such information is thus valuable for the understanding of processes causing, for example, failure of NIF to demonstrate clinical efficacy in stroke patients.

The study was in particular concerned with the effects of NIF on the

adhesion of human neutrophils to protein-coated surfaces. In the experiments presented, the protein albumin served as ligand for the receptor CD11b/CD18. Although the protein is not a physiological ligand of the receptor, CD11b/CD18-induced migration on and adhesion to albumin immobilised on surfaces has previously been established for neutrophils [Edwards, 1994; Rainger et al., 1997; Smith and Hollers, 1980; Anderson et al., 1986].

Different imaging and force measuring techniques were used to study the receptor-ligand interactions at the single cell level. Namely, confocal microscopy served to visualise and thus quantify neutrophil binding of protein-coated beads. Optical tweezers in combination with a CCD camera system also offered visual information. Furthermore, this technique provided access to crude information on adhesion force, using the laser trap to separate protein-coated beads from the surface of a neutrophil. Optical tweezers thus served as an intermediate technique between the purely imaging confocal microscopy and force measuring AFM experiments. In AFM studies, a large percentage of receptors were blocked using NIF. Such an approach allows the detection of single molecule interactions, by effectively reducing the number of available receptor binding sites on the surface. The study thus presents the development of a single molecule assay for the investigation of drug effects on cell-ligand interactions.

6.1 Neutrophil adhesion

Neutrophils are large white blood cells of approximately 12 μm diameter. They make up $\gtrapprox$ 60 % of all white blood cells in human blood, and are thus

abundantly available ($>$ 2 x 10^{10} cells in circulation [Gabrilovich, 1999]). Their half life of only 7 hours [Virella, 1999], however, makes them difficult cells to work with experimentally. Nevertheless, they have been (and are still) intensely studied experimentally due to their important role in immunological defence, and their interesting system of cell activation [Gabrilovich, 1999; English, 1999].

Very diverse neutrophil functions are mediated by receptors on the surface of the cells. For example, phagocytosis of specifically marked antigens and the production of toxic substances to attack pathogenic particles (intra- and extracellular) are induced by ligand binding to cell surface receptors. These processes form part of the neutrophil's effective warfare against invading organisms. In order to fight these particles, neutrophils are capable of migrating from blood circulation through the bordering vascular endothelium to the sites of infected tissue. For this to occur, initial adhesion of the cells to endothelium is required.

Adhesion of hemopoietic cells is mediated by surface receptors from three protein families, namely immunoglobulins, selectins, and integrins [Isacke and Horton, 2000]. Interactions of selectins on the surface of endothelial cells which line the blood vessel walls, with glycoproteins on neutrophil cell surfaces lead to a rolling movement of the neutrophils along the blood vessel walls. This causes them to slow down and eventually become prone to adhesion to the endothelium [Shappell and Smith, 1994; Isacke and Horton, 2000; Virella, 1999; Ley, 2002]. Adhesion to endothelial cells, however, is based on interactions of integrin receptors on the neutrophil surface with proteins on the endothelium surface [Virella, 1999].

Integrins form heterodimeric glycoprotein molecules that consist of an α and β subunit and function as transmembrane cell surface receptors [Isacke and Horton, 2000]. The integrin family can be further split into subfamilies. The molecules of each subfamily have a common β subunit, combined with different α subunits. So far, 19 different α and 8 different β subunits have been identified [Takagi and Springer, 2002]. Table 6.1 summarises the major subfamilies. Receptor distribution on different cell types, structure, function and ligand specificity vary between different subfamilies.

All integrin receptors require activation for ligand-binding. Activation can be induced by a range of chemotactic factors, which are chemical substances produced as a result of inflammation. They result in conformational changes of the heterodimer which lead to exposure of the ligand binding domain and a subsequent increase in ligand-affinity by almost four orders of magnitude [Shappell and Smith, 1994; Takagi and Springer, 2002]. Activation further affects the cell membrane structure [Virella, 1999] and increases the number of integrin receptors on the neutrophil surface (upregulation) [Virella, 1999; Shappell and Smith, 1994]. Activated neutrophils are able to adhere to and transmigrate through vascular endothelium [Furie et al., 1991], and further migrate along a gradient of chemotaxins to the site of invasion [Virella, 1999; Shappell and Smith, 1994; Francis et al., 1989]. Integrins therefore play an important role in neutrophil adhesion, leading to the cells' recruitment to sites of inflammation. Inhibition of integrin interactions thus presents a potential cure for inflammatory diseases, such as reperfusion injury or rheumatoid arthritis.

Figure 6.1 schematically shows the CD11b/CD18 integrin receptor, which

α subunit	β subunit	name (α/β)	function
α1-6	β1	VLA1-6/platelet gp IIa	cell-matrix and
α7-10	β1	-	intercellular interactions
α_L	β2	CD11a/CD18	immune functions
			intercellular adhesion
			cell aggregation
α_M	β2	CD11b/CD18	roles in inflammation
			adhesion to endothelium
			transmigrate endothelium
			aggregation
			chemotaxis
			apoptosis
			phagocytosis
α_X	β2	CD11c/CD18	receptor of tissue macrophages
			similar to CD11b/CD18
α_D	β2	CD11d/CD18	probably as other β2 integrins
α_V	β3	CD51/platelet gpIIIa	normal bone resorption
			angiogenesis
α_{IIb}	β3	CD41/platelet gpIIIa	platelet adhesion

Table 6.1: Integrin family of adhesion molecules: members of the major subfamilies (β-subunits 1-3), their (often multiple) names, and function [Isacke and Horton, 2000]. A total of 8 different β- and 19 different α-subunits, and 25 possible associations have been characterised to date [Takagi and Springer, 2002].

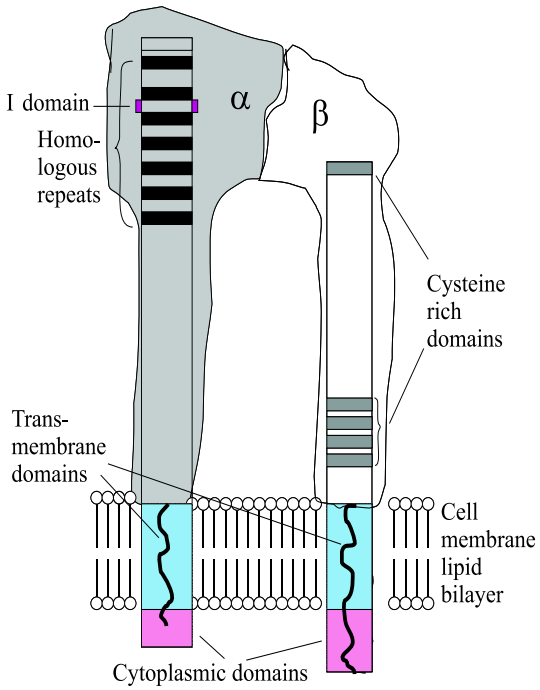

Figure 6.1: CD11b/CD18 integrin receptor, adapted from [Isacke and Horton, 2000]. α and β subunits are 170 and 95 kDa transmembrane glycoproteins. The α part of the receptor consists of a large N-terminal extracellular domain, a short transmembrane region, and a short, hydrophilic cytoplasmic tail. Its N-terminal region contains seven weakly homologous segments. Between the second and third of these segments, an inserted (I) domain of approximately 200 amino acids is positioned, which is involved in ligand binding. The β subunit has a short cytoplasmic tail, which contains potential glycosylation sites for signal transduction. The β subunit further possesses areas of high cysteine content, one at its N-terminal end and one in the C-terminal region (grouped into four segments). Interaction between the two areas supports the inactivated configuration of the receptor, in which the I domain on the α subunit is bent towards the cell surface and thus is difficult to access by ligands.

this particular study is concerned with. The receptor of the $\beta 2$ subfamily is the major adhesion glycoprotein on neutrophils [Isacke and Horton, 2000; Shappell and Smith, 1994]. It provides the binding site for the neutrophil adhesion inhibitor NIF [Moyle et al., 1994].

6.2 Neutrophil inhibitory factor (NIF)

NIF was first isolated from the canine hookworm *Ancylostoma caninum*, as a 41 kDa glycoprotein [Moyle et al., 1994]. It has since been found to be also produced by other hookworms, and can be artificially expressed in yeast vectors [Moyle et al., 1994]. NIF has an estimated molecular weight range of 33 to 66 kDa, due to differing degrees of glycosylation of the polypeptide [Perry, 2000].

In vitro, NIF has been shown to inhibit neutrophil adhesion to various ligands including adhesion to endothelial cells [Moyle et al., 1994]. Muchowski et al. [1994] found that NIF binds specifically to the I domain of the α-subunit of CD11b/CD18 integrin receptors. This was further confirmed by the prevention of NIF binding to the receptor molecules in the presence of a monoclonal antibody against the CD11b I domain [Rieu et al., 1994]. Whereas most I domain ligands bind in an activation-dependent manner, NIF-binding to CD11/CD18 integrins was found to not require receptor stimulation [Rieu et al., 1994; Perry, 2000].

To determine the effect of NIF on the adhesion properties of CD11b/CD18 receptors *in vitro*, Pfizer GR&D were employing a potency assay based on a previously described latex bead binding assay [Smith and Hollers, 1980].

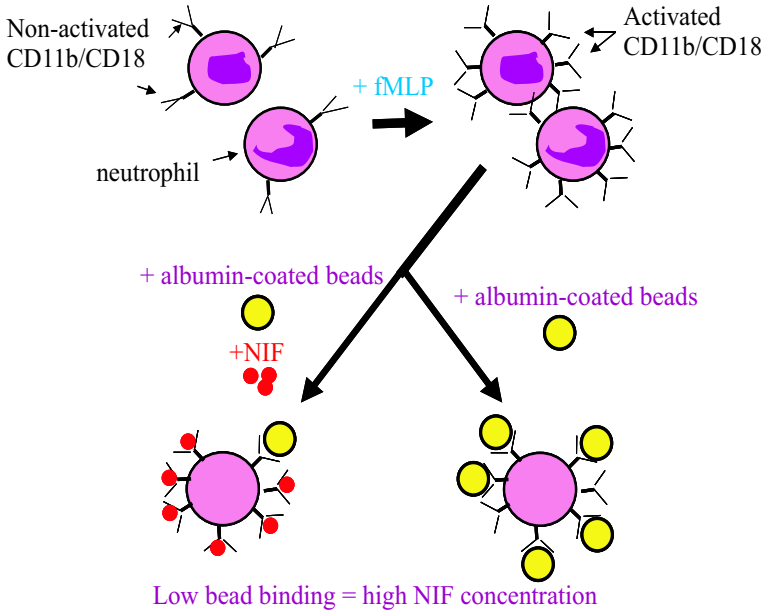

Figure 6.2: Neutrophil adhesion assay [Pfizer GR&D, 2002]. Neutrophils are activated by addition of fMLP, which up-regulates the number of and causes structural changes in CD11b/CD18 receptors. Albumin coated beads are then supplied to the neutrophil solution, and bind to the cell surfaces. In the presence of NIF, which binds specifically to the receptors, less binding sites are available for bead binding. The total number of cell-bound beads is therefore correlated to NIF concentration.

The assay is shown schematically in figure 6.2. Flow cytometry was used to determine the total amount of beads bound to neutrophils in the presence of increasing concentrations of NIF. From this, the average degree of adhesion blocking was obtained for each NIF concentration. Ensemble properties of the researched system, i.e. the collective behaviour of many cells and receptor molecules in the presence of the drug molecules could thus be studied with this method.

The aforementioned problems of NIF applicability found in the *in vivo*

system, can however not be explained from results obtained using such ensemble studies. A deeper understanding of the molecular basis of NIF function will be vital for the correct prediction of adhesion processes. Direct determination of interactions between cell receptor and ligand molecules in single molecule experiments may allow the refinement of models that describe cell adhesion [Pierres et al., 1998]. To this end, different cell systems have recently been investigated in single molecule experiments using for example optical tweezers [Thoumine et al., 2000] and AFM [Benoit et al., 2000; Zhang et al., 2002]. Here, complementary information on NIF effects on neutrophil adhesion to that obtained in flow cytometry ensemble measurements, was obtained using both optical tweezers and AFM. Furthermore, fluorescence confocal microscopy was employed to visualise quantitative NIF effects on neutrophil binding.

6.3 Materials and methods

The different employed experimental techniques afforded slightly different sample preparation procedures. These are therefore described separately within the section on experimental methods. Common to all approaches however, was the requirement of neutrophils.

6.3.1 Neutrophil sample preparation

Neutrophil preparation can be separated into two parts: the isolation of the cells from freshly acquired human venous blood, and their further processing for experimental sample preparation.

Neutrophil isolation from whole blood

Due to their short lifetime, the cells were isolated from human whole blood immediately prior to every experiment. Directly after venepuncture, 45 ml of blood was dispensed into a 50 ml polypropylene centrifuge tube containing 5 ml of a 3.8 % (w/v) solution of sodium citrate anticoagulant (Sigma-Aldrich Company Ltd.). The tube was mixed by hand inversion.

Portions of 10 ml of this were added into 5 polypropylene centrifuge tubes (15 ml volume) with 4ml of 6 % dextran (industrial grade, average molecular weight 148,000 Da; Sigma-Aldrich Company Ltd.) in Hanks buffered saline solution (HBSS, pH 7.1; Sigma-Aldrich Company Ltd.). Again the tubes were mixed by gentle hand inversion. The dextran solution was prepared fresh the day before cell isolation, and kept at room temperature over night. The blood-dextran mixture was then left to stand at room temperature for 45 minutes, to allow sedimentation of the red blood cells.

10 ml of gradient medium, Histopaque-1077 (Sigma-Aldrich Company Ltd.) was measured into two 50 ml polypropylene centrifuge tubes. After the 45 minutes incubation time, the supernatant containing the white blood cells was carefully aspired by a polypropylene Pasteur pipette. 10 ml of this was overlaid on the cushions formed by the gradient medium.

The tubes were then centrifuged in a Beckman Avanti 30 centrifuge (Beckman Coulter Inc., Fullerton, CA, USA) at 400 g for 35 minutes at room temperature. The supernatant would contain mononuclear cells, and was removed using a polypropylene Pasteur pipette. The neutrophil pellet was resuspended in $\approx$ 300 μl of remaining supernatant by gently shaking the

tubes by hand.

10 ml of ice-cold deionised water (purified to 18.2 MΩcm resistivity in Elga Maxima system; Elga Ltd.) was added and the tubes left to incubate for 45 seconds to lyse any remaining contaminating red blood cells. After this time, the immediate addition of 10 ml ice-cold phosphate buffered saline (PBS; 10 mM phosphate buffer, 2.7 mM potassium chloride, 137 mM sodium chloride, pH 7.4; Sigma-Aldrich Company Ltd.) served to restore osmolarity.

The two tubes were then pooled into one and centrifuged at 200 g for 10 minutes at 4°C. Supernatant was carefully removed, and the generated pellet gently resuspended in 2 ml of ice-cold HBSS buffer. The neutrophil suspension was then put on ice immediately.

Using this method, 100 to 200 million neutrophil cells/ml are generally expected to be gained from 50 ml whole blood. A viability count was performed to determine the number of neutrophils per ml. The employed test is based on the ability of viable cells to resist the uptake of 0.4 % Tripan Blue (Sigma-Aldrich Company Ltd.). An improved Neubauer counting chamber with depth 0.1 mm and area 1/400 mm^2 (Weber Scientific International Ltd., Teddington, Middlesex, UK) was used for cell counting. Cells that appeared blue (and often misshaped) could be easily distinguished as non-viable from healthy, round cells, which were yellow and semitransparent. In our neutrophil isolation process there were generally between 3 and 20 million cells retrieved per ml. The reason for the low efficiency is unclear. The number of cells was however sufficient for the presented experimental requirements.

Neutrophil sample preparation

Experiments were conducted as soon as possible after cell isolation, since the cells only have a half-life of 7 hours [Virella, 1999]. For all AFM and optical tweezers experiments, the required amount of original neutrophil cell solution was diluted with HBSS buffer to a working concentration of approximately 4 million cells per milliliter. The remaining cells were kept on ice at the higher cell concentration, to avoid cell clumping.

Neutrophil integrin receptors require stimulation by an activator in order to recognise and bind their ligands. Activation is believed to both upregulate the number of receptors presented on the cell surface and change their conformation [Arnaout et al., 1984; Todd et al., 1984; Dransfield and Hogg, 1989]. *In vivo*, this activation is supplied by a gradient of chemotaxins, which also directs the cells to the site of tissue injury [English, 1999; Rothlein and Scharschmidt, 1994]. In the experiments presented, a chemoactive peptide of bacterial origin, N-formyl-methionyl-leucyl-phenylalanine (fMLP; Sigma-Aldrich Company Ltd.), was used to stimulate neutrophil adhesion. fMLP has been shown to increase neutrophil adhesion to monolayers of different cell types as well as protein coated surfaces [Smith and Hollers, 1980; Tonnesen, Smedley and Henson, 1984; Chang et al., 1999]. In our experiments, fMLP was added to the working concentration cell solution immediately prior to experimental sample preparation. The required amount was calculated for each individual cell solution volume, equivalent to 900 μl of 10^{-5} M fMLP in 45 ml of whole blood.

6.3.2 Experimental techniques

The combination of the three experimental approaches, confocal microscopy, optical tweezers, and AFM, was exploited to gain a more complete picture of the observed processes.

Confocal Microscopy

Experiments with this imaging technique were based on neutrophil binding of albumin coated latex beads, as previously employed to investigate adhesive behaviour of neutrophils [Smith and Hollers, 1980; Anderson et al., 1986]. Whereas the coating of latex beads with albumin was found to inhibit bead binding and phagocytosis by unstimulated neutrophils [Beukers et al., 1978], cells that were stimulated with chemotactic factors such as fMLP exhibited an increased degree of binding of the beads [Smith and Hollers, 1980]. In the presented experiments, albumin (human serum albumin, HSA) coated polystyrene-latex beads were added to a solution of activated neutrophils. Further, different concentrations of the neutrophil adhesion inhibitor NIF were applied. The quantity of bead attachment to the cells was determined under the confocal microscope.

Sample preparation (confocal microscopy)

Fluorescently labelled beads of 1 μm diameter were provided by Pfizer RG&D. The fluorescein dye molecules on their surfaces allowed for the beads to be conveniently located with the confocal microscope. The beads were coated with HSA (Sigma-Aldrich Company Ltd.), following the protocol for the es-

tablished adhesion assay described in figure 6.2. Briefly, beads were washed three times in PBS in a volume ratio of 1:2 bead to buffer solution. Washing involved 30 seconds vortex mixing of buffer and beads, centrifuging for 5 minutes at 13,000 rounds per minute (rpm) with a microcentrifuge (MicroCentaur, MSE, Sanyo Gallenkamp PLC, Loughborough, UK), and then removing the supernatant. For a further wash step the formed bead pellet was redissolved with PBS buffer (same volume as before). The beads were then incubated for 10 minutes at ambient temperature in a 10 mg/ml HSA solution (in dH_2O, purified in Elga Maxima system (Elga Ltd.) to 18.2 MΩcm resistivity) at a volume ratio of 1:2 (original bead solution to HSA solution). After incubation, an equal amount of buffer solution was added (ratio 1:2 original bead solution to buffer solution). The mixture was then vortex mixed for 30 seconds and again washed four times. The albumin coated beads were finally diluted to a 0.4 % (v/v) solution in PBS, and stored at 4°C for up to a maximum of 10 hours.

For the experiments, mixtures of activated neutrophils and beads were incubated for 10 minutes with different concentrations of NIF. After this, samples were centrifuged for 1 minute with the microcentrifuge at 13,000 rpm. The resulting pellet then contained the formed neutrophil/bead complexes, the supernatant the remaining unbound beads. The pellet was redissolved in 90 μl HBSS buffer solution for preparation of the experimental sample cell. Centrifugation thus served to remove the large percentage of unbound beads from the solution, which disturbed sample imaging. An increasing effect of centrifugation on cell adhesion has, however, been observed with strong dependence on cell type, and centrifugation speed and time [Milam

et al., 1973]. This factor is thus taken into account when comparing the result from this technique with results from optical tweezers and AFM, which did not involve a centrifugation step during sample preparation.

50 μl of this solution was pipetted onto a glass cover slip (22 x 22 mm^2, size 1.5; Chance Propper Ltd.), the edges of which were thinly covered with silicon grease. A static liquid sample cell was made up between the cover slip and a micrsocope slide (76 x 26 x 1.0-1.2 mm^3; BDH laboratory supplies). The grease provided both the seal and the spacing for the sample cell formed between the cover slip and microscope slide. Sealing prevents the samples from drying out too quickly; spacing is necessary so that cells are not squeezed between the two surfaces. This technique gives sample cell dimensions of circa 200 μm depth and 20 x 20 mm^2 area.

Experiment (confocal microscopy)

Confocal microscopy is a technique that enables the acquisition of high resolution images of relatively thick samples [White et al., 1987]. To achieve this, the information collected in each 2D image is restricted to a single layer through the sample. This further offers the possibility of acquiring 3D images by re-assembling the images through the separate layers. In contrast to conventional light microscopy, extended focus images of thick slices through the sample are thus possible at consistently high resolution.

A tunable laser serves to illuminate the sample. The technique utilises pinhole constructions to produce a point source and point detector. As illustrated in figure 6.3, this leads to selective imaging in the specific sample plane in focus by blocking out information from all other planes. The point

detector is scanned over the sample (using mirror scanners) to achieve a full image of the sample plane. The small dimension of the light source in the focal plane also causes minimal stray light, increasing image resolution.

The diameter of the pinhole and the numerical aperture of the objective, which serves to focus the light onto the sample, determine the maximal focal depth. To a lesser extent the wavelength of the laser light also affects the precise depth of the focal plane. The pinhole diameter is limited to a size above which loss of the confocal effect occurs.

The laser light excites fluorescence in the sample at different wavelengths. Simultaneous detection of fluorescence of different wavelengths from the sample and of backscattered light from the focal plane through the sample produces the image. The detector consists of a photomultiplier, which is selectively sensitive within a wide range of the electromagnetic spectrum. The output signals are converted via an analog to digital converter, to be displayed and further processed using PC software.

The independently sampled information allows 3D visualisation of the sample from all directions. This was exploited in the described experiments, to determine the exact position of fluorescently labelled HSA coated beads with respect to neutrophil surfaces.

For the acquired images, cells were visualised using the scattered, reflected laser light detected at 470 nm to 500 nm. Beads were detected from their strong fluorescence signals at 500 nm to 550 nm. For both, fluorescence and reflectance signals, an excitation laser wavelength of 488 nm was employed. Between 19 and 75 cells were investigated for each of the applied concentrations of 0, 5 x 10^{-15}, 7 x 10^{-15}, 1 x 10^{-14}, and 2 x 10^{-14} mol NIF/cell.

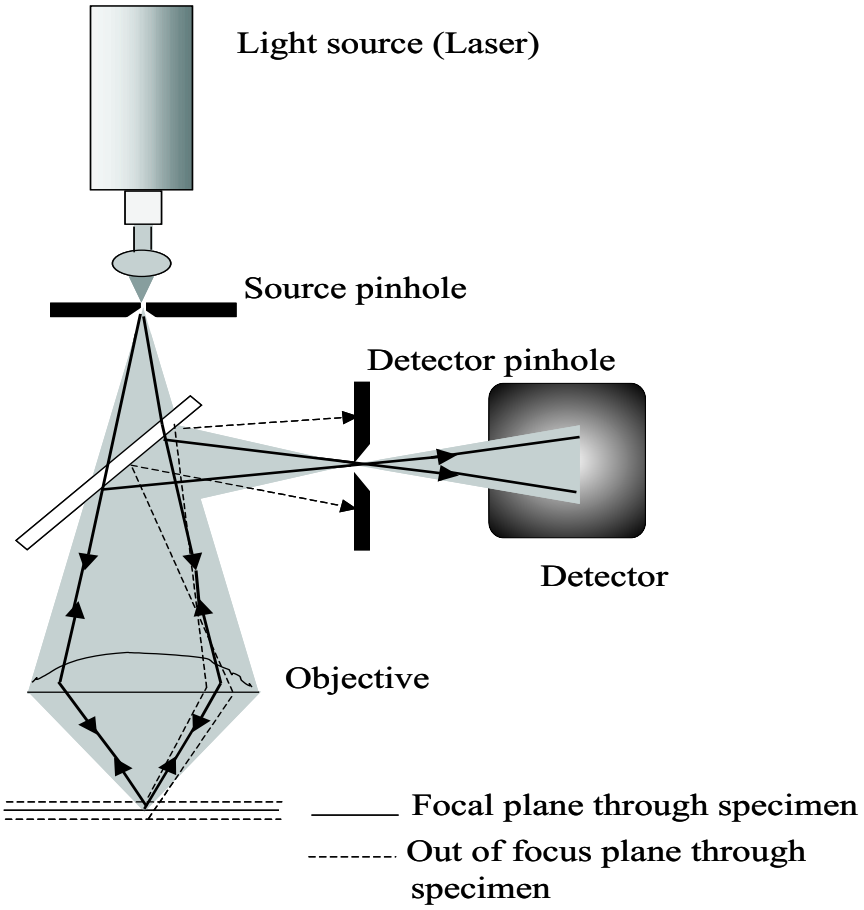

Figure 6.3: Schematic of confocal microscope, adapted from [Ladic, 1995].

Optical Tweezers

In the optical tweezers experiments, HSA coated plastic beads were detached from neutrophil cell surfaces using the optical trap in the axial direction. The percentage of beads that could be separated from cells served to quantify bead/cell adhesion.

Sample preparation (optical tweezers)

Polystyrene-latex beads of a larger diameter (2 μm) than in the confocal microscopy experiments (1 μm) were chosen here, due to their improved visibility with the optical light microscope and the CCD camera. 1 μm diameter beads resembled structures on the cell surfaces and could therefore not easily be differentiated from the granular cell appearance. The 2 μm beads were supplied carboxylated and with a diameter standard deviation of $\pm$ 0.16 μm from Sigma-Aldrich.

The beads were coated with HSA, as described above in the sample preparation for confocal microscopy experiments. In the optical tweezers experiments, the neutrophil cells were required to adhere well to a glass surface, in order to resist detachment by the optical trap. A qualitative comparison of activated neutrophils on non-coated and HSA coated glass showed a larger percentage of cells being solidly attached to the coated than to the non-coated surfaces. Therefore, glass surfaces for the optical tweezers experiments were coated with HSA. For this, glass cover slips were cleaned in an isopropanol bath and blow dried in pressurised nitrogen. They were then incubated over night at 4°C in 500 μl of a 1 mg/ml HSA solution (in PBS) each, to allow protein physisorption to the glass surfaces. After incubation, they were rinsed with 10 ml PBS, to remove excess protein.

10^{-5} M fMLP was added to 50 μl of working cell solution (4 million cells/ml). The exact amount of fMLP required was calculated for each neutrophil solution according to the concentration of isolated cells. The mixture was vortexed briefly (10 seconds) to assist homogeneous mixing. The ac-

tivated cell solution was applied to a HSA coated glass cover slip surface, and left to incubate at ambient temperature for 10 minutes. This served to achieve cell adhesion to the glass surface before blocking by NIF.

30 μl of the required NIF concentration was then added, as well as 4 μl of a 0.4 % (v/v) solution of HSA coated beads. Care was taken to ensure that the beads were evenly distributed over the cell solution with a micropipette. The sample mixtures contained 200,000 cells, 20 beads per cell, and varying NIF concentrations (0, 10^{-15}, 10^{-14} mol/cell). To achieve a higher NIF concentration, 10^{-13} mol/cell, a larger volume of NIF solution had to be applied. The number of cells in this sample was reduced to 100,000, in order to keep the overall sample volume close to the 92 μl of the other samples (121 μl). The mixtures were incubated on the cover slip surfaces for 45 minutes at 37°C in an incubation chamber (Amersham Biosciences UK Ltd., Little Chalfont, Buckinghamshire, UK).

Experiment (optical tweezers)

For the optical tweezers experiments, static liquid sample cells were made up, as described for confocal microscopy experiments, between a protein coated cover slip and a microscope glass slide. The liquid sample cell was placed on the object table of the optical tweezers microscope. Using a combination of the eye pieces and the CCD camera image, a bead on the surface of a neutrophil was brought into focus, and the optical trap then switched on. The laser diode current was kept constant, resulting in a constant trapping power of 3 mW ($\pm$ 10 %), as determined using the calibration graphs of figures 3.5 to 3.7 in chapter 3. The trap was slowly moved away from the

cell surface, resulting in detachment from the cell, for only weakly bound (or unbound) beads. A schematic of the experimental set-up is shown in figure 6.4.

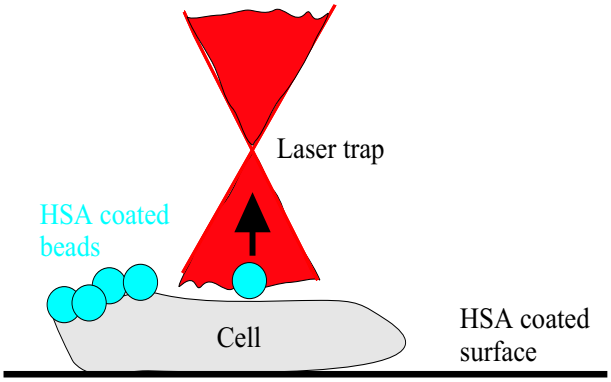

Figure 6.4: Optical tweezers experimental set-up for measuring neutrophil adhesion.

The number of receptor-ligand interactions formed between the HSA molecules on the bead and the receptors on the cell surface was assumed to be inversely proportional to the ease of bead detachment. The percentage of bead detachment events thus reflects the amount of adhesion events.

Experiments were carried out in the presence of different concentrations of NIF, to determine the effect of NIF binding on neutrophil adhesion. Between 12 and 56 single beads on cell surfaces were tested for each of the different conditions (0, 10^{-15}, 10^{-14}, and 10^{-13} mol NIF/cell). Experiments were repeated up to 3 times for the different conditions, to observe variations between individual experiments. The results were, however, found to be consistent, demonstrating good experimental reproducibility. This is reflected by the small standard deviations in the results (see table 6.3).

AFM force-distance experiments

AFM in its force-distance mode was employed to measure adhesion between neutrophil cell surfaces and albumin molecules. For this, cells were immobilised on a protein coated glass surface. A HSA coated AFM tip was then brought into contact with a neutrophil surface. The rupture forces measured upon tip retract were recorded and give the distribution of interaction forces. These are plotted in frequency histograms. Different concentrations of the CD11b/CD18 integrin inhibitor NIF were applied and the effect on the measured interaction force and frequency observed.

Sample preparation (AFM)

HSA was covalently bound to the surface of AFM cantilever tips (NP tips; Veeco Metrology Systems, Santa Barbara, CA, USA). The preparation process has been reported previously by Allen et al. [1997], and is based on a method for protein-coating of silicon and silicon containing surfaces that was first introduced by Vinckier et al. [1995].

For the AFM adhesion experiments, neutrophils were required to be immobilised on a glass surface. To enhance neutrophil attachment to the surfaces, cover slip surfaces were coated with HSA by physisorption, following the procedure described in the section on optical tweezers sample preparation, but with a 10-fold concentration of HSA to ensure maximum protein surface coverage. In the AFM experiments, strong attachment of neutrophils to the glass surface was particularly important, to prevent cells from sticking to and contaminating the AFM tip.

Prior to applying neutrophil solution to the protein coated glass surfaces, the cells were activated with fMLP. 10^{-5} M fMLP was added to a solution of freshly isolated neutrophils. Gentle vortex mixing ensured a homogeneous distribution of the activator. The mixture was incubated on ice for 10 minutes, and subsequently diluted to a concentration of approximately 2 million cells/ml. 600 μl of the mixture was applied to the HSA coated cover slip surface and incubated for 10 minutes at ambient temperature to allow for the cells to attach to the surface.

The required concentration of NIF was then added. Ratios of between 10^{-17} and 10^{-13} mol NIF/cell were applied. Samples were incubated for 45 minutes either at 37°C in an incubation chamber (Amersham Biosciences UK Ltd.) or at ambient temperature. Incubation at 37°C was intended to provide near physiological conditions for NIF binding, whereas incubating the system at ambient temperature served to identify effects of temperature on the binding of NIF. Immediately prior to the AFM experiment, excess cells were gently washed off the glass surface with filtered HBSS buffer.

Experiment (AFM)

Experiments were performed with a Molecular Force Probe (MFP) AFM (Asylum Research, Santa Barbara, CA, USA), using Igor Pro software (Wavemetrics, Lake Oswego, OR, USA). Knowledge of the AFM cantilever spring constant is essential for the force measuring function of the AFM, as discussed in chapter 2. This was calibrated for each HSA functionalised AFM tip prior to the experiment from the cantilever's thermal distribution spectrum [Hutter and Bechhoefer, 1993].

A custom-built CCD camera allowed the identification of cells on the glass surface, and positioning of the AFM tip directly above a cell. The cantilever was then repeatedly approached to the cell surface and retracted, each time measuring the force and distance, at which the (often multiple) attachment(s) between tip and cell broke. Such rupture events were identified from the recorded force curves, by the jumping back of the cantilever into its free level position. Figure 6.5 gives a schematic of the applied experimental set-up.

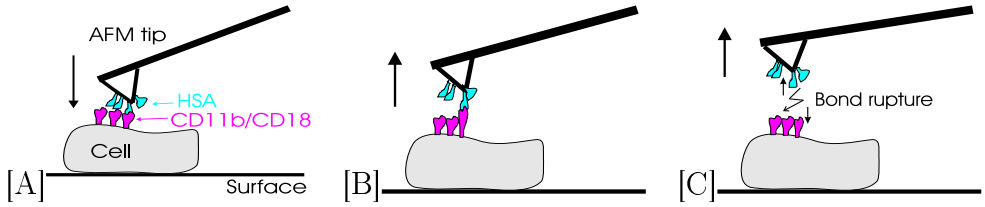

Figure 6.5: AFM experimental set-up for measuring neutrophil adhesion. The AFM tip is functionalised with HSA, which serves as a ligand for the neutrophil cell surface receptor CD11b/CD18. The cells are immobilised on a substrate surface. (A) Upon tip-cell contact, bonds are formed between receptor and ligand molecules. The tip is then retracted from the surface (B), until bond rupture occurs (C).

The coating of each, surface and AFM tip, was checked prior to experiment. For this, a range of force-distance measurements were taken with the HSA coated tip on $\geqq 4$ different positions of a HSA coated glass surface, before application of the cell solution to the surface. A representative force curve is shown in figure 6.6. Complete lack of adhesion is apparent from the curve, in which approach and retract paths are identical. Minimal adhesion indicated complete HSA coverage of both tip and glass cover slip surface.

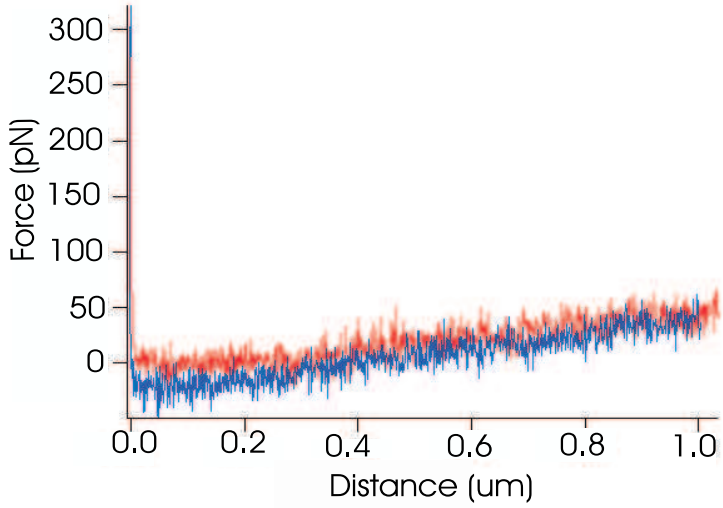

Figure 6.6: Negative control to AFM neutrophil adhesion experiments: force distance curve on HSA coated AFM tip and HSA coated surface.

Force curves were then recorded on 3 to 14 different cells for each condition, with 10 to 54 measurements per cell. Further, to avoid local effects, measurements were performed at various cell surface positions.

6.4 Results and discussion

Results on CD11b/CD18 receptor mediated neutrophil adhesion to protein coated surfaces were obtained at the single cell level using both imaging and force probing techniques. Based on the neutrophil adhesion assay introduced in figure 6.2, HSA coated probes were employed here to investigate neutrophil adhesiveness in different concentrations of NIF. Three different techniques, namely confocal microscopy, optical tweezers, and AFM, were used to obtain complementary data. For each of the different approaches, the concentration

of NIF for which maximum blocking of neutrophil adhesion was achieved, as well as the intermediate NIF concentration for which adhesion was reduced to 50 % of NIF-free adhesion (termed the IC50 concentration) were determined. For improved clarity, before any comparisons are made, the results for each technique will be presented in the following text separately.

6.4.1 Confocal microscopy

Fluorescence confocal microscopy was employed to acquire images of neutrophils and fluorescently labeled HSA coated beads, in the absence and presence of NIF. From the images, the amount of beads attached to a number of individual cells was determined for each of the employed NIF concentrations. This technique allowed direct visualisation of the fluorescently labelled, HSA coated beads on the neutrophil cell surfaces. Confocal microscopy further enabled the assembly of complete 3D views of imaged objects from the obtained data. This facilitated determination of the exact bead position with respect to the cell surfaces, allowing differentiation between beads on the substrate surface below a cell and beads on the cell surface. In figure 6.7A, this is demonstrated. The figure shows a representative image of neutrophils (in red) under near native conditions (in HBSS buffer), attached to a glass surface. Fluorescently labelled beads can be seen (in green) both attached to neutrophil cell surfaces and randomly distributed on the substrate surface. At the right and bottom of the image, vertical cross-sections along lines (shown in pink) through the sample are shown. It can be seen from the figure, that the beads appeared to be arranged inhomogeneously in clusters

on the cell surfaces. This is consistent with the previously reported optimisation of neutrophil adhesion by clustering of CD11b/CD18 receptors on neutrophil cell surfaces [Detmers et al., 1987]. Figure 6.7B shows an image of neutrophils in a high concentration of NIF (10^{-14} mol/cell). Comparison of the two images (A and B) shows a clear reduction of the number of beads bound to cells for the NIF containing sample.

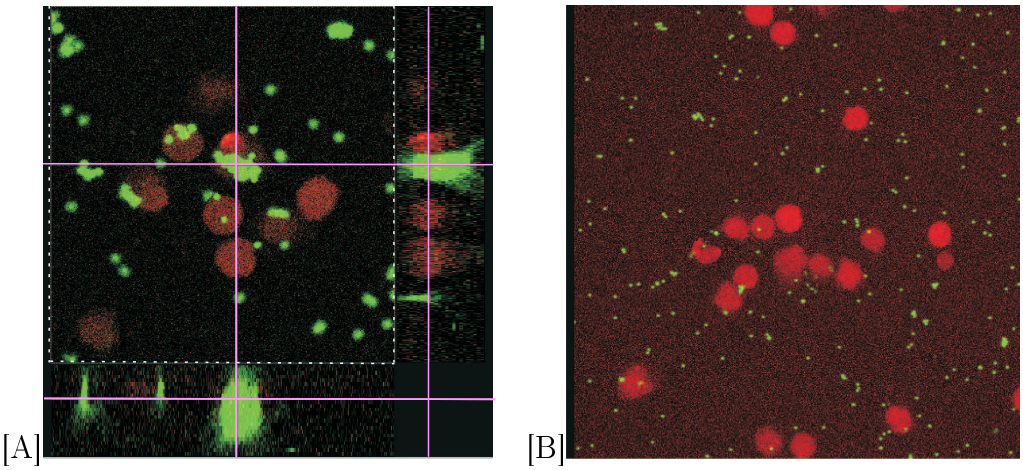

Figure 6.7: Neutrophil adhesion probed with confocal microscopy: (A) no NIF, (B) maximum applied NIF concentration (10^{-14} mol/cell). In (A), pink lines indicate the positions of the cross sections shown at the right and bottom of the image. The images are approximately 80 μm x 80 μm (A), and 160 μm x 160 μm (B).

From the obtained images, both the percentage of bead-carrying cells and the average number of beads bound per cell were determined for different concentrations of NIF. The results are presented in table 6.2. As can be seen, a reduction in the number of cells with beads attached from an average of 77 % for samples in NIF free buffer to 27 % in the maximum applied NIF concentration (3 x 10^{-14} mol NIF/cell) was found. The remaining adhesion

NIF (mol/cell)	**bead-carrying cells (%)**	**beads per cell**
0	77 (± 18 SD)	8.5 (± 3.5)
0.4 x 10^{-14}	54 (± 12)	2.1 (± 0.9)
0.6 x 10^{-14}	49 (± 11)	0.24 (± 0.10)
0.8 x 10^{-14}	47 (± 11)	0.47 (± 0.19)
3 x 10^{-14}	27 (± 6)	0.44 (± 0.18)

Table 6.2: Average percentage of bead-carrying neutrophils and number of beads bound per cell for increasing concentrations of NIF, studied by confocal microscopy. Error margins given in brackets are based on the standard deviations of results obtained for different samples at NIF free conditions (23 % and 41 % for the percentage of cells that show beads bound to their surfaces and for the number of beads per cell respectively).

between the HSA coated beads and the cells still apparent for high concentrations of NIF was the minimum adhesion achievable in our experiments, and remained constant at higher concentrations. It was ascribed to non-specific interactions between bead and cell surfaces. This result is in reasonable agreement with previous findings for maximal NIF inhibition of neutrophil adhesion to endothelial cell monolayer surfaces. Barnard et al. and Moyle et al. reported a reduction from approximately 800 adherent neutrophils to 200, and from 80 % to $>$ 10 %, respectively, using a microtiter plate adhesion assay [Barnard et al., 1995; Moyle et al., 1994]. A similar value of minimum adhesion ($\approx$ 20 %) was also obtained from ensemble measurements using the HSA coated bead assay [Pfizer GR&D, 2002].

Setting the average number of beads bound per neutrophil to 100 % (8.5 beads per cell) for NIF free samples, at 0.4 x 10^{-14} mol NIF/cell only approximately 25 % of the original number of beads were found on cell surfaces. At $\geqq$ 0.6 x 10^{-14} mol NIF/cell only 3 to 6 % remained. The bead number per cell therefore showed a much more rapid decrease than the percentage of bead-carrying cells, which required higher NIF concentrations ($\gtrapprox$ 3 x 10^{-14} mol/cell) for reduction to the minimum measured level. The discrepancy in concentration dependence between the two parameters may be explained by the relatively high level of background non-specific binding events (27 % remaining adhesion), leading to the random attachment of small numbers of beads (1 to 2) to cells.

From the average number of beads per cell for increasing NIF concentrations, as shown in table 6.2, the total blocking concentration was found to be around 6 x 10^{-15} mol NIF/cell. The IC50 concentration of NIF in the confocal microscopy experiments was determined as the concentration at which the number of beads per cell was reduced by 50 %, and was found to be $\approx 10^{-15}$ mol/cell.

6.4.2 Optical tweezers

While confocal microscopy can give information on adhesion frequency, effects of NIF on the strength of the adhesive interactions are inaccessible with such optical techniques. Therefore, the optical tweezers system presented in chapter 3 was employed to investigate adhesion strength between single HSA coated beads and neutrophil cell surfaces in the presence of increasing

concentrations of NIF. For these experiments, neutrophils were incubated with HSA coated beads. The cells were then attached to a substrate surface of a liquid sample cell. The optical trap was used to pull attached beads off neutrophil surfaces (see figure 6.5). The laser trapping power was kept constant. Further, the trap distances from the surface were kept approximately the same for each of the experiments. This ensured that the force with which the beads were pulled from the cell, using the optical trap, was approximately the same each time.

A bead, that could be detached from a neutrophil surface was classed as separable from the cell. Such a bead would have been bound weakly or not at all by the cell surface, whereby a proportionality between the number of formed receptor-ligand bonds and bead-cell adhesion strength was assumed. We were therefore using the percentage of separable beads as an indicator for neutrophil adhesion to the protein coated bead surfaces in the absence and presence of NIF. Table 6.3 gives the results for increasing NIF concentrations. It can be seen, that the percentage of beads that could be pulled off cell surfaces increased from approximately 10 % for the NIF-free system to 50 % for a 10^{-13} mol/cell concentration of NIF. This suggests an approximately 5-fold decreased adhesion. From the results shown in table 6.3, a maximum block of adhesion for NIF concentrations $\gtrapprox 10^{-14}$ mol/cell was found, above which the percentage of separable beads did not increase further in the presented experiments. The IC50 concentration of NIF in the optical tweezers experiments was determined as the concentration at which bead separability was increased by 50 %. From table 6.3, this was found to be approximately 10^{-15} mol NIF/cell.

NIF (mol/cell)	**Bead separation (%)**
0	9.5 (± 1.5)
10^{-15}	22 (± 8)
10^{-14}	52 (± 7)
10^{-13}	50

Table 6.3: Optical tweezers studies on the effect of NIF on adhesion of HSA coated beads to neutrophils. The amount of beads separable from the cell surfaces with the optical trap is given as the average percentage (± standard deviation) of tested beads from 1 to 3 experiments, including between 12 and 56 individual measurements each, at each of the given NIF concentrations.

The experiments were carried out successively, so that there were time differences of up to 5 hours between the first and the last experiment of one series of different NIF concentrations. Because of the short half life of neutrophils, we were concerned that a decrease in cell adhesion with time may occur within the time scale of our experiments. Measurements for NIF free conditions that were repeated after a time interval of 6 hours, however, showed no effect of time on the percentage of separable beads from cells.

Since the set-up incorporates a CCD camera system, it was further possible to obtain visual information from recording light microscopy images on the same samples. Figure 6.8 shows representative images of neutrophils in NIF-free buffer (A) and in 10^{-13} mol NIF/cell (B). Similar to the confocal microscopy images, a reduction in the number of attached beads for the high NIF concentration can clearly be seen. From the images, the average number

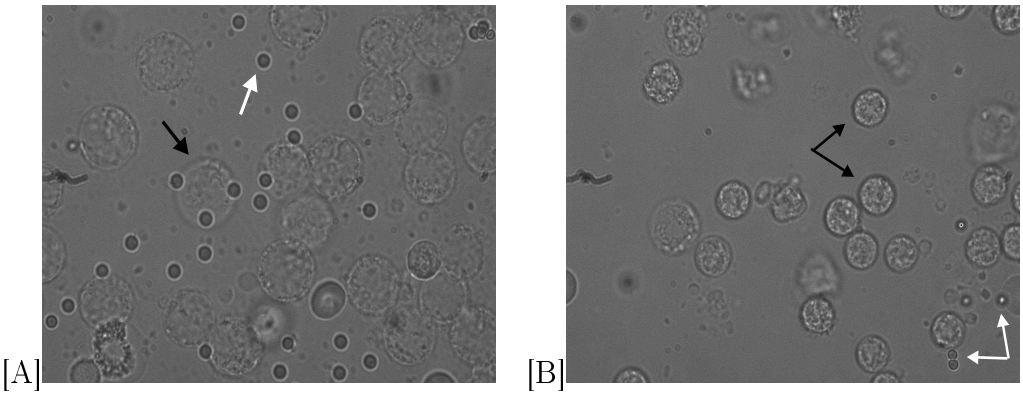

Figure 6.8: Light microscopy image on optical tweezers neutrophil samples: (A) no NIF, (B) maximum applied NIF concentration (10^{-13} mol NIF/cell). White arrows in the images indicate beads, black arrows cells. Images are approximately 70 μm x 90 μm (A), and 100 μm x 120 μm (B).

of beads positioned on neutrophils was determined for each of the different applied NIF concentrations. Averages were obtained from 4 to 11 different sample positions for each applied NIF concentration. Table 6.4 summarises the results. It can be seen, that the ratio of cell-bound beads to cells is much reduced in the presence of 10^{-14} and 10^{-13} mol NIF/cell, consistent with adhesion blocking by NIF. Surprisingly, for 10^{-15} mol NIF/cell an increase in the average number of beads per cell (ratio of cell-bound beads to cells) was observed, compared to NIF free condition. Variations in the bead per cell ratio were, however, large between different sample areas for samples with high numbers of beads attached to cells (see standard deviation values in table 6.4), accommodating for the changes between NIF free samples and samples containing 10^{-15} mol NIF/cell.

As can be seen from table 6.4, results from the light microscopy images

NIF (mol/cell)	**beads per cell**
0	0.40 (± 0.32)
10^{-15}	0.95 (± 0.35)
10^{-14}	0.11 (± 0.04)
10^{-13}	0.08 (± 0.05)

Table 6.4: Light microscopy on optical tweezers samples: the average number (per image) of beads positioned on neutrophils is given for each of the applied NIF concentrations. Standard deviations of 4 to 11 measurements for each NIF concentration are given in brackets.

confirmed maximum blocking of neutrophil adhesion for NIF concentrations $\gtrapprox 10^{-14}$ mol/cell. Further, a baseline level of 20 % adhesion was found in these studies, in agreement with the observations from the confocal microscopy studies. The IC50 concentration of NIF was again determined as the concentration at which the average number of beads per cell was reduced by 50 %, as for the confocal microscopy experiments. This was, however, difficult to identify from the results obtained from the images, but appeared to be between 10^{-15} and 10^{-14} mol/cell.

Comparing images from confocal microscopy and optical tweezers samples, the average number of beads per cell (tables 6.2 for confocal microscopy and 6.4 for optical tweezers) was found to be one order of magnitude higher in the confocal microscopy samples. The diameter of the beads used for the optical tweezers experiments was 2 μm, twice the diameter of those used in

the confocal microscopy studies. Although the increased surface area partly explains the decreased number of beads per cell, this only correlates to an increase in surface area and thus predicted decrease in bead per cell ratio by a factor of 4. However, confocal microscopy sample preparation involved centrifugation of the bead-cell mixtures. The increase in cell adhesion found in the presented experiments is in good agreement with previous studies on the enhancing effects of centrifugation on cell adhesion [Milam et al., 1973]. Comparable reduction of percentage adhesion was found for the same inhibitor concentrations in both confocal microscopy and optical tweezers experiments. Bead-cell separability and adhesion frequency therefore showed correlation. Both optical tweezers and confocal microscopy experiments suggested a decrease in the number of receptor-ligand interactions for increasing NIF concentration. Single molecule interactions could, however, not be probed with the large contact areas employed.

6.4.3 AFM

In AFM experiments, the diameter of the force probing tip is two orders of magnitude smaller than that of the bead in the optical tweezers experiments. Therefore, a HSA coated tip offers a much reduced contact area and the presentation of less ligand molecules to the cell surface than the bead. This increases the probability of measuring single receptor-ligand interactions, providing information on adhesion events at the single molecule level. In our experiments, the effect of NIF on neutrophil adhesion receptor interactions was further exploited to obtain isolated available binding sites on the

cell surfaces.

Coating of the AFM tip with HSA was confirmed in a series of negative controls prior to every experiment (see section 6.3.2). Cells were then incubated on the substrate surfaces for 45 minutes at ambient temperature ($\approx$ 23°C) in the presence of the chemotactic agent fMLP and different concentrations of NIF. In the experiments, the HSA molecules on the tip were brought into contact with receptor molecules on a neutrophil surface by lowering the AFM tip towards the cell surface. Care was taken to keep contact forces constant and low (between 200 and 300 pN), in order to minimise the probe-sample contact area and thus the number of induced interactions. Upon tip retract, any formed receptor-ligand complexes were ruptured (de-adhesion event). Rupture produces a discontinuity in the obtained force distance curve. Figure 6.9 shows a representative force-distance curve obtained on a neutrophil cell surface under near native conditions (in NIF-free HBSS buffer).

Each measured de-adhesion force may be the result of a different number of receptor-ligand interactions rupturing. Therefore, each de-adhesion force only represents a particular sample from a distribution of forces [Evans and Williams, 2002]. However, receptor-ligand interaction strengths and frequencies can be determined from the distribution of measured de-adhesion forces from a large number of measurements (several hundreds) [Evans and Williams, 2002].

Figure 6.10 shows the histograms of detected de-adhesion forces between neutrophils and HSA for a NIF-free system, and the same sample with 1.5 and 3 x 10^{-13} mol NIF/neutrophil. Since NIF binding to the receptors in-

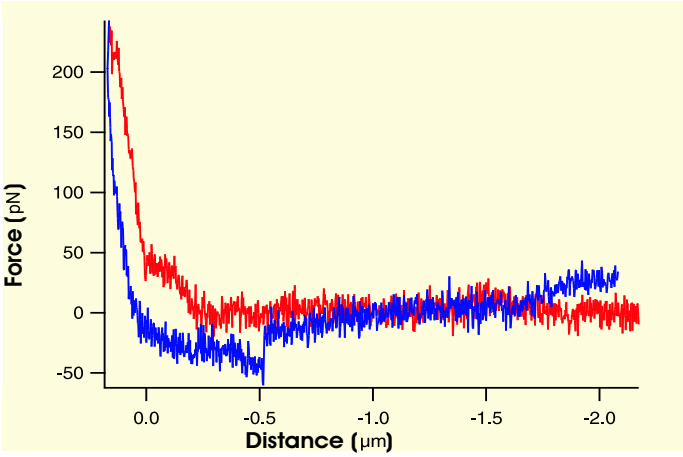

Figure 6.9: AFM force-distance curve with a HSA-coated AFM tip on an activated neutrophil cell surface. The measured force of approximately 40 pN relates to the rupturing of interactions formed between the cell surface and the HSA ligands.

hibits neutrophil adhesion, the application of NIF should reduce both the percentage of adhesion events (i.e. adhesion becomes less likely) and the observed rupture forces (i.e. less receptors contribute to adhesion). The percentage of adhesion was determined from the ratio of force distance curves showing de-adhesion events to the total number of recorded curves, for each of the applied NIF concentrations. 0 pN force in the distributions represents the amount of force curves without de-adhesion. For the NIF-free system, 60 % of measurements displayed adhesion, compared to 50 % and 14 % for 1.5 and 3 x 10^{-13} mol NIF/cell, respectively. The percentage of adhesion found for 3 x 10^{-13} mol NIF/cell suggests a complete block of cell surface receptor sites, since negative control measurements of interactions between the employed HSA coated tip and the HSA coated substrate surface gave a similar percentage of adhesion (13 %, data not shown).

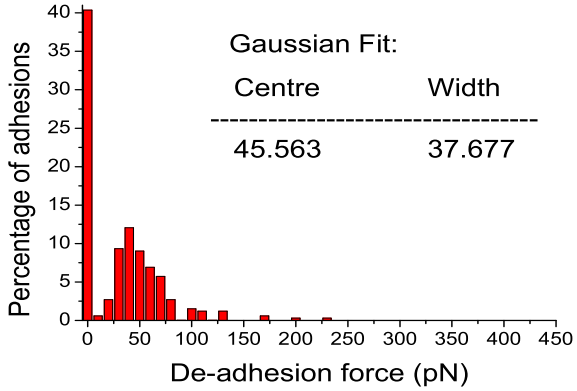

[A]

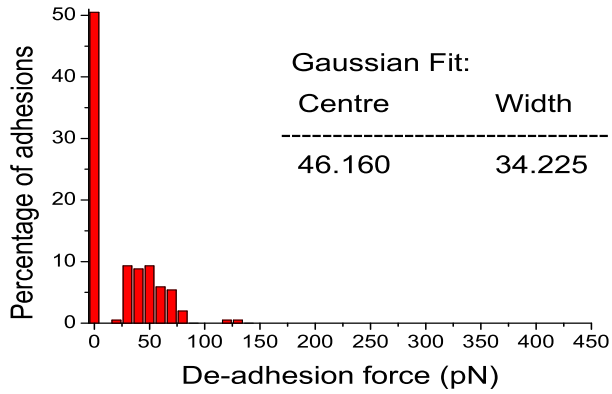

[B]

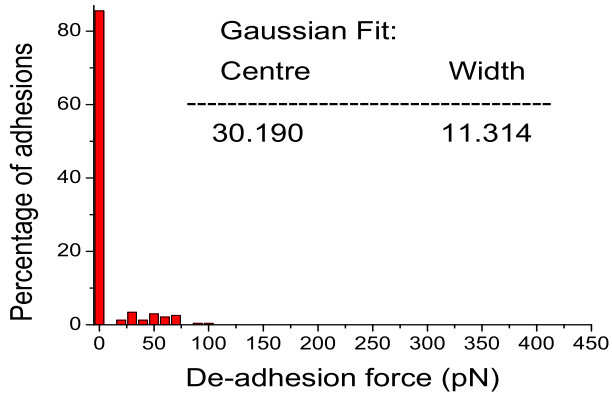

[C]

Figure 6.10: Histograms of measured interaction forces between neutrophil receptors and HSA for increasing concentrations of NIF, obtained by AFM. The applied NIF concentrations were (A) 0, (B) 1.5, and (C) 3 x 10^{-13} mol/cell. For each concentration, parameters of Gaussian fits to the force distributions are given.

Further, for each histogram of measured de-adhesion forces, the centre and the width of Gaussian curves fitted to the obtained force distributions are also given in the figure. Although the Gaussian distribution does not entirely correctly describe de-adhesion of multiple interactions [Evans and Williams, 2002], they can serve to give an estimate of the average measured interaction force as its centre value and the spread in the force distribution as its width. A change in the measured interaction force is difficult to see from the histograms of figure 6.10. However, for a series of lower concentrations of NIF, a decrease in this force could be observed. Figure 6.11 shows a reduction in the measured average rupture force for a NIF-free sample and samples with NIF concentrations of 6 and 8 x 10^{-14} mol/cell from approximately 39 pN to 27 pN and 19 pN, respectively. This relates to a decrease in average measured interaction force by 4 to 2 pN per 10^{-14} mol NIF/cell added. For single molecule interactions, the measured force would be expected to remain unaltered, while the frequency of adhesion events would decrease. The results therefore suggest that multiple interactions contributed to the forces measured in the NIF free system, and that the number of contributing molecules was reduced in the presence of NIF.

In the presented experiments, high concentrations of NIF were exploited to reduce the available ligand binding sites on the neutrophil surfaces. When sufficiently reduced for the AFM tip to effectively approach an isolated, single receptor molecule, single molecule interactions should be measurable. The measured average force of 19 pN for the highest degree of blocking in the experimental series shown in figure 6.11 is of the order of magnitude found in AFM experiments for interactions of other cell receptors at the single

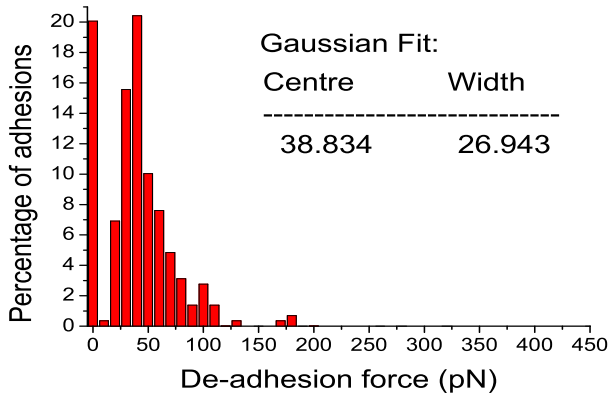

[A]

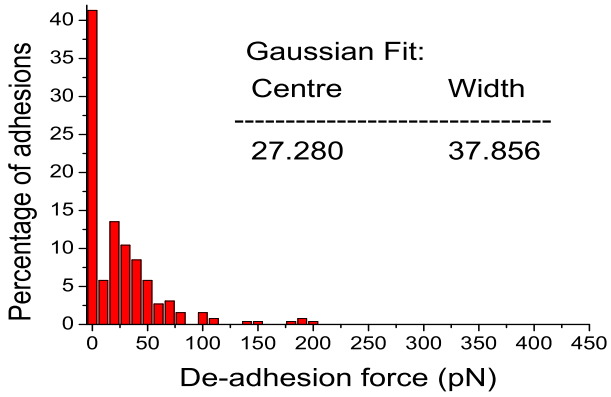

[B]

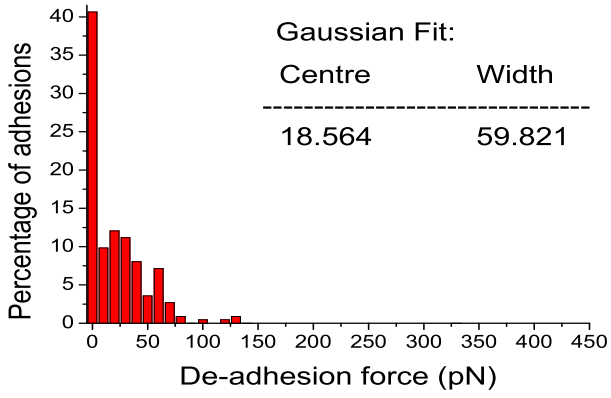

[C]

Figure 6.11: Histograms of measured interaction forces between neutrophil receptors and HSA for increasing concentrations of NIF, obtained by AFM. The applied NIF concentrations were (A) 0, (B) 6, and (C) 8 x 10^{-14} mol/cell. Parameters of Gaussian fits to the distributions are given for each NIF concentration.

molecule level [Benoit et al., 2000]. This suggests, that single molecule conditions were achieved in the experiment with 8 x 10^{-14} mol NIF/cell. The exact amount of inhibitor needed for sufficient receptor blocking will however vary between different series of experiments with the amount of protein on the AFM tip. The percentage of adhesion obtained in the negative control (interactions between HSA coated tip and HSA coated substrate surface) indicates the degree of protein coating of the tip [Allen et al., 1997; Lee et al., 1994b]. Only tips with negative control adhesion of $\lessapprox$ 16 % were used for the presented experiments, in order to enable comparison of the obtained results.

The detection of single molecular interactions by AFM is characterised by a small percentage of measurements showing adhesion ($\lessapprox$ 20 %). The fraction of single receptor-ligand rupture events in the obtained force distribution can be determined from the percentage of adhesion [Evans and Williams, 2002]:

$$\frac{N_s}{N_t} = \frac{N_t}{N_f}\overline{N}exp(-\overline{N}) = \frac{N_t - N_f}{N_f}ln(\frac{N_t}{N_t - N_f}) \tag{6.1}$$

where N_i is the number of total tests ($i = t$), of forces measured ($i = f$), and of single rupture events ($i = s$). $\overline{N}$ is the mean number of attachments per contact. For 20 % adhesion, almost 90 % of all measured forces are thus due to single molecule events. A narrow peak (small variance of fitted curve) at the single molecule interaction force further characterises the force histograms of predominantly single molecule interactions [Evans and Williams, 2002].

The results from figure 6.10 therefore indicate single molecule conditions (14 % adhesion, 93 % single molecule events). However, a higher number

of measurements will be required, in order to resolve the maximum in the distribution of de-adhesion forces obtained.

A higher and more consistent degree of neutrophil adherence to endothelial cells has previously been reported for pre-incubation of neutrophils with fMLP at 25°C than at 37°C [Tonnesen, Smedley and Henson, 1984]. Tonnesen et al. found that activation of neutrophils appeared to be less transient for pre-incubation at the lower temperature. However, since a temperature of 37°C provides conditions closer to those found *in vivo*, in this study measurements were further carried out after pre-incubation at 37°C. Results obtained from these measurements on neutrophil interaction with HSA were compared to results from measurements after pre-incubation at ambient temperature (approximately 23°C). For near native conditions (NIF-free buffer), adhesion was found in 70 % (± 10 % SD) of measurements after incubation at ambient temperature, and in 82 % (± 8 % SD) after incubation at 37°C. Maxima in the distribution of measured adhesion forces were at 42 pN (± 4 pN) and 35 pN (± 5 pN) for pre-incubation at ambient temperature and 37°C, respectively. No significant differences in neutrophil-HSA interaction forces or frequencies were thus found in the AFM studies using different pre-incubation temperatures.

Table 6.5 summarises the results from AFM experiments on neutrophil-HSA interactions in the presence of different concentrations of NIF. In agreement with confocal microscopy and optical tweezers studies, 23 % (± 9 %) remaining adhesion was found for NIF concentrations that provided total

Experiment series	**NIF (mol/cell)**	**Adhesion (%)**	$\overline{F}_{adh}$ **(pN)**
1	0	90	42
2	0	80	39
3	0	60	46
1	10^{-17}	75	35
2	4 x 10^{-14}	62	32
2	6 x 10^{-14}	59	27
2	8 x 10^{-14}	59	19
3	1.5 x 10^{-13}	50	46
3	3 x 10^{-13}	14	30
3	6 x 10^{-13}	32	31

Table 6.5: AFM force-distance experimental results on neutrophil adhesion for increasing concentrations of NIF. Adhesion was determined as the percentage of measurements showing de-adhesion events. The average measured adhesion force $\overline{F}_{adh}$ is further given, as obtained from Gaussian fits to the force distributions. The three ranges of NIF concentrations (10^{-17}, 10^{-14}, and 10^{-13} mol/cell) were applied in separate experimental series (experiments 1, 2, and 3 respectively), with different HSA coverage of the adhesion probing AFM tip, leading to the differences in forces observed between them.

blocking of CD11b/CD18 receptors. From the percentage of adhesion found for the different inhibitor concentrations, the maximum blocking concentration of NIF in the AFM force distance experiments was determined to be of the order of 10^{-13} mol/cell. The IC50 concentration of NIF in the AFM experiments was determined as the concentration at which measured adhesion frequency was reduced to 50 %. From our results, it was estimated to be of the order of 10^{-14} mol/cell. However, it should be noted that exact concentrations required for complete or 50 % adhesion blocking will vary between experiments, as they depend on the degree of protein coverage of the AFM tip.

The fact that with AFM, higher concentrations were required for receptor blocking is likely to result from the different nature of the experiments. Here, HSA and neutrophil receptors were forced together and separated in a non-equilibrium process. In order to withstand the forced formation of adhesive interactions between HSA proteins on the tip and CD11b/CD18 receptors on the neutrophil surfaces, a greater number of receptors may need to be occupied by NIF molecules. This would hence lead to an increase in concentration of NIF required for blocking of neutrophil adhesion. Reducing the contact force between the HSA coated tip and the neutrophil surface further ($\lessapprox$ 200 pN), may improve measurement conditions and enable a reduction of the number of interactions measured.

6.5 Conclusions

In this study, NIF was shown to reduce CD11b/CD18 receptor based neutrophil adhesion to HSA at the single cell level. For this, both force measuring and imaging techniques were employed. The obtained results suggested total adhesion blocking for NIF concentrations of the order of $\gtrapprox 10^{-14}$ mol/cell. The inhibitor concentration at which half the receptors were blocked for interactions was found to be of the order of 10^{-15} mol NIF/neutrophil. Reduction of neutrophil adhesion in the presence of NIF was interpreted as due to specific blocking of the receptors on the neutrophil surface. Approximately 20 % remaining adhesion was found consistently for all employed techniques for high concentrations of NIF. This remaining percentage of adhesive interactions was interpreted as due to non-specific adhesion, with all specific CD11b/CD18 receptor interactions being blocked by the inhibitor. Our results are in reasonable agreement with results obtained on large numbers of neutrophils using bulk property measuring techniques. Advantages of a cell adhesion assay on single cell basis would be the reduction of sample material required, and the separation of potential effects due to intercellular interactions in multi-cell systems. Furthermore, detailed information on variations in individual cell behaviour can be obtained from such experiments with large numbers of single cells being investigated.

In this study, information on the strength of the CD11b/CD18 interactions with HSA could further be obtained using AFM. For NIF free systems, average interaction forces of between 39 and 46 pN were measured. The exact value depends on the surface density of available receptors on the cell

surface and of protein on the AFM tip, which varies between different experimental series. Upon application of NIF, we found a decrease in the average measured interaction force with increasing NIF concentration. This was interpreted as NIF binding reducing the number of receptor molecules available for ligand interactions. The exact value of force decrease per applied concentration of NIF, however, again depends on the degree of protein coverage of the AFM tip. Careful determination of the required inhibitor concentration is necessary for single molecule measurements. Unfortunately, due to time limitations, only preliminary results were achieved for single molecule conditions in the present study. The obtained value of 19 pN for a high degree of receptor blocking by NIF is of the same order of magnitude as previously found interaction forces of other cell adhesion molecules.

HSA was here employed as ligand for CD11b/CD18. It is not a specific, natural ligand of the receptor. However, this study was concerned with the determination of experimental conditions required for a single cell or single molecule adhesion assay. Replacement of HSA by any specific ligand to CD11b/CD18 of interest, such as fibrinogen or CD11b/CD18-antibody fragments, is easily possible. Future studies will be required to determine a close range of suitable blocking concentrations of NIF for the measurement of single receptor interactions. Variations in the surrounding conditions may then show interesting effects on the blocking potential of NIF.

Chapter 7

General Conclusions

Single molecule techniques have been shown to provide structural and functional information on individual molecules. Both imaging and force measuring techniques have been developed to enable the resolution of heterogeneities in a population of molecules. Furthermore, time-dependent molecular processes which pose problems for conventional, ensemble measurements with their need for population synchronisation can be studied with such techniques. Within the last decade, their high temporal and force resolution has also inspired efforts to determine mechanical properties of biopolymers, and to elucidate the nature of biomolecular interactions. Considerable achievements include, for example, results on the elastic behaviour of DNA which have also been exploited to study DNA-ligand binding interactions. Mechanical properties have been determined for several other macromolecules, and the interactions of a wide range of receptor-ligand systems have been probed using a variety of single molecule techniques. This has enabled the development of improved theoretical models for the description of biomolecules.

The studies presented here compared and contrasted two of the main single molecule techniques, optical tweezers and AFM, on diverse biological systems. Within the context of each of the different applications, the advantages of the utilised technique have been highlighted. Particular attention was focussed on optical tweezers, the instrumental development of which (including calibration and preliminary applications) has been described within this thesis.

A position sensitive photodetection system for the optical tweezers set-up was further designed and built. As described within this work, this allows the measurement of nm-range displacement of trapped particles and the determination of the spring constant of the optical tweezers trapping potential. We have shown a proportionality between the illumination power and the signal-to-noise ratio of the photodetector. Future developmental work on the system will thus include the replacement of the microscope illumination pillar, in order to achieve stronger contrasts between image and background. The detector signal to noise ratio has further been demonstrated to increase with the size of the object's image on the photodetector array. Further image magnification can be achieved, for example, by insertion of a lens within the microscope side port (in front of the detector). For force measurements with optical tweezers, beads of diameters < 3 μm are typically employed as force probes. For objects of this size range, additional image magnification may still be necessary, even for an increased illumination power.

An advanced optical tweezers based force transducer was employed to investigate the binding of small molecules (such as drugs) to DNA. The low force regime resolvable with this technique allowed quantitative analy-

sis of the effects of molecule attachment on the DNA mechanical properties, contour length and persistence length. Differentiation was thus possible between different modes of binding to DNA. By comparing the effects of the drug berenil on the mechanical properties of DNA with those of the minor-groove binder netropsin and the intercalator ethidium bromide, we found a combination of minor groove-binding and intercalation for berenil at high drug concentrations. Further experiments will enable the separation of the mechanical contributions from each binding mode, and the determination of their individual binding affinities.

The mechanical properties of DNA are closely connected with molecular superstructure, which can thus be altered by the attachment of molecules. Visually detectable aspects of this were illustrated using AFM high resolution imaging. In these studies, the effects of the novel protein RdgC on DNA contour length and supercoiling were measured. Binding of the protein to DNA appeared to unwind negatively supercoiled DNA, and to further wind the molecule strand upon increasing protein concentration, producing positively supercoiled DNA. Our data suggested an increase in DNA contour length compared to native DNA by approximately 10 % for protein/DNA ratios of 10:1. It may therefore be concluded that RdgC binding unwinds negatively supercoiled DNA, increasing DNA contour length. From studies on linear DNA, valuable information on binding positions of RdgC was further obtained. We found an initial slight preference for RdgC binding at the ends of the linear dsDNA, while the protein was not observed to specifically target any DNA sequence. Binding also appeared to either induce bends or preferentially occur at pre-existing bends within the DNA strands. An

introduction of bends would also be consistent with the interpretation of the effects on DNA superstructure in terms of unwinding of DNA supercoiling. Based on our results, further ensemble studies using gel retardation assays are being performed in order to confirm the effect of RdgC on DNA supercoiling.

With the effects of NIF on the interactions of the cell adhesion receptor molecule CD11b/CD18, a very different biological system was studied using the same techniques. Optical tweezers results suggested that total cell adhesion blocking was achieved in the presence of NIF concentrations $\gtrapprox 10^{-14}$ mol/cell, whereas a 50 % inhibition of adhesion was found at approximately 10^{-15} mol NIF/neutrophil. These findings were confirmed by results from fluorescence confocal microscopy. Our results on adhesion blocking were found to be in reasonable agreement with results obtained on large numbers of neutrophils using bulk property measuring techniques. In order to further measure single molecular interactions, AFM was here employed as a force measuring device. The strength of the average measured interaction of the adhesion receptor with its (non-physiological) ligand HSA showed a decrease with increasing NIF concentration. This is indicative of a reduction in either the number of formed receptor-ligand interactions, or in the strength of the individual bond. Due to time restrictions, the number of interactions collected for the resulting de-adhesion force distributions only allowed a rather crude determination of the single molecule interaction force. For maximum blocking and a thus enhanced probability for measuring single molecule interactions of $\gtrapprox$ 90 %, the strength of a single interaction was found to be approximately 19 pN. The nature of the applied statistical analysis requires larger numbers of individual measurements in future experiments, in order

to obtain definite results. Further studies are also required to determine a closer range of suitable blocking concentrations of NIF for the measurement of single receptor interactions. The current study has however demonstrated the successful measurement of drug effects on single molecule interactions of cell adhesion receptors. Further optimisation of the presented assay may thus allow effects of variations in the surrounding conditions on the blocking potential of NIF to be measured directly on single molecular interactions. This may enable the resolution of individually contributing effects, and facilitate the understanding of the complex interplay of influencing factors *in vivo*.

Single molecule approaches have thus been successfully used to provide new and complementary information on a range of biological systems from interactions of drugs and proteins with DNA to cell adhesive interactions. The range of studied systems and accessible details demonstrates the great diversity of these techniques. This diversity, combined with the high degree of spatial and force resolution under near physiological conditions shown in the presented studies, signifies the great potential for single molecule techniques in biology. Recent and ongoing developments of new applications further combine different single molecule techniques, such as for example, FRET and AFM. The introduction of fluorescence into force measuring experiments allows simultaneous access to structural information on the molecular system. This will be interesting, particularly in the context of our studies, concerning the effect of different drug binding modes on the elastic properties of DNA. The combination of such techniques thus promises to further stretch the limits of resolution and accessibility of molecular properties.

Acknowledgements

I would like to thank my supervisors Dr Stephanie Allen, Dr Clive J Roberts, Dr Phillip M Williams, Prof Saul JB Tendler, and Martyn C Davies, for many helpful discussions. Special thanks go to Saul and Clive and in particular to Stephanie for their multiple advice and patience.

My greatest thanks also go to my industrial supervisors, Dr Eddie French and Dr Astrid Pappenberger at Pfizer GR&D Ltd., for extremely interesting and enjoyable visits to the company sites in Sittingbourne and Sandwich and for their input into my work.

I thank a lot of my present and past colleagues in LBSA for good company and especially for their blood! In particular I want to acknowledge Dr David Armitage for his help with the optical tweezers development.

For very pleasant and fruitful collaborations I would like to thank Dr Justin E Molloy, Dr Christoph G Baumann, Dr Gary M Skinner, Prof Robert Lloyd, and Dr Tim Moore.

For keeping me (relatively) sane in a world of research I would like to thank my friends, in particular Railene, who also contributed to the grammatical perfection of this thesis, and Ali.

I also would like to take the opportunity to thank my parents for being

extremely supportive and forgiving throughout my life.

None of the work included in this thesis would have been possible without the funding by the University of Nottingham and Pfizer GR&D Ltd., for which I am deeply grateful.

Publications

The following publication came out of the work presented within this thesis:

I Tessmer, CG Baumann, GM Skinner, JE Molloy, JG Hoggett, SJB Tendler, and S Allen [2003]. Mode of drug binding to DNA determined from the elasticity of single DNA molecules, *Journal of Modern Optics*, in press

Bibliography

Ahsan, A., Rudnick, J. and Bruinsma, R. [1998]. Elasticity theory of the b-dna to s-dna transition, *Biophysical Journal* **74**: 132–137.

Alberts, B., Bray, D., Lewis, J., Raff, M., Roberts, K. and Watson, J. [1990]. *Molecular biology of the cell*, 2nd edn, VCH Publishers, New York, NY, USA.

Allen, S., Chen, X., Davies, J., Davies, M., Dawkes, A., Edwards, J., Roberts, C., Sefton, J., Tendler, S. and Williams, P. [1997]. Detection of antigen-antibody binding events with the atomic force microscope, *Biochemistry* **36**: 7457–7463.

Allen, S., Davies, J., Dawkes, A., Davies, M., Edwards, J., Parker, M., Roberts, C., Sefton, J., Tendler, S. and Williams, P. [1996]. In situ observation of streptavidin-biotin binding on an immunoassay well surface using an atomic force microscope, *FEBS Letters* **390**: 161–164.

Allison, D., Kerper, P., Doktycz, M., Thundat, T., Modrich, P., Larimer, F., Johnson, D., Hoyt, P., Mucenski, M. and Warmack, R. [1997]. Mapping individual cosmid dnas by direct afm imaging, *Genomics* **41**: 379–384.

Alon, R., Hammer, D. and Springer, T. [1995]. Lifetime of the p-selectin-carbohydrate bond and its response to tensile force in hydrodynamic flow, *Nature* **374**: 539–542.

Anderson, D., Miller, L., Schmalstieg, F., Rothlein, R. and Springer, T. [1986]. Contributions of the mac-1 glycoprotein family to adherence-dependent granulocyte functions: structure-function assessment employing subunit-specific monoclonal antibodies, *The Journal of Immunology* **137**(1): 15–27.

Ansari, A., Mapp, A., Nguyen, D., Dervan, P. and Ptashne, M. [2001]. Towards a minimal motif for artificial transcriptional activators, *Chemical Biology* **8**: 583–592.

Anselmetti, D., Fritz, J., Smith, B. and Fernandez-Busquets, X. [2000]. Single molecule dna biophysics with atomic force microscopy, *Single Molecules* **1**(1): 53–58.

Arai, Y., Yasuda, R., Akashi, K., Harada, Y., Miyata, H., Kinosita, K. and Itoh, H. [1999]. Tying a molecular knot with optical tweezers, *Nature* **399**: 446–448.

Arnaout, M., Spits, H., Terhorst, C., Pitt, J. and Todd, R. I. [1984]. Deficiency of a leukocyte surface glycoprotein (lfa-1) in two patients with mo1 deficiency, *Journal of Clinical Investigation* **74**: 1291–1300.

Ashkin, A. [1970a]. Acceleration and trapping of particles by radiation pressure, *Physical Review Letters* **24**: 156–159.

Ashkin, A. [1970b]. Atomic-beam deflection by resonance-radiation pressure, *Physical Review Letters* **24**: 1321–1324.

Ashkin, A. [1974]. Trapping of atoms by resonance radiation pressure, *Applied Physics Letters* **19**: 283–285.

Ashkin, A. [1992]. Forces of a single-beam gradient laser trap on a dielectric sphere in the ray optics regime, *Biophysical Journal* **61**: 569–582.

Ashkin, A. and Dziedzic, J. [1985]. Observation of radiation pressure trapping of particles using alternating light beams, *Physical Review Letters* **54**: 1245–1248.

Ashkin, A. and Dziedzic, J. [1987]. Optical trapping and manipulation of viruses and bacteria, *Science* **235**(4795): 1517–1520.

Ashkin, A., Dziedzic, J., Bjorkholm, J. and Chu, S. [1986]. Observation of a single-beam gradient force optical trap for dielectric particles, *Optical Letters* **11**(5): 288–290.

Ashkin, A., Dziedzic, J. and Yamane, T. [1987]. Optical trapping and manipulation of single cells using infrared laser beams, *Nature* **330**: 769–771.

Barnard, J., Biro, M., Lo, S., Ohno, S., Carozza, M., Moyle, M., Soule, H. and Malik, A. [1995]. Neutrophil inhibitory factor prevents neutrophil-dependent lung injury, *The Journal of Immunology* **155**: 4876–4881.

Bassler, B., Wright, M. and Silvermann, M. [1994]. Multiple signalling systems controlling expression of luminescences in vibrio harveyi, *Molecular Microbiology* **13**: 273–286.

Bates, A. and Maxwell, A. [1993]. *DNA Topology*, IRL Press, Oxford, UK, pp. 33–36.

Bauer, W. and Vinograd, J. [1968]. The interaction of closed circular dna with intercalative dyes, *Journal of Molecular Biology* **33**: 141–171.

Baumann, C., Bloomfield, V., Smith, S., Bustamante, C., Wang, M. and Block, S. [2000]. Stretching of single collapsed dna molecules, *Biophysical Journal* **78**: 1965–1978.

Baumann, C., Smith, S., Bloomfield, V. and Bustamante, C. [1997]. Ionic effects on the elasticity of single dna molecules, *Proceedings of the National Academy of Sciences of the USA* **94**: 6185–6190.

Bell, G. [1978]. Models for the specific adhesion of cells to cells, *Science* **200**: 618–627.

Bennink, M., Schärer, O., Kanaar, R., Sakato-Sogawa, K., Schins, J., Kanger, J., de Grooth, B. and Greve, J. [1999]. Single-molecule manipulation of double-stranded dna using optical tweezers: interaction studies of dna with reca and yoyo-1, *Cytometry* **36**: 200–208.

Benoit, M., Gabriel, D., Gerisch, G. and Gaub, H. [2000]. Discrete interactions in cell adhesion measured by single-molecule force spectroscopy, *Nature Cell Biology* **2**: 313–317.

Berge, T., Jenkins, N., Hopkirk, R., Waring, M., Edwardson, J. and Henderson, R. [2002]. Structural perturbations in dna caused by bis-

intercalation of ditercalinium visualised by atomic force microscopy, *Nucleic Acids Research* **30**(13): 2980–2986.

Beukers, H., Deierkauf, F., Blom, C., Deierkauf, M. and Riemersma, J. [1978]. Effects of albumin on the phagocytosis of polystyrene spherules by rabbit polymorphonuclear leukocytes, *Journal of Cell Physiology* **97**: 29–36.

Binnig, G., Quate, C. and Gerber, C. [1986]. Atomic force microscope, *Physical Review Letters* **56**(9): 930–933.

Binnig, G., Rohrer, H., Gerber, C. and Weibel, E. [1982]. Surface studies by scanning tunnelling microscopy, *Physical Review Letters* **49**: 57–61.

BLC [2002]. Dna, web site of the Biology Learning Center, University of Arizona, USA.

Block, S. [1992]. Making light work with optical tweezers, *Nature* **360**: 493–495.

Block, S., Goldstein, L. and Schnapp, B. [1990]. Bead movement by single kinesin molecules studied with optical tweezers, *Nature* **348**: 348–352.

Bostock-Smith, C., Laughton, C. and Searle, M. [1999]. Solution structure and dynamics of the a-t tract dna decamer duplex d(ggtaattacc)$_2$: implications for recognition by minor groove binding drugs, *Biochemical Journal* **342**: 125–132.

Bronkhorst, P., Streekstra, G., Grimbergen, J., Nijhof, E., Sixma, J. and Brakenhoff, G. [1995]. A new method to study shape recovery of

red blood cells using multiple optical trapping, *Biophysical Journal* **69**: 1666–1673.

Bruinsma, R. [2002]. *Physics of protein-DNA interaction*, Ecole de Physique des Houches: Physics of biomolecules and cells, Session LXXV (Editors: H Flyvbjerg, F Jülicher, P Ormos, F David), EDP Sciences, Les Ulis, France; Springer-Verlag, Heidelberg, Germany, pp. 1–68.

Bustamante, C., Macosko, J. and Wuite, G. [2000a]. Grabbing the cat by the tail: manipulating molecules one by one, *Nature* **1**: 130–136.

Bustamante, C., Marko, J., Siggia, E. and Smith, S. [1994]. Entropic elasticity of λ-phage dna, *Science* **265**: 1599–1600.

Bustamante, C. and Rivetti, C. [1996]. Visualizing protein-nucleic acid interactions on a large scale with the scanning force microscope, *Annual Review of Biophysics and Biomolecular Structure* **25**: 395–429.

Bustamante, C., Smith, S., Liphardt, J. and Smith, D. [2000b]. Single-molecule studies of dna mechanics, *Current Opinion in Structural Biology* **10**: 279–285.

Butt, H., Wolff, E., Gould, S., Dixon-Northern, B., Peterson, C. and Hansma, P. [1990]. Imaging cells with the atomic force microscope, *Journal of Structural Biology* **105**: 54–61.

Chang, C., Lieberman, S. and Moghe, P. [1999]. Leukocyte spreading behaviour on vascular biomaterial surfaces: consequences of chemoattractant stimulation, *Biomaterials* **20**: 273–281.

Chen, S. and Springer, T. [2001]. Selectin receptor-ligand bonds: formation limited by shear rate and dissociation governed by the bell model, *Proceedings of the National Academy of Sciences of the USA* **98**(3): 950–955.

Clausen-Schaumann, H., Seitz, M., Krautbauer, R. and Gaub, H. [2000]. Force spectroscopy with single bio-molecules, *Current Opinion in Chemical Biology* **4**: 524–530.

Cleveland, J., Manne, S., Bocek, D. and Hansma, P. [1993]. A nondestructive method for determining the spring constant of cantilevers for scanning force microscopy, *Review of Scientific Instruments* **64**(2): 403–405.

Cluzel, P., Lebrun, A., Heller, C., Lavery, R., Viovy, J.-L., Chatenay, D. and Caron, F. [1996]. Dna: an extensible molecule, *Science* **271**: 792–794.

Colson, P., Bailly, C. and Houssier, C. [1996]. Electric linear dichroism as a new tool to study sequence preference in drug binding to dna, *Biophysical Chemistry* **58**: 125–140.

Colton, R., Baselt, D., Dufrene, Y., Green, J. and Lee, G. [1997]. Scanning probe microscopy, *Current Opinion in Chemical Biology* **1**: 370–377.

Coury, J., McFail-Isom, L., Dean-Williams, L. and Bottomley, L. [1996]. A novel assay for drug-dna binding mode, affinity, and exclusion number: scanning force microscopy, *Proceedings of the National Academy of Sciences of the USA* **93**: 12283–12286.

Crawford, L. and Waring, M. [1967]. Supercoiling of polyoma virus dna measured by its interaction with ethidium bromide, *Journal of Molecular Biology* **25**: 23–30.

Creighton, T. [1993]. *Proteins. Structures and molecular properties*, Freeman, New York, USA.

daSilva, L. [2002]. Atomic force microscopy and proteins, *Protein and Peptide Letters* **9**(2): 117–125.

Database, N. A. [1995]. Atlas of nucleic acid containing structures, Rutgers, the State University of New Jersey, USA, web site.

Davenport, R., Wuite, G., Landick, R. and Bustamante, C. [2000]. Single-molecule study of transcriptional pausing and arrest by e. coli rna polymerase, *Science* **287**: 2497–2500.

Deniz, A., Dahan, M., Grunwell, J., Ha, T., Faulhaber, A., Chemla, D., Weiss, S. and Schultz, P. [1999]. Single-pair fluorescence resonance energy transfer on freely diffusing molecules: observation of förster distance dependence and subpopulations, *Proceedings of the National Academy of Sciences of the USA* **96**: 3670–3675.

Deniz, A., Laurence, T., Beligere, G., Dahan, M., Martin, A., Chemla, D., Dawson, P., Schultz, P. and Weiss, S. [2000]. Single-molecule protein folding: diffusion fluorescence resonance energy transfer studies of the denaturation of chymotrypsin inhibitor 2, *Proceedings of the National Academy of Sciences of the USA* **97**(10): 5179–5184.

Denk, W. and Webb, W. [1990]. Optical measurement of picometer displacements of transparent microscopic objects, *Applied Optics* **29**: 2382–2391.

Dervan, P. [2001]. Molecular recognition of dna by small molecules, *Bioorganic & Medicinal Chemistry* **9**: 2215–2235.

Dervan, P. and Bürli, R. [1999]. Sequence-specific dna recognition polyamides, *Current Opinion in Chemical Biology* **3**: 688–693.

Detmers, P., Wright, S., Olsen, E., Kimball, B. and Cohn, Z. [1987]. Aggregation of complement receptors on human neutrophils in the absence of ligand, *Journal of Cell Biology* **105**: 1137–1145.

Doyle, P., Ladoux, B. and Viovy, J. [2000]. Dynamics of a tethered polymer in shear flow, *Physical Review Letters* **84**: 4769–4772.

Drake, B., Prater, C., Weisenhorn, A., Gould, S., Albrecht, T., Quate, C., Cannell, D., Hansma, H. and Hansma, P. [1989]. Imaging crystals, polymers, and processes in water with the atomic force microscope, *Science* **243**: 1586–1589.

Dransfield, I. and Hogg, N. [1989]. Regulated expression of mg^{2+} binding epitope on leukocyte integrin alpha subunits, *EMBO Journal* **8**(12): 3759–3765.

Edidin, M., Kuo, S. and Sheetz, M. [1991]. Lateral movements of membrane glycoproteins restricted by dynamic cytoplasmic barriers, *Science* **254**: 1379–1382.

Edwards, S. [1994]. *Biochemistry and physiology of the neutrophil*, Cambridge University Press, Cambridge, UK.

Engel, A. and Müller, D. [2000]. Observing single biomolecules at work with the atomic force microscope, *Nature Structural Biology* **7**(9): 715–718.

English, D. [1999]. *Molecular basis of neutrophil activation*, Vol. in: The neutrophils: new outlook for old cells (Editor: DI Gabrilovich), Imperial College Press, London, UK, chapter 1, pp. 1–29.

Erie, D., Yang, G., Schultz, H. and Bustamante, C. [1994]. Dna bending by cro protein in specific and nonspecific complexes: implications for protein site recognition and specificity, *Science* **266**: 1562–1566.

Essevaz-Roulet, B., Bockelmann, U. and Heslot, F. [1997]. Mechanical separation of the complementary strands of dna, *Proceedings of the National Academy of Sciences of the USA* **94**: 11935–11940.

Evans, E. [1998]. Energy landscapes of biomolecular adhesion and receptor anchoring at interfaces explored with dynamic force spectroscopy, *Faraday Discussions* **111**: 1–16.

Evans, E. [2001]. Probing the relation between force - lifetime - and chemistry in single molecular bonds, *Annual Reviews of Biophysical and Biomolecular Structure* **30**: 105–128.

Evans, E. and Ritchie, K. [1997]. Dynamic strength of molecular adhesion bonds, *Biophysical Journal* **72**: 1541–1555.

Evans, E., Ritchie, K. and Merkel, R. [1995]. Sensitive force technique to probe moleuclar adhesion and structural linkages at biological interfaces, *Biophysical Journal* **68**: 2580–2587.

Evans, E. and Williams, P. [2002]. *Dynamic Force Spectroscopy*, Ecole de Physique des Houches: Physics of biomolecules and cells, Session LXXV (Editors: H Flyvbjerg, F Jülicher, P Ormos, F David), EDP Sciences, Les Ulis, France; Springer-Verlag, Heidelberg, Germany, pp. 145–204.

Fang, Y. and Hoh, J. [1998]. Early intermediates in spermidine-induced dna condensation on the surface of mica, *Journal of the American Chemical Society* **120**: 8903–8909.

Felgner, H., Müller, O. and Schliwa, M. [1995]. Calibration of light forces in optical tweezers, *Applied Optics* **34**(6): 977–982.

Finer, J., Simmons, R. and Spudich, J. [1994]. Single myosin molecule mechanics: piconewton forces and nanometre steps, *Nature* **368**: 113–118.

Fish, E., Lane, M. and Vournakis, J. [1988]. Determination of equilibrium binding affinity of distamycin and netropsin to the synthetic deoxyoligonucleotide sequence d(ggtatacc)$_2$ by quantitative dnase i footprinting, *Biochemistry* **27**: 6026–6032.

Fixman, M. and Kovac, J. [1973]. Polymer conformational statistics. iii. modified gaussian models of stiff chains, *Journal of Chemical Physics* **58**(4): 1564–1568.

Florin, E.-L., Moy, V. and Gaub, H. [1994]. Adhesion forces between individual ligand-receptor pairs, *Science* **264**: 415–417.

Florin, E.-L., Pralle, A., Stelzer, E. and Hoerber, J. [1998]. Photonic force microscope calibration by thermal noise analysis, *Applied Physics A* **66**: 75–78.

Florin, E.-L., Rief, M., Lehmann, H., Ludwig, M., Dornmair, C., Moy, V. and Gaub, H. [1995]. Sensing specific molecular interactions with the atomic force microscope, *Biosensors and Bioelectronics* **10**: 895–901.

Flory, P. [1969]. *Statistical mechanics of chain molecules*, Interscience Publishers, John Wiley & Sons, New York, USA.

for the Properties of Water, T. I. A. and Steam [1997]. Release on the refractive index of ordinary water substance as a function of wavelength, temperature, and pressure.

Francis, J., Todd, R., Boxer, L. and Petty, H. [1989]. Sequential expression of cell surface c3bi receptors during neutrophil locomotion, *Journal of Cellular Physiology* **140**: 519–523.

Fritz, M., Radmacher, M. and Gaub, H. [1993]. In vitro activation of human platelets triggered and probed by atomic force microscopy, *Experimental Cell Research* **205**: 187–190.

Funatsu, T., Harada, Y., Tokunaga, M., Saito, K. and Yanagida, T. [1995]. Imaging of single fluorescent molecules and individual atp turnovers by single myosin molecules in aqueous solution, *Nature* **374**: 555–559.

Furie, M., Tancinco, M. and Smith, W. [1991]. Monoclonal anitbodies to leukocyte integrins cd11a/cd18 and cd11b/cd18 or the intercellular adhesion molecule-1 inhibit chemoattractant-stimulated neutrophil transendothelial migration in vitro, *Blood* **78**: 2089–2097.

Gabrilovich, D. [1999]. *The neutrophils: new outlook for old cells*, Imperial College Press, London, UK.

Gerthsen, C. and Vogel, H. [1993]. *Physik*, 17 edn, Springer-Verlag. Heidelberg, Germany.

Ghislain, L., Switz, N. and Webb, W. [1994]. Measurement of small forces using an optical trap, *Review of Scientific Instruments* **65**(9): 2762–2768.

Giessibl, F. [1995]. Atomic resolution of the silicon (111)-(7x7) surface by atomic force microscopy, *Science* **267**: 68–71.

Gittes, F. and Schmidt, C. [1998]. Interference model for back-focal-plane displacement detection in optical tweezers, *Optics Letters* **23**: 7–9.

Grandbois, M., Dettmann, W., Benoit, M. and Gaub, H. [2000]. Affinity imaging of red blood cells using an atomic force microscope, *Journal of Histochemistry and Cytochemistry* **48**: 719–724.

Gregg, A., McGlynn, P., Jaktaji, R. and Lloyd, R. [2002]. Direct rescue of stalled dna replication forks via the combined action of pria and recg helicase activities, *Molecular Cell* **9**(2): 241–251.

Grunwell, J., Glass, J., Lacoste, T., Deniz, A., Chemla, D. and Schultz, P. [2001]. Monitoring the conformational fluctuations of dna hairpins

using single-pair fluorecence resonance energy transfer, *Journal of the American Chemical Society* **123**: 4295–4303.

Guckenberger, R., Heim, M., Cevc, G., Knapp, H., Wiegräbe, W. and Hillebrand, A. [1994]. Scanning tunneling microscopy of insulators and biological specimens, based on the lateral conductivity of ultrathin water films, *Science* **266**: 1538–1540.

Guthold, M., Zhu, X., Rivetti, C., Yang, G., Thomson, N., Kasas, S., Hansma, H., Smith, B., Hansma, P. and Bustamante, C. [1999]. Direct observation of one-dimensional diffusion and transcription by *escherichia coli* rna polymerase, *Biophysical Journal* **77**: 2284–2294.

Hagerman, P. [1988]. Flexibility of dna, *Annual Review of Biophysical Chemistry* **17**: 265–286.

Hansma, H. and Hoh, J. [1994]. Biomolecular imaging with the atomic force microscope, *Annual Review of Biophysics and Biomolecular Structure* **23**: 115–139.

Hansma, H. and Laney, D. [1996]. Dna binding to mica correlates with cationic radius: assay by atomic force microscopy, *Biophysical Journal* **70**: 1933–1939.

Hansma, H. and Pietrasanta, L. [1998]. Atomic force microscopy and other scanning probe microscopies, *Current Opinion in Chemical Biology* **2**(5): 579–584.

Hansma, H., Sinsheimer, R., Groppe, J., Bruice, T., Elings, V., Gurley, G., Bezanilla, M., Mastrangelo, I., Hough, P. and Hansma, P. [1993]. Recent advances in atomic force microscopy of dna, *Scanning* **15**: 296–299.

Hansma, P., Cleveland, J., Radmacher, M., Walters, D., Hillner, P., Bezanilla, M., Fritz, M. and Hansma, H. [1994]. Tapping mode atomic force microscopy in liquids, *Applied Physics Letters* **64**(13): 1738–1740.

Happel, J. and Brenner, H. [1965]. *Low Reynolds number hydrodynamics*, Prentice Hall, Englewood Cliffs, NJ, USA.

Hegner, M. [2000]. Dna handles for single molecule experiments, *Single Molecules* **1**(2): 139–144.

Heinecke, J. [1999]. *The respiratory burst of neutrophils: oxidative pathways for the initiation of tissue damage at sites of inflammation*, Vol. in: The neutrophils: new outlook for old cells (Editor: DI Gabrilovich), Imperial College Press, London, UK, chapter 2, pp. 31–57.

Helmerson, K., Kishore, R., Phillips, W. and Weetall, H. [1997]. Optical tweezers-based immunosensor detects femtomolar concentrations of antigens, *Clinical Chemistry* **43**: 379–383.

Hénon, S., Lenormand, G., Richert, A. and Gallet, F. [1999]. A new determination of the shear modulus of the human erythrocyte membrane using optical tweezers, *Biophysical Journal* **76**: 1145–1151.

Heymann, B. and Grubmüller, H. [2000]. Dynamic force spectroscopy of molecular adhesion bonds, *Physical Review Letters* **84**(26): 6126–6129.

Hinterdorfer, P., Baumgartner, W., Gruber, H., Schilcher, K. and Schindler, H. [1996]. Detection and localization of individual antibody-antigen recognition events by atomic force microscopy, *Proceedings of the National Academy of Sciences of the USA* **93**: 3477–3481.

Hinterdorfer, P., Gruber, H., Schilcher, K., Baumgartner, W., Haselgruebler, T. and Schinler, H. [1995]. Antibody-antigen unbinding forces measured by force microscopy using antibodies bound to afm tips via a specially designed flexible crosslinker, *Biophysical Journal* **68**: 139 (Abstract).

Hirschfeld, T. [1976]. Optical microscopic observation of single small molecules, *Applied Optics* **15**(12): 2965–2966.

Husale, S., Grange, W. and Hegner, M. [2002]. Dna mechanics affected by small dna interacting ligands, *Single Molecules* **3**(2-3): 91–96.

Hutter, J. and Bechhoefer, J. [1993]. Calibration of atomic force microscope tips, *Review of Scientific Instruments* **64**(7): 1868–1873.

Isacke, C. and Horton, M. [2000]. *The adhesion molecule*, Facts Book Series, 2 edn, Academic Press, London, UK.

Ishijima, A., Doi, T., Sakurada, K. and Yanagida, T. [1991]. Sub-piconewton force fluctuations of actomyosin *in vitro*, *Nature* **352**: 301–306.

Israelachvili, J. [1992]. *Intermolecular and surface forces*, 2nd edn, Academic Press, San Diego, CA, USA.

Izrailev, S., Stepaniants, S., Balsera, M., Oono, Y. and Schulten, K. [1997]. Molecular dynamics study of unbinding of the avidin-biotin complex, *Biophysical Journal* **72**: 1568–1581.

Janshoff, A., Neitzert, M., Oberdörfer, Y. and Fuchs, H. [2000]. Force spectroscopy of molecular systems - single molecule spectroscopy of polymers and biomolecules, *Angewandte Chemie International Edition* **39**: 3212–3237.

Jenkins, T., Lane, A., Neidle, S. and Brown, D. [1993]. Nmr and molecular modeling studies of the interaction of berenil and pentamidine with $d(cgcaaatttgcg)_2$, *European Journal of Biochemistry* **213**: 1175–1184.

Kasas, S., Thomson, N., Smith, B., Hansma, H., Zhu, X., Guthold, M., Bustamante, C., Kool, E., Kashlev, M. and Hansma, P. [1997]. E coli rna polymerase activity observed using atomic force microscopy, *Biochemistry* **36**: 461–468.

Kellermayer, M., Smith, S., Granzier, H. and Bustamante, C. [1997]. Folding-unfolding transitions in single titin molecules characterized with laser tweezers, *Science* **276**: 1112–1116.

Kirke, D. [2002]. Properties of vanp, unpublished work, personal communication.

Kishino, A. and Yanagida, T. [1988]. Force measurements by micromanipulation of a single actin filament by glass needles, *Nature* **334**: 74–76.

Koch, S., Shundrovsky, A., Jantzen, B. and Wang, M. [2002]. Probing protein-dna interactions by unzipping a single dna double helix, *Biophysical Journal* **83**: 1098–1105.

Kopka, M., Yoon, C., Goodsell, D., Pjura, P. and Dickerson, R. [1985]. The molecular origin of dna-drug specificity in netropsin and distamycin, *Proceedings of the National Academy of Sciences of the USA* **82**: 1376–1380.

Krautbauer, R. [1999]. *Dns als organisches templat zur ausbildung metallischer nanodrähte*, Master's thesis, Angewandte Physik, Ludwig Maximilians Universität München.

Krautbauer, R., Clausen-Schaumann, H. and Gaub, H. [2000]. Cisplatin changes the mechanics of single dna molecules, *Angewandte Chemie International Edition* **39**(21): 3912–3915.

Krautbauer, R., Fischerländer, S., Allen, S. and Gaub, H. [2002b]. Mechanical fingerprints of dna drug complexes, *Single Molecules* **3**: 97–103.

Krautbauer, R., Pope, L., Schrader, T., Allen, S. and Gaub, H. [2002a]. Discriminating small molecule dna binding modes by single molecule force spectroscopy, *FEBS Letters* **510**: 154–158.

Kuo, S. and Sheetz, M. [1990]. Force of kinesin-dependent microtubule translocation measured by optical trapping, *Biophysical Journal* **57**(2): A399 (Abstract).

Ladic, L. [1995]. The process of making 3-d reconstructions from laser scanning confocal microscopy data, web site.

Lane, A., Jenkins, T., Brown, T. and Neidle, S. [1991]. Interaction of berenil with ecori dodecamer d(cgcgaattcgcg)$_2$ in solution studies by nmr, *Biochemistry* **30**: 1372–1385.

Laughton, C., Jenkins, T., Fox, K. and Neidle, S. [1990]. Interaction of berenil with the *tyrt* dna sequence studied by footprinting and molecular modelling. implications for the design of sequence-specific dna recognition agents, *Nucleic Acids Research* **18**(15): 4479–4488.

Laughton, C., Tanious, F., Nunn, C., Boykin, D., Wilson, W. and Neidle, S. [1996]. A crystallographic and spectroscopic study of the complex between d(cgcgaattcgcg)$_2$ and 2,5-bis(4-guanylphenyl)furan, an analog of berenil - structural origins of enhanced dna-binding affinity, *Biochemistry* **35**(18): 5655–5661.

Lebrun, A. and Lavery, R. [1996]. Modelling extreme stretching of dna, *Nucleic Acids Research* **24**(12): 2260–2267.

Leckband, D. [2000]. Measuring the forces that control protein interactions, *Annual Review of Biophysics and Biomolecular Structure* **29**: 1–26.

Leckband, D., Schmitt, F.-J., Israelachvili, J. and Knoll, W. [1994]. Direct force measurements of specific and nonspecific protein interactions, *Biochemistry* **33**: 4611–4624.

Lee, G., Chrisley, L. and Colton, R. [1994a]. Direct measurement of the forces between complementary strands of dna, *Science* **266**: 771–773.

Lee, G., Kidwell, D. and Colton, R. [1994b]. Sensing discrete streptavidin-biotin interactions with atomic force microscopy, *Langmuir* **10**: 354–357.

Léger, J., Robert, J., Bourdieu, L., Chatenay, D. and Marko, J. [1998]. Reca binding to a single double-stranded dna molecule: a possible role of dna conformational fluctuations, *Proceedings of the National Academy of Sciences of the USA* **95**: 12295–12299.

Léger, J., Romano, G., Sarkar, A., Robert, J., Bourdieu, L., Chatenay, D. and Marko, J. [1999]. Structural transitions of a twisted and stretched dna molecule, *Physical Review Letters* **83**: 1066–1069.

Ley, K. [2002]. Integration of inflammatory signals by rolling neutrophils, *Immunological Reviews* **186**: 8–18.

Liphardt, J., Onoa, B., Smith, S., Tinoco, I. and Bustamante, C. [2001]. Reversible unfolding of single rna molecules by mechanical force, *Science* **292**(5517): 733–737.

Lüthi, R., Meyer, E., Howald, I., Haefke, H., Anselmetti, D., Dreier, M., Ruetsche, M., Bonner, T., Overney, R., Fromer, J. and Güntherodt, H. [1994]. Progress in non-contact dynamic force microscopy, *Journal of Vacuum Science Technologies B* **12**: 1673–1676.

Maganov, S. and Whangbo, M.-H. [1996]. *Scanning probe microscopes*, Vol. in: Surface analysis with STM and AFM, VCH Publishers, New York, NY, USA, chapter 3, pp. 21–49.

Mao, C., Sun, W., Shen, Z. and Seeman, N. [1999]. A nanomechanical device based on the b-z transition of dna, *Nature* **397**: 144–146.

Marko, J. and Siggia, E. [1995a]. Stretching dna, *Macromolecules* **28**: 8759–8770.

Marko, J. and Siggia, E. [1995b]. Statistical mechanics of supercoiled dna, *Physical Reviews E* **52**: 2912–2938.

Martin, A., Davies, M., Rackstraw, B., Roberts, C., Stolnik, S., Tendler, S. and Williams, P. [2000]. Observation of dna-polymer condensate formation in real time at a molecular level, *FEBS Letters* **480**: 106–112.

Merkel, R. [2001]. Force spectroscopy on single passive biomolecules and single biomolecular bonds, *Physics Reports* **346**: 343–385.

Merkel, R., Nassoy, P., Leung, A., Ritchie, K. and Evans, E. [1999]. Energy landscapes of receptor-ligand bonds explored with dynamic force spectroscopy, *Nature* **397**: 50–53.

Meyer, G. and Amer, N. [1988]. Novel optical approach to atomic force microscopy, *Applied Physics Letters* **53**: 1045–1047.

Milam, M., Grinnell, F. and Srere, P. [1973]. Effect of centrifugation on cell adhesion, *Nature New Biology* **244**: 83–84.

Moerner, W. and Orrit, M. [1999]. Illuminating single molecules in condensed matter, *Science* **283**: 1670–1676.

Molloy, J., Burns, J., Kendrick-Jones, J., Tregear, R. and White, D. [1995]. Movement and force produced by a single myosin head, *Nature* **378**: 209–212.

Moore, T. [2002]. *The RdgC protein of Escherichia coli*, Phd thesis, Institute of Genetics, University of Nottingham.

Moy, V., Florin, E.-L. and Gaub, H. [1994]. Intermolecular forces and energies between ligands and receptors, *Science* **266**: 257–259.

Moyle, M., Foster, D., McGrath, D., Brown, S., Laroche, Y., de Meutter, J., Stanssens, P., Bogowitz, C., Fried, V., Ely, J., Soule, H. and Vlasuk, G. [1994]. A hookworm glycoprotein that inhibits neutrophil function is a ligand of the integrin cd11b/cd18, *The Journal of Biological Chemistry* **269**(13): 10008–10016.

Muchowski, P., Zhang, L., Chang, E., Soule, H., Plow, E. and Moyle, M. [1994]. Functional interaction between the integrin antagonist nif and the i domain of cd11b/cd18, *Journal of Biological Chemistry* **269**: 26419–26423.

Müller, D., Baumeister, W. and Engel, A. [1996]. Conformational change of the hexagonally packed intermediate layer of *deinococcus radiodurans* imaged by atomic force microscopy, *Journal of Bacteriology* **178**(11): 3025–3030.

Müller, D., Baumeister, W. and Engel, A. [1999b]. Controlled unzipping of a bacterial surface layer with atomic force microscopy, *Proceedings of the National Academy of Sciences of the USA* **96**: 13170–13174.

Müller, D. and Engel, A. [1997]. The height of biomolecules measured with the atomic force microscope depends on electrostatic interactions, *Biophysical Journal* **73**: 1633–1644.

Müller, D., Engel, A., Carrascosa, J. and Velez, M. [1997]. The bacteriophage phi29 head-tail connector imaged at high resolution with the atomic force microscope in buffer solution, *EMBO Journal* **16**(10): 2547–2553.

Müller, D., Sass, H.-J., Mueller, S., Büldt, G. and Engel, A. [1999a]. Surface structures of native bacteriorhodopsin depend on the molecular packing arrangement in the membrane, *Journal of Molecular Biology* **285**(5): 1903–1909.

Murata, K., Mitsuoka, K., Hirai, T., Walz, T., Agre, P., Heymann, J., Engel, A. and Fuliyoshi, Y. [2000]. Structural determinants of water permeation through aquaporin-1, *Nature* **407**: 599–605.

Nahmias, Y. and Odde, D. [2002]. Analysis of radiation forces in laser trapping and laser-guided direct writing applications, *IEEE Journal of Quantum Electronics* **38**(2): 131–141.

Neidle, S. [2002]. *Nucleic acid structure and recognition*, Oxford University Press, Oxford, UK, chapter 5, pp. 89–138.

Neto, P. and Nussenzveig, H. [2000]. Theory of optical tweezers, *Europhysical Letters* **50**(5): 702–708.

Neuman, K., Chadd, E., Liou, G., Bergman, K. and Block, S. [1999]. Characterization of photodamage to *escherichia coli* in optical traps, *Biophyiscal Journal* **77**: 2856–2863.

Nordmeier, E. [1992]. Absorption spectroscopy and dynamic and static light-scattering studies of ethidium bromide binding to calf thymus dna: implications for outside binding and intercalation, *Journal of Physical Chemistry* **96**: 6045–6055.

Oberhauser, A., Marszalek, P., Carrion-Vasquez, M. and Fernandez, J. [1999]. Single protein misfolding events captured by atomic force microscopy, *Nature Structural Biology* **6**: 1025–1028.

Oesterhelt, F., Oesterhelt, D., Pfeiffer, M., Engel, A., Gaub, H. and Müller, D. [2000]. Unfolding pathways of individual bacteriorhodopsins, *Science* **288**: 143–146.

Ohnesorge, F. and Binnig, G. [1993]. True atomic resolution by atomic force microscopy through repulsive and attractive forces, *Science* **260**: 1451–1456.

Patel, N., Davies, M., Lomas, M., Roberts, C., Tendler, S. and Williams, P. [1997]. Stm of insulators with the probe in contact with an aqueous layer, *Journal of Physical Chemistry B* **101**: 5138–5142.

Perkins, T., Smith, D., Larson, R. and Chu, S. [1995]. Stretching of a single tethered polymer in a uniform flow, *Science* **268**: 83–87.

Perry, J. [2000]. *Structural studies of cell surface glycoproteins*, Phd thesis, Department of Biochemistry, University of Cambridge.

Pfizer GR&D [2002]. Evaluation of nif efficiency in neutrophil adhesion assay, personal communication.

Pierres, A., Benoliel, A.-M. and Bongrand, P. [1995]. Measuring the lifetime of bonds made between surface-linked molecules, *Journal of Biological Chemistry* **270**: 26586–26592.

Pierres, A., Benoliel, A.-M. and Bongrand, P. [1998]. Studying receptor-mediated cell adhesion at the single molecule level, *Cell Adhesion and Communication* **5**: 375–395.

Pilch, D., Kirolos, M., Liu, X., Plum, G. and Breslauer, K. [1995]. Berenil [1,3-bis(4'-amidinophenyl)triazene] binding to dna duplexes and to a rna duplex: evidence for both intercalative and minor groove binding properties, *Biochemistry* **34**: 9962–9976.

Pohl, D., Denk, W. and Lanz, H. [1984]. Optical stethoscopy - image recording with resolution $\lambda/20$, *Applied Physics Letters* **44**: 651–653.

Pope, L., Davies, M., Laughton, C., Roberts, C., Tendler, S. and Williams, P. [2000]. Atomic force microscopy studies of intercalation-induced changes in plasmid dna tertiary structure, *Journal of Microscopy* **199**(1): 68–78.

Pralle, A., Florin, E.-L., Stelzer, E. and Hoerber, J. [1998]. Local viscosity probed by photonic force microscopy, *Applied Physics A* **66**: 71–73.

Pralle, A., Prummer, M., Florin, E.-F., Stelzer, E. and Hoerber, J. [1999]. Three-dimensional high-resolution particle tracking for optical tweezers by forward scattered light, *Microscopy Research and Technique* **44**: 378–386.

Pulleyblank, D. and Morgan, A. [1975]. The sense of naturally occuring superhelices and the unwinding angle of intercalated ethidium, *Journal of Molecular Biology* **91**: 1–13.

Quake, R., Babcock, H. and Chu, H. [1997]. The dynamics of partially extended single molecules of dna, *Nature* **388**: 151–154.

Raab, A., Han, W., Badt, D., Smith-Gill, S., Lindsay, S., Schindler, H. and Hinterdorfer, P. [1999]. Antibody recognition imaging by force microscopy, *Nature Biotechnology* **17**: 902–905.

Radmacher, M., Fritz, M., Hansma, H. and Hansma, P. [1994]. Direct observation of enzyme activity with the atomic force microscope, *Science* **265**: 1577–1579.

Rainger, G., Buckley, C., Simmons, D. and Nash, G. [1997]. Cross-talk between cell adhesion molecules regulates the migration velocity of neutrophils, *Current Biology* **7**: 316–325.

Rees, W., Keller, R., Vesenka, J., Yang, G. and Bustamante, C. [1993]. Evidence of dna bending in transcription complexes imaged by scanning force microscopy, *Science* **260**: 1646–1649.

Rief, M., Clausen-Schaumann, H. and Gaub, H. [1999]. Sequence-dependent mechanics of single dna molecules, *Nature Structural Biology* **6**(4): 346–349.

Rief, M., Fernandez, J. and Gaub, H. [1998]. Elastically coupled two-level systems as a model for biopolymer extensibility, *Physical Review Letters* **81**(21): 4764–4767.

Rief, M., Gautel, M., Oesterhelt, F., Fernandez, J. and Gaub, H. [1997b]. Reversible unfolding of individual titin ig-domains by afm, *Science* **276**: 1109–1112.

Rief, M., Oesterhelt, F., Heymann, B. and Gaub, H. [1997a]. Single molecule force spectroscopy on polysaccharides by atomic force microscopy, *Science* **275**: 1295–1297.

Rieu, P., Ueda, T., Haruda, I., Sharma, C. and Amin-Arnaout, M. [1994]. The a-domain of $\beta 2$ integrin cr3 is a receptor for the hookworm derived neutrophil adhesion inhibitor nif, *Journal of Cell Biology* **127**: 2081–2091.

Rigby-Singleton, S. [2002]. *Scanning probe and optical tweezers investigations of biomolecular interactions*, Phd thesis, School of Pharmaceutical Sciences, University of Nottingham.

Rigby-Singleton, S., Allen, S., Davies, M., Roberts, C., Tendler, S. and Williams, P. [2002]. Direct measurement of drug-enzyme interactions by atomic force microscopy; dihydrofolate reductase and methotrexate, *Journal of the Chemical Society, Perkin Trans.* **2**: 1722–1727.

Rippe, K., Guthold, M., von Hippel, P. and Bustamante, C. [1997]. Transcriptional activation via dna-looping: visualization of intermediates in the activation pathway of e. coli rna polymerase x sigma 54 holoenzyme by scanning force microscopy, *Journal of Molecular Biology* **270**: 125–138.

Rothlein, R. and Scharschmidt, L. [1994]. *Leukocyte adhesion in inflammation: from discovery to the clinic*, Vol. Adhesion molecules (Editor: CD Wegner) of *The handbook of immunopharmacology (Editor: C Page)*, Academic Press Limited, London, UK, chapter 1, pp. 1–8.

Rouzina, I. and Bloomfield, V. [2001a]. Force-induced melting of the dna double helix. 2. effect of solution conditions, *Biophysical Journal* **80**: 894–900.

Rouzina, I. and Bloomfield, V. [2001b]. Force-induced melting of the dna double helix.1. thermodynamic analysis, *Biophysical Journal* **80**: 882–893.

Rugar, D., Mamin, H., Guenther, P., Lambert, S., Stern, J., McFadyen, I. and Yogi, T. [1990]. Magnetic force microscopy - general principles and application to longitudinal recording media, *Journal of Applied Physics* **68**: 1169–1183.

Ryder, L., Sharples, C. and Lloyd, R. [1996]. Recombination-dependent growth in exonuclease-depleted recbc sbcbc strains of escherichia coli k-12, *Genetics* **143**(3): 1101–1114.

Saenger, W. [1984]. *Principles of nucleic acid structure*, 226 edn, Springer-Verlag, New York, USA.

Sakato-Sogawa, K., Kurachi, M., Sogawa, K., Fujii-Kuriyama, Y. and Tashiro, H. [1998]. Direct measurement of dna molecular length in solution using optical tweezers: detection looping due to binding protein interactions, *European Biophysical Journal* **27**: 55–61.

Scheuring, S., Ringler, P., Borgnia, M., Stahlberg, H., Müller, D., Agre, P. and Engel, A. [1999]. High resolution afm topographs of the *escherichia coli* water channel aquaporin z, *EMBO Journal* **18**(18): 4981–4987.

Schmidt, T., Schütz, G., Baumgartner, W., Gruber, H. and Schindler, H. [1996]. Imaging of single molecule diffusion, *Proceedings of the National Academy of Sciences of the USA* **93**: 2926–2929.

Schneider, B., Bradl, J., Kirsten, I., Hausmann, M. and Cremer, C. [1998]. High precision localization of fluorescent targets in the nanometer range by spatially modulated excitation fluorescence microscopy, *Fluorescence Microscopy and Fluorescent Probes* **2**: 63–68.

Schütz, G., Trabesinger, W. and Schmidt, T. [1998]. Direct observation of ligand colocalization on individual receptor molecules, *Biophysical Journal* **74**: 2223–2226.

Shao, Z., Mou, J., Czajkowsky, D., Yang, J. and Yuan, J.-Y. [1996]. Biological atomic force microscopy: what is achieved and what is needed, *Advances in Physics* **45**(1): 1–86.

Shappell, S. and Smith, C. [1994]. *Acute inflammatory response: granulpcyte migration and activation*, Vol. Adhesion Molecules of *The handbook of immunopharmacology (Editor: C Page)*, Academic Press Limited, London, UK, chapter 3, pp. 29–70.

Shepherd, G., Corey, D. and Block, S. [1990]. Actin cores of hair-cell stereocilia support myosin motility, *Proceedings of the National Academy of Sciences of the USA* **87**: 8627–8631.

Simmons, R., Finer, J., Chu, S. and Spudich, J. [1996]. Quantitative measurements of force and displacement using an optical trap, *Biophysical Journal* **70**: 1813–1822.

Singer, W., Bernet, S., Hecker, N. and Ritsch-Marte, M. [2000]. Three-dimensional force calibration of optical tweezers, *Journal of Modern Optics* **47**(14/15): 2921–2931.

Sivasankar, S., Subramaniam, S. and Leckband, D. [1998]. Direct molecular level measurements of the electrostatic properties of a protein surface, *Proceedings of the National Academy of Sciences of the USA* **95**: 12961–12966.

Smith, C. and Hollers, J. [1980]. Motility and adhesiveness in human neutrophils, *Journal of Clinical Investigations* **65**: 804–812.

Smith, S., Cui, Y. and Bustamante, C. [1996]. Overstretching b-dna: The elastic response of individual double-stranded and single-stranded dna molecules, *Science* **271**: 795–799.

Smith, S., Finzi, L. and Bustamante, C. [1992]. Direct mechanical measurements of the elasticity of single dna molecules by using magnetic beads, *Science* **258**: 1122–1126.

Sobel, E. and Harpst, J. [1991]. Effects of na^+ on the persistence length and excluded volume of t7-bacteriophage dna, *Biopolymers* **31**: 1559–1564.

Sokolov, I. Y., Henderson, G. and Wicks, F. [1997]. The contrast mechanism for true atomic resolution by afm in non-contact mode: quasi-non-contact mode?, *Surface Science Letters* **381**: 558–562.

Sperrazza, J., Register, J. I. and Griffith, J. [1984]. Electron microscopy can be used to measure dna supertwisting, *Gene* **31**: 17–22.

Stasiak, A., Capua, E. D. and Koller, T. [1981]. Elongation of duplex dna by reca protein, *Journal of Molecular Biology* **151**: 557–564.

Steubing, R., Cheng, S., Wright, W., Numajiri, Y. and Berns, M. [1991]. Laser induced cell fusion in combination with optical tweezers: the laser cell fusion trap, *Cytometry* **12**: 505–510.

Strick, T., Allemand, J., Bensimon, D., Bensimon, A. and Croquette, V. [1996]. The elasticity of a single supercoiled dna molecule, *Science* **271**: 1835–1837.

Strick, T., Allemand, J.-F., Bensimon, D. and Croquette, V. [1998]. Behavior of supercoiled dna, *Biophysical Journal* **74**: 2016–2028.

Strigl, M., Simson, D., Kacher, C. and Merkel, R. [1999]. Force-induced dissociation of single protein a-igg bonds, *Langmuir* **15**: 7316–7324.

Svoboda, K. and Block, S. [1994a]. Force and velocity for single kinesin molecules, *Cell* **77**: 773–784.

Svoboda, K. and Block, S. [1994b]. Biological applications of optical forces, *Annual Review of Biophysical Structure* **23**: 247–285.

Svoboda, K., Schmidt, C., Branton, D. and Block, S. [1992]. Conformation and elasticity of the isolated red blood cell membrane skeleton, *Biophysical Journal* **63**: 784–793.

Svoboda, K., Schmidt, C., Schnapp, B. and Block, S. [1993]. Direct observation of kinesin stepping by optical trapping interferometry, *Nature* **365**: 721–722.

Takagi, J. and Springer, T. [2002]. Integrin activation and structural rearrangement, *Immunological Reviews* **186**: 141–163.

Tanaka, H., Homma, K., Iwane, A., Katayama, E., Ikebe, R., Saito, J., Yanagida, T. and Ikebe, M. [2002]. The motor domain determines the large step of myosin-v, *Nature* **415**: 192–195.

Taquet, A., Labarbe, R. and Houssier, C. [1998]. Calorimetric investigation of ethidium and netropsin binding to chicken erythrocyte chromatin, *Biochemistry* **37**: 9119–9126. and references within.

Tees, D., Coenen, O. and Goldsmith, H. [1993]. Interaction forces between red blood cells agglutinated by antibody. iv. time and force dependence of break-up, *Biophysical Journal* **65**: 1318–1334.

Tees, D., Waugh, R. and Hammer, D. [2001]. A microcantilever device to assess the effect of force on the lifetime of selectin-carbohydrate bonds, *Biophysical Journal* **80**: 668–682.

Tha, S. and Goldsmith, H. [1988]. Interaction forces between red blood cells agglutinated by antibody. iii. micromanipulation, *Biophysical Journal* **53**: 677–687.

Tha, S., Shuster, J. and Goldsmith, H. [1986]. Interaction forces between red blood cells agglutinated by antibody. ii. measurement of hydrodynamic force of breakup, *Biophysical Journal* **50**: 1117–1126.

Thoumine, O., Kocian, P., Kottelat, A. and Meister, J.-J. [2000]. Short-term binding of fibroblasts to fibronection: optical tweezers experiments and probabilistic analysis, *European Biophysical Journal* **29**: 398–408.

Thundat, T., Zheng, X.-Y., Sharp, D., Allison, D., Warmack, R., Joy, D. and Ferrell, T. [1992]. Calibration of atomic force microscope tips using biomolecules, *Scanning Microscopy* **6**: 903–910.

Todd, R. I., Arnaout, M., Rosin, R., Crowley, C., Peters, W. and Babior, B. [1984]. Subcellular localization of the large subunit of mo1 ($mo1_1$; formerly gp110), a surface glycoprotein associated with neutrophil adhesion, *Journal of Clinical Investigation* **74**: 1280–1290.

Tonnesen, M., Smedley, L. and Henson, P. [1984]. Neutrophil-endothelial cell interactions: modulation of neutrophil adhesiveness induced by complement fragments c5a and c5a$_{desArg}$, and formyl-methionyl-leucyl-phenylalanine *in vitro*, *Journal of Clinical Investigations* **74**: 1581–1592.

Tonnesen, M., Smedly, L. and Henson, P. [1984]. Neutrophil-endothelial cell interactions, modulation of neutrophil adhesiveness induced by complement fragments c5a and c5a des arg and formyl-methionyl-leucyl-phenylalanine in vitro, *Journal of Clinical Investigation* **74**: 1581–1592.

Trifonov, E., Tan, R.-Z. and Harvey, S. [1987]. *Structure and expression*, Vol. 3, Adenine, chapter DNA bending and curvature, pp. 243–253.

Tskhovrebova, L., Trinick, J., Sleep, J. and Simmons, R. [1997]. Elasticity and unfolding of single molecules of the giant muscle protein titin, *Nature* **387**: 308–312.

Unger, V. [2001]. Electron cryomicroscopy methods, *Current Opinion in Structural Biology* **11**: 548–554.

Vale, R., Funatsu, T., Pierce, D., Harada, L. R. Y. and Yanagida, T. [1996]. Direct observation of single kinesin molecules moving along microtubules, *Nature* **380**: 451–453.

Veigel, C., Bartoo, M., White, D., Sparrow, J. and Molloy, J. [1998]. The stiffness of rabbit skeletal actomycin cross-bridges determined with an optical tweezers transducer, *Biophysical Journal* **75**: 1424–1438.

Vesenka, J., Guthold, M., Tang, C., Keller, D., Delaine, E. and Bustamante, C. [1992]. Substrate preparation for reliable imaging of dna molecules with scanning force microscope, *Ultramicroscopy* **42**(44): 1243–1249.

Vickery, S. and Dunn, R. [2001]. Combining afm and fret for high resolution fluorescence microscopy, *Journal of Microscopy* **202**(2): 408–412.

Vinckier, A., Heyvaert, I., D'Hoore, A., McKittrick, T., van Haesendonck, C., Engelborgs, Y. and Hellemans, L. [1995]. Immobilizing and imaging microtubules by atomic force microscopy, *Ultramicroscopy* **57**: 337–343.

Virella, G. [1999]. *Diagnostic evaluation of neutrophil function*, Imperial College Press, London, UK, chapter 8, pp. 275–297. in: The neutrophils: new outlook for old cells (Editor: DI Gabrilovich).

Visscher, K., Gross, S. and Block, S. [1996]. Construction of multiple-beam optical traps with nanometer-resolution position sensing, *IEEE Journal of Selected Topics in Quantum Electronics* **2**(4): 1066–1076.

Vologodskii, A. [1994]. Dna extension under the action of an external force, *Macromolecules* **27**: 5623–5625.

Vologodskii, A. and Cozzarelli, N. [1994a]. Supercoiling, knotting, looping and other large-scale conformational properties of dna, *Current Opinion in Structural Biology* **4**: 372–375.

Vologodskii, A. and Cozzarelli, N. [1994b]. Conformational and thermodynamic properties of supercoiled dna, *Annual Review of Biophysics and Biomolecular Structure* **23**: 609–643.

Walters, D., Cleveland, J., Thomson, N., Hansma, P., Wendman, M., Gurley, G. and Elings, V. [1996]. Short cantilevers for atomic force microscopy, *Review of Scientific Instruments* **67**(10): 3583–3590.

Wang, J. [1974]. The degree of unwinding of the dna helix by ethidium, i. titration of twisted pm2 dna molecules in alkaline cesium chloride density gradients, *Journal of Molecular Biology* **89**: 783–801.

Wang, M., Schnitzer, M., Yin, H., Landick, R., Gelles, J. and Block, S. [1998]. Force and velocity measured for single molecules of rna polymerase, *Science* **282**: 902–907.

Ward, B., Rehfuss, R., Goodisman, J. and Dabrowiak, J. [1988]. Determination of netropsin-dna binding constants from footprinting data, *Biochemistry* **27**: 1198–1205.

Wegner, M. and Grummt, F. [2001]. Netropsin, distamycin and berenil interact differentially with a high-affintiy binding site for the high mobility group protein hmg-i, *Biochemical and Biophysical Research Communications* **166**(3): 1110–1117.

Weiss, S. [1999]. Fluorescence spectroscopy of single biomolecules, *Science* **283**: 1676–1683.

White, J. [1969]. Self-linking and the gauss integral in higher dimensions, *American Journal of Mathematics* **91**: 693–728.

White, J., Amos, W. and Fordham, M. [1987]. An evaluation of confocal versus conventional imaging of biological structures by fluorescent light microscopy, *Journal of Cell Biology* **105**: 41–48.

Williams, C. and Wickramasinghe, H. [1986]. Scanning thermal profiler, *Applied Physics Letters* **49**: 1587–1589.

Wong, S., Joselevich, E., Woolley, A., Cheung, C. and Lieber, C. [1998]. Covalently functionalized nanotubes as nanometre-sized probes in chemistry and biology, *Nature* **394**: 52–55.

Wright, W., Sonek, G. and Berns, M. [1994]. Parametric study of forces on microspheres held by optical tweezers, *Applied Optics* **33**: 1735–1748.

Wuite, G., Smith, S., Young, M., Keller, D. and Bustamante, C. [2000]. Single-molecule studies of the effect of template tension on t7 dna polymerase activity, *Nature* **404**: 103–106.

Wyman, C., Grotkopp, E., Bustamante, C. and Nelson, H. [1995]. Determination of heat-shock transcription factor 2 stoichiometry at looped dna complexes using scanning force microscopy, *EMBO Journal* **14**: 117–123.

Wyman, C., Rombel, I., North, A., Bustamante, C. and Kustu, S. [1997]. Unusual oligomerization required for activity of ntrc, a bacterial enhancer-binding protein, *Science* **275**: 1658–1661.

Yin, H., Wang, M., Svoboda, K., Landick, R., Block, S. and Gelles, J. [1995]. Transcription against an applied force, *Science* **270**: 1653–1657.

Yuan, C., Chen, A., Kolb, P. and Moy, V. [2000]. Energy landscape of streptavidin-biotin complexes measured by atomic force microscopy, *Biochemistry* **39**: 10219–10223.

Zemánek, P., Jonáš, A., Šrámek, L. and Liška, M. [1998]. Optical trapping of rayleigh particles using a gaussian standing wave, *Optics Communications* **151**: 273–285.

Zhang, X., Wojcikiewicz, E. and Moy, V. [2002]. Force spectroscopy of the leukocyte function-associated antigen-1/intercellular adhesion molecule-1 interaction, *Biophysical Journal* **83**(4): 2270–2279.

Zweier, J. [1999]. *Mechanism of leukocyte accumulation in postischemic tissues: role of oxygen free radicals*, Vol. in: The neutrophils: new outlook for old cells (Editor: DI Gabrilovich), Imperial College Press, London, UK, chapter 3, pp. 59–77.